Non-adiabatic Photodissociation Dynamics of BrCl and BrNO

by

Hans - Peter Loock
Dipl.-Ing., University of Darmstadt, Germany, 1991

A Dissertation submitted in Partial Fulfillment of the
Requirements for the Degree of
DOCTOR OF PHILOSOPHY
in the Department of Chemistry

We accept this dissertation as conforming to the required standard

Dr. C. X. W. Qian, Supervisor (Department of Chemistry)

Dr. T. E. Gough, Departmental Member (Department of Chemistry)

Dr. D. A. Harrington, Departmental Member (Department of Chemistry)

Dr. A. Watton, Outside Member (Department of Physics)

Dr. J. W. Hepburn, External Examiner
(Department of Chemistry, University of Waterloo)

University of Victoria

Abstract

Photodissociation experiments on expansion cooled bromine chloride (BrCl) and nitrosyl bromide (BrNO) were conducted using a pump / probe scheme. Resonance-enhanced-multiphoton-ionization (REMPI) spectroscopy allowed for state selective ionization of the photofragments. Using time-of-flight mass spectrometry (TOF-MS), it was possible to make use of the **E**-**μ**-**v** vector correlation in order to identify, and characterize, the parent molecule's excited electronic states.

Photodissociation experiments on BrCl were carried out at six wavelengths between 500 nm and 389 nm. These experiments established the $Br^*(^2P_{1/2}) + Cl^*(^2P_{1/2})$ fragment channel as one of the diabatic dissociation limits of the B $^3\Pi(0^+)$ state. Application of the theory of diatomic dissociation as developed by Singer, Freed and Band (J. Chem. Phys., **79**, (1983), 6060) led to a new diabatic correlation diagram. This correlation diagram explained not only our experimental results well, but was also coherent with earlier experimental and theoretical investigations on other interhalogens.

The UV-Vis absorption spectrum of BrNO was recorded. At ten wavelengths between 740 nm and 225 nm photodissociation experiments were carried out. Guided by comparison with the well-studied ClNO dissociation dynamics, we propose the BrNO frontier orbitals and assign the absorption bands to the various low lying electronic transitions. The absorption from 740 nm to 370 nm is dominated by transitions to triplet states, which borrow intensity from the higher energy singlet state, S_5. A diabatic correlation diagram was constructed to aid an understanding of the photodissociation dynamics. These considerations combined with the recorded fragment quantum state distributions led to a qualitative understanding of the topology of the excited state potential energy surfaces.

Non-adiabatic interactions following excitation to the $T_5(A')$ state of BrNO were investigated and could be understood with our correlation diagram. We observed a strong correlation of the adiabaticity of the photodissociation process to the NO rotational levels.

This indicates that the interaction region of the $T_5(A')$ state with the S_3 and/or S_4 state is located early in the dissociation coordinate but late in the bending coordinate.

The lowest lying triplet state, T_1 absorbs *via* two vibrational adiabats which correlate to NO fragments in their v" = 0 and v" = 1 vibrational state, respectively. The NO rotational distribution is bimodal indicating that the excited state is rather shallow.

Following excitation at 355 nm a narrow oscillation of the spatial distribution from a $\cos^2\theta$ distribution to a $\sin^2\theta$ distribution was observed as a function of the NO rotational excitation. Assuming that this effect is due to an interference betwen different excitation/dissociation pathways, two tentative explanations based on the new correlation diagram are offered.

Examiners:

Dr. C. X. W. Qian, Supervisor (Department of Chemistry)

Dr. T. E. Gough, Departmental Member (Department of Chemistry)

Dr. D. A. Harrington, Departmental Member (Department of Chemistry)

Dr. A. Watton, Outside Member (Department of Physics)

Dr. J. W. Hepburn, External Examiner (Department of Chemistry, University of Waterloo)

Table of Contents

List of Tables

Table of Figures

Acknowledgements

Many people contributed to this dissertation. I am especially grateful to

- Dr. Charles X. W. Qian for his continous advice, support, encouragement and friendship.

- Bob Jianying Cao for his help in conducting the photodissociation experiments. Bob contributed to the interfacing of the experimental apparatus, the writing of the TOF-profile fitting routine, and helped with the analysis and interpretation of the data. He is a great person to work with.

- The members and former members of Dr. Charles Qian's research group, Dr. Chi Zhou and Dr. Yifei Wang, as well as Roy Jensen, Michael Vasseur and Will Long for many instructive discussions and the friendly atmosphere they created in the lab.

- Garth Irwin, Pedro Montoya and Daniela Heberle for proofreading this dissertation and many valuable comments.

- Dr. Terence Gough for his comments concerning the time-independent view of non-adiabatic interactions.

Für Daniela

1 Introduction

"Chemistry is the science of the causes and effects of electron addition, subtraction and redistribution on atoms and molecules." (translated from *Meyer's Taschenlexikon*)

Chemical reactions as described in the above quote from an encyclopedia form the core of chemistry. Only the simplest reactions, however, can be described in full detail by theoretical means that are based on first -- quantum mechanical -- principles. An understanding of the physical principles, that underly the "redistribution of electrons", is necessary, if one wants to predict the outcome of chemical reactions.

In an attempt to gain insight about these physical principles one often turns to simplified and idealized systems. The knowledge gained from the study of these systems can then be applied to more complicated and realistic cases.

As a prototypical chemical reaction, consider a collision of a diatomic molecule (or radical) AB with an atom C leading to formation of the products A and BC (scheme 1a). Detailed information about this process, such as spatial distribution, kinetic and internal energy of the products is, to a large extent, dictated by the electronic structure of the unstable intermediate $ABC^{\#}$. In particular, the nuclear motion, which determines the energy redistribution is governed by the potential energy surfaces (PESs) of this unstable complex. Thus, with the knowledge of all relevant electronic states of $ABC^{\#}$ and their energy dependence on the nuclear coordinates (the PES), one can, in principle, predict the outcome of *any* reaction that contains $ABC^{\#}$ as an unstable intermediate.

Inelastic collision processes (scheme 1c) are mediated by the same PES as the reactive collision processes. Here, no bond will be broken or formed, but the colliding particles will exchange energy, and hence their quantum state distribution will change. The atomic and molecular quantum numbers are collectively notated "i" and "j" in the scheme. Electronic quenching, which is the process of converting electronic excitation into internal or translational motion, is important in research areas such as atmospheric chemistry and laser

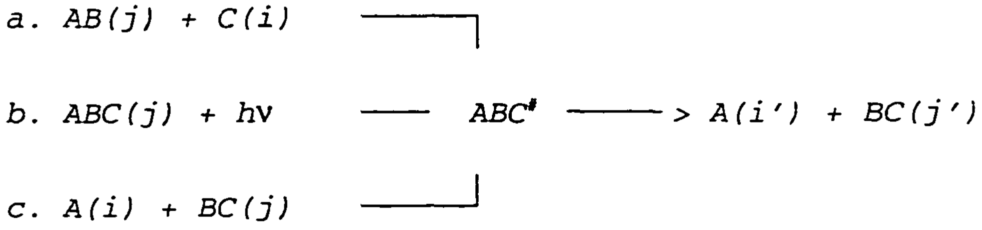

Scheme 1: Processes that are mediated by an unstable excited complex: a. reactive collision; b. photodissociation; c. inelastic collision.

action.

An alternative and "cleaner" route to form the unstable complex $ABC^{\#}$ is by electronic excitation of the stable molecule ABC using visible or near-UV radiation[1]. By adjusting the excitation wavelength one can selectively excite the electronic state(s), that one is interested in. In this way it is possible to initiate the fragmentation process on a single PES and, hence, with a well defined initial state. Performance of such photodissociation experiments in a collision-free environment and preparation of the sample in known quantum states allow for nearly perfectly defined initial conditions. Technically this is usually achieved by supersonic expansion of the sample compound into high vacuum chambers and consequent adiabatic cooling of the molecules. Given that the parent molecule's quantum state is well defined, one can obtain true "state-to-state correlations" by measuring the photofragments kinetic and internal energy distribution. Due to the enormous advances in laser technology over the past decades much progress has been made towards perfection of the fragment detection techniques, and today a variety of

---

[1] A successful alternative to electronic excitation of a stable molecule ABC, is the electron photodetachment of a stable anion ABC^- (105,106). This technique allows the spectroscopic study of complexes $ABC^{\#}$, that do not have a stable neutral ground state and also accesses a different and often more chemically relevant region of the PESs.

techniques is employed. Finally, by combining the experimental information with theoretical investigations, it becomes possible to identify and characterize the excited state PESs.

Knowledge of the excited state PES is important not only with respect to collisional processes; photodissociation processes form an interesting and important class of reactions by themself. Many atmospheric reactions are photoinitiated and a quantification of photodissociation cross sections is crucial for an in depth understanding of atmospheric chemistry. For example, a recent study of ozone photodissociation(1, 2) helped to elucidate the ozone "deficit" in the stratosphere and yielded a more accurate picture of ozone decomposition pathways.

Electronic spectroscopy can be viewed as a counterpart of photodissociation studies, since it probes the bound (not repulsive) electronically excited states and hence the *stable* complexes $ABC^{\#}$ (Figure 1). Information about the energy levels formed in the bound parts of excited states often leads to a very accurate -- and sometimes analytical -- description of the PESs. Photodissociation studies, in contrast, yield information about the repulsive parts of the PESs. Although a larger number of PESs can be studied in this way, the information gained is often less quantitative compared to spectroscopic data. By combination of the two complementary experimental approaches, spectroscopic and photodissociative, one can obtain a complete picture of the excited state PESs.

In this work, photodissociation experiments will be used in order to gain information about the excited electronic states, their interactions, the potential energy surfaces they form, and the dynamic processes, which take place on such PESs. Consideration of spectroscopic and theoretical studies will aid in the understanding of the molecular dynamics. Comparative studies between molecules of similar electronic structures will prove very useful in understanding the influence of such structure on the dissociation dynamics.

The diatomic molecule BrCl and the triatomic molecule BrNO were chosen, because a large body of information already exists on interhalogen molecules and nitrosylhalides, thereby allowing for comparison with similar molecules. The dynamics of these two

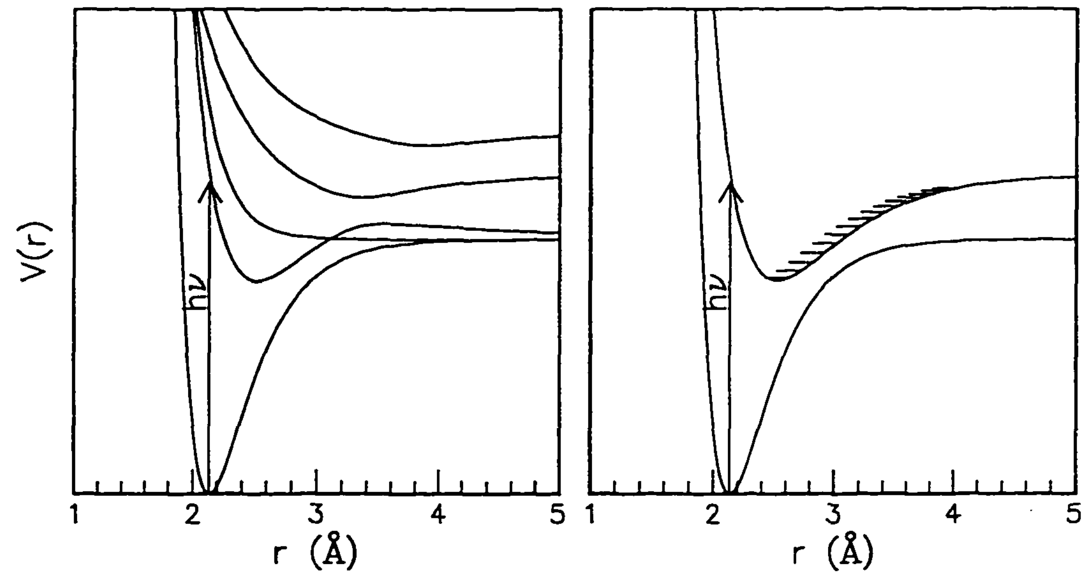

Figure 1: Photodissociation dynamics and spectroscopy of electronically excited states

particular molecules, on the other hand, have not been studied in much detail, although they both possess a large number of repulsive excited electronic states. These electronic states are strongly interacting due to the large spin-orbit coupling term introduced by the bromine atom. It is convenient that these PESs are easily accessible by visible or near-UV laser radiation and both molecules are safe to work with and easy to prepare.

1.1 Dissociation dynamics: classical and quantum mechanical descriptions

1.1.1 Classical models of energy redistribution

When a molecule is excited to a repulsive electronic state and falls apart, energy conservation requires that the excitation energy is matched by the fragment's internal and kinetic energy. There is, however, no simple rule for the partitioning of energy among the various translational, rotational, vibrational and electronic degrees of freedom. The study of the partitioning of the excess energy among the various degrees of freedom provides valuable clues about the nature of the photodissociation process. This section addresses several approaches that are used in explaining the excess energy redistribution.

The large majority of photodissociation studies reported to date deal with the excitation and subsequent fragmentation of a neutral, closed shell molecule. If one chemical bond in such a molecule cleaves homolytically, two radical fragments are formed. Since the spin of the unpaired electron in these fragments can "align" either parallel or antiparallel to the orbital angular momentum, each of the two fragments can have two energetically different spin-orbit states. One therefore has to consider *four* fragmentation channels. The magnitude of the spin-orbit energy, i.e., the energy needed to promote the radical fragment from its spin-orbit ground state to the excited state, depends on the nature of the molecular electronic wavefunction(3). The spin-orbit coupling increases with the mass of the atoms involved. Table 1 lists the spin-orbit enrgies for atoms and molecular radicals, which are relevant in this study.

In addition to the electronic degrees of freedom one also has to consider the internal and the translational degrees of freedom. For a diatomic molecule, energy partitioning appears to be relatively simple. The available excess energy, i.e., the difference between excitation and dissociation energies,

$$E_{avail} = E_{h\nu} - D_0 = E_{el} + E_{kin} \tag{1}$$

can only be distributed between translation and the electronic degrees of freedom. While this simplifies the process considerably, the problem of predicting the fine structure branching ratio is nevertheless quite complicated. A large portion of this thesis is directed towards an understanding of the processes, which govern the distribution of fragments among the four exit channels.

Of course, introduction of additional degrees of freedom in larger polyatomic molecules does not simplify the problem. Triatomic molecules, for example, must be described using *three* normal mode (or alternatively: Jacobian) coordinates, resulting in a four-dimensional PES. The nuclear motion on an

X•	A (cm^{-1})
NO	123
F	440
Cl	881
Br	3685
I	7660

Table 1: Spin-orbit energies

excited state PES is almost always represented by a nontrivial coupling between these coordinates. For the most detailed description of a dissociation process one has to consider the motion of a wavepacket on a multidimensional PES, an undertaking which is often limited by the difficulty in obtaining accurate excited state PESs. Very few *ab initio* packages are able to produce reliable excited state surfaces and the improvement of existing theories and algorithms is an active area of research.

However, there also exists a number of reasonably accurate models, which use a combination of quantum theory and classical mechanics to describe complex dissociation processes. These models describe the redistribution of excess energy among the electronic, vibrational, rotational and translational degrees of freedom in the dissociating molecule. In this way one can predict the quantum state distributions of the photofragments. In the following paragraphs a brief description of these models will be given.

Statistical theories require no knowledge about the excited state PES. It is assumed that the lifetime of the excited state complex is long compared to the time necessary for excess energy redistribution among the available degrees of freedom. This implies that the dissociation process is slow enough to allow for ("thermal") equilibration of the internal energy. All quantum states of the excited state complex are populated according to their statistical weight and after the bond cleavage the photofragment internal state distribution will reflect the parent molecule's state distribution. The most widely used statistical theories are the Rice-Ramsberger-Kassel-Marcus (RRKM) theory(4, 5) and the Phase Space Theory (PST)(6). More recent developments are the Separate Statistical Ensemble (SSE)(7) method, which restricts the energy flow to selected degrees of freedom and the prior distribution method(8), which lifts the constraint of angular momentum conservation. All statistical theories require that the mean lifetime of the excited state is comparable to the timespan of vibrational energy redistribution, a condition that is rarely fulfilled in the dissociation dynamics of small molecules. Even for van der Waals molecules, which have remarkably long lived excited states, energy redistribution is too slow, because of the low density of states and the weak coupling between the various modes. Triatomic molecules, which dissociate fast *and* have a low density of states, will certainly show non-statistical photofragment internal energy distributions.

The *impulsive model*(9) also does not require any information about the excited state PES or even the electronic structure of the molecule. It is assumed that, upon breaking the bond, the sudden release of energy will create a torque, which induces rotation of the fragments. Using classical mechanics and the relevant force constants the vibrational excitation of the fragments may also be calculated. However, since the impulsive model completely neglects the angular dependence of the excited state PES, it is rarely capable of reproducing or predicting experimental results. For instance, in a bent triatomic molecule the impulsive model always predicts an initial closing of the bending angle - an assumption which is not true in many cases.

Very recently a combination of the impulsive model and statistical theory has been presented. North *et al.*(10) introduced the *barrier impulsive model* (BIM), to describe the photodissociation of acetone. It was assumed that the available energy of a reaction, which has a large barrier to recombination, is divided into two "energy reservoirs"; one of which is denoted statistical and the other one impulsive. Once the molecule has travelled beyond the transition state, or barrier, the kinetic energy will be localized in the dissociation coordinate and can be described by the impulsive model. The remaining energy is partitioned among the product degrees of freedom according to the statistical methods. The impulsive energy is therefore not dependent on the available energy but on the barrier height for recombination.

The *Franck-Condon model* is used to estimate the rovibrational distribution in the dissociation of small molecules. The parent molecular (bending) wavefunctions are expanded in terms of the final dissociative state wavefunctions. The squares of the expansion coefficients give the partial cross sections of each rotational state, and thus the rotational distribution. Since the harmonic oscillator wavefunction is symmetric around the equilibrium angle, the FC-model will predict equal probabilities of angle opening and closing. In a modified version of this model(11) exit channel interactions are included and thereby the anisotropy of the excited state PES is accounted for.

The vibrational and rotational *reflection principle*(9) has found many applications in photodissociation processes. Just as the slope of an electronically excited state can be accurately estimated from the width of the absorption bands and the width of the ground state wavefunction, one can also obtain the vibrational and rotational photofragment state distribution by reflecting the square of the bending wavefunction on a previously calculated excitation function. The excitation function is obtained from a number of classical trajectory calculations on a calculated or estimated PES. The reflection principles combine quantum mechanical characteristics with classical calculations and work best if the excited state is a simple non-interacting low-dimensional PES.

However, for modelling of many photodissociation processes of small molecules one often has to determine the excited state PES and calculate the product state distributions by classical or quantum procedures. Once an initial guess of the PES is obtained, e.g. by low level *ab initio* calculations, improvement through comparison with experimental results is possible. Very often *classical trajectory calculations* can be used to obtain a photofragment state distribution. Ehrenfest's theorem(9) states that the path of the maximum of the propagating wavepacket can, to a good approximation, be described by a classical trajectory. Similarly the product state distribution can be calculated using a swarm of trajectories, which have been properly weighted according to the probability density function of the ground state wavefunction projected onto the Franck-Condon region (Wigner distribution).

None of the simple models described above is able to predict the outcome of the photodissociation processes of *all* molecules. In the following section the more rigourous quantum-mechanical methods will be introduced.

1.1.2 Quantum mechanical picture: time-dependent and time-independent view

Two complementary views on excited state dynamic processes -- the time-dependent and the time-independent approach -- will be presented in the coming paragraphs. In this discussion it will be assumed that an accurate PES for the excited state under study has already been obtained. This is, in fact, a rather outrageous assumption, since excited state PES are notoriously difficult to calculate and large efforts are still going into improvement of the theoretical methods of determination of the PES. Because excited states are often closely spaced and extensively mixed, one has to accurately account for correlation energy. Apart from the elaborate full *configuration interaction* method only the most sophisticated theoretical methods are able to produce reliable PES. It will also be assumed, that the dissociation process is confined to only one PES, which is not perturbed by other excited states. In the next section this restriction will be lifted and non-adiabatic processes will be discussed.

Exact calculation of the product state distribution in a photodissociation process is equivalent to determining the excited state wavefunctions and transforming them into the "free fragments" limit. Here, one can use the time-independent approach and solve for the various wavefunctions labelled n as functions of the nuclear coordinates Q at a preselected energy E_f,

$$0 = \left[\hat{H}(Q,n) - E_f\right]\Psi(Q,n) \tag{2}$$

Alternatively, one can use the time-dependent approach

$$0 = \left[i\hbar\frac{\partial}{\partial t}\ \hat{H}(Q,n)\right]\Phi(Q,n,t) \tag{3}$$

at a preselected time t. The two wavefunctions are related by the time-evolution operator

$$\Phi(Q,t,n) = \exp\left(-\frac{iE_f t}{\hbar}\right)\Psi(Q,n) \tag{4}$$

In photodissociation and scattering studies it is most convenient not to use normal coordinates, but Jacobian coordinates. For a triatomic molecule an illustration of this body

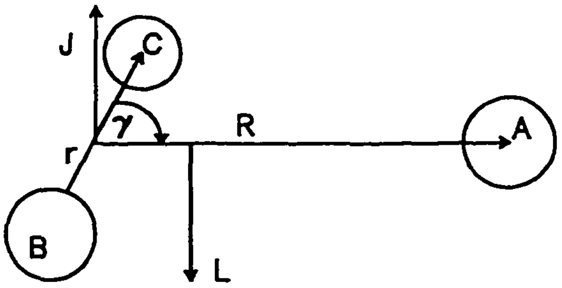

Figure 2: Jacobian coordinates for the molecule ABC.

fixed system is given in Figure 2. The dissociation coordinate **R** connects the atom *A* with the centre of mass of the diatomic moiety. The diatomic angular momentum **J** is balanced by the total angular momentum **L**.

The Hamiltonian in these coordinates is

$$\hat{H}(R,\gamma,r) = -\frac{\hbar^2}{2\mu_{A-BC}R}\frac{\partial^2}{\partial R^2}R + \frac{1}{2\mu_{A-BC}R^2}\hat{L} - \frac{\hbar^2}{2\mu_{B-C}r}\frac{\partial^2}{\partial r^2}r + \frac{1}{2\mu_{B-C}r^2}\hat{J} + V(R,\gamma,r) \qquad (5)$$

where the Hamiltonian

$$\hat{h}(r) = -\frac{\hbar^2}{2\mu_{B-C}r}\frac{\partial^2}{\partial r^2}r + V_{BC}(r) \qquad (6)$$

describes the internal vibration of the diatomic moiety BC. Often the diatomics internuclear distance r can assumed to be constant at the free fragments equilibrium position r_e. In this rigid-rotor approximation the Hamiltonian depends only on R and the Jacobian bending angle γ.

The potential energy surface V(R, γ, r) in the above equation describes the coupling between the coordinates and can be divided in the diatomic potential for internal vibration and the fragment interaction potential

$$V_{A-BC}(R,\gamma,r) = V(R,\gamma,r) - V_{BC}(r) \qquad (7)$$

This interaction potential approaches a constant value (which is usually defined as zero) in the limit of infinite fragment separation.

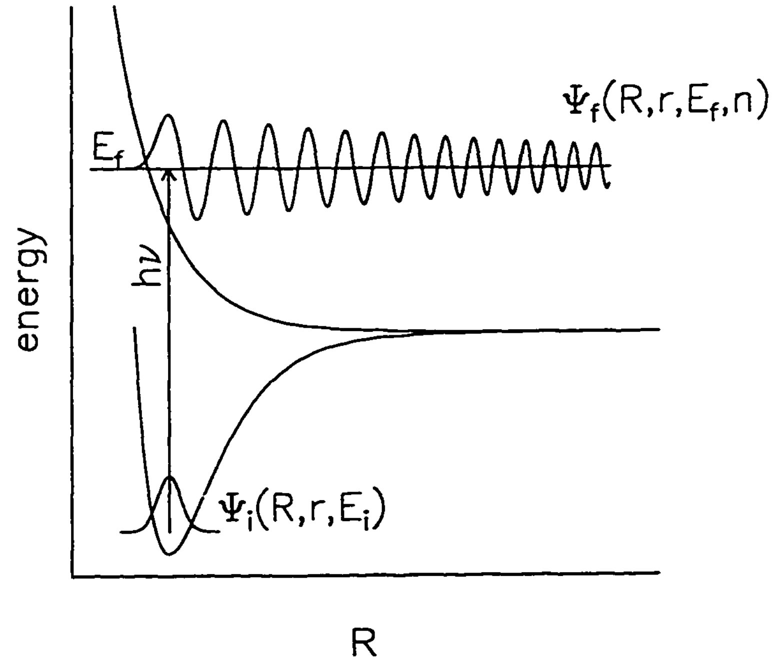

Figure 3: Time-independent view of photodissociation

$$\lim_{R \to \infty} V_{A\text{-}BC}(R,\gamma,r) = 0 \tag{8}$$

Solving the *time-independent* Schrödinger equation for a given energy term yields a set of wavefunctions $\Psi(E_f, R, r, n)$, which describes the degenerate and independent solutions for the various vibrational and fine structure states (Figure 3). All $\Psi(E_f, R, r, n)$ are restricted by two boundary conditions: they must transform into the fragment wavefunctions at infinite separation and they must vanish at $R = 0$. As more than one solution for the time-independent Schrödinger equation exists, it is clear that the photofragments will form a distribution of vibrational states. These were labelled "*n*" in equation (4). The partial photodissociation cross section of one such state can be determined using the relation⁽⁹⁾

$$\sigma(\omega,n) = \frac{1}{2\hbar^2 \varepsilon_0 c} E_{photon} |t(E_f,n)|^2 \tag{9}$$

Where $t\,(E_f,\, n)$ is the partial photodissociation amplitude

$$t(E_f,n) = \langle \Psi_f(R,r,E_f,n) | \mu_{fi}^{(e)}(R,r) | \Psi_i(R,r,E_i) \rangle \qquad (10)$$

Here E_{photon} is the excitation energy to the Ψ_f continuum state, and Ψ_i denotes the parent ground state wavefunction. The transition dipole moment operator $\mu_{fi}^{(e)}$ is not easy to evaluate, since it is a function of both ground state and excited state. Equation (10) is a variant of Fermi's Golden Rule(9) adapted for photodissociation processes.

Summation over the partial cross sections gives the total photodissociation cross section

$$\sigma_{tot}(\omega) = \sum_n \sigma(\omega,n) \qquad (11)$$

Alternatively the dissociation process can be described using a *time-dependent* view. In this picture a wavepacket is created at t_0 in the Franck-Condon region on the excited state PES and evolves on this PES as time proceeds (Figure 4). The excitation process is usually idealized by assuming that it is infinitely short and thus only mediated by the transition dipole function.

$$\Phi_f(R,r,t_0) = \mu_{fi}^{(e)} \Psi_i(R,r,E_i) \qquad (12)$$

The wavepacket is a coherent superposition of stationary states $\Psi(E_f, R, r, n)$, with each state being multiplied by the time evolution factor $exp(-iE_f t / \hbar)$. At each time t the energy distribution, i.e., the sampling of the $\Psi(E_f, R, r, n)$, will be different (Figure 4). The time dependent view is more likely to resemble the intuitive classical picture of a molecule, which follows the contour of a PES on its way to separation[2].

---

[2] Recent ultra-short excitation and detection schemes have allowed for probing of the wavepacket as it moves along the excited state PES(107-109). Femtosecond laser pulses generate a coherent superposition of several excited states. This is in contrast to the infinite number of states generated by a hypothetically infinitely short pulse and the single state prepared by a long laser pulse. The wavetrain that is formed is then interrogated by a second delayed femtosecond pulse. If the PESs are known, experimental "snapshots" of the photodissociation process are obtained.

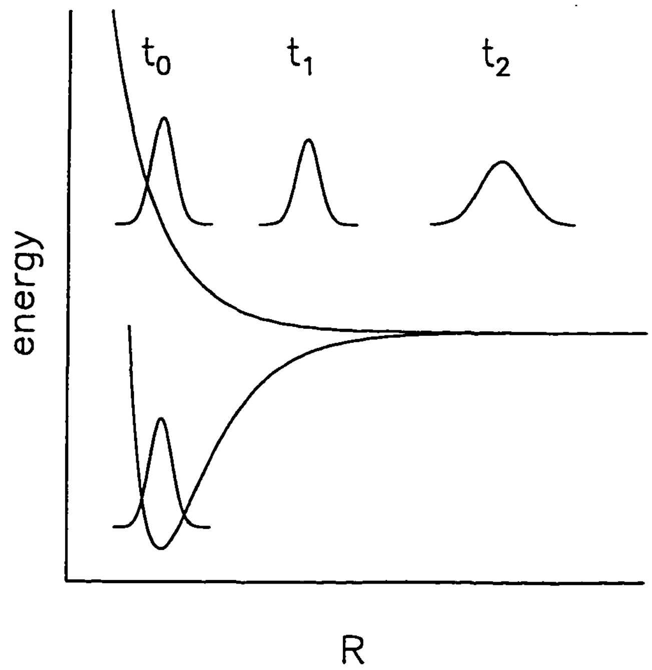

Figure 4: Time-dependent view of photodissociation

The time-dependent and the time-independent pictures are equivalent. In the time-dependent picture the energy is fixed and the wavefunction contains the complete temporal behaviour of the dynamical process, i.e., the uncertainty of time is infinite. In the time-dependent picture snapshots are taken at a given "sharp" time t and each wavepacket contains the complete energy range.

The time-independent *total* dissociation wavefunction $\Psi(E_f)$ is just the Fourier transform of the time dependent wavepacket $\Phi(t)$

$$\Psi_{tot}(E_f) = \int exp\left(\frac{iE_f t}{\hbar}\right)\Phi_f(t)\,dt \tag{13}$$

The considerations that were briefly outlined above are not limited to photodissociation studies. Other dynamical processes such as predissociation or even excitation to a bound part of the PES are often described with the time-dependent formalism in alternation with the more commonly used time-independent view. However, on a bound PES in the time-dependent view, we will observe recurrences of the wavepacket. In an idealized case of a bound-to-bound transition with an excited state of infinite lifetime, all energies, except the resonance energy, will vanish due to destructive interference.

1.1.3 Non-adiabatic interactions

In the previous discussion of dynamical processes on excited state PESs it was assumed that the molecular dynamics are governed by a single excited state PES. However, the excited states of all molecules are mixed to some extent. Even though a fragmentation process may be initiated on a single PES, crossings with other states often lead to a "hopping over" to other PESs. This process is schematically illustrated in Figure 5. Excitation to the repulsive limb of the lower excited state yields fragments evolving through both the lower and higher exit channels. The dissociation process *via* the lower exit channel is termed "adiabatic" and takes place on the adiabatic PES, whereas the process of hopping to the higher adiabatic PES is called "non-adiabatic" and takes place on the diabatic PES[3]. Both sets of PESs, the adiabatic and the diabatic, are included in Figure 5.

The probability of hopping to another adiabatic surface depends on the time which the molecule spends in the interaction region and thereby indirectly on the excitation energy. It also depends on the magnitude of the energy gap between the adiabatic PES.

Non-adiabatic interactions are a consequence of the breakdown of the Born-Oppenheimer approximation. In the following discussion we will therefore start with a review of the Born-Oppenheimer approximation, define the adiabatic and diabatic PESs and present the Landau-Zener equation of the hopping probability. Finally, the non-adiabatic interactions will be discussed using the time-dependent and the time-independent picture of the

---

[3] διαβαῖνω : to go through; to pass over

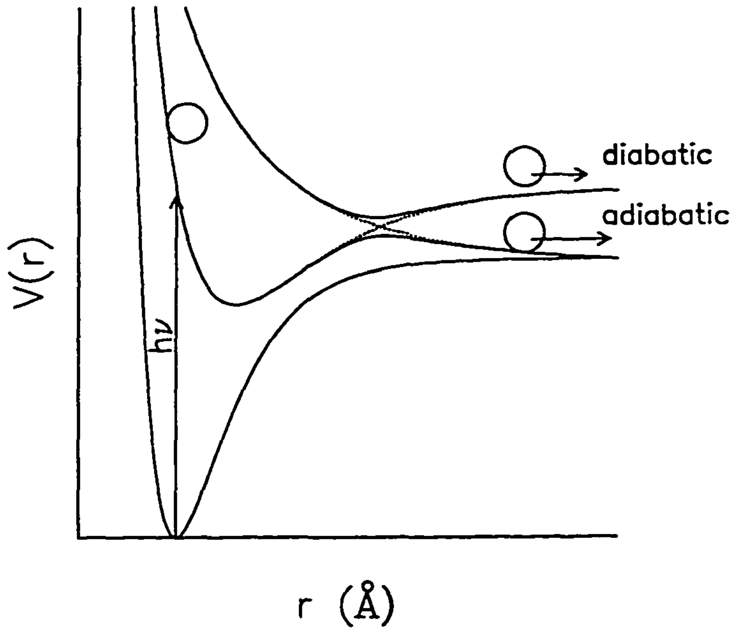

Figure 5: Simple representation of diabatic and adiabatic dissociation processes: Photodissociation on adiabatic PES (solid) and diabatic PES (dotted) leads to different products.

photodissociation dynamics.

The Schrödinger equation for a dynamical molecular system

$$\langle \Psi | \hat{H}_{tot} | \Psi \rangle = E_{tot} \tag{14}$$

contains the full Hamiltonian

$$\hat{H}_{tot} = \hat{H}_{el} + \hat{H}_{rot} + \hat{T}^{N}(R) \tag{15}$$

The nuclear kinetic energy operator $T^N(R)$ governs the motion of the nuclei with respect to each other, whereas the rotational Hamiltonian H_{rot} describes the rotation of the molecule as a whole. In the Born-Oppenheimer approximation it is assumed, that the electrons are moving in a static field defined by the positions and charges of the nuclei(12). This is equivalent to assuming that the motion of the electrons is much faster than the motion of the nuclei. In this approximation the nuclear part of the wavefunction can be separated from the electronic part. The electronic component

$$\langle \psi_{el}(q) | \hat{H}_{el} | \psi_{el}(q) \rangle = E_{el} \tag{16}$$

with the Hamiltonian

$$\hat{H}_{el} = -\sum_{i=1}^{N} \frac{1}{2} \nabla_i^2 - \sum_{i=1}^{N} \sum_{A=1}^{M} \frac{Z_A}{r_{iA}} + \sum_{i=1}^{N} \sum_{j>i}^{N} \frac{1}{r_{ij}} \tag{17}$$

describes the motion of the electrons in terms of their kinetic energy, their attraction to the nuclei and their electrostatic repulsion from the other electrons. The eigenvalues for the electronic energy will therefore depend parametrically on the nuclear coordinates and can be calculated for any given molecular geometry. The *total* energy of the fixed nuclei system also includes the Coulombic repulsion of the nuclei

$$E_{tot} \approx E_{el} + \sum_{A=1}^{M} \sum_{B>A}^{M} \frac{Z_A Z_B}{R_{AB}} \tag{18}$$

The Born-Oppenheimer approximation is only valid if the electronic component is considered dependent only on the position of the nuclei and not on their momentum.

For fast dynamical processes this approximation often breaks down. The couplings between nuclear and electronic degrees of freedom can be divided into two categories. The interaction between the excited states can be caused by spin-orbit coupling, or - in polyatomic molecules - by vibronic and/or Coriolis coupling.

In the second category the coupling between nuclear and electronic component is caused by rotation and vibration of the dissociating molecule. This kind of coupling can be observed, when a change in molecular symmetry takes place. For instance, bending of a linear polyatomic molecule will split the doubly degenerate Π state into a pair of A' and A" states, and electron-nuclear vibronic interactions will couple these two PESs. This is known as the Renner-Teller effect in molecular spectroscopy. Dixon(13) has presented a detailed account of this type of non-adiabatic dissociation.

In this dissertation another type of interaction, caused by spin-orbit coupling, will be discussed. The spin-orbit operator couples orbital angular momentum and electron spin. Since the spin-orbit coupling is *independent* of the nuclei's motion one can solve the resulting equations still in the Born-Oppenheimer framework and obtain the energetically lowest state of the system (the adiabatic PES). In a dynamic process, however, the kinetic energy may be of the same magnitude or larger than the spin-orbit coupling. In this case, the diabatic representation is more appropriate. Here one must calculate the interactions occurring at the individual points on a particular trajectory(9). These interactions are strongest between states (i) and (j) of identical symmetry (i.e., identical Λ, Σ and S). Usually one tries to find eigenfunctions of the total Hamiltonian which include both the nuclear kinetic energy operator $T^N(R)$ and the electronic Hamiltonian.

$$\langle\Psi_i|\hat{H}|\Psi_j\rangle = \langle\Psi_i|\hat{H}_{el}|\Psi_j\rangle + \langle\Psi_i|\hat{T}^N|\Psi_j\rangle \tag{19}$$

To obtain the excited state energy one would want to find a set of orbital functions, Ψ_i, that reduces the off-diagonal matrix elements in both terms. But in the case of fast processes it is found that only one term can be diagonalized at a time(3).

The *diabatic* set of wavefunctions yield a diagonal "nuclear motion matrix"

$$\langle\Psi_i^{diab}|\hat{T}^N|\Psi_j^{diab}\rangle = \delta_{ij}V^{diab} \tag{20}$$

but then the electronic component contains off-diagonal terms between the electronic states

$$\langle\Psi_i^{diab}|\hat{H}^{el}|\Psi_j^{diab}\rangle = H_{ij} \tag{21}$$

The interacting term H_{ij} is for molecules containing a heavy atom (such as bromine) predominantly the spin-orbit coupling term mentioned above. Note that these diabatic states can cross, since the non-crossing rule between states of the same symmetry only applies for exact solutions of the electronic Hamiltonian.

In the *adiabatic* representation the situation is reversed and the electronic Hamiltonian eigenfunctions contain only zero off-diagonal elements

$$\begin{aligned} \langle \Psi_i^{adiab} | \hat{T}^N | \Psi_j^{adiab} \rangle &= W_{ij}^{el}(R) \\ \langle \Psi_i^{adiab} | \hat{H}^{el} | \Psi_j^{adiab} \rangle &= \delta_{ij} V^{adiab} \end{aligned} \tag{22}$$

These are the functions that were considered in the discussion of the Born-Oppenheimer approximation above. Since the adiabatic wavefunctions are exact solutions of the electronic Hamiltonian, the noncrossing rule applies to them and an avoided crossing results whenever two states of the same symmetry approach. Therefore, the ordering of the adiabatic states is determined only by their energy. However, upon adiabatic passage through the interaction region the overall character of the electronic wavefunction might change considerably.

From this brief discussion it is evident that there are two ways to generate the two sets of potential energy surfaces. One can calculate the *adiabatic* states by one of the more sophisticated *ab initio* methods thereby accounting for spin-orbit coupling. An estimated "adiabatic coupling matrix element" W^{el}_{ij} (R) is then used to obtain the diabatic curves⁽³⁾

$$\langle \Psi_i^{adiab} | \hat{T}^N | \Psi_j^{adiab} \rangle = W_{el}(R) \approx \frac{a(R) H_{ij}}{4(H_{ij})^2 + a(R)^2 (R-R_c)^2} \tag{23}$$

with

$$a(R) = \frac{V_i^{diab} - V_j^{diab}}{R - R_C} \tag{24}$$

Here the diabatic potential in the interaction region is defined by equation (20). The magnitude of the off-diagonal matrix elements H_{ij} is determined by the characteristics of the operator (e.g. spin-orbit operator) employed in obtaining the adiabatic curves. From equation (23) it is apparent that the coordinate dependence of the non-adiabatic coupling matrix elements is of the Lorentzian type, when the diabatic potentials are assumed to be linear in the intersection region.

Alternatively the *diabatic* eigenfunctions of the T^N operator can be computed and equation (25), below, can be used to derive the adiabatic curves. In a two state crossing problem

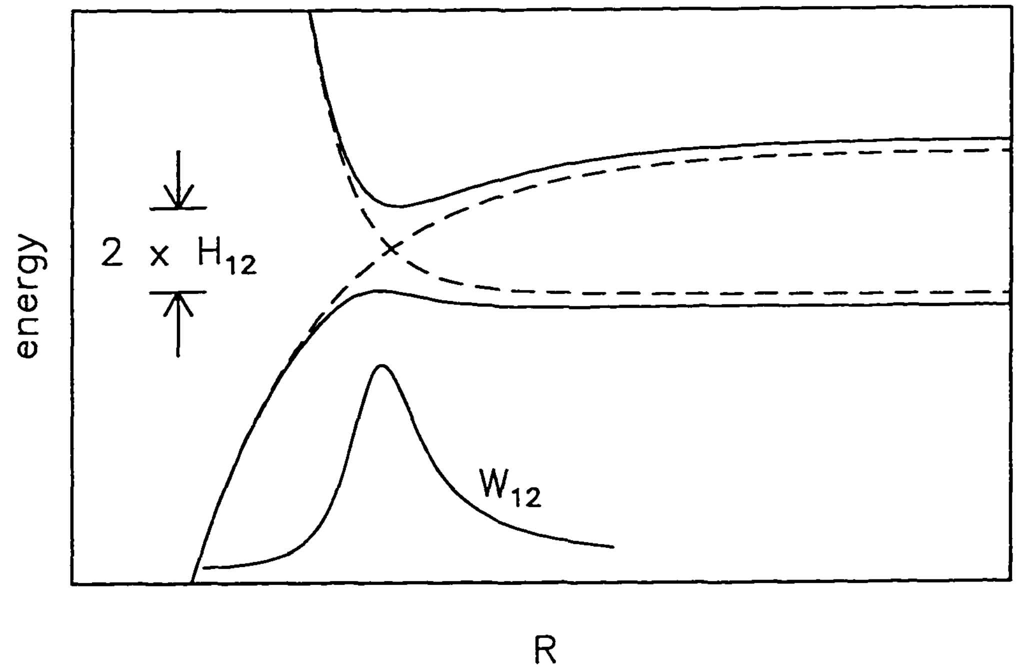

Figure 6: Schematic illustration of the adiabatic (solid lines) and diabatic (dashed) curves and the coupling matrix element W_{el} *(R)* (solid).

the adiabatic functions are the solutions of the secular equation

$$\begin{vmatrix} V_i^{diab}(R)-V^{adiab} & H_{ij} \\ H_{ij} & V_j^{diab}(R)-V^{adiab} \end{vmatrix} = 0 \qquad (25)$$

The non-adiabatic contribution $W_{el}(R)$ along with the diabatic and adiabatic curves are displayed for a general case in Figure 6.

The diabatic and adiabatic representations are clearly two limiting cases if the Born-Oppenheimer approximation breaks down. Although, strictly speaking, unique PESs are no longer defined for the intermediate cases, the concept of PESs clearly helps in understanding inelastic scattering processes or photodissociation dynamics. The non-adiabatic effect can be studied in both the time-dependent and in the time-independent framework. In the following paragraphs both views will be briefly presented.

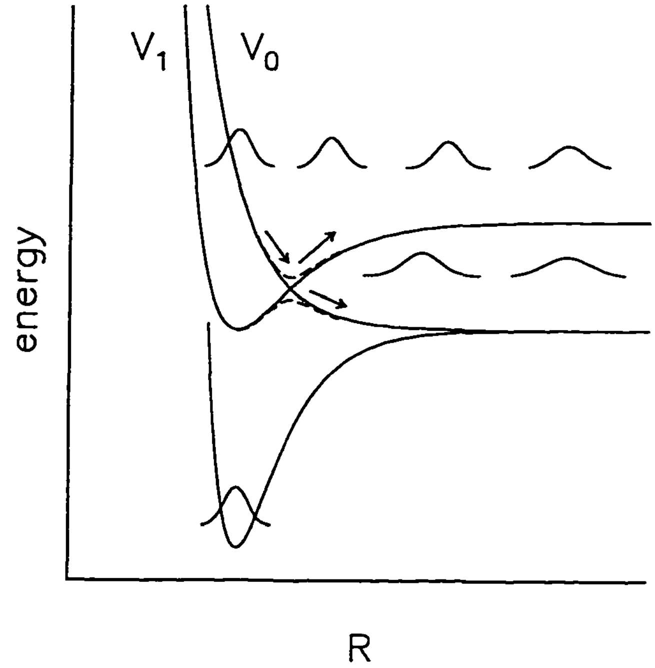

Figure 7: Time-dependent view: the wavepacket splits up in the interaction zone and each component travels separately on the respective PES.

In the *time-dependent picture*, the extent to which the molecule behaves adiabatically depends on its nuclear kinetic energy in the crossing region and the length of the interaction region. If the kinetic energy along the dissociation coordinate is large, the dissociation will procede diabatically (the molecule will "hop" to the other adiabatic PES), whereas if this energy is small, the process will procede adiabatically (Figure 7). One can say that in the latter case there is "enough time" for the wavepacket to adapt to the new electronic environment. Obviously, there is a hopping probability *P* for the intermediate cases. This hopping probability is commonly estimated by the Landau-Zener equation(4, 14).

$$P = \exp(-\pi^2 \xi) \tag{26}$$

The adiabaticity parameter can be viewed as the ratio of the time, t, spent in the interaction region to the spin-orbit precession period, H_{ij} / h

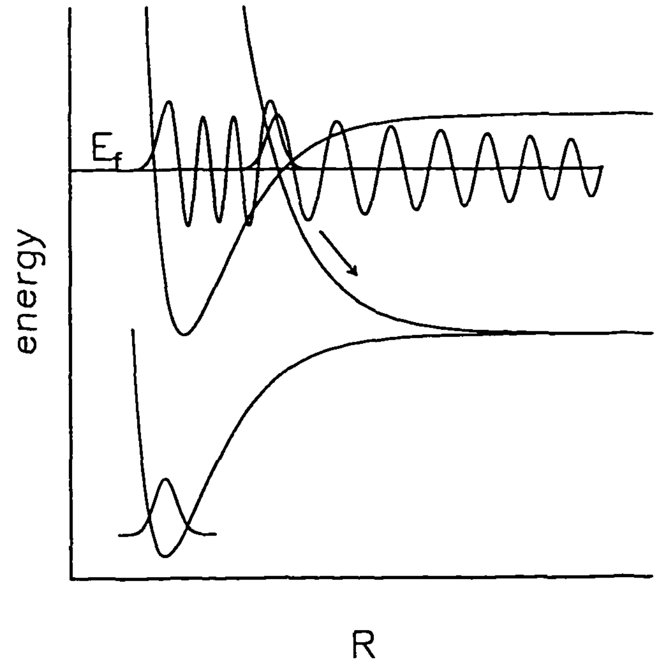

Figure 8: Time-independent view of predissociation dynamics: the predissociation rate depends on the overlap of the bound and the continuum wavefunction.

$$\xi = \frac{tH_{ij}}{h} \tag{27}$$

Assuming the diabatic potentials are linear in the interaction region, this parameter can be expressed as

$$\xi = \frac{H_{ij}^{2}}{\mathrm{v}h\left(\frac{dV_i^{diab}}{dR} - \frac{dV_j^{diab}}{dR}\right)} \tag{28}$$

Here, v is the nuclear velocity along the dissociation coordinate. The "surface-hopping" problem has been reviewed by many authors(15, 16) and a number of approximations, which are better than the semi-classical Landau-Zener equation, have been developed. Alternatively one can estimate the hopping probability in a *time-independent* picture(17). This approach is routinely used in the calculation of predissociation rates, but may also be

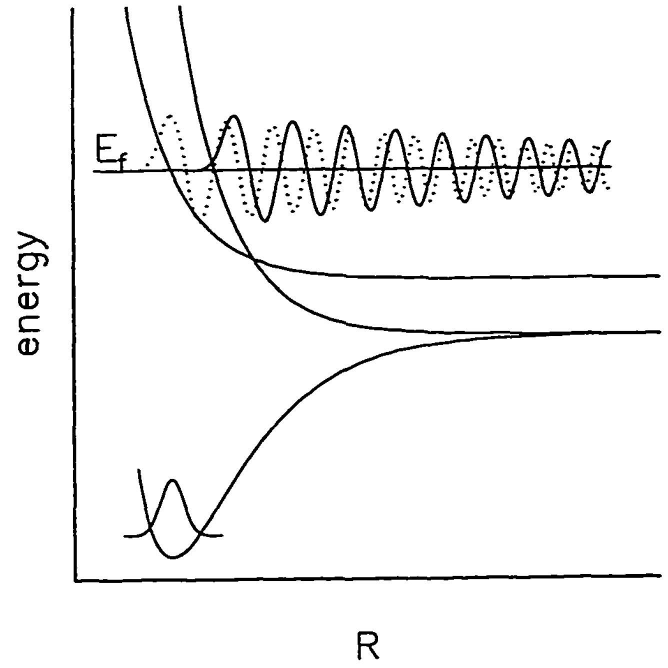

Figure 9: Time-independent view of non-adiabatic dissociation dynamics: the extent of adiabaticity increases with the overlap between the two continuum wavefunctions.

adapted for the crossings of two purely repulsive states. Consider first the intersection between a diabatic bound state and a repulsive state (Figure 8). Predissociation here is explained in terms of the coupling of a bound wavefunction pertaining to a discrete energy level (at a given energy E_f) with a continuum wavefunction(9). The coupling arises from the non-diagonal term in the electronic Hamiltonian matrix, which connects the continuum with bound states of equal energy. The bound-to-continuum transition is the *adiabatic* process. Its probability is thus just the opposite of the hopping probability described above and depends on the magnitude of the overlap integral

$$p = (1 - P) \propto \langle \Psi_{vib} | H_{ij} | \Psi_{cont} \rangle \tag{29}$$

Using this approach one can show that transitions to predissociated levels will exhibit broadened and asymmetric lineshapes (so-called Fano profiles(3, 17, 18)).

Similarly the time-independent view may also be used to understand the non-adiabatic interactions between two repulsive states as displayed in Figure 9(19). The bound-to-continuum or continuum-to-continuum transition probability (i.e., the adiabaticity) depends on the same molecular properties in both the time-dependent and the time-independent view. The adiabaticity of the process increases with the electronic interaction term, which may be the spin-orbit coupling term, and it depends upon the slope of the repulsive states and the energy difference between excitation energy and crossing point. This energy difference translates into nuclear kinetic energy and hence into internal velocity at the crossing point.

1.2 Vector correlation

The previous sections addressed theoretical means of describing excited state molecular dynamics. Here, we will decribe experimental methods of probing these dynamics and discuss briefly the concepts underlying some experimental techniques.

In an attempt to identify and characterize the excited state PES, and to describe the dynamical processes on these surfaces, one has to find ways of probing the molecular motion during a dissociation process. Useful information can be obtained from the measurements of the photofragments vector properties with respect to the molecular frame. The correlation between the parent molecule's transition dipole moment **μ**, the fragments velocity **v** and their rotational (or orbital angular) momentum **J** provides valuable information about both the type of electronic transition involved and fragmentation dynamics(20). The molecular frame is connected to the laboratory frame *via* the electric field component of the photolysis laser light, **E**.

1.2.1 E-μ-v correlation

Most important for our purposes is the correlation between **E** and the vectors **μ** and **v**, where **E** is the electric field component of the photolysis laser beam. As first described by Herschbach and Zare in 1963(21), linearly polarized light will preferentially interact with molecules whose transition dipole moment **μ** is aligned with the electric field component of the interacting light **E**. In this way a vector defined in the molecular frame (**μ**) is fixed with respect to a vector chosen in the laboratory frame (**E**). Since **μ** is in a given geometrical relationship to the dissociation coordinate **R** and therefore to the recoil velocity vector **v**, a correlation of **E**, **μ** and **v** exists (Figure 10).

In a diatomic molecule, for example, **μ** can either be parallel or perpendicular to the bond, corresponding to transitions with $\Delta\Lambda$ (or $\Delta\Omega$) = 0 and $\Delta\Lambda$ (or $\Delta\Omega$) = ± 1, respectively. Here Λ is the projection of the orbital angular momentum vector **L** on the molecular axis and Ω is the projection of the total angular momentum vector **J**. Since the initial recoil velocity **v** is parallel to the bond, the fragment angular distribution is either mainly parallel or perpendicular to **E**. In a parallel transition there is $\mu \parallel v$ and $\Delta\Lambda$ (or $\Delta\Omega = 0$) whereas for a perpendicular transition $\mu \perp v$ and $\Delta\Lambda$ (or $\Delta\Omega$) = ± 1.

The photofragments angular distribution is given by

$$I(\theta) = \frac{1}{4\pi}\left[1 + \beta P_2(\cos\theta)\right] \qquad (30)$$

where θ is the angle between **E** and **v**. $P_2(x) = (3x^2-1)/2$ is the second Legendre polynomial and β is a parameter that characterizes the degree of spatial anisotropy.

$$\beta = 2P_2(\cos\phi) \qquad (31)$$

Here ϕ is the angle between **μ** and **v**. The spatial anisotropy parameter has the limiting values of $\beta = 2$ for a parallel transition ($\mu \parallel v$) and $\beta = -1$ for a perpendicular transition ($\mu \perp v$). The equation shows that the former case generates a $\cos^2(\theta)$ distribution of fragments and in the latter case a $\sin^2(\theta)$ distribution results (Figure 10).

For polyatomic molecules the transition dipole moment has a less well defined orientation in the molecular frame. In a bent triatomic molecule with C_S symmetry, for example, **μ** may either be in the molecular plane or normal to the plane. The former case indicates "parallel type" (A' →A') and (A" → A") transitions, whereas the latter case indicates "perpendicular" (A' → A") and (A" → A') transitions. In a parallel-type transition --

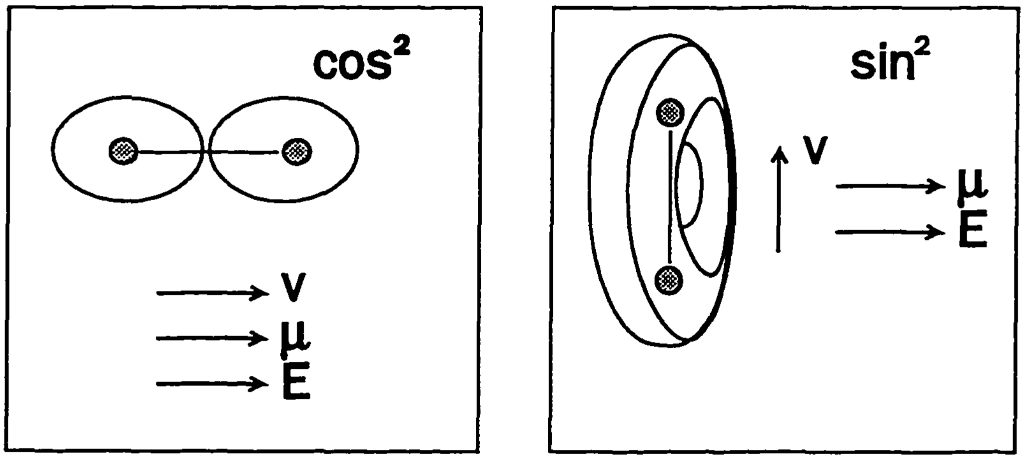

Figure 10: Vector correlations in a diatomic molecule dissociation: The transition dipole moment μ is either parallel or perpendicular to the molecular bond.

depending on the exact orientation of μ in the molecular plane -- the spatial anisotropy can assume all values between $\beta = -1$ for $\mu \perp v$ and $\beta = 2$ for $\mu \parallel v$. In the case of a perpendicular transition, on the other hand, there is always $\mu \perp v$ and $\beta = -1$, since all nuclear motion vectors in a triatomic molecule lie within the molecular plane (Figure 2).

1.2.2 E-μ-J correlation and v-J correlation

In the photodissociation of a polyatomic molecule a molecular fragment will usually possess rotational angular momentum **J**, which can be aligned with respect to the parent molecular frame. For a triatomic molecule this is illustrated in Figure 2. The angular momentum vector **J** of the diatomic fragment will always be perpendicular to the molecular plane, since the dissociation process and hence the diatomic rotation, can only take place within this plane. Depending on the alignment of the transition dipole moment μ, one can observe different correlations between J and $E \parallel \mu$. Determination of the direction of μ relative to J may help to identify the excited state.

The correlation between recoil velocity **v** and **J** is different from the **E**-**μ**-**J** and **E**-**μ**-**v** correlation, because it is independent of the alignment of **μ**. The **v**-**J** correlation therefore persists even in very slow dissociation processes, in which the information about the alignment of **μ** would have been lost, due to rotation of the parent molecule. Especially in the study of large polyatomic molecules the molecular **v**-**J** correlation has proven to be instructive(22).

The alignment of the fragment rotational angular momentum, **J**, in the laboratory frame can be probed through absorption spectroscopy of the fragment or by detection of emission, if the fragments are produced in an excited electronic state. In the case of absorption one makes use of the preferential absorbance of linearly polarized light $\mathbf{E}_{probe}$ by different ro-vibronic branches in the excitation spectrum. In the latter case the polarization of the emitted light is correlated to different branches in an emission spectrum(23). Taking spontaneous fragment fluorescence as an example, the fluorescence polarization can be expressed by(24)

$$R(\phi_r) = \frac{1}{2} h^{(2)} A_0^{(2)}(\phi_r) \tag{32}$$

Here $h^{(2)}$ is a geometric factor allowing for the anisotropy of the fluorescence transition dipole. It has the limiting values of $h^{(2)} = +1$ for fluorescence *via* a Q-branch and $h^{(2)} = -1/2$ for fluorescence *via* a P and R branch. The rotational alignment parameter $A_0^{(2)}$ is defined in analogy to the spatial anisotropy parameter

$$A_0^{(2)} = \frac{4}{5}\left[P_2(\cos\phi_r')\right] = 2\left[P_2(\cos\phi_r)\right] \tag{33}$$

where ϕ'_r is the angle, in the molecular frame, between **μ** and **J** and ϕ_r is the angle between the laboratory frame unit vector **z** and **J**. The alignment parameter takes the limiting values of $A_0^{(2)} = -2/5$ and $A_0^{(2)} = 4/5$ for $\mathbf{\mu}\perp\mathbf{J}$ and $\mathbf{\mu}\parallel\mathbf{J}$, respectively.

Recently our group has observed and described the alignment of atomic fragment *orbital* angular momentum **J** with respect to **v** and **μ** in the photodissociation of Cl_2(25). The principle underlying the measurements of atomic **v**-**J** correlation is similar to the ones described above. Again the atomic fragments interact differently with linearly polarized light depending on the angle between $\mathbf{E}_{\text{probe}}$ and **J**.

1.3 Experimental techniques

Using the **E-μ-v** or **E-μ-J** correlation one can determine the symmetry of the excited state, if the symmetry of the ground state of the parent molecule is known. *Measuring* the spatial distribution of the fragments, however, is not an easy task. In the previous section we have briefly described fluorescence detection as one method of determining the alignment of **J** in the lab frame. In this section four additional experimental methods that make use of the **E-μ-v** correlation shall be briefly discussed. These methods are sub-Doppler spectroscopy, time-of-flight mass spectrometry combined with resonance-enhance multiphoton ionization (TOF-MS / REMPI), photofragment TOF core-sampling, and the ion-imaging technique. Sub-Doppler spectroscopy probes the Doppler-shift of the departing fragment by absorption to an excited state, of which fluorescence is detected. Less frequently the Doppler shift can be observed in emission, if the fragment is formed in an electronically excited state. The resonance frequency for either transition is shifted depending on the fragments velocity component $\mathbf{v}_Z$ with respect to the interrogating beam.

$$\mathrm{v} = \mathrm{v}_0\left[1-\frac{\mathrm{v}_Z}{c_0}\right] \tag{34}$$

The Doppler profile of such an absorption line is described by

$$I(\theta) = \frac{1}{4\pi}\left[1+\beta\, P_2(\cos\alpha)\, P_2(\cos\theta)\right] \tag{35}$$

where θ is the angle between the velocity vector **v** and the photolysis electric field vector **E**. This angle can be related to the Doppler shift via $\cos(\theta) = \mathrm{v}_z/\mathrm{v}$. The angle α is between **E** and the propagation direction of the probe beam **z**(26).

Increasingly, resonance-enhanced multiphoton-ionization (REMPI) combined with time-of-flight mass spectrometry (TOF-MS) is used to determine the photofragment spatial distribution(27). This technique will be described in some detail later, since it is the method employed in this work. Briefly, the photolysis and probe beams are aligned colinearly and the interaction region, which is defined by the overlapping focal points of the tunable laser sources, is placed in a constant electrical field. The **E** vector of the photolysis beam determines the fragments spatial distribution in the lab frame and the probe beam state-selectively ionizes some of these fragments. These ions are then accelerated by the electric field towards the ion detector. Their arrival time depends upon their initial direction and speed of recoil or, more specifically, upon the recoil velocity component v_z in the direction of the TOF-MS axis. The equation that describes the photofragment TOF profile is similar to equation (35) above but here α is the angle between **E** and the TOF-MS axis. The REMPI/TOF-MS method has the advantage over sub-Doppler spectroscopy in that by varying the electric field strength measurement of a large range of photofragment velocities is possible. Also the requirements on the light sources are not as stringent as they are for sub-Doppler spectroscopy. Finally, the REMPI/TOF-MS method allows for the simultaneous detection of all fragment masses, as well as all v_z components. Figure 11 gives a simple illustration of this experimental technique.

If the photofragments are produced *via* different dissociation channels, their kinetic energy and spatial distribution will be different. Sub-Doppler spectroscopy and TOF-MS/REMPI can not easily resolve the various components of the photofragment signal. With the TOF core-extraction technique(28, 29) one overcomes this problem by placing a mask with a pinhole in front of the ion detector. Only fragments which have small velocity components perpendicular to the TOF axis will be sampled, and -- at the price of a smaller total ion signal -- the kinetic energy resolution is substantially enhanced. This technique is described in more detail later, since it was also employed in this work.

A related technique was employed by Reisler and coworkers(30). The kinetic energy resolution of the TOF signal was improved by delaying the probe laser pulse with respect to the photolysis laser pulse. During the delay time, the photofragments spread and only a small portion can be ionized by the probe laser. From the arrival time at the ion detector the fragments' position and momentum at the moment of ionization can be calculated and

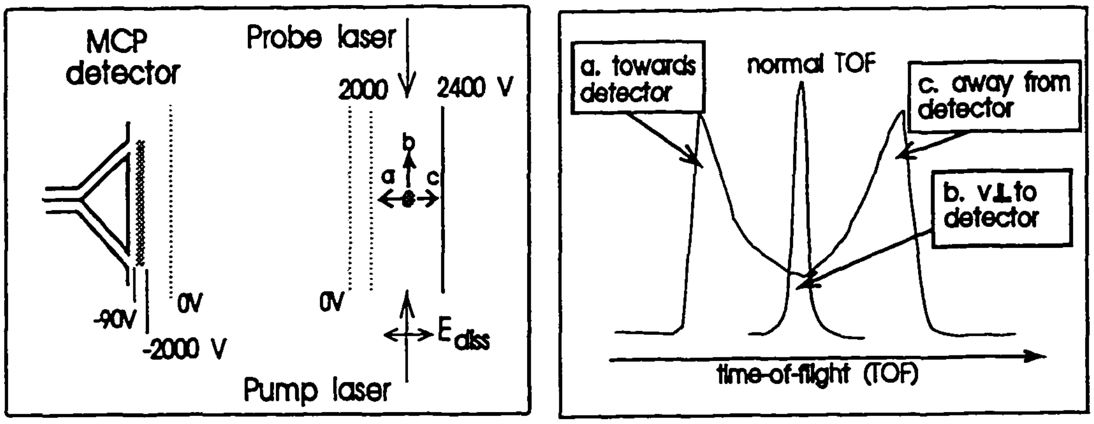

Figure 11: Measuring the fragments spatial distribution using a TOF-MS; ions travelling away from the detector (c) have to turn in the electric field and are delayed by the turn-around time.

their spatial distributions inferred.

Photofragment translational spectroscopy (also called Kinetic Energy TOF-MS) is another variant of the TOF method. In this approach the photofragments are not accelerated by an electric field but their arrival time is solely determined by their fragmentation kinetic energy(31-34). At some distance from the interaction zone the neutral fragments are ionized (e.g., by electron bombardment) and are then mass selected by a quadrupole-mass spectrometer. The photofragments' spatial distribution is measured by correlating the polarization plane of the photolysis light to the intensity of the ion signal. Since only a small solid angle is measured at a time, the ion signal is very weak. The technique, however, allows for accurate measurements of kinetic energy and spatial resolution and is therefore suitable for photodissociation studies of larger molecules. In polyatomic molecules with four or more atoms different dissociation pathways may compete and lead to a variety of photofragments with different and characteristic kinetic energy and spatial distribution.

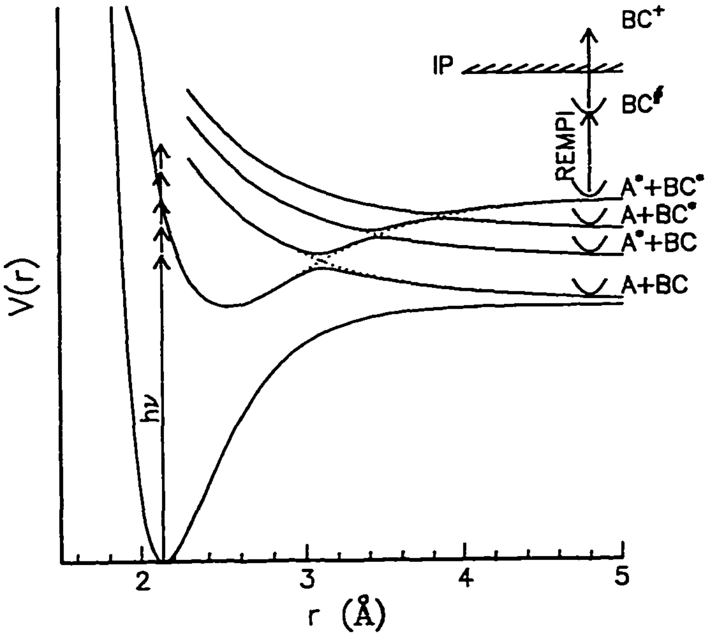

Figure 12: Illustration of the pump and probe scheme. The photolysis laser pulse prepares the excited state, whereas the delayed probe pulse state-selectively ionizes the fragments

Two-dimensional ion imaging techniques have been developed most recently(1, 35). The method is related to the REMPI/TOF-MS technique, but here a position sensitive ion detector is used to allow for simultaneous measurement of *all* velocity components. As before, the velocity component in direction of the TOF-MS axis v_Z will translate into arrival time. In addition the v_X and v_Y component at each arrival time is given by the two dimensional projection of the ion signal onto the position sensitive detector. Coincidence measurement of both departing photofragments allows for a nearly noise-free determination of the spatial distribution.

1.4 The TOF-MS / REMPI technique

Our experiments follow a simple "pump - probe" scheme. A dilute sample gas is expanded through a pulsed nozzle into the first of two high vacuum chambers. Jet expansion cooled the rotation of the parent molecules to 10 - 50 K. The jet was skimmed before entering the first electric field of a two-stage TOF mass spectrometer. The polarized and focused photolysis laser beam photodissociated the sample. Depending on the wavelength of the photolysis light, different excited states were prepared and photofragments were formed in different quantum states (Figure 12). The photofragments were then ionized state-selectively by a second, delayed, laser beam. Both laser beams were counterpropagating with respect to each other and are at right angles to both the TOF-axis and the molecular beam. The ionized photofragments were accelerated towards the ion detector in the two stage TOF-MS (Figure 11). Ions initially travelling away from the detector turned around in the first stage of the TOF-MS and were therefore delayed by a timespan which depended on their initial velocity, the angle between the initial velocity vector and the TOF axis, and the electric field strength. In the second stage of the TOF-MS all ions were strongly accelerated towards the detector.

The REMPI technique allows for state-selective ionization of the photofragments. The ionization process requires two or three photons from a tunable second laser. Since each of the two or three absorption steps requires a large population in the lower level, the whole process will be greatly enhanced if one of the intermediate states is stable. In this resonant case a large number of ions is produced, which can then be detected using a TOF-MS. Of course, for the resonant transitions the same selection rules apply as for any other kind of spectroscopy. The REMPI processes are called, e.g. 2+1 REMPI or 1+1 REMPI, depending on the number of photons needed for the resonant step to the intermediate level and for the ionization step.

As described above the vector correlations between the polarization plane of the photolysis laser and the direction of recoil are reflected in the spatial distribution of the photofragments. The TOF technique allows for determination of this spatial distribution and thereby for characterization of the parent molecules' excited state. Furthermore, if the parent molecules state is determined and the fragments quantum state has been measured spectroscopically, it is possible to obtain true state-to-state correlations with high accuracy and deduce the photodissociation dynamics (Figure 12). Thus this method enabled us to

- prepare the parent molecule in a defined quantum state distribution by molecular beam expansion
- detect the photofragments mass-selectively *via* their overall flight time
- detect the photofragments state-selectively (rotational, vibrational, spin-orbit, Λ-doublet state selective) *via* REMPI transitions
- determine the kinetic energy release correlated to each REMPI transition *via* the width of the photofragment TOF signal
- determine the spatial distribution *via* the shape of the PF-TOF signal.

In the following chapter the components of the experimental setup will be described in detail.

2 Details of the Experiments

This chapter describes the technical details of the photodissociation experiments conducted on BrCl and BrNO. The order in which the following sections are presented is meant to reflect the "flow of information". In this sense it is natural to start with sample preparation, continuing with the procedure that led to the absorption spectrum, and the molecular beam arrangement. The light sources and the TOF-mass spectrometer are discussed next, followed by signal sampling by the oscilloscope and the data accumulation and manipulation by the data acquisition computer.

The experimental section is somewhat detailed. Since this is the first full description of our experimental apparatus, it is justifiable to elaborate on a relatively common and straightforward technique.

2.1 Sample preparation and purification

BrCl and BrNO were prepared by gas phase reactions of Br_2 vapour (Aldrich) with Cl_2 (Matheson 99%) or purified NO (Alphagaz 99%), respectively.

[1] $Br_2 + Cl_2 \rightleftharpoons 2\,BrCl$ $K^0_{eq} = 6.5$ ref. 24

[2] $Br_2 + 2\,NO \rightleftharpoons 2\,BrNO$ $K^0_{eq} = 0.15\ \mathrm{Torr}^{-1}$ ref. 36

Br_2 was purified from dissolved air by three freeze-pump-thaw cycles at -78°C and room temperature, while Cl_2 was used as purchased. NO_2 impurities were removed from NO by using a series of three cold traps (-78°C). The product gases BrCl and BrNO were checked for impurities using UV-Vis absorption spectrometry.

Reactions [1] and [2] lead to equilibrium amounts of product gases. In both cases the equilibrium reaction is fast compared to the duration of a photodissociation experiment. Purification of the products was therefore not attempted, but the initial ratio of reactant gases was chosen such that the equilibrium is forced away from the interfering reactant

	T_m [°C]	T_b [°C]	D_0 [kJ/mol]	ΔH_{form} [kJ/mol]
Cl_2	-101.00	-34.06	243.52	0
Br_2	-7.25	58.78	192.99	0
BrCl	-66	~5	218.21*	+14.7
BrNO	~0	55.5	116#	+82.23
ClNO	-59.6	-6.4	155#	+51.75
NO	-163.65	-151.77	626.8†	+90.31
N_2O_2	**	**	9.4	+190.0
NO_2/N_2O_4	-11.20	21.15	300.6‡	+33.20 (NO_2) +9.17 (N_2O_4(g)) -19.51 (N_2O_4(l))

All data from reference 75 unless specified; * ref. 69; # ref. 101; † ref. 41; ‡ ref. 110; **equilibrium with solid and liquid NO.

Table 2: Thermodynamic data

gases.

When probing bromine photofragments in photodissociation experiments, the gas mix was prepared by exposing Br_2 to a 5 to 20-fold excess of Cl_2 or NO (depending on the photolysis wavelength) to avoid Br photofragment formation from Br_2 dissociation. However, the majority of the photodissociation experiments were conducted by probing chlorine or nitric oxide photofragments. Here a 5-20 fold excess of Br_2 was used when preparing the sample.

The partial pressures of the reactant gases were chosen such that the overall pressure after the reaction in the 2 L reaction bulb was less then 200 Torr. Helium (Airgas 99.99%) was added to the equilibrated gas mix to a total pressure of approximately 1 atm. After thorough mixing the gases were expanded into a previously evacuated 10 L storage bulb. The sample was diluted with Helium to a total pressure of slightly above 1 atm. In all experiments the partial pressure of the sample gas was 2-5 % of the total pressure.

This diluted gas mixture was frequently checked for impurities using absorption spectroscopy and was replaced when either impurities appeared or the total pressure in the storage bulb went below 500 Torr. As a further precaution, the sample was replaced within two weeks after preparation. The absence of metal surfaces in reaction bulb and storage bulb was found to be important for the chemical stability of the compounds. All gases used are not only powerful poisons but also strong oxidizing agents, which react readily with many materials. Table 2 lists melting and boiling points, as well as dissociation and formation energy of all relevant compounds.

2.2 Absorption spectrum of BrNO

The absorption spectrum of BrNO spans four orders of magnitude of absorbance and was therefore assembled from a UV and a visible component, which were recorded separately at different pressures. At room temperature there are always substantial equilibrium amounts of NO and/or Br_2 present, both of which absorb in the region under investigation. Furthermore, the equilibrium reaction is fast compared to the recording time. Obtaining a pure sample was therefore not possible and a different approach was chosen in recording the absorption spectrum.

A series of spectra with the same amount of Br_2 but changing fractions of NO was recorded. The isosbestic point (at 391.3 ± 0.3 nm) together with the known absorption of Br_2(37) not only gave a calibration factor for the BrNO spectrum but also indicated the absence of impurities which absorb in this region, specifically NO_2. To suppress Br_2 absorption, the spectrum between 300 nm and 800 nm was recorded with an approximate 5-fold excess of NO, which is transparent in this region. The UV portion of the spectrum was then recorded under approx. 20 fold excess of Br_2 and at lower overall pressure. Seven of those UV spectra recorded at different pressures were scaled relative to each other and then to the visible part by overlapping the the 280 nm to 320 nm region of the spectrum. BrNO was obtained by reacting gasous Br_2 (Aldrich) with NO (Alphagaz 99.9%, oxygen free). Prior to reaction nitric oxide was cleansed of NO_2 impurities using a cold trap (-78.5°C), while Br_2 was cleaned *via* three freeze-pump-thaw cycles (-78.5°C to 20°C). The absorption spectrum was recorded in 0.1 nm increments with a spectral bandwidth of 0.3 nm using a CARY 5 absorption spectrometer and a 10 cm glass absorption cell with quartz windows.

The UV part of the spectrum may be slightly inaccurate due to the overlapping procedure, but consecutive runs gave an error well below 15 % in absorbance and high accuracy in peak position.

2.3 Molecular beam

The 2-5 % sample gas in Helium was expanded into the high vacuum chamber through a homemade pulsed nozzle(38). The jet expansion was skimmed 10-80 mm downstream by a 0.5 mm skimmer (Beam Dynamics, Inc). The molecular beam then entered the first stage of the TOF-MS and interacted with the two laser beams approximately 50 mm downstream of the skimmer. Unreacted gases left the TOF-MS through a 10 mm exit hole and were carried out by an Edwards Diffusion pump. A sketch of the vacuum chambers is given in Figure 13.

Both chambers were evacuated to operating pressures of $p_1 = 2\text{-}5 \cdot 10^{-6}$ Torr and $p_2 = 0.5\text{-}1 \cdot 10^{-6}$ Torr using two diffusion pumps (Edwards, Diffstak 250; 2300 L/s) both backed by a two-stage rotary pump (Edwards E2M 28; 10 L/s). The chamber pressure was monitored using two ion gauges (Granville-Phillips, 274012 ion gauge and controller) combined with two thermocouple gauges (Granville-Phillips, 270006), while the backing pressure was monitored using two thermocouple gauges of the same type.

The design of the pulsed molecular beam valve followed closely the description by Proch & Trickl(38). A piezoelectric disk translator (Physik Instrumente, P286.20) was driven by

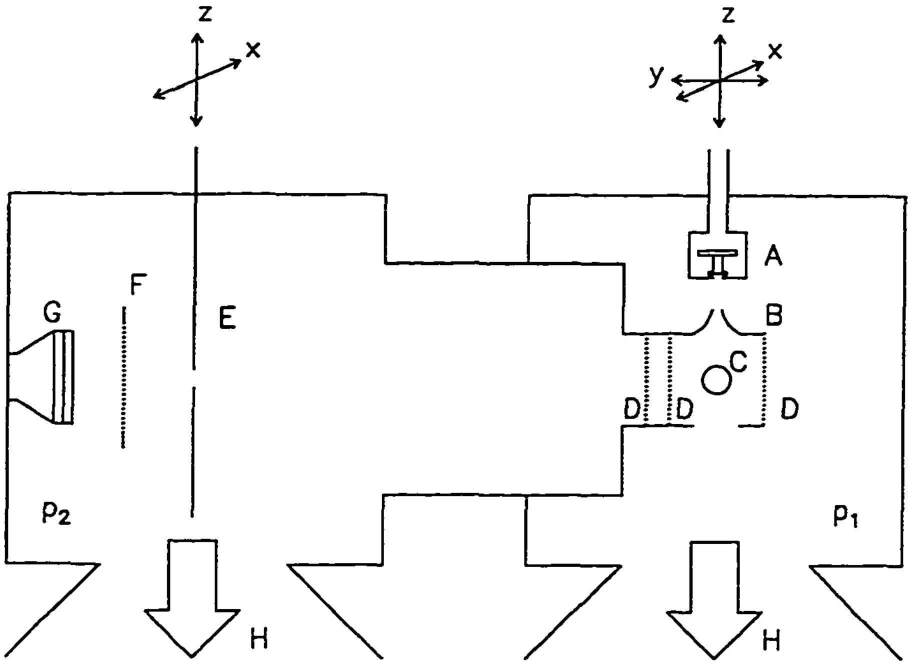

Figure 13: The high vacuum chambers: A. pulsed valve; B. skimmer; C. focal points of the laser beams; D. TOF-MS grids; E. mask with pinhole; F. ion screen; G. ion detector; H. to diffusion pumps

a homemade power supply to move an aluminium piston surrounded by diluted sample gas. The tip of this piston opens a 0.5 mm nozzle for an adjustable period of time such that the sample gas (backing pressure 500-760 Torr) can expand into the vacuum chamber, and cool adiabatically to low rotational temperatures. The pulsed, high voltage power supply allowed for adjustment of the driving voltage (typically 300 V), the pulse duration (typically 200 μs) and the delay with respect to the incoming trigger.

The pulse duration and the driving voltage largely determined the molecular beam conditions. A large voltage leads to a large amplitude motion of the piezocrystal and therefore to a large gas throughput. This causes low beam temperatures, but allows cluster formation. High driving voltages also cause excessive strain on the disk translator and possible damage. Long pulse durations increase the load on the diffusion pumps and therefore the pressure in the vacuum chamber, without influencing the sample gas' density in the interaction region or its temperature. It was therefore attempted to optimize the driving voltage in order to suppress cluster formation, yet obtain low molecular beam temperatures, and to reduce the pulse duration to the shortest possible time. The pulse delay was set in order to be in the "early" part of the expansion, because cluster formation was expected to increase over time.

The position of the pulsed valve could be adjusted in height and in the x-y plane, using a homemade translator. The height above the interaction zone *H* is an important parameter, since it influences the molecular beam temperature, its density, and the molecules radial velocity distribution in the interaction region. This distribution determines the extent of translation perpendicular to the expansion direction and is reflected in the Doppler width of the resonant transitions. The height of the nozzle was typically set to only 20 mm above the skimmer, but it was set differently in experiments in which a low molecular beam temperature is considered more important than a high density of molecules in the interaction region.

The speed of the molecular beam was estimated to be around 2 mm/μs. Its rotational temperature was determined by measuring the rotational state distribution of NO and was between 10 K and 50 K depending on the expansion conditions.

Cluster formation was observed, but was found to give only a weak and easily distinguishable ion signal, provided the expansion conditions had been carefully optimized.

2.4 Lasers and Optics

In most experiments two light pulses were employed; the first pulse photodissociates the parent molecules and the second probes the photofragments. Both laser pulses were ultimately generated by Nd:YAG lasers, which gave pulses of approximately 6-7 ns duration. It is the pulse width of the probe laser which limits the time resolution of the experiments.

The photolysis light source was the output of a Nd:YAG laser or a Nd:YAG pumped dye laser configuration. When using the Nd:YAG laser (Continuum NY61-10) as a light source.

Wavelength [nm]	Generation	Dye	Solvent	Power [mJ]
740-680	532 nm pumped ND 60	LDS 698	Methanol	40
600-660	532 nm pumped ND 60	Rhodamine 640	Methanol	30
532	2nd Nd:YAG harmonic	-	-	100*
500	355 nm pumped ND 60	Coumarin 500	Methanol	2-5
470	355 nm pumped ND 60	Coumarin 480	Methanol	2-5
450	355 nm pumped ND 60	Coumarin 460	Methanol	2-5
420	355 nm pumped ND 60	Stilbene	Methanol	2-5
398	355 nm pumped ND 60	Excalite 398	Methanol	2-5
389	355 nm pumped ND 60	Excalite 389	Methanol	2-5
355	3rd Nd:YAG harmonic	-	-	100*
266	frequency doubled 532 nm	-	-	10
215-225	Nd:YAG (355 nm) pumped HD-300; freq.doubled	Coumarin 440	Methanol	0.01-0.05
220-230	Nd:YAG (355 nm) pumped HD-300; freq.doubled	Coumarin 450	Methanol	0.01-0.05
225-235	Nd:YAG (355 nm) pumped HD-300; freq.doubled	Coumarin 460	Methanol	0.01-0.05

* reduced fom 300 mJ (532 nm) or 150 mJ (355 nm)

Table 3: Generation of photolysis and probe laser light using either the 2nd or 3rd harmonic of a Nd:YAG laser, or a Nd:YAG laser pumped dye laser configuration

the second harmonic at 532 nm was generated using a "Type II" crystal (KD_2PO_4). Similarly, to generate light at 355 nm (3rd harmonic), the SHG "Type I" crystal (KD_2PO_4) was used and the 1064 nm fundamental was mixed with the 532 nm second harmonic in another harmonic generation (KD_2PO_4) crystal to generate the third harmonic. Light at 266 nm was obtained by frequency doubling the 532 nm Nd:YAG output with a BBO (β-BaB_2O_4) crystal, followed by harmonic separation using an equilateral quartz prism. Various wavelengths between 390 nm and 740 nm were obtained by using a Nd:YAG pumped Continuum dye laser (ND60).

The laser power could be smoothly reduced without a change in beam alignment or beam quality by slightly misaligning the SHG-crystals. Especially when using 355 nm and 532 nm light for photolysis, reduction of laser power was necessary if one wanted to reduce background signal caused by nonresonant ionization.

When using the dye laser as a photolysis source, the intensity and quality of the beam depended crucially on the specific dye / pumping - source combination used. An overview about the various configurations is given in Table 3. The laser dye was purchased from Exciton.

Bromine, chlorine or nitric oxide photofragments were probed *via* their REMPI lines between 215 nm and 235 nm. A Lumonics Nd:YAG laser (YM 600) operating at 355 nm was used to pump a Lumonics dye laser (HD-300). The dye lasers output was frequency doubled using a Lumonics Hypertrak with a BBO crystal and harmonic separator. The Hypertrak was programmable to facilitate the scanning operation. The setup of the light sources is schematically shown in Figure 14.

The output wavelength of the photolysis laser was checked to an accuracy of approximately 1 nm using a Lambda-Physik dye laser (Type unknown, probably protoype) as a wavemeter. The probe laser was calibrated using a neon hollow cathode lamp. When detecting NO fragments the well-known REMPI transitions *via* the $A\ ^2\Sigma \leftarrow X\ ^2\Pi$ γ-band of the cold background NO also served as calibration.

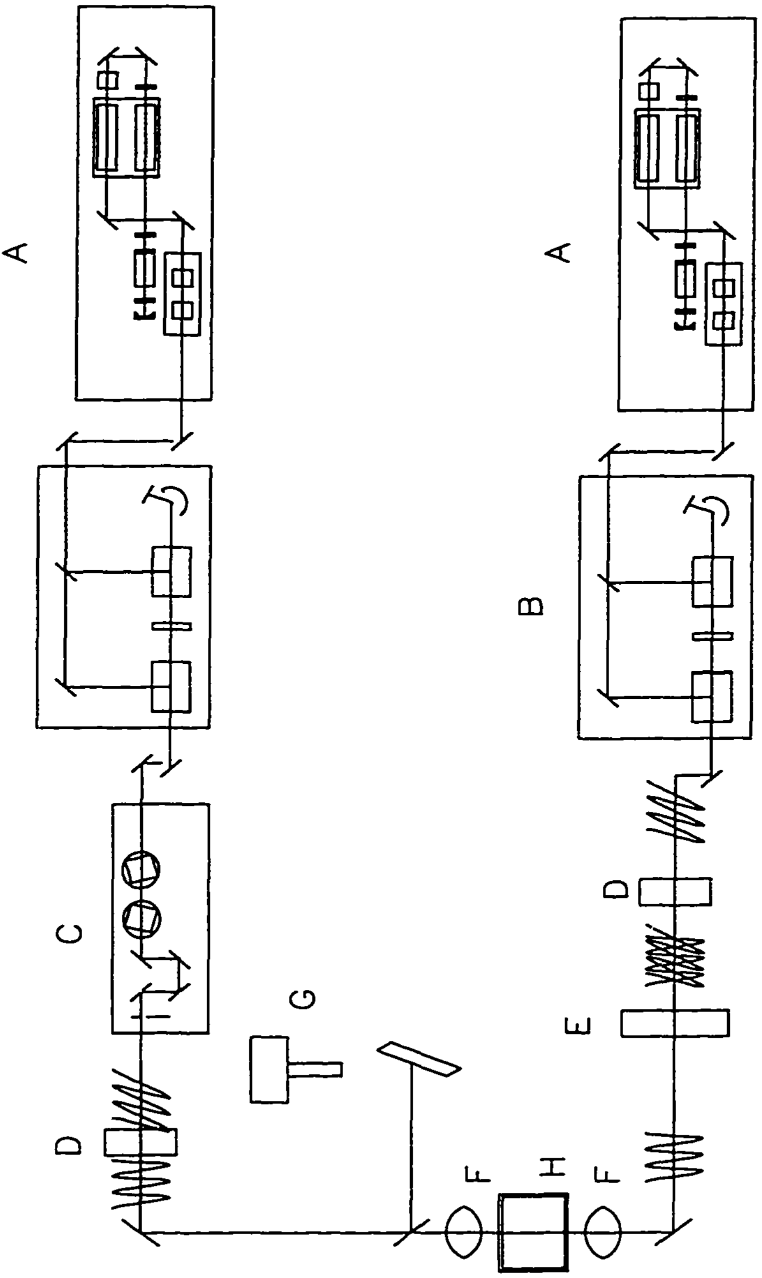

Figure 14: The light sources and optical devices used in a typical experiment.: A. Nd:YAG laser; B.Dye laser; C. tunable frequency doubler; D. adjustable waveplate; E. photoelastic modulator; F. lenses; G. photodiode; H. vacuum chamber.

The output power of the Nd:YAG lasers and dye lasers was routinely monitored with a GENTEC portable power meter (PS310; range 200-400 nm). While the absolute power measurements, especially at long wavelength, are very inaccurate with this instrument, the power meter fulfilled its purpose as an aid when maximizing the laser output or when monitoring laser power changes during the course of an experiment. The absolute output power of the frequency doubled probe beam was estimated using a photodiode which was calibrated to the PS310. These estimates are lower limits and are given in Table 3. The *relative* output power of the laser, which was scanned (in most experiments the probe laser) was monitored by a photodiode (Motorola, MRD 500) on a shot-to-shot basis. A spot of reflected laser light was scattered off a sheet of fluorescent paper into the photodiode. The photodiode signal was sampled simultanously with the ion signal. In this way, the ion signal could be corrected for laser power fluctuations using an independently measured power dependence. It was observed that only the probe laser suffered from power fluctuations. These were attributed to the burning of the Coumarin dyes, the dye emission curves and inhomogenieties in the frequency doubling curve. The photolysis source delivered approximately constant power over the course of all "fixed wavelength" experiments.

In case of photolysis using 266 nm and 355 nm light, separation from the Nd:YAG 2nd harmonic at 532 nm became necessary. For 355 nm light, the 2nd and 3rd harmonics are polarized differently. Here, a crystal quartz wollaston (Karl Lamprecht Corp.,WQ 12-05) served as a polarizer, which separated incoming light into a perpendicular and a parallel polarized component. The quartz wollaston has the advantage over the more commonly employed calcite crystals in that it is transparent between 210 nm and 800 nm. The wollaston could be used for 355 / 532 nm separation but not for 266 / 532 nm separation because only in the former case a large portion of the 532 nm light has been converted into 355 nm light and thus the 532 nm light was not able to damage the wollaston. Frequency doubling to 266 nm using BBO crystal is much less efficient and the 532 nm harmonic carries enough power to burn the wollaston. For the 266 nm beam harmonic separation was therefore achieved using an equilateral triangular prism and utilizing the different refractive indices of 532 nm and 266 nm light.

In some BrNO photodissociation experiments a second adjustable waveplate was used to change the polarization plane of the probe laser light from the prepolarized horizontal plane to an approximate vertical plane. Since the probe laser wavelength is tuned over a range of approximately 150 cm^{-1} the outcoming light is somewhat elliptically polarized.

A large number of experiments were carried out using a photoelastic modulator (Hinds Instruments, PEM-90) in order to switch the polarization plane of the photolysis laser from horizontal to vertical on a shot-to-shot basis. The PEM was driven by an AC-voltage, the amplitude of which was adjusted to match the laser light wavelength. To yield linearly polarized light the beam entering the PEM is required to be circularly polarized. Using quarter-wave retardation, the phase of the horizontal and vertical components of the incoming light were matched to obtain linearly polarized light. The incoming circularly polarized light was created using an adjustable waveplate (Karl Lamprecht Corp., Babinet-Soleil Compensator, crystal quartz, BSA-13-1) on the linearly prepolarized laser beam. The "purity of the polarization" was checked before each experiment using the wollaston.

Using a number of quartz prisms the light beams were directed into the vacuum chambers. They were focused with two lenses of identical focal length (both either 500 mm, 300 mm, or 200 mm) to a spot of approximately 20 μm diameter in the center of the first stage of the TOF-MS. A good overlap of the two focal points is crucial for a successful experiment, but difficult to achieve, since the only indicator for good alignment is the intensity of the ion signal. This signal, in turn, depends on molecular beam conditions and molecular beam alignment with respect to the laser beams. It was easiest to first optimize the overlap of the molecular beam with the photolysis laser using a non-resonant ion signal and then align the probe laser with respect to the power reduced photolysis laser. Alternatively, a resonant NO-REMPI line from background NO can be used to first align the probe laser wih respect to the molecular beam. The photolysis laser can then be aligned with respect to the probe laser.

2.5 Time of Flight Mass Spectrometer

The ionized photofragments were mass selected and their spatial distribution mapped using a homemade TOF-MS of the Wiley-McLaren type[(39)]. Three stainless steel grids (Unique Wire Weaving Co, Inc., 95% transmittance, 25 µm diameter) defined the two acceleration regions. They are mounted on a Teflon® (diam. 72 mm) frame at distances of 20 mm and 7 mm for the first and second fields, respectively. The repeller grid and the first grid were typically biased to 3000 V and 2800 V, respectively, while the second grid was held at ground potential, thereby defining the beginning of the field free flight tube. The end of the flight tube was defined by another grid (diam. 45 mm) held at ground potential and the microchannel plate ion detector (Galileo MCP-FTD 2003; gain $5 \cdot 10^6$).

The width of the TOF ion signal depends on the kinetic energy release of the photodissociation process and the electric field in the first TOF-MS stage. The turn-around time for ions initially flying away from the detector is given by

$$\Delta t = \frac{2s_0(2mE_{kin})^{1/2}}{q\Delta U_1} \tag{36}$$

The residence times of the ions in the first and the second region are

$$t_1 = \left(\frac{2m\,s\,s_0}{q\Delta U_1}\right)^{1/2} \tag{37}$$

$$t_2 = \frac{d_0}{\Delta U_2}\left(\frac{2m}{q}\right)^{1/2}\left[\left(\frac{s}{s_0}\Delta U_1 + \Delta U_2\right)^{1/2} - \left(\frac{s}{s_0}\Delta U_1\right)^{1/2}\right] \tag{38}$$

Finally, the residence time in the field free region is

$$t_D = D\left(\frac{2q}{m}\left(\frac{s}{s_0}\Delta U_1 + \Delta U_2\right)\right)^{1/2} \tag{39}$$

Here, s_0, d_0 and D are the length of the first TOF stage, the acceleration region, and the field free zone respectively, whereas s is the distance between the interaction region and the second grid. The variables q, m and E_{kin} stand for the photofragments charge, mass and initial kinetic energy, respectively. Finally, ΔU_1 and ΔU_2 are the potential differences in the first and second stages of the TOF-MS, respectively.

The electric field strengths in the first and second stage were optimized separately for each experiment. One wanted to ensure that the voltage in the first field is low enough to allow for sufficient photofragment kinetic energy resolution, yet high enough to ensure that all ions produced are reaching the detector. The latter also depended on the overall flight time which was determined by both the first and second stage of the TOF-MS. For experiments in which isotope separation is not important, the field in the first region should be as low as possible without losing ionized photofragments (~200 V / 20 mm). However, when detecting $^{35}Cl^+$,$^{37}Cl^+$, $^{79}Br^+$ or $^{81}Br^+$ ions, the isotopes needed to be separated and there was another lower limit to the field strength in the first region (300 V - 400 V / 20 mm). The optimum field strength also depended on the kinetic energy release of the dissociation process, in the sense that large kinetic energy release went along with wider peaks and higher optimum fields.

The ion detector consisted of two microchannel plates (channel diameter 10 μm, 12 μm spacing between centres) biased at -1800 V. An incoming positive ion induced a cascade of electrons falling through this field leading to a measurable current. This current led to a voltage pulse of approximately 1 mV per ion, in the case of a typical ion kinetic energy of 2 keV. The recovery time per channel was not specified by the manufacturer, but was certainly shorter than 100 ms and therefore influenced only the strongest signals. In all experiments the ion density on the MCP (max. 10^4 cm^{-2}) was small compared to the number of available microchannels (min. 10^6 cm^{-2}). Saturation effects were therefore not observed.

When determining the spatial distribution two experimental details were of importance. Firstly, it was necessary that all photofragments, regardless of their initial direction of flight, had the same chance to be ionized, i.e., in recording the TOF profile one had to scan the probe laser wavelength over the Doppler width of the REMPI line. Secondly, one had to ensure that all photofragment-ions produced in this way were mapped onto the detector. In case of anisotropic spatial distributions, the latter condition could easily be verified. Here, one compared the total ion signal (i.e., the integral area of the TOF profile) associated with photolysis laser polarizations, which were horizontal and vertical to the TOF axis. Only if they were equal and both TOF profiles were symmetric, had the ion beam been completely mapped.

In a different experiment, a fraction of the ions was deliberately discarded by placing a mask (1 mm Copper sheet with 4 mm hole) in front of the detector (Figure 13). The mask skimmed those ions with a large velocity component perpendicular to the TOF axis, and an improved kinetic energy resolution was obtained at the price of a much smaller signal. This setup proved useful when independently measuring the spatial distribution of photofragments with different kinetic energies. In these experiments the ion signal was recorded with the photolysis laser polarization plane both parallel and perpendicular to the TOF axis. The ratio of photofragments dissociating along the TOF axis in both configurations was determined by the photofragment's spatial distribution. The mask was mounted on a home-made x-translator and could be adjusted in height.

2.6 Oscilloscope

The signal from the microchannel plate detector was directed to a digital oscilloscope (Tektronics 2440; 500 MHz) for acquisition and basic manipulation. The oscilloscope could acquire and digitize input signals in different ways. The instrument had two input channels that could be set differently for deflection, input resistance and coupling. Calibrated deflection factors were available in a 1-2-5 sequence from 2 mV to 5 V per division. Input resistance could be set to 1 MΩ or 50 Ω and coupling could be AC (only if resistance is 1 MΩ), DC or ground. In all experiments the coupling was set to DC and the input resistance to 50 Ω to match the impedance of the MCP detector. This was necessary for transmitting fast signals.

The acquisition rate could be selected in a 1-2-5 sequence between 2 ns to 5 s per channel. All signals were recorded at 100 ns/division. The delay time from "trigger zero" to the actual sampling interval could be adjusted to match the flight time of the photofragment for the respective experimental conditions. This sampling interval consisted of 1024 channel-voltage data pairs. While the time resolution is 2 ns between points, the voltage resolution was determined by the 8 bit A/D converter to be 1/250 of the full deflection, i.e., 80 µV at the minimum deflection of 2 mV/div.

The instrument allowed for averaging of consecutive waveforms to improve the signal to noise ratio. However, this feature was only used when optimizing the laser alignment and not during data collection. As shown schematically in Figure 15 and Figure 16 the oscilloscope was triggered by a 5 V external trigger, which defined t_0 in the time domain. The general purpose interface bus (GPIB) (National Instruments NI 488.2) allowed for fast data transfer from the oscilloscope to the data acquisistion computer (Powerwave, 386 PC 25MHz). The GPIB was set to the "Fast transmit" mode in order to load the acquired waveform at the highest possible rate. When in "normal mode" the oscilloscope was waiting for a request from the computer before starting to send the waveform, whereas the "Fast transmit" mode worked in an "acquire-transmit-rearm" sequence. Since the number of requested waveforms was given in a single command at the beginning of each sequence, and the oscilloscope did not "listen" to the computer before the last waveform was transmitted, there was very little dead time between acquisitions. In this way the acquisition rate for a large number of waveforms could be greatly improved. Only by using the "Fast transmit" mode could the data acquisition, transmission and some basic manipulations be done at the experiments' pace of 10 Hz.

2.7 Triggering, interfacing and software

The data acquisition computer is a 386 / 25 MHz IBM compatible PC, which was equipped with a GPIB board (National Instruments NI 488.2), a counter/timer card (Advantech Co. Ltd., PCL-830 with a Advanced Micro Devices chip, Am9513), an A/D converter board (Laboratory Technologies Corp., PCL-711S), one parallel port and one serial port. All these interfaces were manipulated *via* a suite of QuickBasic® (QB)

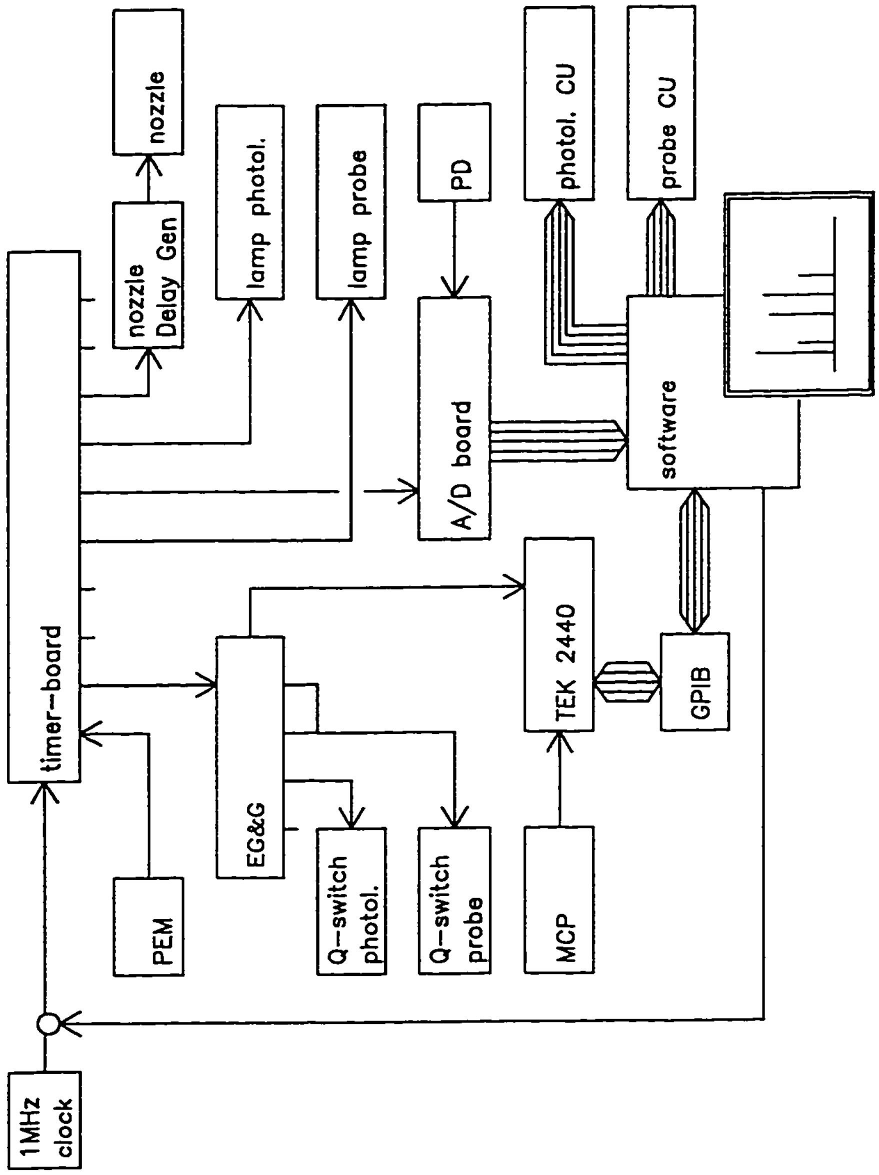

Figure 15: Diagram of the signal (single line) and data (broad lines) flow. PEM: photoelastic modulator; EG&G: delay generator; MCP: ion detector; TEK2440: oscilloscope; GPIB: data bus; CU: control unit; PD: photodiode

programs, which were written by Jianying Bob Cao to automate the experiments. The interfacing layout is given in Figure 15.

The GPIB board was accessed *via* the QuickBasic driver (QBIB.COM), which was made accessible by a QuickBasic declaration file (QBDECL.BAS) at the beginning of each program. Similarly the timer card was programmed *via* an assembly code software driver (PCL830.BIN). The timer card had a 1 MHz on board timebase and 10 independent counters, which were used to trigger the series of events. A separate QuickBasic program was written to modify the individual pulsewidths and delay times (TIMER.BAS). The A/D converter board was accessed *via* a homewritten assembly code driver (ADCONV.ASM). The standard serial communication port (COM1) was used as an interface to the HyperDye probe laser. The serial communication port was used as an interface to a 286 / 16 MHz IBM compatible personal computer. This PC in turn controlled the Continuum ND 60 dye laser *via* a commercial driver program (ND60.EXE).

Accurate triggering was crucial for all experiments. Generally the master trigger frequency was defined by the clock of the timer/counter card and set to 10 Hz. When using the photoelastic modulator a slightly different operation was necessary, since the PEM's modulator frequency was fixed to the quartz crystal's eigenfrequency (50.027 kHz) and could not be modified. However, the exact timing between the PEM phase and the Q-switch of the laser was crucial. Here, the timer opened a gate every 100 ms, and the first modulator amplitude maximum after opening of the gate defined the mastertrigger pulse. By shifting the phase by $\pi/2$, the retardation of the light passing through the PEM was phase shifted. When the incoming light was circularly polarized the outcoming linearly polarized light will have switched its polarization (Similarly, if the incoming light was linearly polarized the outcoming circularly polarized light will have switched its handedness). Experiments using the PEM were operated through QB-programs with the suffix " -p" (e.g. TOFP, MPIP).

As shown schematically in Figure 16, the timer board triggered a whole series of events. The two Nd:YAG laser lamps were triggered by channels 5 and 7 of the timer board and

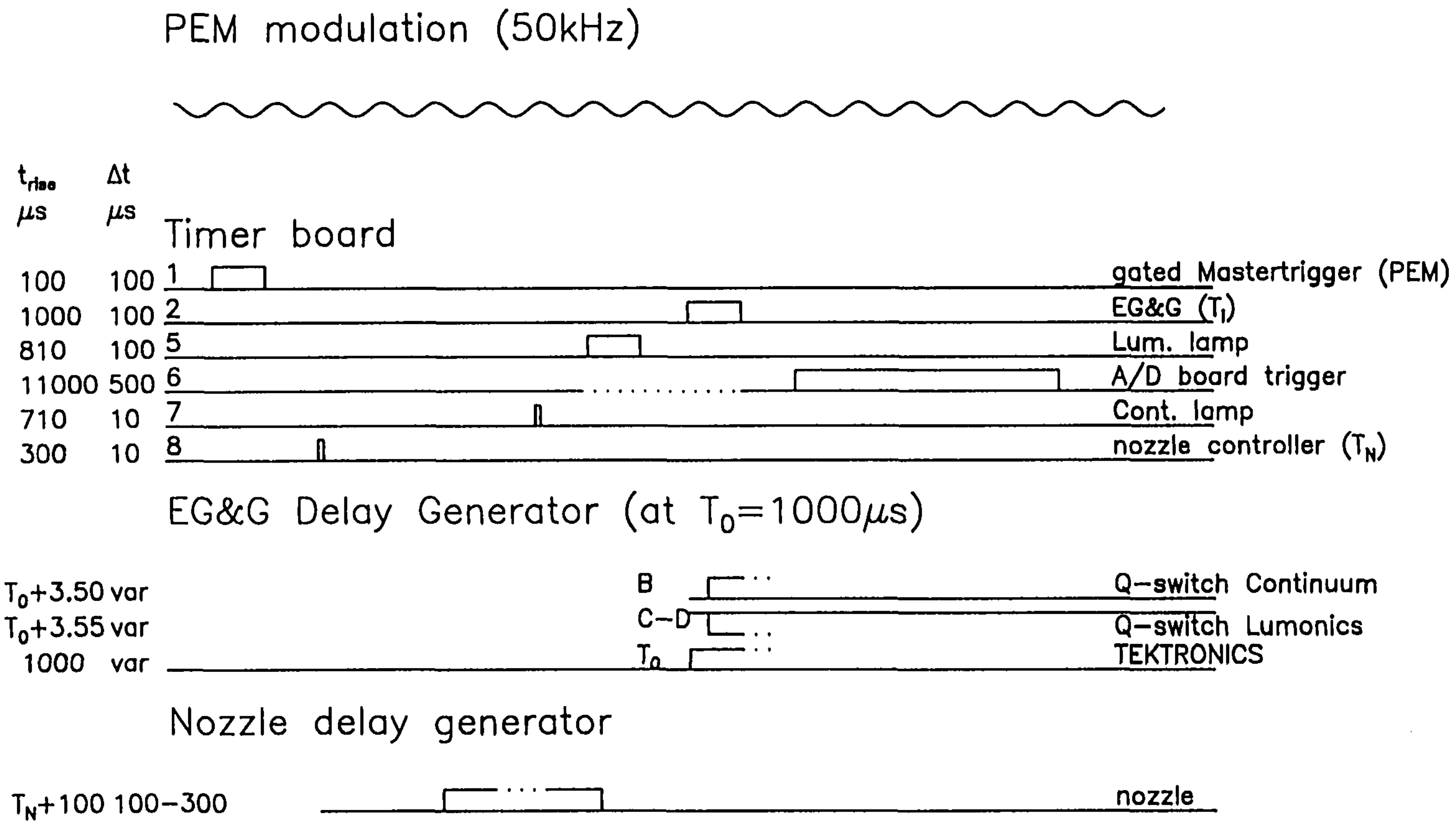

Figure 16: Diagram of the triggering sequence, see text for details.

the homemade nozzle delay generator by channel 9. The Q-switching of the lasers and the triggering of the oscilloscope was done *via* a commercial four-channel delay generator (Princeton Applied Research, EG&G 9650), which in turn was triggered by channel 2 of the timer board. The delay generator offered a variable delay of four outgoing triggers with respect to the incoming trigger in the range of 0 to 100 ms in steps of 10 ps. The jitter was specified by the manufacturer as being $< (50 \text{ ps} + 10^{-8}\, \Delta t_{delay})$ for successive pulses. The delay between the Q-switches was fixed such that the delay of the laser pulses in the interaction zone was 5 - 10 ns. This delay time was adjusted after each laser realignment by directing scattered light from both lasers onto a photodiode (EG&G; FND-100) which had a response time of ~2 ns.

The slower photodiode, which was used to synchronously monitor the laser power in the course of an experiment, was self triggered. It was automatically reset using a homemade control unit, which sampled, held and variably amplified the input. The amplified PD signal was sent to the A/D board. Channel 6 of the timer card opened a gate for the A/D board (AD-0) and the QB-programs waited for the rising edge of this trigger before reading the converted laser power in AD-1. In this way it was assured that the program does not read the AD-1 before the lasers have been fired.

As described before, the ion signal was directed from the detector to the oscilloscope, then *via* the GPIB to the computer. After reading AD-1 the QB-program proceeded to interrogation of the GPIB and storing of the digitized waveform. When sampling more than one waveform the triggering sequence repeated "N" times, before the signal was averaged and stored in memory. The "Fast transmit" mode was then turned off and the program proceeded to either scanning one of the lasers, changing the polarization plane of the laser light or waiting for the operator's input.

The experimental QB-programs performed tasks such as sampling of time of flight profiles at a fixed wavelength, recording of TOF profiles at different wavelengths by scanning the probe laser, scanning of the photolysis laser while monitoring the integrated ion signal and others. Each program can stand alone or can be used as a subroutine of a management

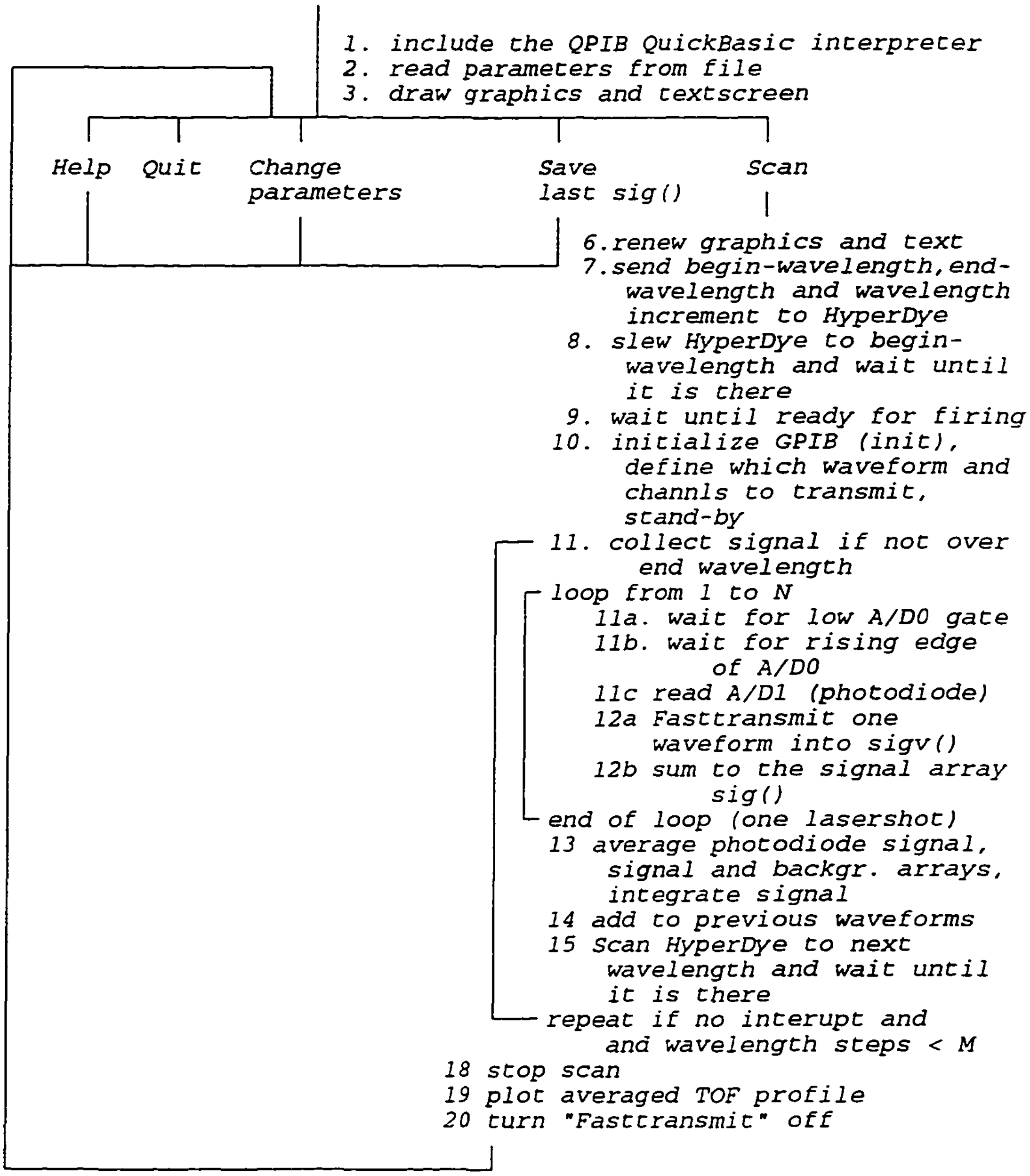

2: Flow diagram of the program "Scan.bas" program (EXPT.BAS).

A flow diagram of a homewritten program is given in Diagram 2. This program (appendix 6.1) samples TOF profiles which were recorded in "M" probe laser wavelength steps to cover the Doppler width of the REMPI line. At each probe laser wavelength "N" TOF profiles were recorded. After the last sequence of waveforms had been transmitted the profile was averaged and displayed. The program then requested input to save the data, quit or restart.

Briefly the other programs of this suite are described below:

TOF: records TOF profiles at fixed preset photolysis and probe laser wavelengths.

SCAN: samples TOF profiles at different probe laser wavelengths and averages them to a single TOF profile (fixed photolysis laser wavelength)

MPI: as SCAN, but the ion signal is integrated and the integral is recorded with respect to probe wavelength

FSCAN: as MPI but the number of averages is set to 2 when the ion signal is below a given threshold

MPC: as MPI but the Continuum ND 60 dye laser wavelength is scanned, while the Hyperdye wavelength is kept constant

TOFP, MPIP, FSCANP: as their equivalents, but each sequence of waveforms is recorded with both polarizations before the probe laser is scanned.

3 Analysis

In this chapter the extraction of information from the experimentally recorded data is described and the relevant expressions are given in analytical form.

The first part of this chapter addresses the analysis of TOF-profiles that were recorded with or without mask. In the second part the analysis of the REMPI spectra of the NO photofragment and the atomic fragments will be discussed. Line-strength factors and saturation effects will be briefly addressed.

3.1 TOF profiles

3.1.1 Full TOF profiles

For a monoenergetic dissociation process with a single exit channel, the angular distribution of the fragments following excitation with linearly polarized light can be written as (see eq.(30))

$$\frac{d\sigma}{d\Omega}=\frac{\sigma}{4\pi}[1+\beta P_2(\cos\theta)] \tag{40}$$

where $P_2(x)=(3x^2-1)/2$ and is the second Legendre polynomial and θ refers to the angle between the fragment recoil velocity v and the polarization direction of the photolysis laser E. The spatial anisotropy parameter lies between $\beta = -1$ and $\beta = 2$ corresponding to the limits for a perpendicular and parallel transition, respectively. The photofragment TOF profile associated with the distribution given in equation (40) can be expressed as

$$I(t)=\frac{1}{2\Delta t}\left[1+\beta_{eff}P_2\left(\frac{t-t_0}{\Delta t}\right)\right] \qquad |t-t_0|<\Delta t \tag{41}$$

with

$$\beta_{eff}=\beta\, P_2(\cos\alpha) \tag{42}$$

where t_0 is the flight time in absence of fragment kinetic energy and Δt is the maximum time lag resulting from the photofragment kinetic energy release (see equation (36)). The angle α in equation (42) is defined between the TOF axis z and the electric field component of the photolysis laser light E. Three cases are of special interest to our experiments. If $\alpha = 0°$ then $\beta_{eff} = \beta$, i.e., the fitting routine delivers the "correct" anisotropy for the transition. If $\alpha = 90°$ then $\beta = -2\beta_{eff}$, and at the "magic angle" $\alpha = \arccos (1/3)^{1/2} = 54.74°$ and $\beta_{eff} = 0$, regardless of the symmetry of the transition.

There are four pieces of information, that one can obtain from the REMPI-TOF profiles:

- the total intensity (σ),
- the spatial anisotropy parameter β,
- the half-width of the TOF profile (Δt),
- the dispersion or spread of the width (ΔT).

This information provides us with a wealth of details about the photodissociation process. For instance, the total intensity of the signal σ_i can be used to determine the photofragment state population as will be described later. The recoil anisotropy parameter β holds information about the symmetry of the excited electronic state of the parent molecule. The half width is related to the kinetic energy release, and the dispersion of the width relates to the distribution of the fragment kinetic energy, if more than one channel can lead to the detected photofragment. When only two or three dissociation channels are open to a specific fragment, it is possible to fit the TOF profile to a sum of individual TOF profiles and derive a branching ratio.

The following is relevant for the analysis of a TOF profile of an *atomic* fragment that has been produced by dissociation of a polyatomic molecule (in this dissertation detection of Br fragments following BrNO dissociation but see also ref. 39). For a photodissociation of a triatomic there is normally an internal energy distribution associated with the diatomic fragment. Energy conservation leads to a distribution of the kinetic energy of the atomic photofragment. A similar contribution to equation (41) arises from the system response function related to experimental parameters such as the cross sections of the laser beams and the probe laser pulse duration. If one assumes Gaussian functions for both the fragment recoil speed distribution and the system response, the TOF profile of the atomic fragment can be written as:

$$I(t) = A\int_{t_0+\Delta t}^{t_0-\Delta t}\left[1+\beta_{eff}P_2\left(\frac{\tau-t_0}{\Delta t}\right)\right]\exp\left(-\frac{(\tau-t)^2}{\Delta T^2}\right)d\tau \tag{43}$$

The convoluting Gaussian function in this equation, with an effective width ΔT, is introduced to take into account both the fragment velocity distribution and the response time of the detection system. With the assumption of two Gaussian functions, the overall width can be resolved into two components using $\Delta T^2 = \Delta t_{KE}{}^2 + \Delta t_{det}{}^2$. The width of the system response function Δt_{det} is essentially determined by the pulsewidth of the photolysis laser and can be determined experimentally. Hence, with the measured ΔT one can deduce Δt_{KE} and the spread of the kinetic energy release may be calculated.

$$\Delta KE = 2(ln2)^{1/2}\Delta t_{KE}\cdot\frac{KE}{\Delta t} \tag{44}$$

On the other hand, the detection of the *diatomic* fragment provides more detail about the correlation between the quantum states of the photofragments, compared to detection of the atomic fragment. For each diatomic fragment state probed the correlated atomic fragment states are limited to a small number (in case of NO + Br only the $\Omega = 3/2$ and 1/2 spin-orbit states of Br). The TOF profiles are simplified in that one has to consider only the system response function and a few distinct channels, rather than a quantum state distribution. When both spin-orbit states correlate to the same diatomic or atomic fragment state, the convoluting Gaussian with width Δt_{KE} is replaced by a sum of separate channels

$$I(t) = \sum_{1}^{N}\left(A_i\int_{t_0+\Delta t_i}^{t_0-\Delta t_i}\left[1+\beta_{eff}P_2\left(\frac{\tau-t_0}{\Delta t_i}\right)\right]\exp\left(-\frac{(\tau-t)^2}{\Delta t_{\mathrm{det}}^2}\right)d\tau\right) \tag{45}$$

with relative intensity A_i for the N atomic fragment channels. If only two channels are present $A_1/(A_1+A_2)$ is the branching ratio.

Equation (43) is integrated analytically yielding

$$I(t)=\frac{\Delta t}{2}\left[1+\beta\frac{3x^{2}-1}{2}+\frac{3}{4}\left(\frac{2\Delta T}{\Delta t}\right)^{2}\right]\left[erf\left(\frac{t-t_{0}-\Delta t}{2\Delta T}\right)-erf\left(\frac{t-t_{0}+\Delta t}{2\Delta T}\right)\right]$$
$$+\frac{3\beta\Delta T}{2\sqrt{\pi}}\left[(x-1)\,exp\left(-\left(\frac{t-t_{0}+\Delta t}{2\Delta T}\right)^{2}\right)-(x+1)\,exp\left(-\left(\frac{t-t_{0}-\Delta t}{2\Delta T}\right)^{2}\right)\right] \quad \textbf{(46)}$$

with the error function *erf(x)* and

$$x=\frac{t_{0}-t}{\Delta t} \quad \textbf{(47)}$$

Similarly equation (45) can be integrated into a sum of the above expressions with different width Δt for each one of the N fragment channels. The experimental TOF profiles were fitted to this function using the non-linear least square fit algorithm of a commercial graphic and analysis program (GENPLOT). The width of the TOF-profile Δt, the centre position t_0 and the spatial anisotropy parameter β were determined by this fitting procedure. The baseline and signal height are additional, very stable fitting parameters. The width of the system response function $\Delta T = \Delta t_{det}$ determined from the REMPI TOF profile of cold NO was 7 ns and was kept constant in any fitting routine.

3.1.2 TOF profiles recorded using a mask (core extraction)

If the TOF signal has two kinetic energy components, it can be fitted using equation (45) in order to determine the branching ratio. However, determination of β^{i}_{eff} for the different channels by such a fit is not reliable if the spatial anisotropy is different for the two channels. In this case we separated the two kinetic energy components by placing a mask with a 4 mm pinhole in the field free region of the TOF-MS(28, 29).

When using a mask in front of the detector, only those photofragments which are ejected at a small angle relative to the TOF axis will not be skimmed. In the ideal case the pinhole is infinitely small, the angle of ejection approaches zero and the TOF profile becomes a pair of peaks for each channel. These peaks are separated according to the photofragments' kinetic energy and their width is determined by the system response. The intensity of the peak-pairs depends on the spatial distribution. Maximum intensity occurs for $\beta_{eff} = 2$ and zero intensity for $\beta_{eff} = -1$ as can be seen from equation (41). It is, therefore, straightforward to obtain β from β_{eff} if one records TOF profiles with two different photolysis laser polarizations, i.e., $\alpha = 0°$ and 90°.

$$\beta = \beta^{\parallel}_{eff}$$
$$\beta = -2\beta^{\perp}_{eff} \tag{48}$$

In the limiting case of a small pinhole $(t - t_0)/\Delta t = 1$. The ion signal I, thus, becomes proportional to $\beta_{eff} + 1$ as can be seen from equation (41). It can then easily be derived that the ratio of the ion signals from both polarizations $\gamma = I^{par}/I^{perp}$ is related to the actual spatial anisotropy parameter by

$$\beta = \frac{\gamma - 1}{\gamma/2 + 1} \tag{49}$$

In an experiment there is, of course, a lower limit to the size of the pinhole and TOF profiles were simulated using the given pinhole size and other fixed parameters (system response time, kinetic energy). These simulations were repeated for different polarizations and β parameters. The ratio γ obtained from these simulated profiles was then used as a calibration for the experimental TOF profiles. In this way it was possible to obtain β independently for different fragmentation channels, i.e., for different kinetic energy components of the same TOF-profile.

3.2 Analysis of the REMPI spectra

3.2.1 MPI lines of halogen atoms

Detection of $(^2P_{3/2})$ Cl and $(^2P_{1/2})$ Cl* in BrCl photodissociation experiments and $(^2P_{3/2})$ Br and $(^2P_{1/2})$ Br* in BrNO experiments was carried out using a 2+1 resonance enhanced multiphoton ionization (REMPI) scheme. The REMPI wavelengths, and intermediate state configurations are given in Table 4.

	lower state	intermed. state	resonance wavelength
Cl	$3p^5\,(^2P_{3/2})$	$3p^4\,(^3P)\,4p^1\,^2D_{3/2}$	235.338 nm
Cl*	$3p^5\,(^2P_{1/2})$	$3p^4\,(^3P)\,4p^1\,^2P_{1/2}$	235.204 nm
Br	$4p^5\,(^2P_{3/2})$	$4p^4\,(^3P)\,6p^1\,^2P_{3/2}$	229.220 nm
Br*	$4p^5\,(^2P_{1/2})$	$4p^4\,(^1S)\,5p^1\,^2P_{3/2}$	231.980 nm

Table 4: States of Br and Cl and REMPI wavelengths

Assuming that the ionization step is saturated, the two-photon transition probabilities for the $4p\,^2P_{1/2} \leftarrow 3p^2P_{1/2}$(Cl*) and $4p^2D_{3/2} \leftarrow 3p^2P_{3/2}$(Cl) transitions used in our experiment were determined. This calculated ratio Cl*/Cl = 0.9 was verified experimentally by measuring the ratio between the intensities of the $4p^2P_{1/2} \leftarrow 3p^2P_{1/2}$(Cl*) and $4p^2D_{3/2} \leftarrow 3p^2P_{1/2}$(Cl*) transitions. This ratio was determined to be 2.0 ± 0.5. Through division by the reported [1 : 2.5] ratio of the line-strengths of the $4p^2D_{3/2} \leftarrow 3p^2P_{1/2}$(Cl*) and $4p^2D_{3/2} \leftarrow 3p^2P_{3/2}$(Cl) - transitions(40) we found that the above number of 0.9 is accurate within our experimental error.

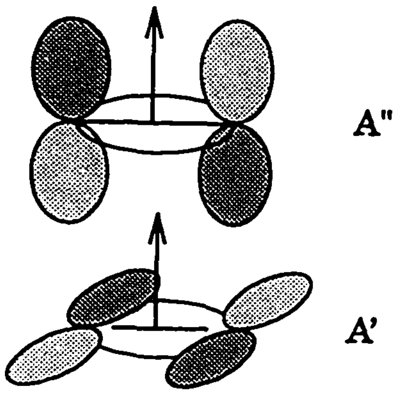

Figure 17: The electronic alignment of the π lobes is probed via the two different Λ-doublet transitions

Relative line-strengths for the Br and Br* REMPI lines were also obtained indirectly. Since dissociation of BrNO at 355 nm produces approximately 10% Br and 90% Br* and the ion signal intensity ratios of the 2+1 REMPI process were close to 1:2, we estimated the line-strength factors to be in the order of 80:20. This assumes that the probe laser light did not contribute to the formation of Br-atoms - a condition which is not necessarily fulfilled given the strong absorption

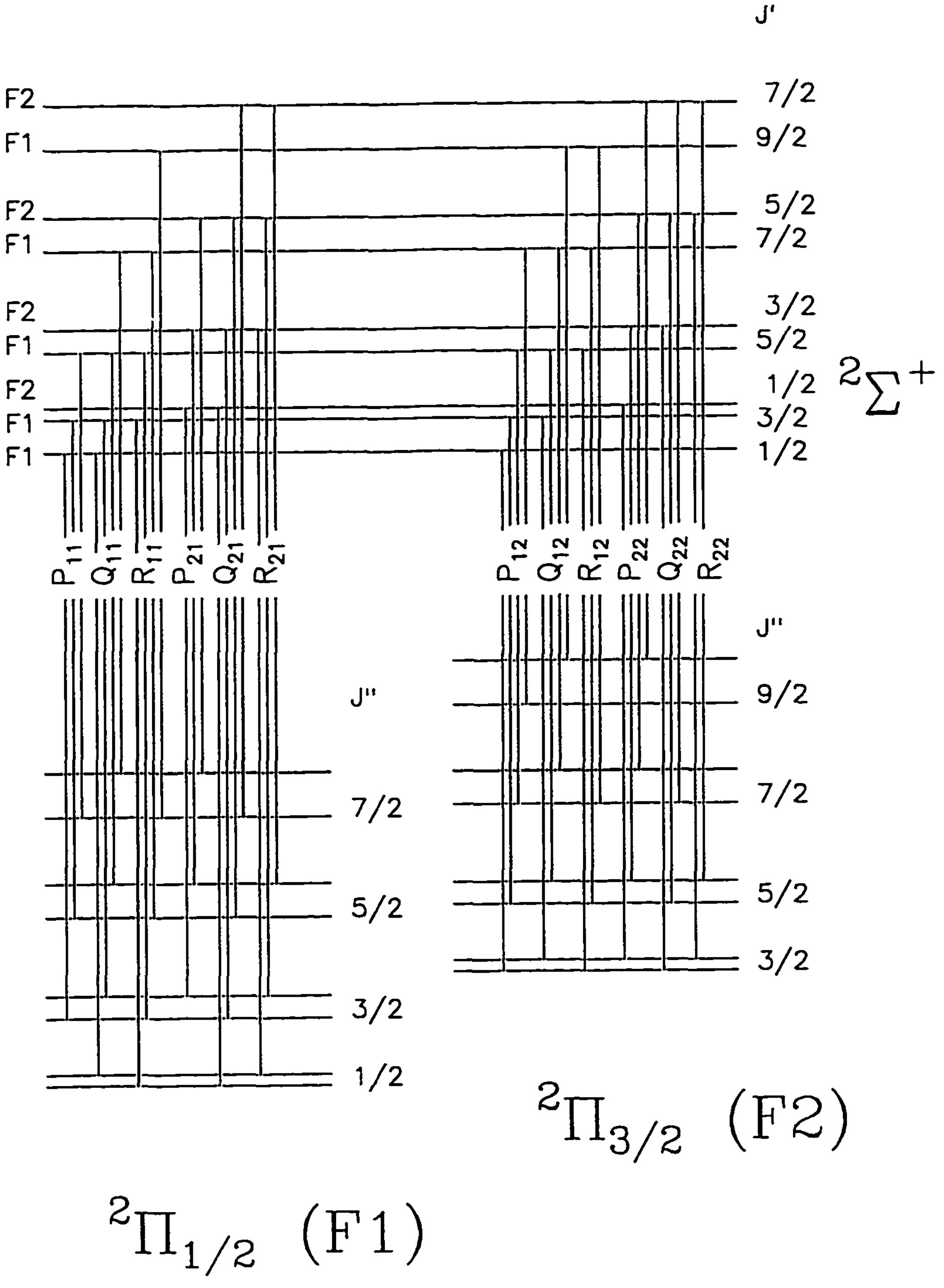

Figure 18: Energy level diagram of the NO ($A^2\Sigma^+ \leftarrow X^2\Pi$) γ-band

of BrNO in the UV-region. However, under conditions of complete bleaching of the sample molecules in the molecular beam by the photolysis light the above approximation is valid.

3.2.2 MPI lines of NO

NO photofragments were detected state selectively using 1+1 REMPI *via* the γ-band transition $A\ ^2\Sigma \leftarrow X\ ^2\Pi$. For small rotational excitation NO belongs to Hund's case (a) ($A_{SO} = 123\ \mathrm{cm}^{-1}$), whereas at higher rotational excitation ($J > 50.5$) the spin-orbit splitting becomes smaller, i.e., L and S uncouple, and NO becomes a Hund's (ab) intermediate case(41,42).

Each of the two NO spin-orbit states is twofold degenerate, as is the case for all linear molecules with nonzero orbital angular momentum projections on the symmetry axis ($\Lambda \neq 0$). Rotation lifts the degeneracy, because the Λ-doublet states interact differently with higher electronic states. The Λ-doublet splitting is therefore strongly dependent on the rotational excitation (for NO: $\Delta E = 0.35\ \mathrm{cm}^{-1}$ at $J = 45.5$). Since the electron spin vector S is coupled to N (the result of coupling the rotation R with L) one of the components will preferably direct the electron probability distribution into the plane of rotation (A'), and the other out of the plane (A")(43) (see Figure 17). For NO R and S only couple strongly at high rotational excitation, and therefore this degree of electronic alignment will increase with J(44). The parity of the Λ doublet states, however, is still well defined even at low J, which is important for the investigation of dynamic processes. In Figure 18 the transitions used in the first absorption step are schematically displayed.

The possibility of probing the alignment of the electron cloud with respect to the plane of rotation permits one to deduce the dynamics of elementary reactions such as photodissociation processes. However, when trying to determine the population of the spin-orbit, Λ-doublet, rotational and vibrational states from REMPI line-strengths, one has to consider various effects.

Rotational line-strength factors (Hönl-London factors) of the γ-band determine the probability of absorption of the first photon in the 1+1 REMPI process. The Hönl-London factors for a ${}^2\Sigma \leftarrow {}^2\Pi$ transition have been calculated by Earl(45) and recent measurements on NO have demonstrated the accuracy of these early equations(46). Within the error of our experiment the relative transition probability for the different branches can be expressed as

R_{11}/P_{11} : Q_{11} : R_{22}/P_{22} : Q_{22} : R_{21}/P_{12} : Q_{21}
1 : 2 : 1 : 2 : 1/3-1/7 : 2/3-2/7

For J > 10 the main branches can assumed to be independent of J. The intensities of the satellite branches are weaker than the main branches and are also more strongly J dependent. Since all desired information is contained in the main branches, these satellites were only used for rough estimates of trends.

The probe laser power shot-to-shot intensity had fluctuations of up to 30 %. Thus it is important to determine the power dependence of the ion signal and then correct for power fluctuations. The dependence on the power may be assumed to be quadratic for a two photon process and linear for a one photon process. However, in a discussion of the REMPI spectra of NO, Zare and coworkers(47) demonstrated that even different lines of the same band show different dependences upon laser power. This is due to three effects.

The intermediate state alignment is important at low laser powers and affects P/R bands differently than Q bands. Since this effect depends strongly on laser power, it is difficult to account for. A second complication is the different extent of saturation of the ionization step. States which are easier to ionize (corresponding to transitions that saturate more readily) result in a lower power dependence than those which are not easily ionized. Finally, one has to avoid inhomogenieties of the laser field in the interaction zone. It was noted that the use of lenses with short focal length leads to strong intensity gradients near the focal point. In the regime of partial saturation the resulting differences in power dependences are very difficult to account for.

All three complications were overcome by choosing the highest possible laser power for the REMPI step combined with relaxed focussing conditions. The different intermediate state levels are then bleached and at the highest power densities the ionization step is completely saturated for *all* transitions. One then expects a linear power dependence. This was verified for each experiment by determining the dependence of the ion signal of different REMPI lines on the laser power measured using a photodiode (PD). The parameters obtained from the linear fit of a *log (I) vs. log (PD)* plot were the power dependence (typically 1.0 ± 0.2) and the PD offset. They were used to correct the ion signal for the probe laser power fluctuations.

The resulting corrected REMPI spectra were then assigned to the well known $A \leftarrow X$ transitions by comparison with the tables of reference 48. Relative populations were obtained through division by the line-strength factors. These populations are presented in the results section. The error associated with the given populations is mainly due to the assumptions made above and the shot-to-shot fluctuations of the photolysis laser which were not corrected for.

3.3 Bleaching of the molecular beam sample

In BrNO photolysis experiments to detect the bromine fragment, it was necessary to bleach the molecular beam sample in the photolysis step to avoid interference with BrNO dissociation initiated by the delayed probe laser beam. Bleaching is also desirable in other experiments to suppress signal fluctuations due to small photolysis power changes. The molecular beam can be bleached easily using high photolysis laser intensities and relaxed focussing conditions. Since the "rotational period" is in the order of picoseconds, and thus small compared to the pulse duration of the probe laser, each molecule will eventually be able to orient itself with its transition dipole moment aligned with respect to the electric field component of the laser field. The velocity of the molecular beam is approximately 2 µm/ns; so the sample volume exposed to the ~10 ns laser beam has roughly twice the cross section of the 20 µm laser focal spot. Assuming a "path length", i.e., molecular beam width, of 1 mm the extent of bleaching can be calculated from the deviation of the absorbed energy with respect to the absorbed energy using Lambert-Beers law(49). We consider the case of a collimated beam in the interaction region with a Gaussian intensity profile

$$I(r)=\frac{2E}{\pi\omega_0^2}\,exp\left(-\frac{2r^2}{\omega_0^2}\right) \tag{50}$$

with the size of the focal spot, ω_0, and the incident laser energy E. The absorbed energy can then be derived(49)

$$E_{abs}=E-\int_0^{\infty}dr\ 2\pi r\ \frac{h\nu}{\sigma}ln\left[1+exp^{-\sigma nl}\left(exp^{\sigma I/h\nu}-1\right)\right] \tag{51}$$

With the known absorption cross section σ at photon energy $h\upsilon$ one can calculate at which number densities n bleaching is dominant. Generally, bleaching is important if $I/h\upsilon \gg nl$. Since the number density of the molecular beam is extremely low, it can be shown that even a laser beam carrying only little energy is able to completely bleach the sample. An illustrative calculation was carried out assuming relaxed focussing conditions ($\omega_0 = 50$ μm), a very high number density $n = 10^{22}$ m^{-3}, an absorption cross section of $\sigma_{abs} = 10^{-23}$ m^2 at 480 nm, and a molecular beam width of $l = 5$ mm. Even under those conditions bleaching was significant for $E = 100$ μJ/pulse.

4 Photodissociation dynamics of BrCl

4.1 Introduction

4.1.1 Electronic structure and correlation diagram

The diatomic halogen and interhalogen compounds have a long history of spectroscopic, photochemical and theoretical investigations. All four homonuclear and all six heteronuclear diatomics are stable. The halogen atoms show clear trends in, for example, electronegativity, electron affinity and spin-orbit coupling constants. These trends affect the electronic structure of the diatomic molecules, which is similar, yet changes systematically as one increases the mass of the atomic components. Consequently, the halogen and interhalogen molecules invite comparative studies, of which Mulliken's analysis of the halogen spectra in 1930(50) was one of the first. More recent studies have frequently focused on the study of excited state interactions and non-adiabatic effects (see e.g., references 17, 51-53). These interactions together with the apparent simplicity of the electronic structure make halogen and interhalogen molecules ideal systems for exploring novel ideas such as coherent radiative control of photodissociation(54) and femtosecond probing of solvent cage dynamics(55).

The electronic states of the halogen and interhalogen molecules may be described using simple Linear Combination of Atomic Orbitals (LCAO)(56). The LCAO model predicts that the configuration of the ground and excited states can be expressed by various distributions of the 10 valence electrons in the σ, π, π^*, σ^* molecular orbitals (MO). In this picture the ground state is characterized by the $(\sigma)^2$, $(\pi)^4$, $(\pi^*)^4$, $(\sigma^*)^0$ configuration ([2440] in Mulliken's notation) and the ordering of the excited states can be well estimated using the energy differences between the MO's(57).

For each excited electron configuration there exist states of different multiplicity which are separated by the electron exchange energy. The left hand side of the correlation diagrams (Figure 19 and Figure 20) indicates the splitting of the molecular states and the breakdown of states with the same multiplicity into their multiplet components. These components are

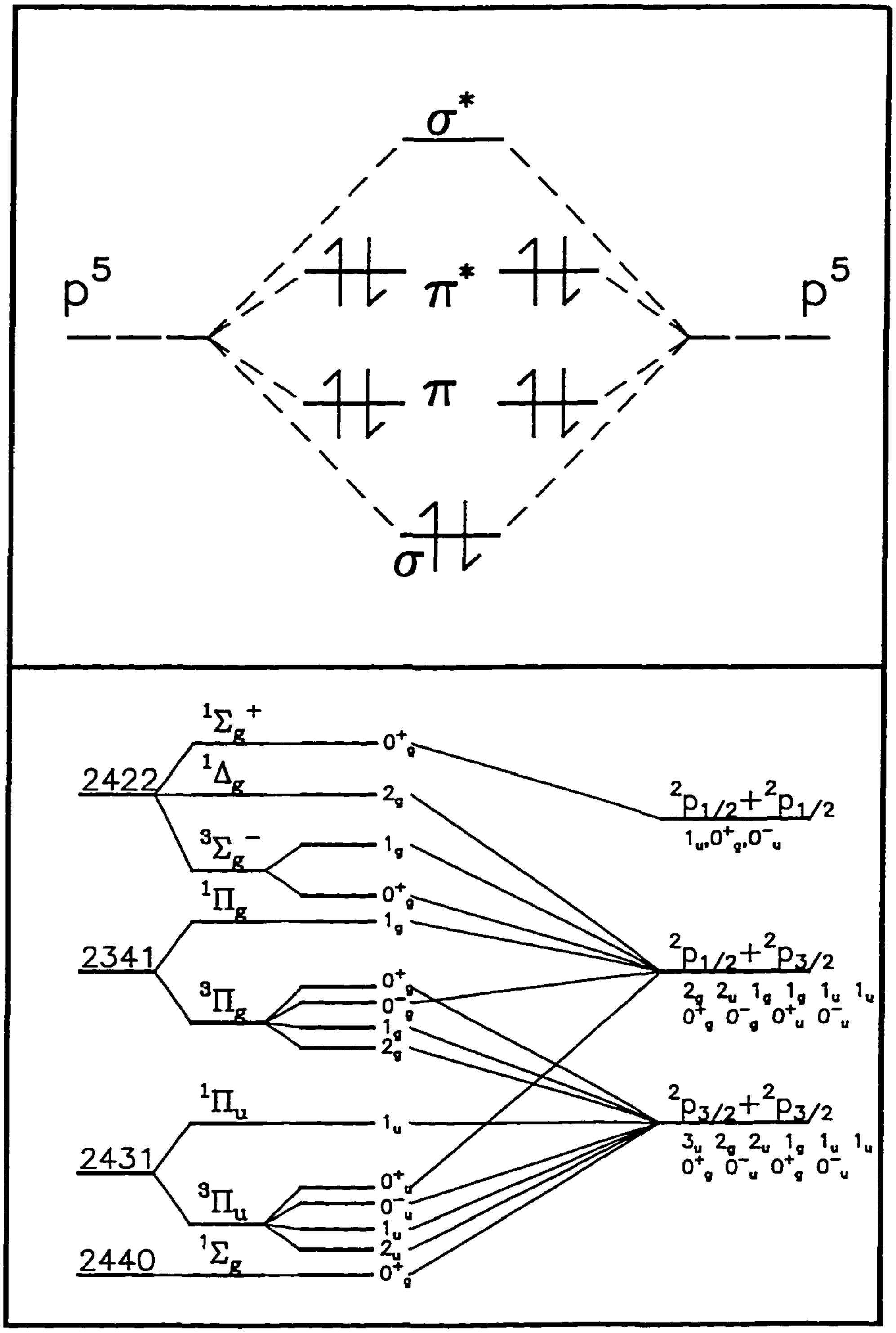

Figure 19: Molecular orbital diagram and adiabatic correlation diagram for a halogen molecule

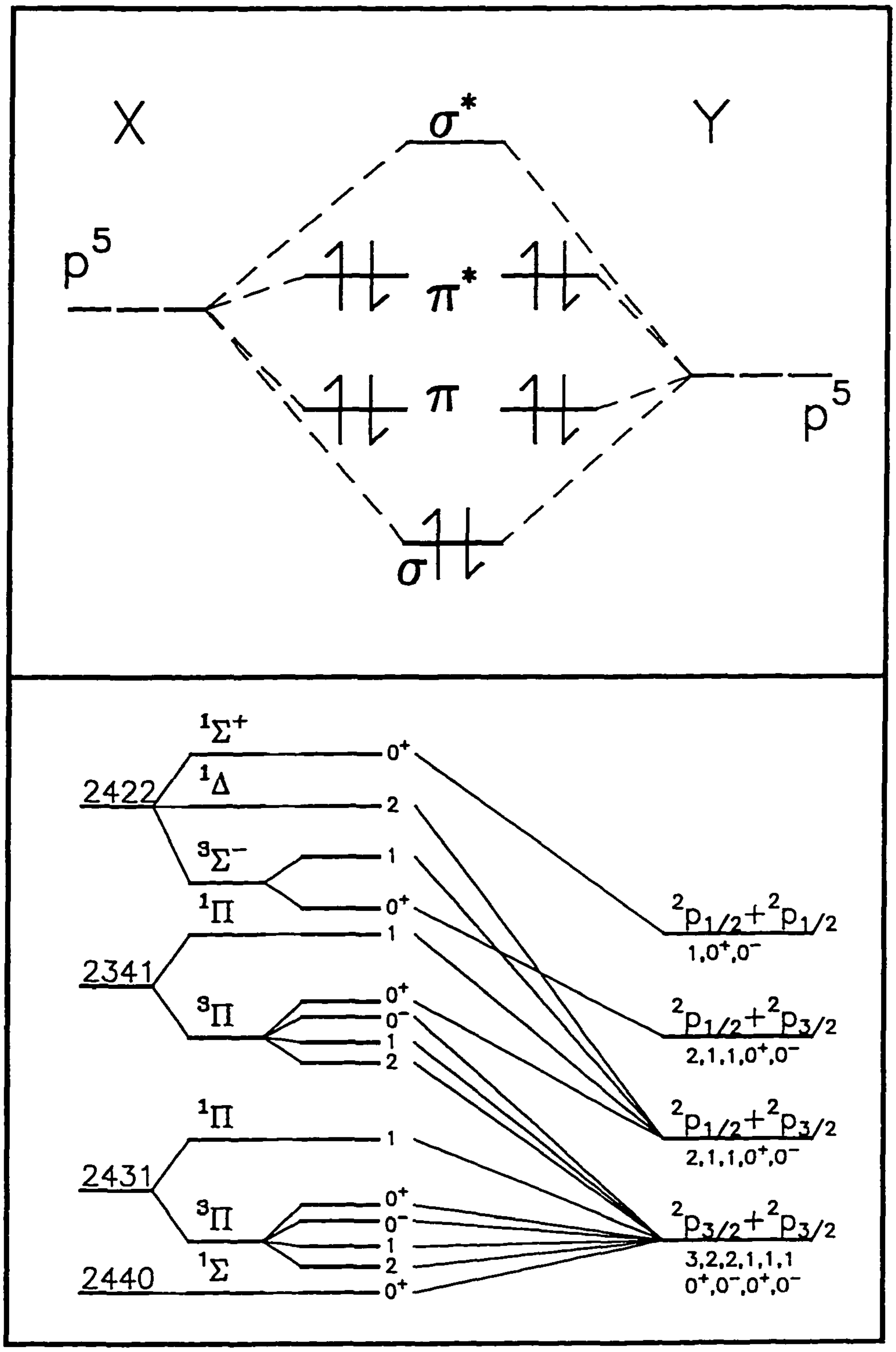

Figure 20: Molecular orbital diagram and adiabatic correlation diagram for an interhalogen molecule

labelled by their quantum number $\Omega = \Lambda + \Sigma$, which is the only good quantum number in the case of strong spin-orbit interactions, i.e., in Hund's case (c).

All halogen atoms appear in two spin-orbit states - X ($^2P_{3/2}$) and X ($^2P_{1/2}$) (abbreviated X and X* in the following). Therefore for homonuclear halogens there are three energetically different, neutral fragment channels (X+X, X+X* and X*+X*), whereas for the interhalogens there exist four fragment channels (X+Y, X+Y*, X*+Y and X*+Y*). Here, "X" stands for the heavier atom in the diatomic "XY". The quantum number Ω for the fragment states can be found by j-j coupling , i.e., by linear combination of the atoms $j = l + s$ quantum number. The adiabatic correlation between parent and fragment states is usually established assuming that Ω is a valid quantum number throughout the dissociation process and that states of the same Ω do not cross.

The difference between halogen and interhalogen correlation diagrams lies mainly in the relaxed symmetry restrictions. While the homonuclear halogen molecules conserve parity upon dissociation ("gerade" states correlate only with "gerade" states, and "ungerade" with "ungerade"), the interhalogens do not have symmetry upon inversion.

The two correlation diagrams illustrated are adiabatic constructs, i.e., states of the same symmetry are not allowed to cross. However, as outlined in section 1.1.3, the adiabatic picture will likely fail in dynamic processes such as fast photodissociation. A correlation diagram, which incorporates the diabatic dissociation channels, is therefore more useful in describing and predicting these processes. In principle, a diabatic correlation diagram can be used to construct the adiabatic correlation diagram by introducing avoided crossings wherever two states of the same symmetry cross. The gap between the resulting adiabatic curves is directly proportional to the electronic coupling term. In the case of the halogens and interhalogen compounds this is predominantly the molecular spin-orbit coupling introduced by the spin-orbit coupling of the halogen atoms. The spin-orbit coupling term increases from approximately 440 cm^{-1} for fluorine to 7600 cm^{-1} for iodine atoms.

However, diabatic correlation diagrams, as they often appear in the literature, are very idealized constructs, since they tacitly imply that each molecular state will transform diabatically into only one fragment channel state. As will be shown later, a completely diabatic dissociation process starting from a "pure" molecular wavefunction usually yields a linear combination of fragment channel wavefunctions. The molecular states are generally not a proper basis for the asymptotic description of the fragments when interactions, such as spin-orbit coupling, which does not vanish for large internuclear separations, are included. This point of view not only questions the meaning of the "diabatic correlation diagrams", but also the idea of a "diabatic dissociation limit". The diabatic dissociation limit is often used in terms of the *one* fragment channel into which the molecular wavefunction is transformed - given an idealized diabatic process. Again, since more than one fragment channel is usually involved, even in the axial recoil limit, we have to specify whether the highest accessible or the most probable dissociation channel is meant.

In this study we attempt to characterize a strongly diabatic dissociation process. By photolysing the sample molecule we will first identify the fragment channels involved, and then try to gain an understanding of the physical principles that govern this dissociation process by using different theoretical approaches.

The remainder of this introduction is organized in the following way: First an overview of the characteristics of the low lying electronic states of the halogen and interhalogen molecules will be provided; then we will focus on the dynamics of one state, the $B\ {}^3\Pi(0^+)$ - state, of the specific compound under investigation, BrCl.

4.1.2 The electronic states of halogen and interhalogen molecules

Apart from the ground state, the most deeply bound states are those with the 2431 ${}^3\Pi(\Omega)$ configuration(58), specifically the $B\ {}^3\Pi(0^+)$ -, $A\ {}^3\Pi(1)$ - and $A'\ {}^3\Pi(2)$ - states. Transitions between the X ${}^1\Sigma(0^+)$ ground state and the B-state - and occasionally the A-state - are observed in the visible region of the absorption spectra. This absorption, together with a third continuum absorption arising from excitation to the 2431 ${}^1\Pi(1)$ state, is thus responsible for the colour of the halogen and interhalogen gases. The formally spin-forbidden transitions to the triplet states are strong for the heavier molecules, since *via* spin-orbit coupling certain components of the triplet states can borrow intensity from singlet states. For instance, the A←X transition of Cl_2, Br_2 and I_2 is enhanced by mixing of the A $^3\Pi(1)$-state with the $^1\Pi(1)$ state. Similarly, the B←X transition gains intensity from mixing of the B $^3\Pi(0^+)$-state with the 1441 $^1\Sigma(0^+)$ state and by mixing of the ground state X $^1\Sigma(0^+)$ with the 1342 $^3\Pi(0^+)$ ion-pair state(57).

In *halogens* the B-state is adiabatically correlated to the X + X* fragment channel, since the lowest fragment channel does not provide a 0^+_u component (Figure 19). In the case of *interhalogen* molecules, one expects an adiabatic correlation to the lowest X + Y fragment channel, since parity is not a good quantum number (Figure 20). Diabatically, the B-state correlates to a higher exit channel as has been observed in numerous spectroscopic and photodissociation experminents on interhalogens(58-63). This diabatic curve crosses a purely repulsive 0^+ state (commonly named $Y(0^+)$), which correlates to the lowest atomic limit and thereby causes an avoided crossing. Since this interaction is relatively strong ($\Delta\Omega = 0$), it was formerly believed that a new set of adiabatic curves, namely the lower $\tilde{B}$ state and the $\tilde{B}$' upper adiabat (Figure 21), is formed. The higher adiabatic state is weakly bound and for several molecules (IBr(64), ICl(65) and BrF(66)) levels have been identified. The lower adiabatic $\tilde{B}$ state exhibits a barrier, the height of which is dependent on the mixing term and the separation of the fragment channels. Later, Child representatively showed for IBr(64) that, despite the strong spin-orbit coupling term, the coupling between the $Y(0^+)$ and the B-state belongs to one of the intermediate coupling cases. The levels found above the barrier were well described by assuming an intermediate between an adiabatic and diabatic potential energy curve, and not a purely adiabatic curve.

We can expect similar avoided crossings of the diabatic B-state curve with other 0^+-states which lie above the $Y(0^+)$ state. These interactions are expected to be strong, since the 0^+ states can strongly couple to the B-state ($\Delta\Omega = 0$), and, at least for the lighter interhalogens, are energetically close. The number and the position of such avoided crossings would then depend on the "diabatic correlation limit(s)" of the B-state. It is, therefore, necessary to establish to which fragment channels the B-state diabatically dissociates, because only this information allows the prediction of higher excited state potential energy curves in this manifold.

There exists some information about the diabatic limit(s) of the B-state obtained from spectroscopic experiments. These limit(s) are commonly identified as the second lowest fragment channel X + Y* for ICl, IBr, BrCl and the third lowest channel X* + Y for FCl, FI and FBr(58). However, higher diabatic dissociation limits can not be excluded, since the parity restrictions which forbid dissociation to X* + Y* in homonuclear halogens do not exist in interhalogens. Spectroscopically, it is difficult to establish the diabatic dissociation limits, since they can only be obtained by extrapolation of the bound part of the B-state curve.

The aim of this study is to describe the dissociation processes *via* the B $^3\Pi(0^+)$-state of one of these molecules, BrCl, in its axial recoil limit and to identify diabatic dissociation limit(s). The diabatic and adiabatic potentials involved in the dissociation process will be qualitatively characterized. It is attempted to give guidelines for the construction of a *diabatic* correlation diagram, which may be generalized and then be used to understand and predict the interactions between the low lying excited states at large internuclear distance of other (inter)halogens.

4.1.3 The B-state of BrCl

The B $^3\Pi(0^+)$-state of BrCl has been accurately described by various spectroscopic experiments. It has a well-defined minimum located at r = 2.54 Å and 16795 cm^{-1} above the minimum of the ground state potential(59, 67). The strong interaction with the Y(0^+) state described above leads to a barrier which is approximately 245 cm^{-1} above the dissociation limit of 18245 cm^{-1} (67, 68). It was observed that the v' = 9 state has rotational levels above this rotationless barrier. They are bound by a combination of this barrier and the centrifugal barrier (Figure 21).

The B-state is weakly predissociated for the levels v' = 6 (only J' > 42), 7 and 8, i.e., below the rotationless barrier(69). This is likely due to a weak interaction with the $^1\Pi(1)$

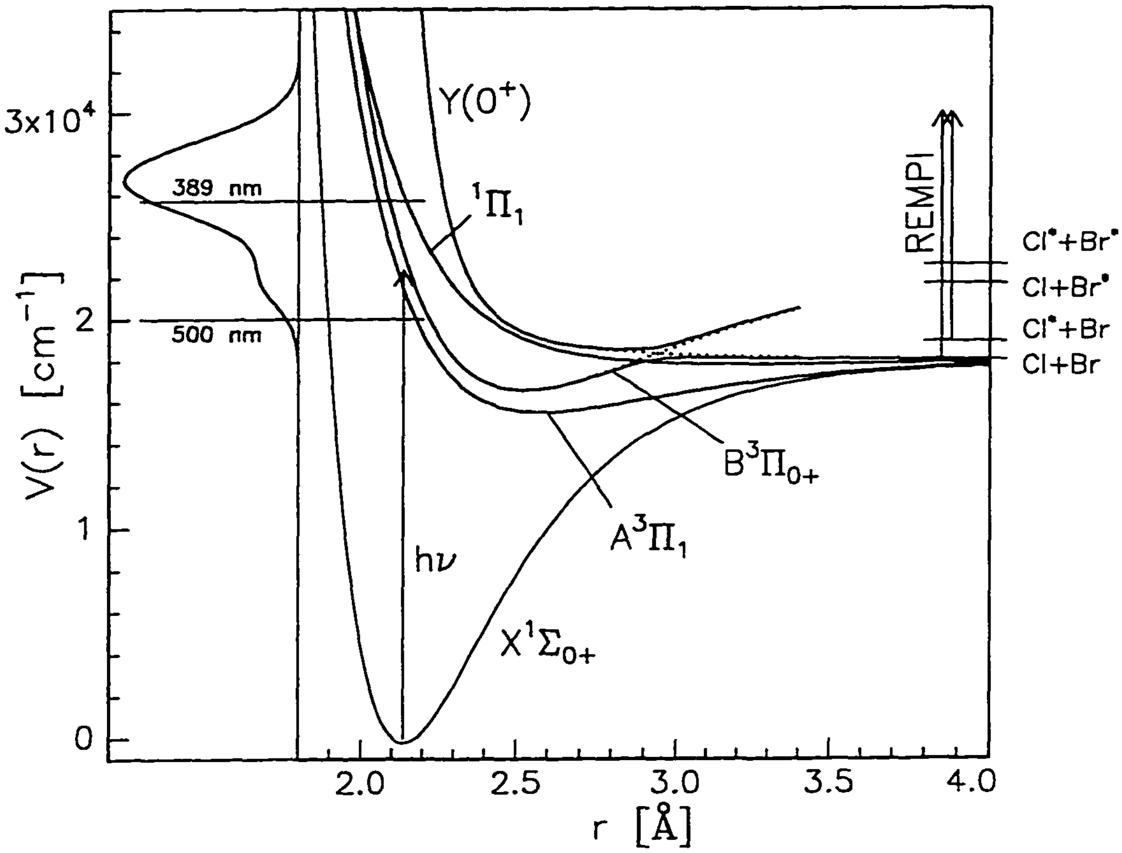

Figure 21: Potential energy curves and absorption spectrum of BrCl. The B $^3\Pi(0^+)$ state is intersected by the $^1\Pi(1)$ state and has an avoided crossing with the Y(0^+) state.

state. The $^1\Pi(1)$ state intersects the B-state almost horizontally at r ~ 3.05 Å and at an energy near the dissociation limit. The $^1\Pi(1)$ state has not been well characterized spectroscopically but it is known that it has a shallow minimum at a long internuclear distance. Photodissociation via the $^1\Pi(1)$ state is expected to be mainly adiabatic, yielding bromine and chlorine atoms in their spin-orbit ground state(69) (Figure 20 and Figure 21). The A $^3\Pi(1)$ state absorbs only weakly.

Complementary information about the avoided crossing of the B-state with the Y(0^+) state can be obtained by studying the $\tilde{B}$'-state curve and the higher adiabatic curves. Hopkirk *et al.*(70) observed dispersed fluorescence following 153 nm and 147 nm excitation from the

$E(0^+)$ state to those 0^+ states of BrCl which correlate to the two higher neutral fragment channels. They proposed that these states are, at large internuclear distances, roughly parallel to both the X-state and the $\tilde{B}$-state and that shallow minima exist.

The most recent analytical form for the adiabatic B-state curve expresses the potential as arising from a Morse curve and an exponentially decaying function which are coupled via a local interaction term(67). It was noted that the asymptote of the Morse function is 5300 cm^{-1} above the ground state atomic limit, hinting that the diabatic dissociation limit is Br*+Cl* or Br*+Cl rather than Br+Cl*.

In an earlier study, Coxon carried out a B-state rotational analysis(60) which also implied a crossing of the two diabatic curves above the Br+Cl* channel. Both spectroscopic studies, however, suffered from the inherent difficulty of estimating the interaction term. The spectroscopic work only provides information about the bound part of the lower adiabatic state and the fitting parameters are therefore highly correlated and subject to error.

On the other hand, in a photodissociation experiment on BrCl at 460 nm, Baughcum *et al.*(71) failed to observe Br* fragments. If one uses the most recent value for the adiabatic dissociation limit it appears, however, that this excitation energy may be too close to the Br*+Cl dissociation limit and, therefore, formation of Br* may be prevented for energetic reasons. The energetics of the four possible dissociation channels (labelled (a) to (d) in Table 5 and thereafter) and their threshold wavelengths are listed below.

In this study we followed a similar experimental approach. Photodissociation was initiated on the repulsive part of the B-state curve at various excitation energies above the

BrCl	→	$Br(^2P_{3/2}) + Cl(^2P_{3/2})$	555 nm	E_{th}= 18022 cm^{-1}	(a)
		$Br(^2P_{3/2}) + Cl^*(^2P_{1/2})$	529 nm	E_{th}= 18903 cm^{-1}	(b)
		$Br^*(^2P_{1/2}) + Cl(^2P_{3/2})$	461 nm	E_{th}= 21707 cm^{-1}	(c)
		$Br^*(^2P_{1/2}) + Cl^*(^2P_{1/2})$	443 nm	E_{th}= 22588 cm^{-1}	(d)

Table 5: Threshold energies for the four fragmentation channels of BrCl

dissociation limit and the photofragments were detected state-selectively using the REMPI technique. The angular distribution of the chlorine fragments was mapped utilising photofragment time-of-flight (PF-TOF) spectrometry. Since the spatial distribution reflects the symmetry of the excited state, it was possible to distinguish between fragments evolving through the B-state ($\Delta\Omega = 0$; parallel transition) and the $^1\Pi(1)$ state ($\Delta\Omega = 1$; perpendicular transition). Furthermore, this technique provides information about the kinetic energy release of the dissociation process permitting the direct observation of the different exit channels. In addition, the branching ratio Cl*/(Cl+Cl*) and its dependence on the excitation energy provides complementary information about the exit channels of the diabatic passage of the wavepacket through the interaction region(s). Using simple Landau-Zener type calculations an estimate for the interaction term can be given.

Finally, a diabatic correlation diagram, constructed following theoretical considerations, will be given. This diagram will be used to predict qualitatively the interactions among the halogen and interhalogen excited states.

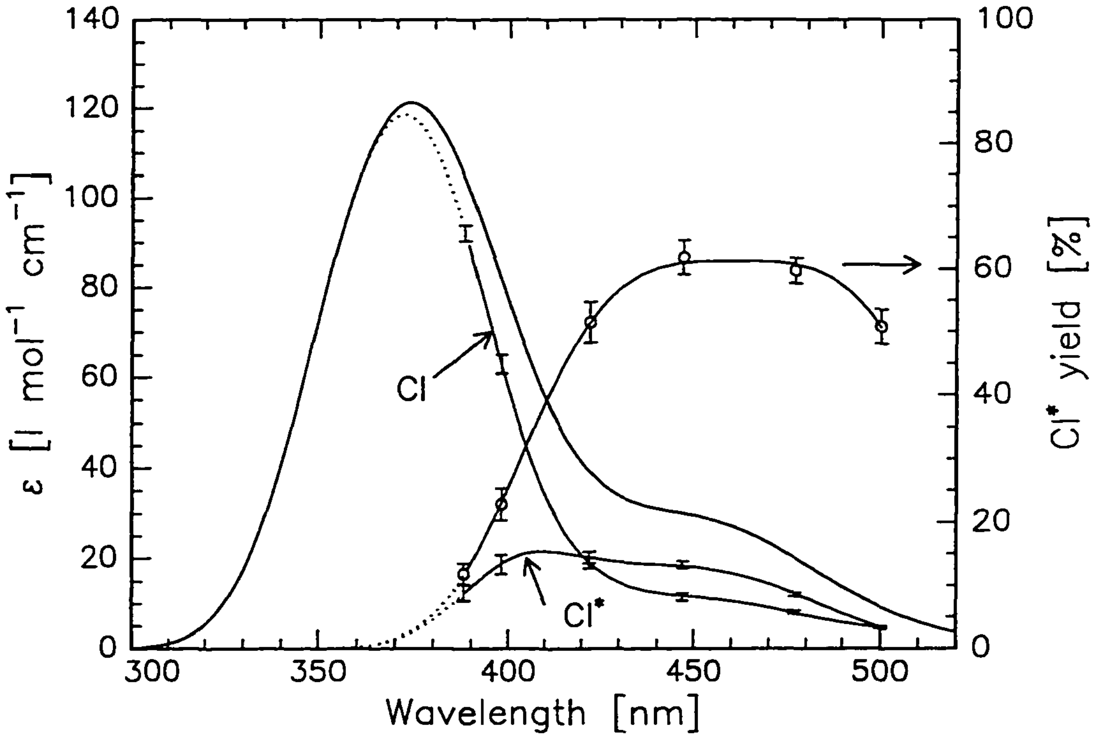

Figure 22: Absorption spectrum of BrCl (after ref. 72). The measured Cl*/(Cl+Cl*) branching ratio is also displayed (right axis). Photofragment yield spectra of both Cl* and Cl fragment states are included.

4.2 Results

The Cl/Cl* REMPI intensity ratio has been determined at six photolysis wavelengths and converted into branching ratios. In Figure 22 the Cl* yield of the BrCl photodissociation is displayed as a function of the photolysis wavelength. A smooth curve is used to serve as a guide for the eye and to interpolate the branching ratio between the data points. The absorption spectrum obtained from reference 72 is also shown. The spectrum exhibits contributions from transitions to at least two excited states. The $^1\Pi(1)$ state peaks at around 370 nm and the $^3\Pi(0^+)$ state forms a shoulder towards the red region. By multiplication of the absorption spectrum and the branching ratio curve one can obtain the product yield spectrum of the Cl* fragment and, similarly, of the Cl fragment. These photofragment yield spectra are also included in Figure 22.

TOF profiles of the Cl* and Cl atomic photofragments were recorded at each one of the six wavelengths (Figure 23). The profiles of the Cl* fragment show predominantly parallel transition characteristics as expected for the ($\Delta\Omega = 0$) transition to the B-state, whereas TOF profiles of the Cl fragment show a strong wavelength dependence of the spatial anisotropy (Table 6). The spatial anisotropy parameter for Cl is $\beta = -1$ for the shortest wavelength studied, as expected for the ($\Delta\Omega = 1$) transition to the $^1\Pi(1)$ state, but increases to $\beta = 0$ at the longest wavelength studied. This indicates that both the B-state, at longer wavelength, and the $^1\Pi(1)$ state, at shorter wavelength, contribute to Cl formation.

The determination of the spatial anisotropy parameter is complicated by the effect of *atomic* fragment v-J correlation as described in reference 25. TOF profiles of the Cl ($^2P_{3/2}$)

λ [nm]	β(Cl*) ± 0.15	$\beta_{\perp}$(Cl) ± 0.15	$\beta_{\parallel}$(Cl) ± 0.15	γ_{total} ± 0.1	$\gamma_{parallel}$ ± 0.15	X(Cl*) ± 0.15
355	1.5	-1.08	-0.70	/	/	/
389	1.84	-0.90	-0.24	0.12	0.79	0.57
398	1.74	-0.60	-0.14	0.23	0.67	0.76
422	1.77	-0.20	-0.12	0.52	0.79	0.95
447	1.52	0.04	0.20	0.62	0.80	1.0
477	1.58	0.20	/	0.60	0.76	1.0
500	/	/	/	0.51	/	1.0

Table 6: Summary of experimental results on BrCl: Spatial anisotropy parameters β for Cl and Cl* channels, branching ratio γ=Cl*/(Cl+Cl*), and branching ratio of channel (b) X(Cl*)=(b)/[(b)+(d)]

fragment recorded using different polarizations of the probe laser are shown to be different due to the electronic alignment of the atomic fragments. In Table 6 β-values using both polarization planes are listed, with the probe laser **E** vector parallel, or perpendicular, to the **E** vector of the photolysis beam. An average $(\beta_{\perp}+ \beta_{\parallel})/2$ is used in the analysis below. Assuming a purely parallel transition for the B-state and purely perpendicular transitions for both the $^1\Pi(1)$- and A-states, it is possible to calculate from β values the fraction of Cl and Cl* which have evolved through B-state excitation. This information was used to determine the branching ratio $\gamma_{parallel}$ = Cl*/(Cl+Cl*) of the B-state alone (Table 6).

Further analysis of the TOF profile showed that at high excitation energies the profiles of Cl* fragments can no longer be fitted satisfactorily using only the width corresponding to the Br + Cl* channel (Figure 23). The residual indicates a second channel for the Cl* formation involving a lower kinetic energy release. The shape, however, suggests that it is formed via the same excited state PES, i.e., following a parallel transition. A fit allowing for two kinetic energy components separated by 3680 cm^{-1} demonstrates the participation of both the Br+Cl* and Br*+Cl* channels (Figure 24). Similar results are obtained for all profiles recorded at excitation wavelength shorter than 450 nm.

To confirm the existence of two Br*-channels at high excitation energies, a TOF profile was recorded with the probe laser wavelength fixed at the centre of the sub-Doppler spectrum instead of being scanned over the Doppler width[4]. The ion signal originating from photofragments with low velocity components perpendicular to the TOF-axis is displayed in Figure 25. Clearly at this excitation wavelength (389 nm) two channels with different

---

[4] This technique is similar to the core extraction technique described in the introduction and the analysis chapter. A TOF profile recorded at the centre of the Doppler width corresponds to a two-dimensional "slice" through the fragment distribution, which is perpendicular to the probe laser propagation direction. The core extraction technique maps a one-dimensional "core", which is perpendicular to both the propagation direction of the probe laser and the molecular beam.

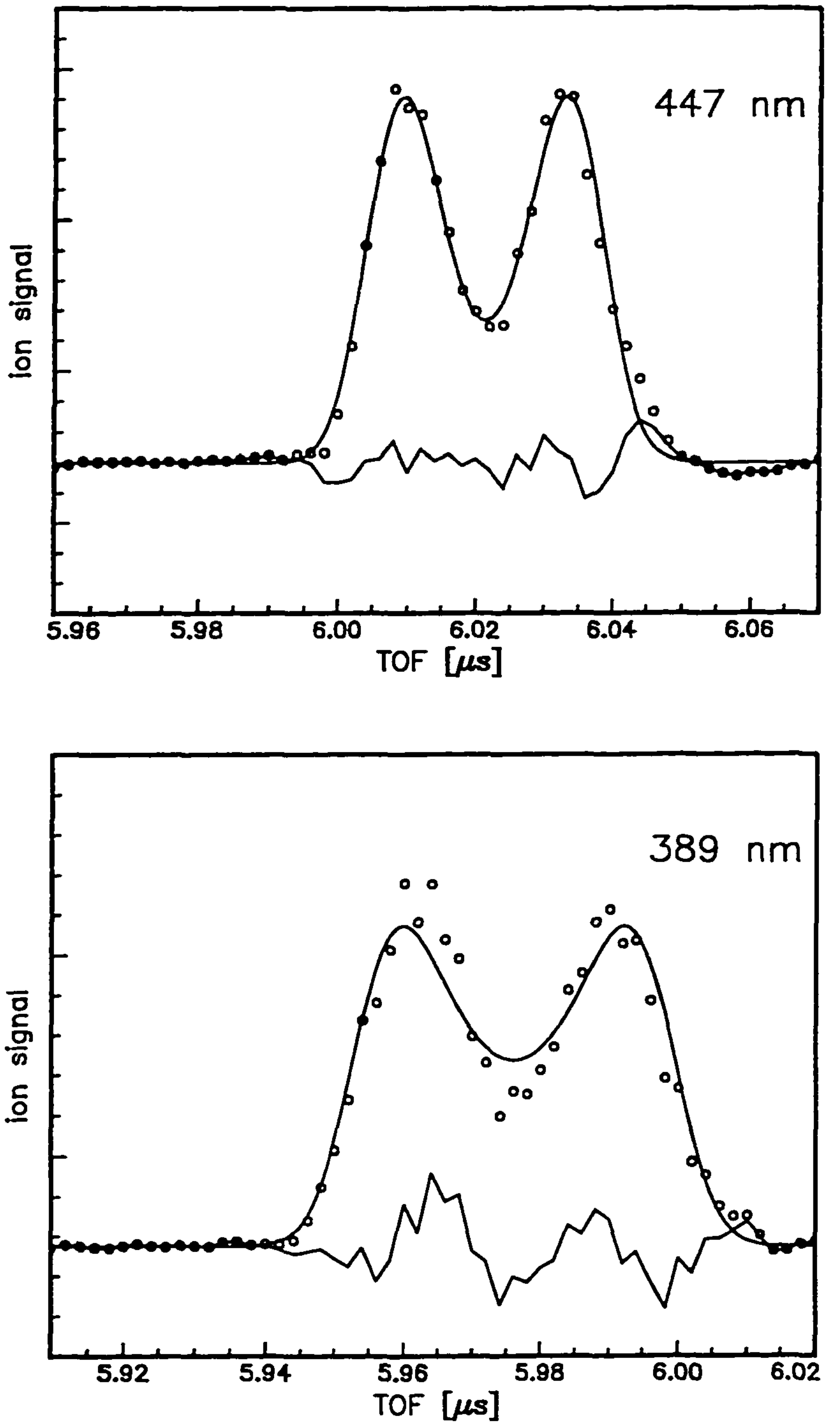

Figure 23: TOF profiles of the Cl* fragment. At short excitation wavelength the profile cannot be fitted well with only one kinetic energy component.

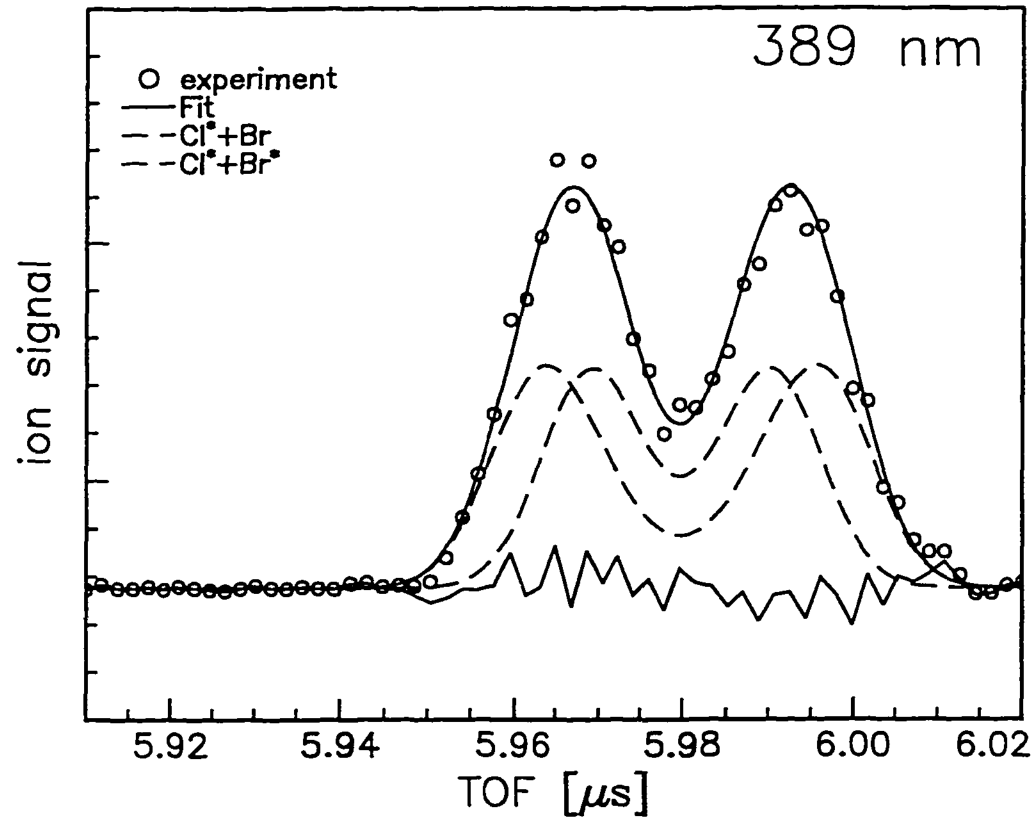

Figure 24: TOF profile as in Figure 23, but fitted for two kinetic energy components

kinetic energy releases contribute to the TOF signal. Because this profile cannot be described by equation (45) a fit is complicated, and determination of the anisotropy parameter and the ratio of the two channels was not attempted.

In principle, the low energy component of the Cl* photofragment TOF profile can also arise from photodissociation of Cl_2. In an equilibrated gas mixture the molar ratio of BrCl: Cl_2: Br_2 never exceeded 55%: 26%: 19%. The 26% Cl_2 molecules also interact with the photolysis beam. Matsumi *et al.*(53) reported a Cl*/(Cl+Cl*) branching ratio of 12% at 390 nm increasing to 32% at 475 nm. This implies that a maximum of 4% to 8% of the molecules present in the beam are Cl_2 molecules dissociating via the Cl+Cl* channel. This is an estimated upper limit, since it was assumed that the molecular beam is completely

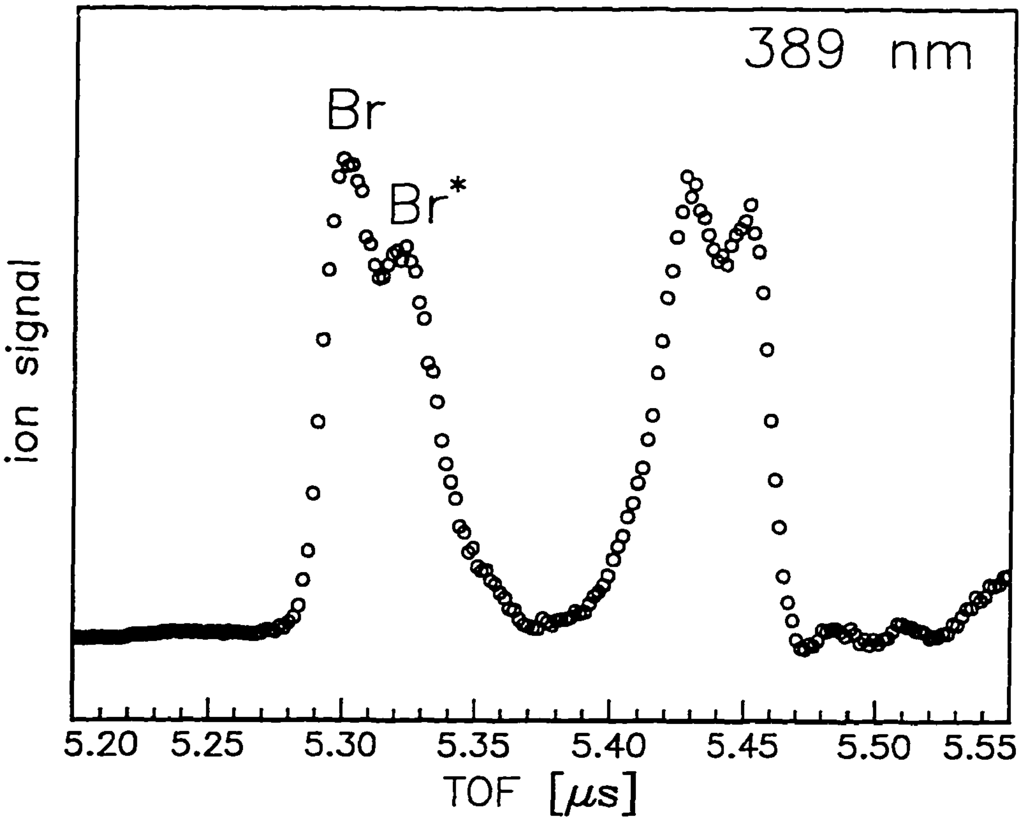

Figure 25: TOF profile of the Cl* photofragment recorded at the centre of the Doppler profile

bleached by the photolysis beam. In case of incomplete bleaching the contribution of Cl_2 to the Cl* formation diminishes further, because of its much smaller absorption cross section in the spectral region that was studied. Two additional observations further support the absence of Cl_2 contributions to the Cl* TOF profile. Firstly, the Cl+Cl* channel is associated with a kinetic energy release that is 1600 cm^{-1} larger than the Br*+Cl* channel and is expected to yield TOF-profiles with more closely spaced kinetic energy components. Secondly, the contribution of the Cl+Cl* channel is expected to increase at *longer* wavelengths, contrary to our observations.

Because of the strong participation of the $^1\Pi(1)$ state a detailed analysis of the Cl TOF-profiles, analogous to that of the Cl*-profiles described above, was not reliable. Hence, we are unable to distinguish the exit channels (a) and (c) in Table 5. We therefore conclude that, following excitation to the B-state, exit channels (a), (b) and (d) are involved in the dissociation process, and that the contribution of channel (c) is possible.

In principle it is possible to distinguish between the Cl*+Br* channel (d) and the Cl+Br* channel (c) by kinetic energy analysis of the Br* TOF profiles in analogy to the procedure described above. However, this experiment provides no new information as the energy spacing between channels (c) and (d) is only 881 cm^{-1} and the difference in the kinetic energy of the Br*-fragments is too small to be resolved.

4.3 Discussion

4.3.1 Non-adiabatic dissociation dynamics

As can be seen in Figure 22, at least two excited states contribute to the photofragment yield spectrum of the Cl fragment. At short wavelengths dissociation through the $^1\Pi(1)$ state is clearly favoured, while at wavelengths longer than 440 nm the $^3\Pi(0^+)$ state becomes dominant. It is also evident from Figure 22 that dissociation through the $^1\Pi(1)$ state yields negligible amounts of Cl* fragments, indicating that the dissociation is mainly adiabatic as described in section 4.1.3 and Figure 20. On the other hand, photodissociation *via* the B -$^3\Pi(0^+)$ state yields comparable amounts of Cl and Cl* fragments. Since, even at wavelengths $\lambda > 460$ nm both Cl and Cl* fragments are observed, one can conclude that the Br+Cl and Br+Cl* channels both participate at these wavelengths. This observation suggests that non-adiabatic transitions among different potential energy curves occur in the B-state dissociation. The shape of the branching ratio curve can be understood qualitatively based on the following consideration. In the short wavelength region the Cl* yield increases as the absorption by the B-state increases. In the long wavelength region there are two possible reasons for the slight decrease of the Cl* yield: (a) the extent of the B-state adiabatic dissociation increases with decreasing excitation energy thereby favouring the lowest fragment channel Br+Cl and (b) the adiabatic dissociation *via* the A-state increases, thereby also generating Br + Cl.

The absorption spectrum was deconvoluted by Seery and Britton(72) into two Gaussian curves as displayed in Figure 22. However, these Gaussian curves can not represent the partial absorption cross sections of the $^1\Pi(1)$ and the $^3\Pi(0^+)$ states based on the following consideration: The onset of the second Gaussian curve is located around 430 nm, whereas considerable amounts of Cl* fragments were observed even at 389 nm. This point is illustrated in Figure 26, where the fraction of the experimentally determined parallel component is compared with the fraction of the low energy Gaussian to the total absorption spectrum. Unfortunately, we are not able to quantify this argument by comparing the magnitude of ion signals recorded independently at different wavelengths, since the ion signal does not only depend strongly on the absorption cross section, but also on the number density of BrCl molecules in the molecular beam. This is a consequence of the high (but unknown) degree of bleaching that was achieved.

The high spatial anisotropy parameter demonstrates that it is unlikely that the $^1\Pi(1)$ state dissociation yields significant amounts of Cl* fragments. The B-state absorption is therefore blue-shifted with respect to the second Gaussian component. This indicates firstly that the partial absorption from the $^1\Pi(1)$ state is narrower than expected from the first Gaussian curve, implying a more shallow excited state potential energy curve(9). Secondly, in order to explain the absorption at long wavelengths the introduction of a third excited state may become necessary. Since the only other accessible excited state lying below the B-state is the A -$^3\Pi(1)$ state, this third contribution must then arise from excitation to the A-state. To illustrate this point, absorption curves arising from transitions to parallel states and perpendicular states have been constructed. Here, we added the parallel / perpendicular components of the Cl* and Cl signals -- each properly weighted with the branching ratio - to obtain the parallel / perpendicular curves in Figure 26.

The shape of the Cl* yield curve is difficult to understand in the region between 400 nm to 470 nm, as in addition to the maximum at 410 nm a shoulder at around 450 nm appears.

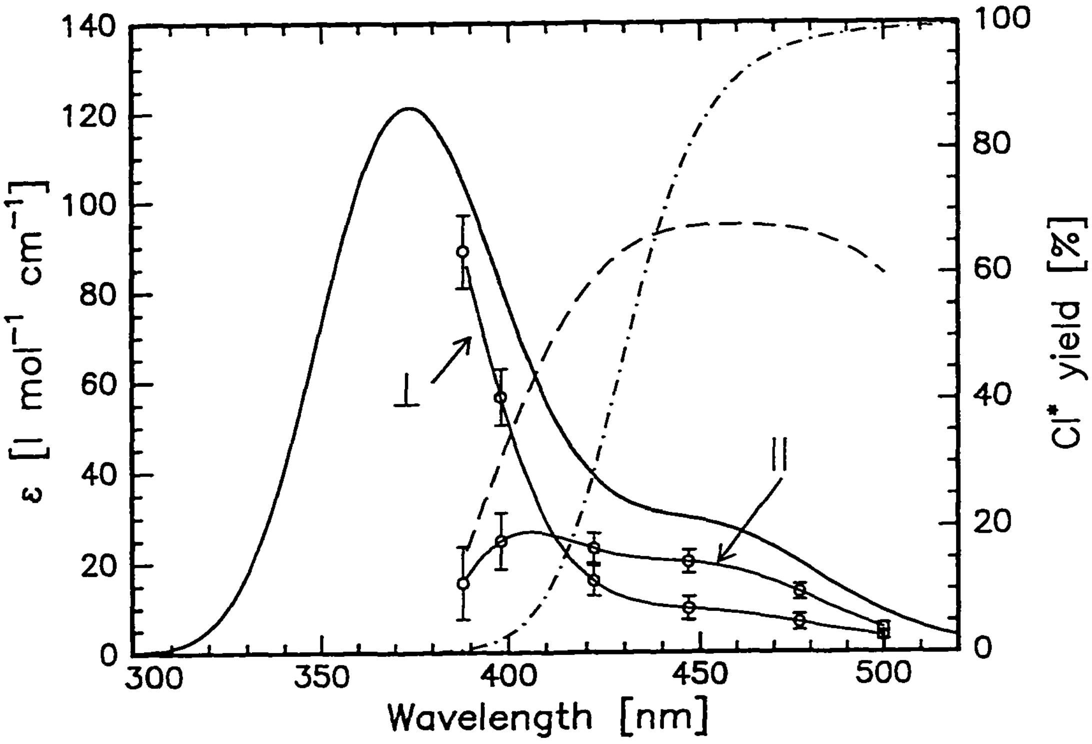

Figure 26: "Parallel" and "perpendicular" contributions to the absorption curve. The measured fraction of the parallel component (dashed line) and the fraction of the 2nd Gaussian component (dash-dotted) are plotted against the right axis

If one considers that the Br* + Cl* channel opens at 443 nm and the Br + Cl* channel opens at 529 nm, a possible explanation for the observed asymmetry of the Cl* yield curve involves contributions occuring from both the Br* + Cl* and the Br + Cl* channels.

The TOF-photofragment profiles give a stronger indication for the participation of the Br*+Cl* channel in a highly non-adiabatic dissociation process. Our experiments demonstrate that two channels leading to Cl* fragments are involved in the B-state dissociation at high excitation energies. Their kinetic energy release corresponds to channels (b) and (d).

The dissociation channels Br*+Cl (c) and Br*+Cl* (d) are open at excitation energies above 460 nm and 440 nm, respectively. The contribution of channel (d) should become dominant at very high excitation energies and this trend can be observed by displaying the ratio Cl*(d) / [Cl*(b)+Cl*(d)] vs. the excitation wavelength as shown in Table 6.

The extent of non-adiabatic character depends largely on the magnitude of the interaction term between the excited states. Correspondingly, we can use the experimental results to obtain information about this mixing term and thereby about the nature of the excited states. In the following section a simple one-dimensional Landau-Zener calculation will be used to estimate the interaction term between the diabatic B-state and the 0^+ states.

The formation of atomic fragments in their excited spin-orbit states is somewhat surprising and certainly in contrast to many earlier observations. Hence, two models will be presented in order to explain why the highest fragment channel is accessible at high excitation energies. The first model uses simple MO-theory arguments, while the second follows closely a theory developed by Singer, Freed and Band(73) for diatomic molecule dissociation processes in the axial recoil limit. The discussion on BrCl photodissociation experiments is closed with a brief review of earlier experiments by other research groups in the light of our findings.

4.3.2 Landau-Zener calculation

Although not much is known about the exact shapes of the the intersecting 0^+ curves and diabatic B-state PES in the region beyond the intersection of the lowest lying 0^+ state, we can obtain a rough estimate of the magnitude of the interactions. In the following paragraphs only 0^+ states will be considered, since interactions of the B $^3\Pi(0^+)$ state with $\Omega = 1$ states will be weak and dissociation will be largely diabatic through such crossing regions. Landau and Zener(14) described, in their pioneering papers, the probability of a radiationless transition from one adiabatic surface to another as

$$p = \exp(-\pi^2\xi) \tag{52}$$

with the adiabaticity parameter

$$\xi = \frac{H_{12}^2}{v h \Delta F_X} \tag{53}$$

Here H_{12} is the local interaction term acting between the diabatic potentials (i.e., 1/2 of the energy gap ΔE_x between the adiabatic surfaces) and ΔF_x is the absolute difference of the slopes of the two diabatic curves at the crossing point. The velocity, v, with which the molecule travels through the interaction region depends directly on the excitation energy. As a first approximation the PESs involved can be described by simple Morse potentials and exponential repulsive potentials. In our calculation we used the following analytical diabatic PES

$$V_1 = 16848 + 5962 * (1 - \exp(-1.656 * (r - 2.54)))^2 \tag{54}$$

$$V_i = 18244 + D + \frac{C_3}{r^3} + \frac{C_4}{r^4} + \frac{C_5}{r^5} + \frac{C_6}{r^6} \tag{55}$$

$$H_{1i} = V_{1i} \exp\left(-\frac{(r - r_{1i})^2}{1 Å} \right) \tag{56}$$

	C_3	C_4	C_5	C_6	D
Y(0^+)	-1.85e5	2.3e6	-8.49e6	1.0e7	0
2nd 0^+	-1.30e5	9.0e5	-2.0e6	4.0e6	881
3rd 0^+	-5.0e5	1.5e5	0	2.0e6	3685

Table 7: Expansion coefficients for the repulsive 0^+ curves of BrCl in [cm^{-1}]

The Landau-Zener calculation was not particularly sensitive to the expansion coefficients C_i, and the parameters listed above were chosen somewhat arbitrarily. The interactions between the diabatic curves were assumed to be localized around the respective crossing region and to be of Gaussian dependance.

The interaction terms were set to $V_{12} = 100\ \mathrm{cm}^{-1}$, $V_{13} = 250\ \mathrm{cm}^{-1}$ and $V_{14} = 35\ \mathrm{cm}^{-1}$ and using equation (25) on page 19 the adiabatic curves were calculated. Care was taken that these potential energy curves yielded a height and position for the lowest lying barrier which are comparable to the spectroscopic results by Tellinghuisen(67). This barrier arises from the interaction between the B-state Morse potential and the Y(0^+) curve. However, our PESs mimic the spectroscopically determined curves in their bound part only qualitatively. They cannot be recommended for the determination of rovibrational levels. For comparison, the potential energy curves from reference 67 and from the above estimation are presented in Figure 27 and Figure 28.

Using these simple potentials along with the interaction terms, and the Landau-Zener equation we calculated the B-state Cl*/(Cl+Cl*) branching ratio (Figure 29). The ratio of channel (b) / [(b)+(d)] which was experimentally obtained through the TOF peak-width analysis was also calculated and included in Figure 29. The agreement between experiment and calculation is satisfactory, but the deviation at high excitation energy is considerable. The limits of the Landau-Zener model are well known and have been described by various authors. Kleyn *et al.* mentioned(16), that the crossings involved have to be sufficiently far apart, a condition which is not satisfied in our treatment. Bates noted(74) that, at high velocities, the Landau-Zener model fails to yield the right energy dependence for the width of the transition region. The model shifts the onset of the formation of the high energy products towards lower excitation energies than that observed.

In Figure 29 the sharp onsets of the various exit channels are evident resulting in a discontinuous branching ratio curve. This is due to the breakdown of the Landau-Zener approximation at low kinetic energies near the interaction regions. If the excitation energy is a little higher than a particular barrier, the probability of dissociation over the barrier is only determined by the probability of the lower lying non-adiabatic transitions. If, on the other hand, the excitation energy is lower than the barrier height, the probability of

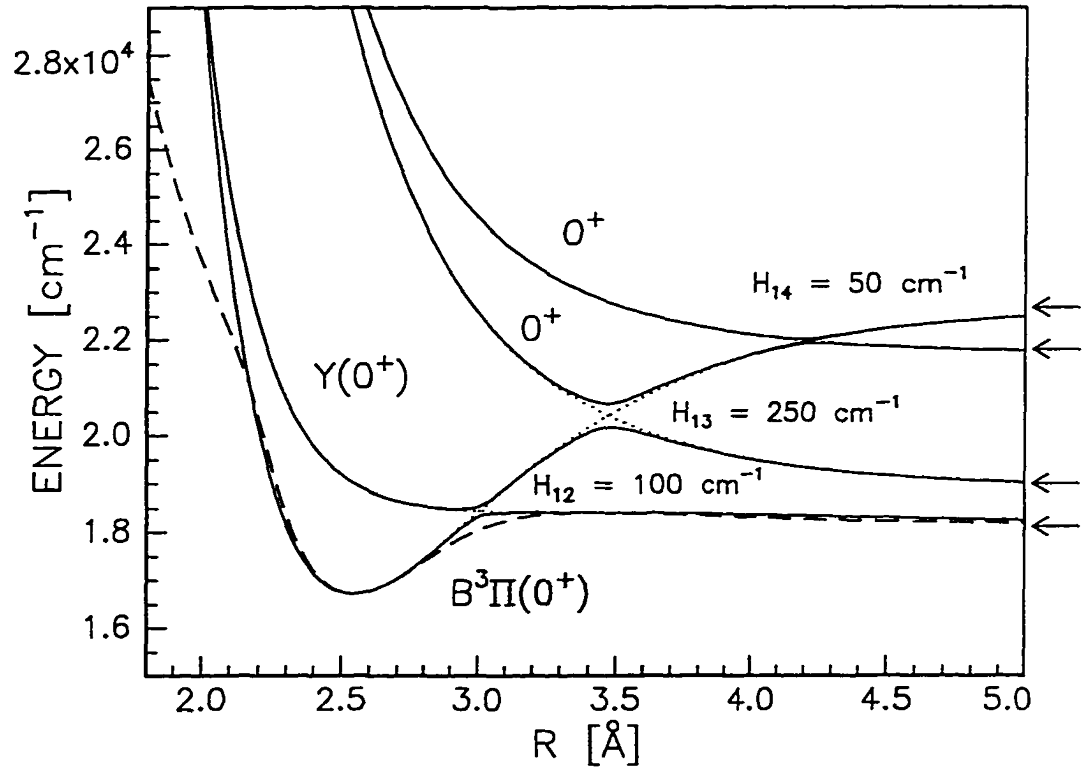

Figure 27 : Potential energy curves of the $^3\Pi(0^+)$ B-state and the low lying (0^+) states. The solid lines are adiabatic curves used in the Landau-Zener calculation; the dashed line is the B-state curve from ref. 67.

occurrence of this particular exit-channel is zero in the Landau-Zener formula. In an exact calculation both statements become weaker. Even at energies above the barrier, the molecules can still be bound by higher rotational states, i.e., by the centrifugal barrier. Below the barrier a small probability of tunnelling exists. Therefore one should expect a smoothing of the onset in an exact treatment.

The most serious drawback of the above LZ-calculation is that it tacitly implies a single "diabatic dissociation limit", i.e., a distinct diabatic potential energy curve, that - in our case - correlates to the Br* + Cl* channel. It will be shown in the following section, that in the axial recoil limit more than one channel is usually involved in a fast diabatic

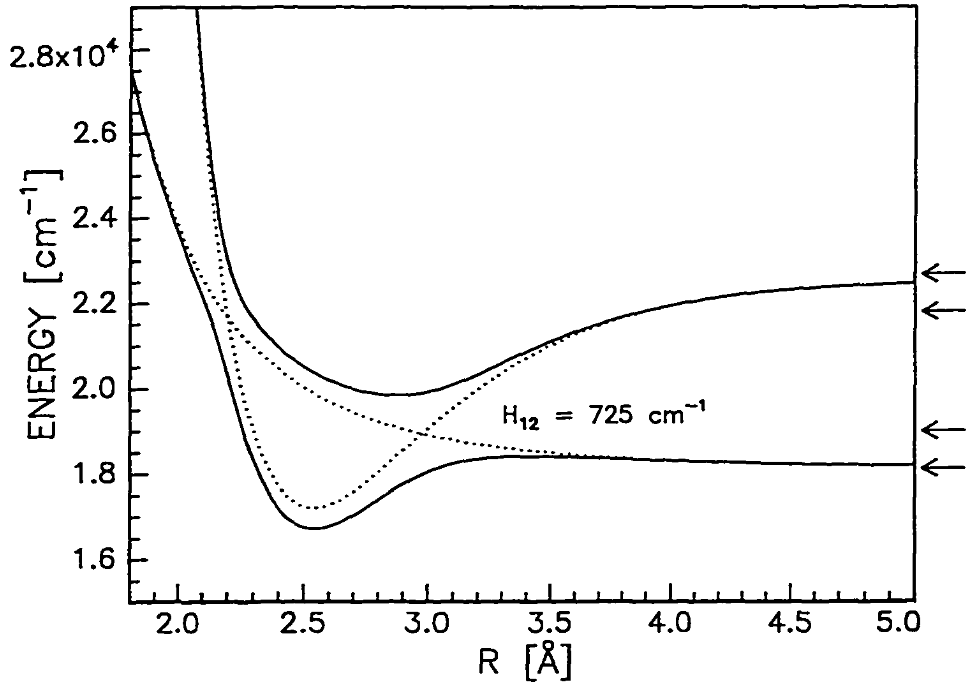

Figure 28: Potential energy curves of the $^3\Pi(0^+)$ B-state and the $Y(0^+)$ state (reproduced from reference 67).

dissociation process.

Nevertheless, the Landau-Zener treatment demonstrates that the interaction between the diabatic B-state curve and the intersecting repulsive states is smaller than previously assumed and, most importantly, that even the highest lying exit channel (d) is accessible at moderate excitation energies. Tellinghuisen proposed an interaction term of 700 cm^{-1} for the avoided crossing of the B-state with the $Y(0^+)$ state[(67)] compared to 100 cm^{-1} in our analysis. The value of Tellinghuisen was obtained using the curvature of the lower adiabatic PES alone and may be in error, because of the difficult nature of such an estimate. In an earlier spectroscopic study on ICl, Gordon and Innes[(65)] observed levels on both the upper and the lower adiabatic PES, and could accurately determine the interaction term to 30 cm^{-1}. Similarly the interaction term V_{12} was determined by Child and Bernstein[(58)] to be approximately 200 cm^{-1} for the respective crossing in the IBr molecule.

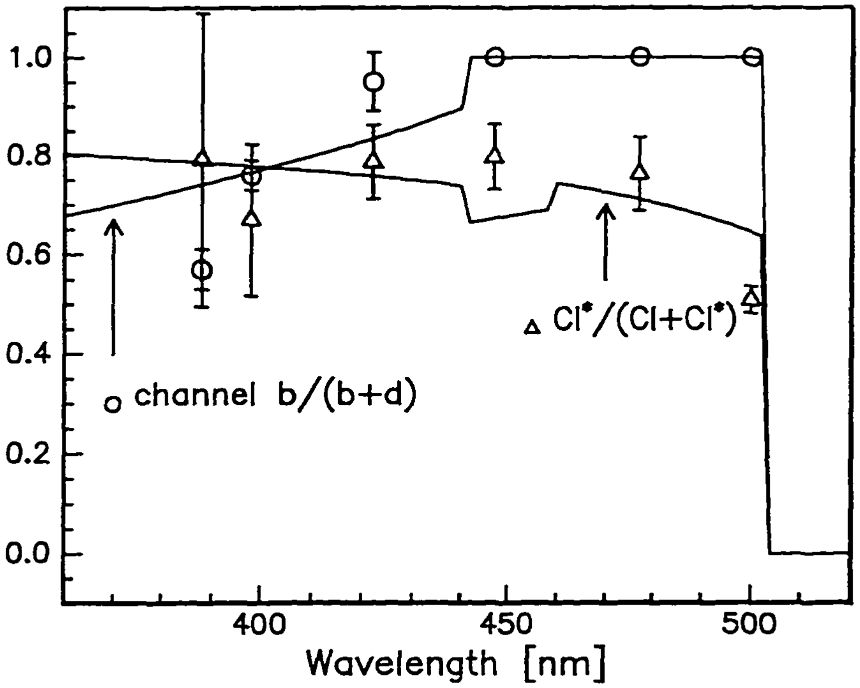

Figure 29: Measured Cl*/(Cl+Cl*) branching ratio (triangles) and ratio of the Cl* producing channels (circles). The solid line are the results of the Landau-Zener calculation.

Since the spin-orbit coupling term responsible for this interaction is most likely comparable to or larger than that of BrCl, it can be expected that the the value obtained by our Landau-Zener calculation is more realistic than the one obtained by Tellinghuisen.

4.3.3 Diabatic correlation

In the adiabatic limit the B-state correlates to the Br+Cl ground state channel as can be seen in Figure 20. The fact that the B-state correlates to the highest of the four fragment channels Br*+Cl* can therefore not be explained using the adiabatic correlation diagram. From spectroscopic studies it has long been known that the B-state does not correlate to the lowest fragment channel(58). Many workers attribute this to "partial homonuclear character" of the interhalogen molecules. Using the partial homonuclear character, it was argued that one has to conserve parity upon dissociation and, therefore, the B-state must adiabatically correlate to one of the fragment states that provide a "ungerade-type" 0^+_u component, i.e., X+Y* or X*+Y. Our observations indicate, however, that the dissociation may even yield X* + Y*, a fragment channel which has "gerade-type" symmetry.

We therefore believe that adiabatic correlation diagrams lack predictive power for these fast dissociation processes and one has to consider diabatic correlations, instead. In such a "diabatic correlation diagram" states with the same symmetry (here, the same Ω) are allowed to cross, since the electronic Hamiltonian matrix is diagonal. The correlation is then determined by the character of the parent molecules molecular orbitals and their energetic behaviour upon separation of the nuclei.

4.3.4 Mixing with ion pair states

In explaining why the highest channel Br*+Cl* is preferred in a fast dissociation process, one can refer to mixing of the excited states of interhalogens with the lowest lying ion-pair states. One expects that the ground state [2440] as well as the [2431] and [2422] configurations have a significant ionic component. These configurations arise from 3 doubly occupied bonding Cl-type orbitals and 2 occupied antibonding Br-type orbitals. Upon fast separation these electronic states will have a strong Cl^- + Br^+ component. This ionic character causes diabatic correlation to the lowest ion-pair states fragment limit, which is 8.23 eV (66000 cm^{-1} or 150 nm) above the molecular ground state(75). Following the same argument the states arising from the [2341] and [2422] configuration may be expected to correlate diabatically to the low lying *neutral* fragment channels. The large number of avoided crossings of the electronic states of the interhalogen compounds, can be explained in this way.

The above argument has some unfamiliar consequences, such as correlation of any interhalogen *ground* state and low lying $^1\Pi(1)$ state to the ion-pair fragment channels. Although the correlation may formally exist, it cannot be easily observed. In case of the ground state correlation one can argue, that there is a lack of fast dynamic processes, which lead to the required internal fragment energy. The $^1\Pi(1)$ state, on the other hand, may have very large avoided crossings with other ($\Omega = 1$) states so that non-adiabatic dissociation is very unlikely.

The model also predicts that molecules with large ground state dipole moments, i.e., strong ion-pair character, will correlate to the ion-pair states to a larger extent and therefore are more likely to dissociate giving fragments far above the adiabatic dissociation limit. The lower lying ion-pair state for very polar molecules will enhance the ionic character of the B-state. Indeed, it has been observed in spectroscopic studies that the B-states of IF, as well as BrF, and ClF correlate to a channel high above the ground state terms. It would be interesting to conduct photodissociation studies on these molecules in order to see whether the highest neutral, or even ionic, fragment channel is also accessible as predicted by this model.

Clearly, the presented model has some drawbacks. Apart from the unlikely diabatic correlation of the interhalogen molecule ground states with the lowest lying ion-pair state, the model is also not able to predict the fine-structure branching ratios of *homonuclear* diatomic dissociation processes. Here one would expect formation of the neutral fragments from states of all configurations.

In the following sections a much more refined theory, that accounts for atomic fine structure, will be presented. This theory, developed by Singer, Freed and Band (SFB)(73), will be summarized in the section 4.3.5. In the next section the SFB theory will be applied to homonuclear and heteronuclear halogen molecules to calculate the fragment fine structure branching ratios.

4.3.5 SFB - Theory of diatomic photodissociation

Instead of replicating the details of the theory, which has been laid out by Singer, Freed and Band in reference 73, only the relevant steps leading to the final expressions will be briefly presented. Singer *et al.* considered the dissociation of a diatomic molecule into atoms which have nonvanishing orbital angular momentum. In this case spin-orbit interactions couple the adiabatic molecular states, which would otherwise be degenerate at infinite internuclear distance, **r**. The problem is reduced to a one state treatment in the axial recoil limit, i.e., assuming infinitely fast dissociation.

In the molecular region the electronic states are described by the adiabatic Born-Oppenheimer approximation. However, these molecular states will not be a good basis for the description of the atomic fragment states, when spin-orbit coupling is included. At all **r** the spin-orbit interaction will couple the molecular states. We therefore need a transformation between the molecular wavefunctions in the molecular frame and the atomic wavefunctions in the lab frame. The expression

$$C_d(j_a,j_b,J) = |\langle j_a j_b | \Lambda S \Sigma p \rangle_J|^2 \tag{57}$$

gives the probability of a rotational level J of a given molecular state $|\Lambda\ S\ \Sigma\ p\rangle$ dissociating *via* the $|j_a\ j_b\rangle$ fragment channel. The total diabatic cross sections will then be obtained by a Boltzmann weighted sum of the $C_d(j_a, j_b, J)$. In the following a summary of the relevant steps in deriving the SFB theory is presented.

In the SFB theory the Hamiltonians and wavefunctions in the molecular and fragment regions are treated separately. Firstly, the Hamiltonians for the molecular and fragment sides are defined. The atomic fragment wavefunctions are then j-j coupled to give intermediate state wavefunctions with good total electronic angular momentum j and its projection Ω. Finally a decoupling scheme was used to express the molecular case (a) wavefunction (with good quantum numbers L S Λ Σ) in terms of the intermediate state wavefunctions with quantum numbers j and Ω.

The molecular Hamiltonian of the diatomic is given by

$$H_{tot}(r) = H_{el}(r) + T^{N}(r) + H_{SO}(r) \tag{58}$$

Here the spin-orbit interaction

$$H_{SO} = \sum_{i} A_i L_i \cdot S_i \tag{59}$$

was included explicitly. It was separated from the electronic term H_{el} and the nuclear motion term $T^{N}(r)$.

At large internuclear distance the Hamiltonian can be expressed as

$$H_{tot} = H^{(0)} + V(r) \tag{60}$$

with

$$H^{(0)} = T^{N}(r) + H_{el} \tag{61}$$

As **r** increases $V(\mathbf{r}) \rightarrow 0$ and the eigenstates of equation (60) become eigenfunctions of equation (61). These wavefunctions are the products of the atomic fine-structure states $|j_a\, m_a\rangle$ and $|j_b\, m_b\rangle$ and the wavefunctions for nuclear motion. These wavefunctions for nuclear motion are further separated for translation and rotation. Thus, the total wavefunctions depend on the atomic fragment angular momenta j_a , j_b and their projections m_a, m_b as well as the rotational quantum number l with projection μ. Due to energy conservation the translational energy will be a function all preceding quantum numbers

$$\frac{1}{r}\Psi_{El\mu j_a m_a j_b m_b}(r)\ Y_{l\mu}(\hat{r})\ |j_a m_a\rangle |j_b m_b\rangle \tag{62}$$

In the limit of a fast dissociation the translational wavefunction $\Psi(r)$ does not depend on the angular momenta and can therefore be neglected. Under this assumption only the angular momentum coupling has to be considered. The wavefunctions can then be expressed in terms of total angular and electronic momentum **J** and its projection **M**.

$$|JM\, jlj_aj_b\rangle = \sum_{m\mu} \langle JM|jlm\mu\rangle\, Y_{l\mu}(\hat{r})\, |jm\, j_aj_b\rangle \tag{63}$$

Next, the molecular wavefunctions have to be expressed in terms of the atomic fragment wavefunctions. Assuming Hunds case (a)[5] the adiabatic Born-Oppenheimer states at large internuclear distance can be written as

$$|\Lambda\; S\Sigma\rangle = \sum_{\lambda_a\lambda_b} |l_a\lambda_a\rangle\, |l_b\lambda_b\rangle\, |S\Sigma\rangle\, \langle\lambda_a\lambda_b|\Lambda\rangle \tag{64}$$

where the spin and angular momentum part have been separated assuming weak spin-orbit interaction. In Figure 30 the angular momenta and their coupling are displayed. The integral $\langle\lambda_a\lambda_b\, |\Lambda\rangle$ will be discussed later in some detail. In order to connect to the fragment wavefunctions in equation (63) transformation of the wavefunctions in the above sum is necessary. Recoupling of the molecular states at large **r** to form fragment electronic states with good j_a and j_b yields

$$|l_a\lambda_a\rangle\, |l_b\lambda_b\rangle\, |S\Sigma\rangle = \sum_{jj_aj_b} |j\Omega j_aj_b\rangle\langle j\Omega j_aj_b|\lambda_a\lambda_bS\Sigma\rangle \tag{65}$$

The expansion coefficients in this equation can be expressed as

$$\begin{aligned}\langle j\Omega j_aj_b|\lambda_a\lambda_bS\Sigma\rangle = \sum_{L} &(2S+1)^{1/2}(2j_a+1)^{1/2}(2j_b+1)^{1/2}(2L+1)^{1/2}\\ &\times \langle L\Lambda|l_a\lambda_al_b\lambda_b\rangle\, \langle j\Omega|LS\Lambda\Sigma\rangle \begin{Bmatrix} l_a & s_a & j_a\\ l_b & s_b & j_a\\ L & S & j\end{Bmatrix}\end{aligned} \tag{66}$$

Finally, it can be shown, that transformation of the body fixed fragment states into the lab frame yields

---

[5] It does not matter which one of the Hund's cases is used to expand the wavefunction as long as the coupling between the molecular states is retained.

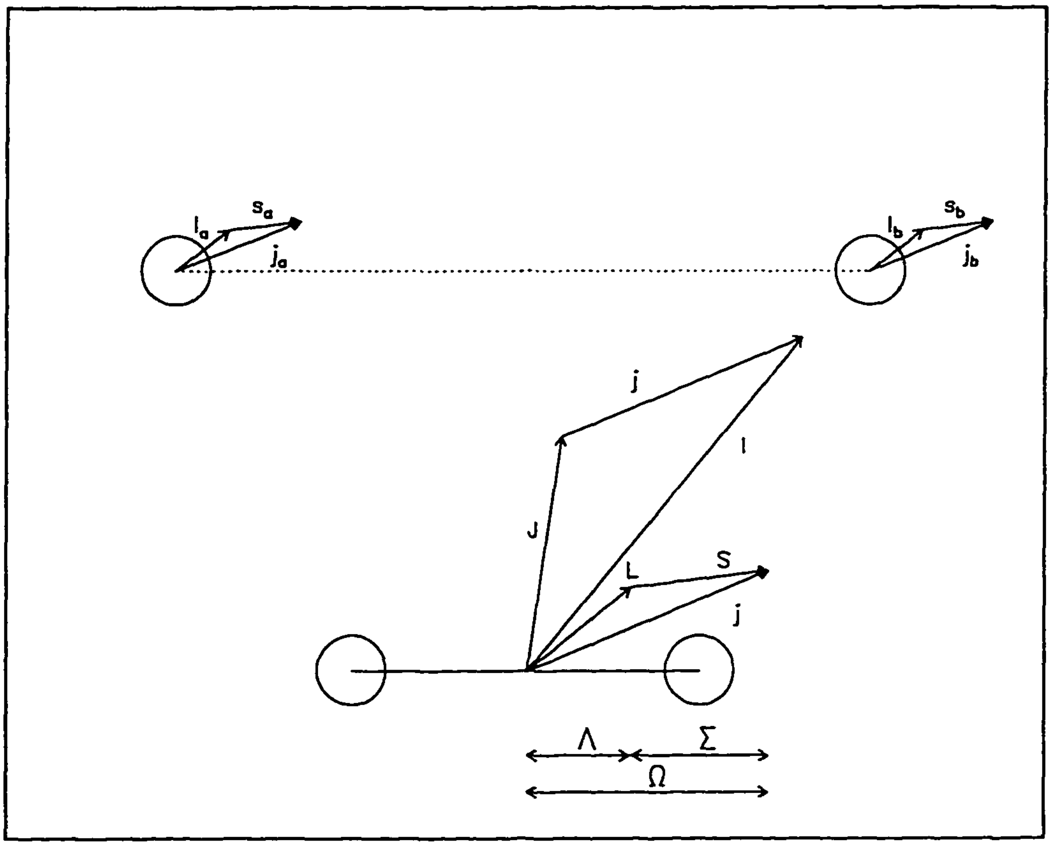

Figure 30: Vector diagram showing the angular momenta used in the SFB - theory

$$
\begin{aligned}
\langle j l j_a j_b | \Lambda S \Sigma\, p \rangle = {} & (2-\delta_{\Lambda 0}\delta_{\Sigma 0})^{1/2}\left[1-(-1)^{l_a+l_b+l+p}\right](-1)^{l-\Omega-J} \\
& \times (2S+1)^{1/2}(2j_a+1)^{1/2}(2j_b+1)^{1/2} \\
& \times \langle l0|jJ-\Omega\Omega\rangle \sum_{L\lambda_a\lambda_b} (2L+1)^{1/2}\langle L\Lambda|l_a\lambda_a l_b\lambda_b\rangle \\
& \times \langle j\Omega|LS\Lambda\Sigma\rangle \begin{Bmatrix} l_a & s_a & j_a \\ l_b & s_b & j_a \\ L & S & j \end{Bmatrix} \langle \lambda_a\lambda_b|\Lambda\rangle
\end{aligned}
\qquad (67)
$$

This transformation recouples the molecular wavefunctions at r → ∞ to give eigenfunctions of the "atomic Hamiltonian" $H^{(0)}$. For computational convenience the above equation was rewritten using the Clebsch-Gordon coefficients in the form of 3j-symbols

$$\begin{aligned}\langle j l j_a j_b | \Lambda S \Sigma p\rangle &= (2-\delta_{\Lambda 0}\delta_{\Sigma 0})^{1/2}\left[1-(-1)^{l_a+l_b+l+p}\right](-1)^{l-\Omega-J} \\ &\times(2S+1)^{1/2}(2j_a+1)^{1/2}(2j_b+1)^{1/2} \\ &\times\begin{Bmatrix} j & J & l \\ -\Omega & \Omega & 0 \end{Bmatrix} \sum_{L\lambda_a\lambda_b} (2L+1)^{1/2} \begin{Bmatrix} l_a & l_b & L \\ \lambda_a & \lambda_b & -\Lambda \end{Bmatrix} \\ &\times\begin{Bmatrix} L & S & j \\ \Lambda & \Sigma & -\Omega \end{Bmatrix} \begin{Bmatrix} l_a & s_a & j_a \\ l_b & s_b & j_a \\ L & S & j \end{Bmatrix} \langle \lambda_a \lambda_b | \Lambda\rangle\end{aligned} \qquad (68)$$

Using this equation (eq. II.13a in reference 73) the diabatic transformation cross sections $\langle j_a\, j_b \mid \Lambda S \Sigma p\rangle$ are obtained by coherently summing over the unobserved momenta *j*, and *l*.

The selection rules for the quantum numbers arise naturally from the properties of the 3j- and 9j-symbols. The value of a 3j-symbol

$$\begin{Bmatrix} j_1 & j_2 & j_3 \\ m_1 & m_2 & m_3 \end{Bmatrix} \qquad (69)$$

is zero, unless

$$\begin{gathered} |j_1 + j_2| \geq j \geq |j_1 - j_2| \\ m_1 + m_2 = m_3 \end{gathered} \qquad (70)$$

similarly the 9j- symbol

$$\begin{Bmatrix} j_1 & j_2 & j_3 \\ j_4 & j_5 & j_6 \\ j_7 & j_8 & j_9 \end{Bmatrix} \qquad (71)$$

is zero, unless

$$\begin{aligned}|j_1+j_2| &\geq j_3 \geq |j_1-j_2|\\ |j_4+j_5| &\geq j_6 \geq |j_4-j_5|\\ |j_7+j_8| &\geq j_9 \geq |j_7-j_8|\end{aligned} \tag{72}$$

Using these restrictions the vector sum, j, of the atomic total angular momenta j_a and j_b is restricted by the total electronic angular momentum L and the total spin S

$$|L+S| \geq j \geq |L-S| \tag{73}$$

The total electronic angular momentum L is in turn restricted by the electronic orbital angular momenta l_a and l_b of the recoiling atoms

$$|l_a+l_b| \geq L \geq |l_a-l_b| \tag{74}$$

The orbital angular momentum of the atoms l is restricted by the total angular momentum J, which includes the rotation of the molecule, and the vector sum j of j_a and j_b

$$|j+J| \geq l \geq |j-J| \tag{75}$$

Furthermore

$$\begin{aligned}|l_a+s_a| &\geq j_a \geq |l_a-s_a|\\ |l_b+s_b| &\geq j_b \geq |l_b-s_b|\end{aligned} \tag{76}$$

Finally, for the projection Λ of the molecular electronic orbital angular momentum L and the projections λ_a and λ_b of l_a and l_b

$$\Lambda = \lambda_a + \lambda_b \tag{77}$$

and as usual

$$\Omega = \Lambda + \Sigma \tag{78}$$

The relations between the angular momentum vectors are schematically shown in Figure 30.

Note, that the first two factors in equation (68) guarantee that parity, which is only a good quantum number in the case of *homonuclear* diatomics, is conserved and that the $^1\Sigma(0)$ states get less statistical weight compared to states with orbital angular momentum and/or spin. By omitting these factors one obtains an expression for cases in which parity is not spin. By omitting these factors one obtains an expression for cases in which parity is not a good quantum number, i.e., for heteronuclear diatomics.

4.3.6 Application of the SFB theory to halogen and interhalogen dissociation

In evaluating the matrix elements $\langle j\ l\ j_a, j_b \mid \Lambda\ S\ \Sigma\rangle_J$ using equation (68) one has to make reasonable estimates for the term $\langle \lambda_a\ \lambda_b \mid \Lambda\rangle$. This term describes the electronic interaction between the recoiling atoms at large distances and can be accurately determined with a small configuration interaction calculation. In the case of neutral fragments these matrix elements are obtained from a calculation of quadrupole-quadrupole interactions and the associated energies can be understood in terms of van der Waals attraction. Here the leading term of the multipole expansion will scale with r^{-6} if one or both of the atoms are in S states, and with r^{-5} if the atoms are in states with $l \neq 0$(41).

Knipp(76) has described a method of calculating the quadrupole-quadrupole interaction of molecular ground state levels arising from atoms in their electronic ground states. Later Chang(77) extended this treatment to a calculation of *all* interaction terms arising from atoms in their ground states. For convenience, this theory is briefly laid out in appendix 6.2 as applied to halogen and interhalogen molecules. It has been demonstrated, that the quadrupole-quadrupole energy depends on the size, the electronic configuration (here np^5) and $\lambda_a\ \lambda_b$ of the recoiling atoms, as well as the orbital angular momentum number, Λ, of the molecular states. The coefficients of the corresponding wavefunctions were not calculated, but it was shown that

$\langle\ 1\ 0 \mid 1\rangle = - \langle\ 0\ 1 \mid 1\rangle$

and

$\langle\ 0\ 0 \mid 0\rangle = \langle\ 1\ {-1} \mid 0\rangle = - \langle\ {-1}\ 1 \mid 0\rangle$.

Similarly, the value of the $\langle\ 1\ 1 \mid 2\rangle$ coefficient was not evaluated. The actual values for these terms were rendered unimportant, since selection rules prohibit the contribution of any coefficient $\langle \lambda_a\ \lambda_b \mid \Lambda\rangle$ to the $\langle j\ l\ j_a, j_b \mid \Lambda\ S\ \Sigma\rangle$ term, except those with the same Λ. Using only the sign of the coefficients the relative values of the $\langle j\ l\ j_a, j_b \mid \Lambda\ S\ \Sigma\rangle$ matrix

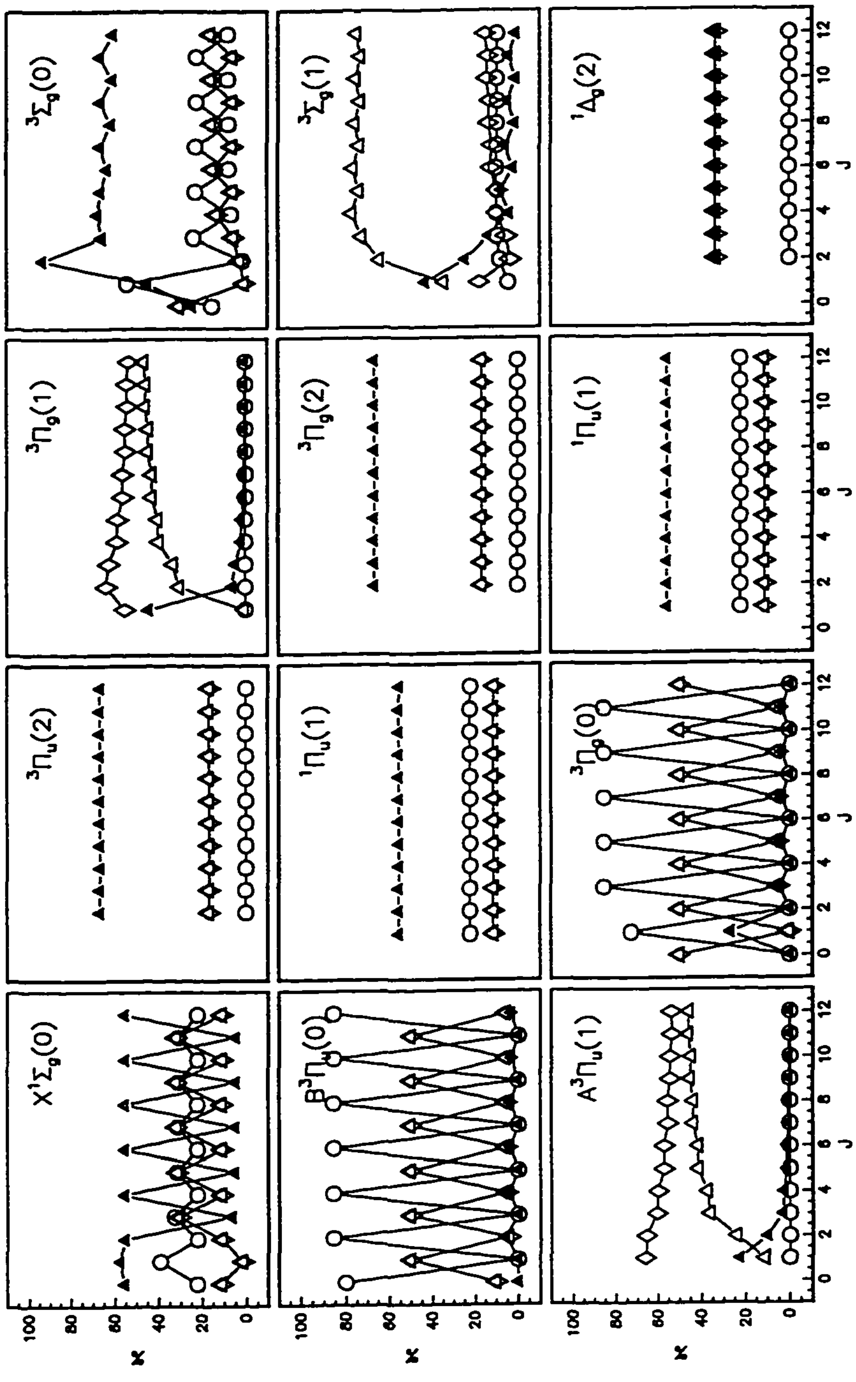

Figure 31: Finestructure branching ratio for a halogen molecule X_2 as calculated by the SFB-theory described in the text. Channel (a) filled triangles; (b) open diamonds; (c) open triangles; (d) open circles

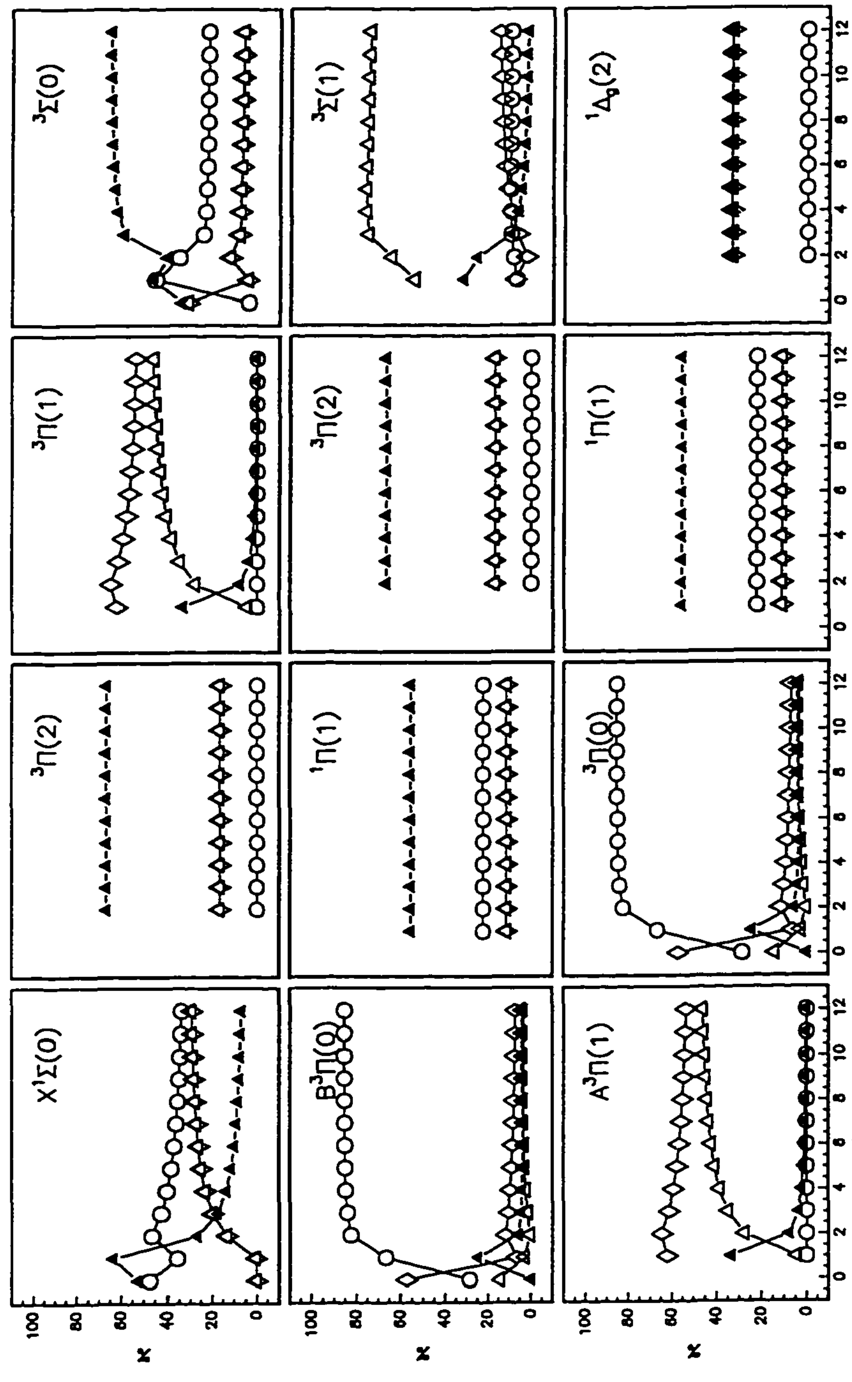

Figure 32: Finestructure branching ratio for an interhalogen molecule XY as calculated by the SFB-theory described in the text. Channel (a) filled triangles; (b) open diamonds; (c) open triangles; (d) open circles

Figure 31 and Figure 32 display the calculated results of the relative branching ratio as a function of the rotational quantum number J for the lowest lying states of halogen and interhalogen molecules. Relative branching ratios were determined using

$$C_J(j_a,j_a) = \left| \sum_{j,l} \langle j l j_a j_b | \Lambda S \Sigma \rangle_J \right|^2 \tag{79}$$

By weighting with a Boltzmann factor the total fragment channel cross sections were computed

$$C(j_a j_a) = \sum_J (2J+1)\, \exp\left(-\frac{BhJ(J+1)}{kT}\right) \left| \sum_{j,l} \langle j l j_a j_b | \Lambda S \Sigma \rangle_J \right|^2 \tag{80}$$

Table 8 and Table 9 list the results for a calculation of these integrated cross sections, using T = 20 K as the rotational temperature of the molecular beam and the rotational constants B_{BrCl} = 1.81 J/mol and B_{Cl2} = 2.92 J/mol.

A number of points are of special interest and will be discussed below:

- Most of the low lying states of Cl_2 and BrCl display the degeneracy expected of the ⟨1/2 3/2| and ⟨ 3/2 1/2| fragment channels. Interesting exceptions are some states with $\Omega = 1$.
- The branching ratio of some parity restricted states of Cl_2 shows a marked oscillation with J, which is qualitatively reversed for gerade and ungerade states with otherwise identical quantum numbers.
- Within a few rotational quanta the classical limit is reached, indicated by an asymptotic value or a stable oscillation for the BrCl and Cl_2 branching ratios, respectively.
- Comparison of Table 8 with Table 9 shows that there are only small differences between rotationally averaged branching ratios of homonuclear and heteronuclear halogen molecules.

The lifted degeneracy of channels (b) and (c) for the $^3\Pi_u(1)$, $^3\Pi_u(1)$ and $^3\Sigma_g(1)$ states in homonuclear diatomic dissociation shows a peculiarity of the SFB theory. While it is

A. Homonuclear halogen molecules

Configuration	State	(a)	(b)	(c)	(d)
2440	$^1\Sigma(0)$	19.21	25.29	25.29	30.22
2431	$^3\Pi(0)$	6.23	6.23	83.80	3.73
	$^3\Pi(1)$	4.02	58.34	37.64	0.00
	$^3\Pi(2)$	66.67	16.67	16.67	0.00
	$^1\Pi(1)$	55.56	11.11	11.11	22.22
2341	$^3\Pi(0)$	8.13	8.13	77.67	6.08
	$^3\Pi(1)$	6.08	57.34	36.58	0.00
	$^3\Pi(2)$	66.67	16.67	16.67	0.00
	$^1\Pi(1)$	55.56	11.11	11.11	22.22
2422	$^3\Sigma(0)$	5.75	5.75	23.68	64.83
	$^3\Sigma(1)$	9.59	10.88	70.69	8.84
	$^1\Delta(2)$	33.33	33.33	33.33	0.00
	$^1\Sigma(0)$	19.21	25.29	25.29	30.22

Table 8: Finestructure branching ratios for channel (a) X+X, (b) X+X*, (c) X*+X and (d) X*+X* calculated from the Boltzmann weighted transformation cross section.

B. Heteronuclear interhalogen molecules

Configuration	State	(a)	(b)	(c)	(d)
2440	$^1\Sigma(0)$	17.45	22.15	22.15	38.24
2431	$^3\Pi(0)$	4.52	10.00	3.52	81.96
	$^3\Pi(1)$	3.88	57.28	38.84	0.00
	$^3\Pi(2)$	66.67	16.67	16.67	0.00
	$^1\Pi(1)$	55.56	11.11	11.11	22.22
2341	$^3\Pi(0)$	4.52	10.00	3.52	81.96
	$^3\Pi(1)$	3.88	57.28	38.84	0.00
	$^3\Pi(2)$	66.67	16.67	16.67	0.00
	$^1\Pi(1)$	55.56	11.11	11.11	22.22
2422	$^3\Sigma(0)$	61.79	7.60	7.60	23.02
	$^3\Sigma(1)$	6.70	10.94	73.20	9.15
	$^1\Delta(2)$	33.33	33.33	33.33	0.00
	$^1\Sigma(0)$	17.45	22.15	22.15	38.24

Table 9: Finestructure branching ratios for channel (a) X+Y, (b) X+Y*, (c) X*+Y and (d) X*+Y* calculated from the Boltzmann weighted transformation cross section.

mathematically straightforward to show why the branching ratio for the ⟨1/2 3/2| channel is different from the ⟨3/2 1/2| channel, the physical meaning is not easily understood. The different dissociation cross section of the channels (b) and (c) implies that the atomic fragments have a different identity in the theory, despite the fact that their quantum numbers and physical identities are the same. This distinction may arise, because the direction of the "z-axis" along the bond has been chosen to give $\Lambda = 1$ and not $\Lambda = -1$. In a calculation of the corresponding negative Ω the branching ratios stay the same, despite the change of direction of the z-axis (and hence the exchange of the atoms). One can therefore suspect, that the branching ratios for channels (b) and (c) should be averaged, with this averaged value then being used for both homonuclear and heteronuclear, diatomics.

This effect is most likely less important in the treatment of heteronuclear diatomics such as BrCl. Here, parity is not a good quantum number and all channels are allowed as far as parity is concerned.

Also the conservation of +/- (reflection through the plane) symmetry, which was neglected in the SFB theory, has to be considered. As indicated in the correlation diagrams (Figure 20 and Figure 19), each $\Omega = 0$, $S = 1$ state have a 0^+ and a 0^- component which correlate differently. Indeed, *all* states with $\Lambda > 0$ are twofold degenerate, but only in case of $\Omega = 0$ is this degeneracy lifted due to configuration interactions, giving rise to 0^+ and 0^- states. Since the SFB theory does not distinguish between, e.g., the $^3\Pi_u(0^+)$ and the optically inactive $^3\Pi_u(0^-)$ state of Cl_2, one obtains a non-zero transformation cross section of the $^3\Pi_u$ to the lowest ⟨3/2 3/2| exit channel, despite the fact, that this channel does not have a 0^+_u component to correlate with the optically active $^3\Pi_u(0^+)$ state. However, since this symmetry property is conserved throughout the dissociation, the symmetry restrictions may be enforced separately.

The SFB theory has been reviewed by several authors, but, to our knowledge, only has twice been applied to actual molecular systems, in this form. In 1987, Williams and Freed(78), studied low energy scattering of C^+ (^2P) ions by atomic hydrogen and investigated resonances in the scattering cross section from a theoretical point of view. Recently, Leahy *et al.*(79) studied the predissociation dynamics of O_2 in the B $^3\Sigma_u^-$ state. It was found that the theoretical results give only qualitative agreement with the experimental data, indicating that the dissociation is not completely diabatic. The theoretical analysis was in the case of oxygen complicated by the fact that the B $^3\Sigma_u^-$ state couples strongly to four repulsive states, and that these interactions determine the final product state distribution. Interference between different fragmentation pathways, as calculated by Williams and Freed(78), cannot be excluded. In our case we completely neglected coupling to other states and assumed a one-state dissociation in the axial recoil limit.

Alternative formalisms have been developed by Zygelman *et al.*(80) for collision induced fine-structure transitions in atomic oxygen, and by Givertz and Balint-Kurti(81) for the photodissociation dynamics of HCl. The difference between the treatment of the Zygelman *et al.* and the SFB theory is an explicit distinction between the total two-center angular momentum and the total angular momentum (both are called **J** in the above outline). Givertz and Balint-Kurti think of their theory as being essentially identical to the SFB-theory, although the formalism is different.

To quantify our computational results one has to improve and modify the above treatment substantially. Firstly, inclusion of +/- symmetry is necessary and will most likely give the largest improvement for homonuclear diatomics. Secondly, exact evaluation of the $\langle\lambda_a\ \lambda_b \mid \Lambda\rangle$ terms by a configuration interaction treatment is useful, and will greatly improve the results for heteronuclear diatomics. Thirdly, inclusion of other states may allow for calculation of processes that are not completely diabatic. Since the axial recoil limit is only the limiting case of an infinitely fast dissociation process that was initiated on a single potential energy curve, coupling to other states has been completely neglected. These states do mix with the state under consideration, thereby giving their own contribution to the fragment channel branching ratio. By considering multiple pathways to the same fragment channel one encounters excitation energy dependent branching ratios and interference effects. Although those effects are important, they are clearly beyond the scope of this

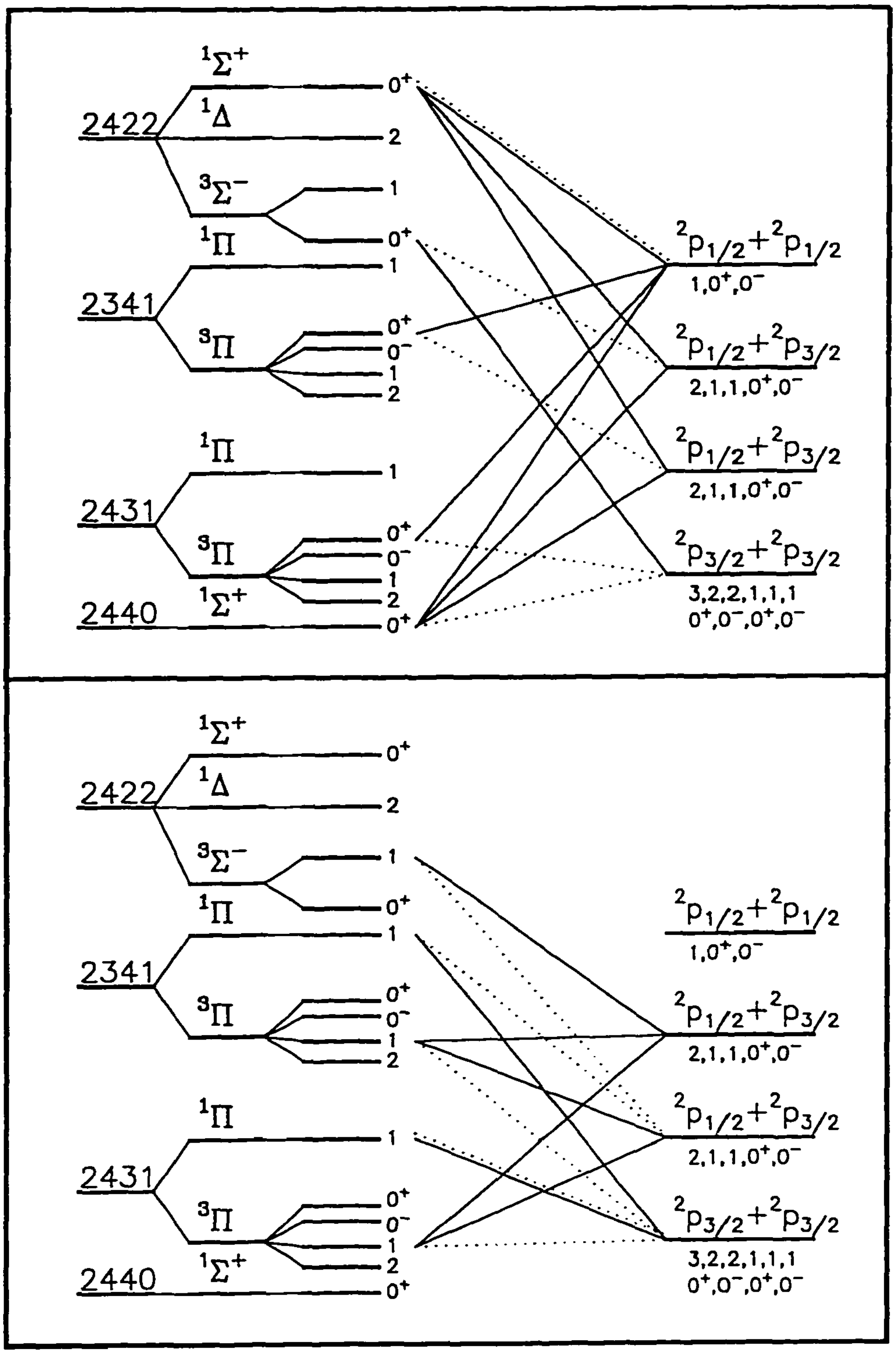

Figure 33: Diabatic correlation diagram of the $\Omega = 0$ states and $\Omega = 1$ states of a rotating heteronuclear interhalogen molecule. The adiabatic correlation (dotted lines) is also included

study.

As is apparent from Figure 31, the branching ratios of homonuclear diatomics display oscillatory behaviour when related to the rotational quantum number. For a purely repulsive potential energy curve, J is given by the thermal distribution of the ground state parent molecules prior to excitation. It was necessary to assume a reasonable distribution of J and to sum over the branching ratios. This results in an averaged branching ratio, which is similar to the branching ratio of the correponding state of the heteronuclear molecule (compare Table 8 and Table 9).

A multiphoton experiment *via* a bound intermediate state would, in principle, allow for the preparation of a single "rotational state" on the repulsive PES. In this way the oscillatory branching ratios may be recovered. The intermediate state can be a higher bound electronic state in a "stimulated emission pumping" (SEP) experiment. Alternatively, one may use an IR laser to prepare higher rovibrational states of the ground-state and use a second photon to prepare the excited state. This scheme has to ensure either complete bleaching of the sample or guarantee that the second photon alone will not provide enough energy to excite the molecule. The latter condition can only be fulfilled if the intermediate level is sufficiently high above the rovibrational groundstate. Obviously such a "two colour - overtone pumping experiment" is very challenging, experimentally.

4.3.7 Implications

The computational results question the validity of the expression "diabatic limit" as it is frequently used for a single fragment channel into which a molecular state transforms. In the axial recoil limit two or three channels often contribute to a similar extent to the fragment formation (Table 8 and Table 9). When specifying the diabatic limit of a molecular state, one usually implies that this is the energetically highest of the accessible channels. The SFB theory shows that this channel may not necessarily be the most favoured one. In what follows the expression "diabatic limit" will refer to the most favoured fragment channel.

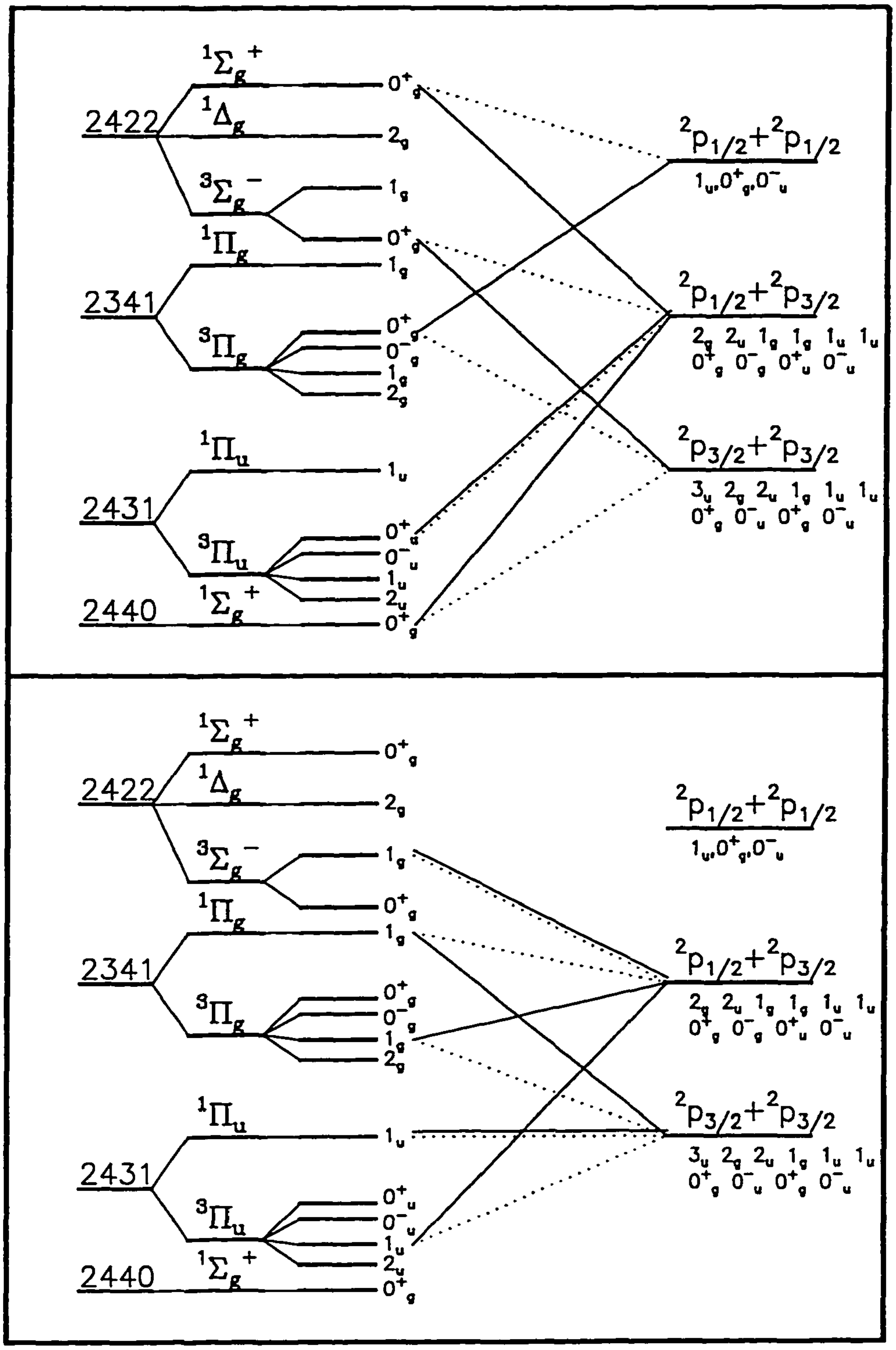

Figure 34: Diabatic correlation diagram of the $\Omega = 0$ states and $\Omega = 1$ states of a rotating homonuclear halogen molecule. The adiabatic correlation (dotted lines) is also included

This critique also leads to a new understanding of "diabatic correlation diagrams". Diabatic correlation diagrams are popular because of their power to predict the interactions which affect excited states. Again, when constructing such a diagram it is usually assumed that each molecular state correlates diabatically to only one exit channel -- a condition which is not necessarily true for any given molecular state. Unless certain states can be ruled out for symmetry reasons, diabatic correlations will usually give a combination of the various diabatically correlated fragment states. Figure 33 and Figure 34 show diabatic correlation diagrams of the rotating X_2 and XY molecules (X, Y = F, Cl, Br, I), that have been constructed using Table 8 and Table 9. Since the SFB-theory, which has been used to calculate the relative branching ratios, does not include +/- symmetry, this constriction has been enforced separately on the halogen molecules by omitting the forbidden (+ ↔ -) correlations.

4.3.8 Dissociation dynamics and comparison with previous studies

4.3.8.1 Following excitation to the [2431] states

Returning to the dissociation dynamics of the B $^3\Pi(0^+)$ state of BrCl, we find that the new correlation diagram and the experimental results agree that the highest of the four exit channels $\langle 1/2\ 1/2|$ is favoured over the lower exit channels in a diabatic process. Indeed, the large fraction of molecules evolving *via* this channel suggests that the dissociation process -- at least at high excitation energy -- is well described by the axial recoil limit. Previous experiments on BrCl and other interhalogens can also be understood using the diabatic model of the SFB-theory. All interhalogens have a number of features in common. The $^3\Pi(0^+)$ B-state is weakly bound and experiences strong interactions with a purely repulsive $Y(0^+)$ state, resulting in a barrier and formation of two new adiabatic PES. For some molecules (ICl, IBr) levels above this barrier have been observed. The $Y(0^+)$ state correlates diabatically to the ground state atoms and thus the interaction with the B-state plays an important role in predissociation processes.

Furthermore a weak interaction with a $\Omega = 1$ state was found to be responsible for predissociation of the B-state close to the ground state dissociation limit. In the case of BrCl and other interhalogens this state has been identified as the $^1\Pi(1)$ state. For a number of compounds such interactions have been studied in detail and the interaction terms quantified.

These observations can be understood using the proposed diabatic correlation diagrams (Figure 34). As we experimentally verified, the $^1\Pi(1)$ state correlates adiabatically *and* diabatically to the atomic fragments in their spin-orbit ground state. The B-state, on the other hand, transforms to 80 % to the highest neutral channel and will yield large amounts of X*+Y* fragments given enough excess energy. This diabatic B-state curve is crossed by the $^3\Sigma^-(0^+)$ curve, which diabatically transforms to the atomic ground state fragments. If this curve crossing is indeed responsible for the barrier that has been described above, the $Y(0^+)$ state can be identified as the diabatic $^3\Sigma^-(0^+)$ state. Two additional interaction regions above this barrier are the result of mixing of the diabatic B-state and the diabatic components of the $^1\Sigma(0^+)$ state, thereby opening the X+Y* and X*+Y channels. These two higher adiabatic curves, which form avoided crossings and correlate to Br*+Cl* and Br*+Cl, may possibly have shallow minima (see Figure 27). Interestingly, Hopkirk *et al.*(70) found evidence for two such curves in the emission spectrum following excitation to the $E(0^+)$-state.

In the case of the three heteronuclear fluorides it is spectroscopically well established that the B-state correlates to an exit channel which yields the spin-orbit excited state of the *heavier* atom. We believe that this is a general phenomenon and also occurs for the other interhalogen compounds. However, the B-state curve is more weakly perturbed in the case of the interhalogen-fluorides and is accessible at high energies by excitation from the ground state. Therefore, it may only be possible for these molecules to spectroscopically establish a correlation to the highest exit channel.

4.3.8.2 Following excitation to the [2341] and [2422] states

Additional information is available from photodissociation studies in the UV-region of the (inter)halogen compounds. This region is less well studied and the UV-bands in the absorption spectrum (not shown in Figure 22) have for most (inter)halogen molecules not been assigned. Very recently Jung *et al.*(82) performed photodissociation studies on IBr, that are similar to the ones described above. By using the TOF-REMPI technique combined with a mask and a pinhole in front of the ion detector, they were able to detect state selectively the iodine fragments in a one colour experiment using 304 nm light. At this wavelength only the repulsive [2341] and [2422] manifolds are excited. In the following their findings and conclusions will be described along with a different interpretation based on the new diabatic correlation diagram.

Jung *et al.* used only adiabatic correlations, which can be expressed in an adiabatic correlation diagram similar to Figure 20. This correlation diagram (Figure 35) is different from Figure 20 in two points. Jung *et al.* assumed that the $^3\Sigma^-(0^+)$ and the $^3\Pi(0^+)$ state switch order and consequently an avoided crossing of these two 0^+ states results high above the exit channels. The possibility that these states are reversed was mentioned earlier by Faist and Bernstein(61). It was also implied that parity is a good quantum number in IBr and thus the $B^3\Pi(0^+)$ [2431] state correlates to I+Br*, whereas the $^3\Pi(0^+)$ [2341] state correlates to the I+Br ground state fragments.

As displayed in Figure 35, in summary, the $^3\Pi(0^+)$, $^3\Pi(1)$, and $^3\Pi(2)$ states of the [2341] manifold correlate to atomic ground state fragments I+Br, whereas the $^1\Pi(1)$ [2341] state correlates to the channel (b) I+Br*. Of the [2422] manifold, the states $^3\Sigma^-(1)$ and $^1\Delta(2)$ correlate adiabatically to channel (b) and the $^3\Sigma^-(0^+)$ and $^1\Sigma(0^+)$ states correlate to channel (c) and (d), respectively.

The experimental findings of Jung *et al.* are summarized in Table 10. Using the experimentally determined spatial anisotropy parameters β along with the respective branching ratios, the relative quantum yield of the parallel and perpendicular component to all four exit channels was determined.

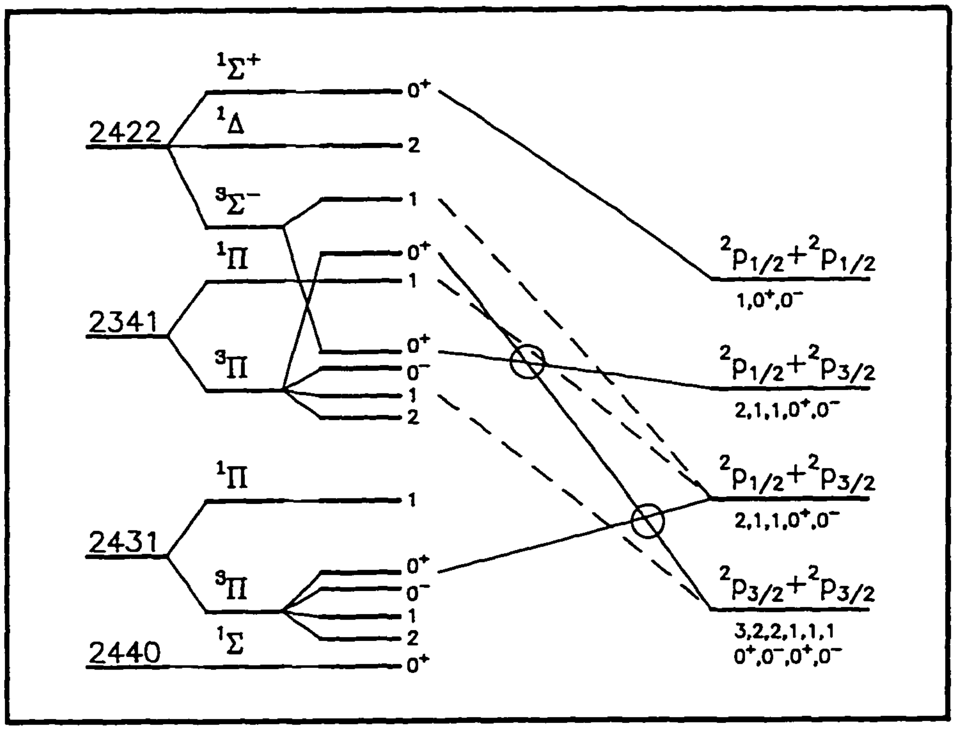

Figure 35: Adiabatic correlation diagram of IBr as implied in the discussion of reference 82.

Based on the experiments the I*+Br channel was populated *via* a parallel transition ($\Delta\Omega = 0$, $\beta = 2$). Using their correlation diagram this can be explained as excitation to $^3\Pi(0^+)$ [2341] and adiabatic dissociation at the curve crossing with $^3\Sigma^-(0^+)$. Similarly, diabatic passage through this crossing yields I+Br and it is suggested by the authors that this process provides the parallel component to channel (a) with $\beta \approx 0$. The perpendicular component to channel (a) was attributed to excitation of the $^3\Pi(1)$ [2341] state and subsequent adiabatic dissociation, whereas the large perpendicular character of the I+Br* channel (b) was attributed to the $^1\Pi(1)$ [2341] state. Finally, the miniscule appearance of the I*+Br* channel was regarded as resulting from transition to the $^1\Sigma(0^+)$ [2422] state and

Channel	β	Assignm. [Jung *et al.*]	Assignm. [this work]	Rel. Q. Yield [Jung *et al.*]
I + Br	0.0	$^3\Pi(1)$	$^1\Pi(1)$ d	0.29
		$^3\Pi(0^+)$	$^3\Pi(0^+)$ a/d	0.32
I + Br*	-0.7	$^1\Pi(1)$	$^1\Pi(1)$ a	0.22
		$^3\Pi(0^+)$	$^3\Pi(0^+)$ a/d	
		$\rightarrow {}^3\Pi(0^+)$		0.07
I* + Br	1.8	$^3\Pi(0^+)$	$^3\Pi(0^+)$ a/d	
		$\rightarrow {}^3\Sigma^-(0^+)$		0.10
I* +Br*	> 0	$^1\Sigma^+(0^+)$	$^3\Pi(0^+)$ d	?

Table 10: Experimentally determined [ref. 82] anisotropy parameter and photofragment yield in the photodissociation of IBr. Assignment according to ref. 82 and using this work (a=adiabatic; d=diabatic).

adiabatic dissociation. These assignments are listed in Table 10.

This picture of the UV-dissociation dynamics is certainly conclusive and has the beauty of being able to explain all observed phenomena with largely adiabatic processes. It implies, however, that four excited states ($^3\Pi(0^+)$ [2341], $^3\Pi(1)$ [2341], $^1\Pi(1)$ [2341] and $^1\Sigma(0^+)$ [2422]) contribute to the UV-absorption spectrum and that non-adiabatic interaction with a fifth dark state ($^3\Sigma^-(0^+)$ [2422]) is involved. It also implies that parity is a good quantum number and that $^3\Sigma^-(0^+)$ [2422] and $\Pi(0^+)$ [2341] have switched order. Finally, the coupling between the two 0^+ states has to be small. This results in a largely diabatic process and gives comparable contributions to both channels (a) and (c).

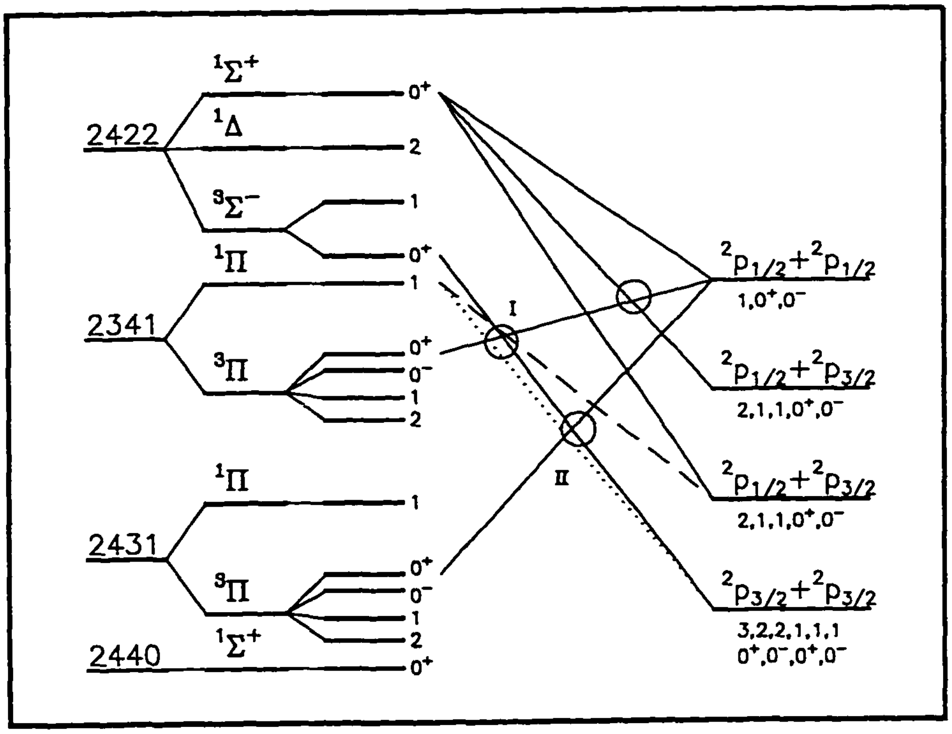

Figure 36: Diabatic correlation diagram showing the ($\Omega = 0^+$) states (solid) and ($\Omega = 1$) states (dashed). The circles indicate strong avoided crossings.

Using the new diabatic correlation diagram presented in Figure 36, an alternative mechanism can be proposed. It is assumed that the ordering of the ${}^3\Sigma^-(0^+)$ and the ${}^3\Pi(0^+)$ states is not reversed. All parallel components of the transitions were assumed to originate from excitation to the ${}^3\Pi(0^+)$ [2341] state. In the axial recoil limit this molecular state transforms to 80 % into the I*+Br* fragment channel (Table 9). The fact that only a small yield of this channel is observed indicates that the process is not diabatic. Mixing of the ${}^3\Pi(0^+)$ [2341] state with the ${}^3\Sigma^-(0^+)$ state opens the I+Br channel in a process that continues diabatically on ${}^3\Sigma^-(0^+)$. The small contribution to the I+Br* channel arises from completely adiabatic dissocation on ${}^3\Pi(0^+)$ [2341] (Figure 20), whereas the parallel contribution to the

I*+Br channel may be explained by diabatic passage through the avoided crossing with $^3\Sigma^-$ (0^+) and subsequent mixing with $^1\Sigma(0^+)$ [2422]. One can expect a largely adiabatic process at the avoided crossing of the $^3\Pi(0^+)$ [2341] and $^3\Sigma^-(0^+)$ states, because of the small internal kinetic energy and the magnitude of the interaction. Since mixing of the diabatic $^3\Sigma^-(0^+)$ state with the B- $^3\Pi(0^+)$ state is much weaker, a process evolving adiabatically through the first avoided crossing (I), will proceed diabatically through the lower crossing (II). We therefore expect, that the I+Br channel has stronger parallel contributions compared to channels (b) and (c). This mechanism is consistent with the experimental observations of Jung *et al.* It was found that the quantum yield of the parallel component is threefold higher for the lowest fragment channel (a) compared to channels (b) and (c).

Contributions of all low lying channels (a), (b) and (c) may also be explained by the 5%-10% contribution they each have in the axial recoil limit (see Table 9). However, this fraction does not compare well with the observed preference of the lowest fragment channel.

In our picture, the perpendicular components of channels (a) and (b) can be explained by excitation to the $^1\Pi(1)$ [2341] state alone. According to the new correlation diagram (Figure 34 and Figure 36), this state transforms diabatically to I+Br. Mixing with all other $\Omega = 1$ states results in an adiabatic curve, which correlates to the I + Br* channel. Both channels appear to be equally important in the photodissociation of IBr at 304 nm (Table 10). We are now able to understand most observations of the UV-photodissociation experiment using only excitation processes to the $^3\Pi(0^+)$ [2341] and $^1\Pi(1)$ [2341] states and different extent of adiabaticity in the dissociation dynamics. The assignment of the transitions is summarized in Table 10 and compared with the assignment of Jung *et al.* Clearly our picture is highly speculative and confirmation by a two colour photodissociation experiment at various excitation wavelengths in the UV-region is necessary.

A second test of the general applicabily of the SFB-theory on interhalogen molecules is direct comparison with accurate *ab initio* predictions of curve crossings. Our diabatic correlation diagram should be able to predict the avoided crossings that arise in the calculation of the adiabatic curves.

Tonokura *et al.*(83) performed photodissociation experiments on ICl on the UV-band using the REMPI/TOF technique to state-selectively probe chlorine fragments and the LIF technique to determine the branching ratio of the iodine fragments. The three curves involved at 235-248 nm were characterized by a high level *ab initio* calculation. This group found that parallel excitation to the $^3\Pi(0^+)$ [2341] and $^3\Sigma^-(0^+)$ [2422] states is responsible for product formation via both the I+Cl and I*+Cl channels. Furthermore, perpendicular excitation and adiabatic dissociation via the $^1\Pi(1)$ [2341] state predominantly yields I+Cl*. In the *ab initio* calculations two avoided crossings of $\Omega = 0$ states were described. The $^3\Pi(0^+)$ [2341] and $^3\Sigma^-(0^+)$ [2422] states form an avoided crossing (I) at high energy and 5.5 bohr. At lower energy and 7 bohr an avoided crossing (II) between the lower adiabat and the B $^3\Pi(0^+)$ [2431] state was found.

Both avoided crossings can unambigiously be accounted for by the diabatic correlation diagram (Figure 36). They arise from mixing of the diabatic $^3\Sigma^-(0^+)$ [2422] state with the $^3\Pi(0^+)$ [2341] and $^3\Pi(0^+)$ [2431] state. In addition, the correlation diagram also predicts another avoided crossing of the diabatic $^3\Pi(0^+)$ [2341] state (or upper adiabat of crossing (I)) with the strongly repulsive $^1\Sigma(0^+)$ [2422] state. Adiabatic passage through this interaction region is responsible for the experimentally observed dominance of channel (c) over channel (d).

It can be concluded, that the correlation diagram, obtained using the diabatic SFB-theory, is consistent with both experimental and theoretical observations. Some limitations overshadow the general applicability of the SFB theory, but do not appear to diminish its predictive power.

4.4 Conclusion and Summary

The photodissociation of BrCl has been studied at various wavelengths using the REMPI-TOF MS technique. The experiments show that the $^3\Pi(0^-)$ B-state dissociates in a highly non-adiabatic process, and that fragments evolve through three or four out of the possible four neutral fine-structure fragmentation channels. In order to gain quantitative information about the interactions between the potential energy curves involved a simple Landau-Zener calculation was carried out. The diabatic correlation of the B-state to the highest of the four channels (Br*+ Cl*) was discussed from two points of view. An explanation using the MO-theory combined with an estimate of ionic character in the B-state led to inconsistent results. Application of the theory of diatomic dissociation developed by Singer Freed and Band was more successful. The diabatic correlation of the low lying excited states of halogen and interhalogen molecules was calculated and the SFB theory gave an axial recoil limit that was consistent with our experimental results. The calculation yielded a new diabatic correlation diagram. Previous experiments on interhalogens other than BrCl from other groups at higher excitation energy could be qualitatively understood using our diabatic correlation diagram.

Implications of this work go beyond the study of BrCl and Cl_2. Since the computational results are identical for all interhalogens regardless of the identity of the halogen atoms, these results may help to shed light on the dissociation dynamics and spectroscopy of all interhalogens. It is believed that the knowledge of diabatic correlation diagrams is crucial for an understanding of fast processes. The theory of Singer, Freed and Band proved to be a useful tool and may help to gain information about excited state PESs.

5 Photodissociation dynamics of BrNO

5.1 Introduction

The nitrosylhalides XNO (X = F, Cl, Br) have been studied extensively using various photofragmentation techniques and today a large body of information is available(9, 11). ClNO has especially been subject to many theoretical and experimental works, starting with the publication of the absorption spectrum in 1930 (84) and continuing today. As is the case for the halogen and interhalogen compounds, the three stable nitrosylhalides allow for comparative studies, since molecular properties such as orbital energy, spin-orbit interaction and consequently mixing of excited electronic states will change monotonously from FNO to BrNO.

In contrast to the lighter nitrosyl halides, there is little data available on the excited states of BrNO. The absorption spectrum has not been reported in detail, yet, but has been described as a structureless band that rises from around 600 nm into the UV-region(85). Later Reisler and Qian(85) reported two weak bands peaking at wavelengths longer than 600 nm. The diffuseness of the absorption bands hints, that all excited states in the visible and near-UV region are repulsive. One can expect interesting cases of avoided crossings and consequently non-adiabatic effects, because of the number of excited states present and the weak to intermediate coupling between them.

Since triatomic molecules XNO have two additional vibrational degrees of freedom compared to the previously discussed (inter)halogens, we can also study the influence of these additional internal modes on the dissociation dynamics. These internal degrees of freedom may influence the dissociation dynamics profoundly, if the non-adiabatic interactions occur close to the Franck-Condon region, where the kinetic energy of the dissociating molecule is comparable in magnitude to the energy in internal modes.

Non-adiabatic effects were shown to be of great importance in the photodissociation dynamics of ClNO(39). ClNO belongs to the weak coupling case, i.e., the electronic wavefunctions in the molecular region can be assumed to have good spin and orbital quantum numbers. The spin-orbit interaction among the states is then added as a perturbation. As the system travels through the region of large internuclear distance, the separation between the electronic states becomes comparable to the spin-orbit term. It is in this region where non-adiabatic interactions influence the dissociation dynamics most strongly(39).

BrNO, on the other hand, belongs to the intermediate coupling case. The spin-orbit term, which is dominated by the bromine atom is expected to be fourfold larger than in the ClNO case. Consequently, the distinction between the parent molecular region and the recoupling region at large distance is void.

It is the purpose of this study to record and assign the absorption spectrum of BrNO and to characterize the electronically excited states in the most detailed fashion. At numerous wavelengths - covering the whole range of the BrNO absorption - photodissociation experiments are carried out. In this way the electronic states are identified and the topology of the corresponding PsESs can be deduced. Construction of a diabatic correlation diagram similar to the ones for the (inter)halogen molecules is helpful in order to understand the dissociation dynamics.

Non-adiabatic interactions following excitation to one of the excited states is studied in detail at several excitation wavelengths. Comparison with FNO and especially ClNO provides additional information about the excited state interactions and leads to an in depth understanding of the dissociation dynamics of the various excited states of BrNO.

5.2 Results

In this section the results of all photodissociation experiments on BrNO will be presented. For clarity the experimental results were sorted by type of experiment rather than wavelength.

The *absorption spectrum* gives information about the number and energy of the electronic transitions. In order to assign these transitions to excited states, photodissociation experiments using state-selective detection of the photofragments were carried out. *Rotational distributions* of the NO photofragment provide information about the electronic fine structure, vibrational, rotational and Λ-doublet state population. The *TOF-profiles* of the NO photofragments contain the information about the alignment of the transition dipole moment and about the fine-structure branching ratio of the correlated bromine fragment. Since NO state-selective experiments were not carried out at the UV-wavelengths, the information about the Br/Br* branching ratio at 225 nm and 266 nm was obtained by probing bromine atoms *via* the *Br/Br* 2+1 REMPI* lines. The section closes with presentation of *photofragment yield spectra* of the NO photofragment, which were recorded in the longest wavelength region of the spectrum.

5.2.1 Absorption spectrum

The UV-Vis absorption spectrum was obtained according to the procedure described in section 2.2 and is displayed in Figure 37. For comparison the ClNO absorption spectrum has been reproduced from references 84 and 86 and is displayed in Figure 38.

The BrNO spectrum exhibits only diffuse bands and there are no indications of rotational structure, suggesting that all electronic states below 50000 cm^{-1} are repulsive. Repulsive electronic states with a planar (not necessarily horizontal) Franck-Condon region can be shown to have Gaussian type absorption spectra(9). It is therefore possible to obtain information about the states from a fit of the absorption spectrum to Gaussian functions. The width of each Gaussian provides an estimate for the gradient of the PES in the Franck-

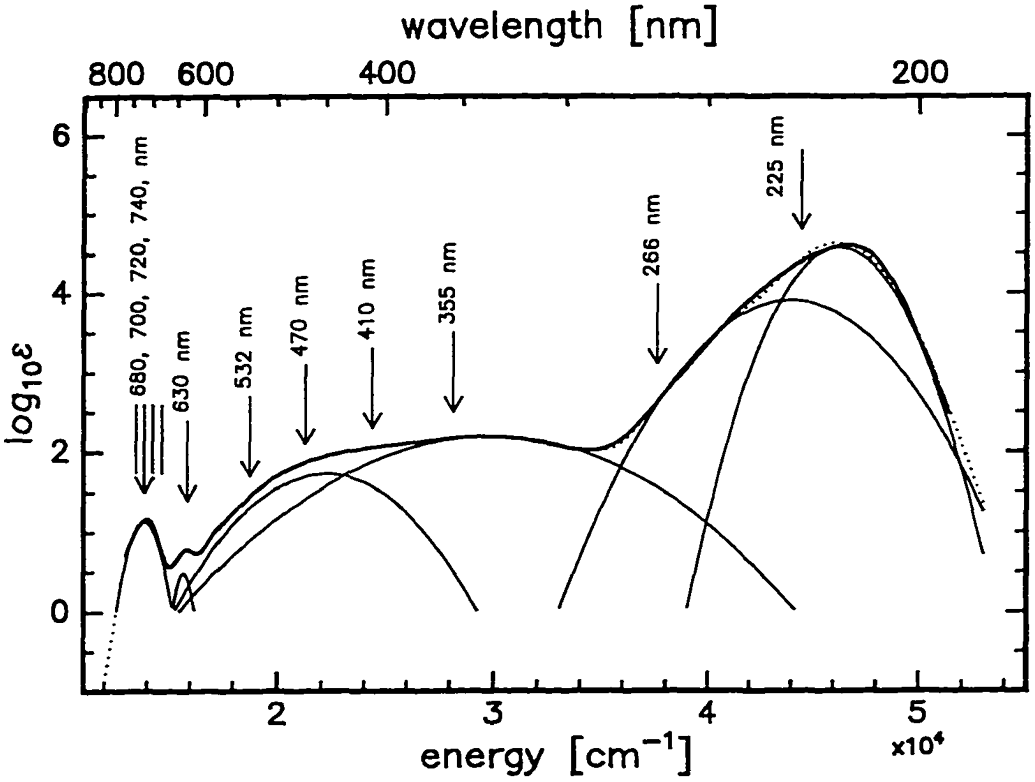

Figure 37: Absorption spectrum of BrNO. The arrows indicate excitation energies at which photodissociation experiments have been carried out. The thin lines indicate the Gaussian fitting functions.

Condon region, and together with the amplitude, an estimate for the oscillator strength. Trivially, the centre of the Gaussian corresponds to the Franck-Condon excitation energy. The BrNO absorption spectrum can be fitted well in the green to near-UV region with two broad Gaussian functions of different width (Figure 37). The UV region may be fit with two Gaussian functions, but the agreement is somewhat less satisfactory indicating that a third state may be involved in this spectral region. The weak red bands are separated by 1920 cm^{-1} and also show some deviations from the Gaussian lineshape.

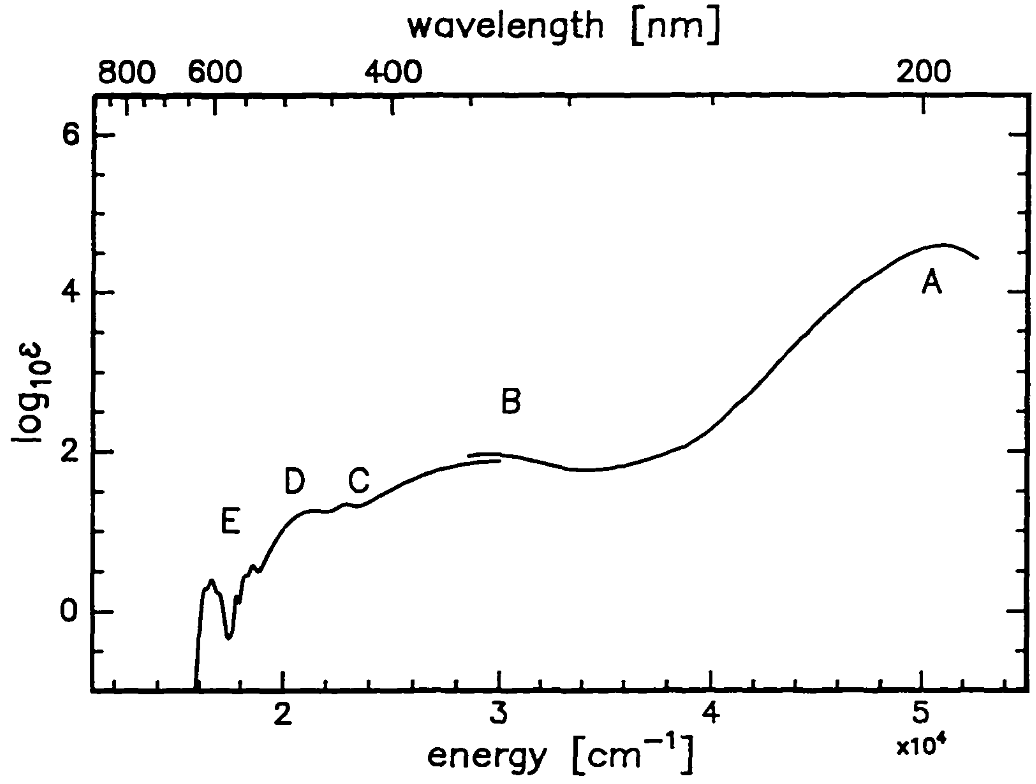

Figure 38: Absorption spectrum of ClNO. The UV region is reproduced from reference 86, whereas the long wavelength region is reproduced from reference 84.

5.2.2 Rotational distributions of the NO fragment

Nine rotational distributions were recorded at photolysis wavelengths, both close to the maxima of the Gaussian fitting functions of the absorption spectrum and between those maxima (Figure 39 and Figure 40). No complete REMPI spectrum of the NO fragment could be obtained following dissociation in the UV region at 266 nm and 225 nm. Here, many NO vibrational states were populated and the corresponding rotational lines strongly overlap. Each rovibrational state had only a small population so that the lines were weak. The large absorption cross section did not lead to an increase of the signal, because at all wavelengths bleaching is nearly complete. Hence, the number of photofragments depends more strongly on the jet-expansion conditions and spatial overlap of the laser focal points

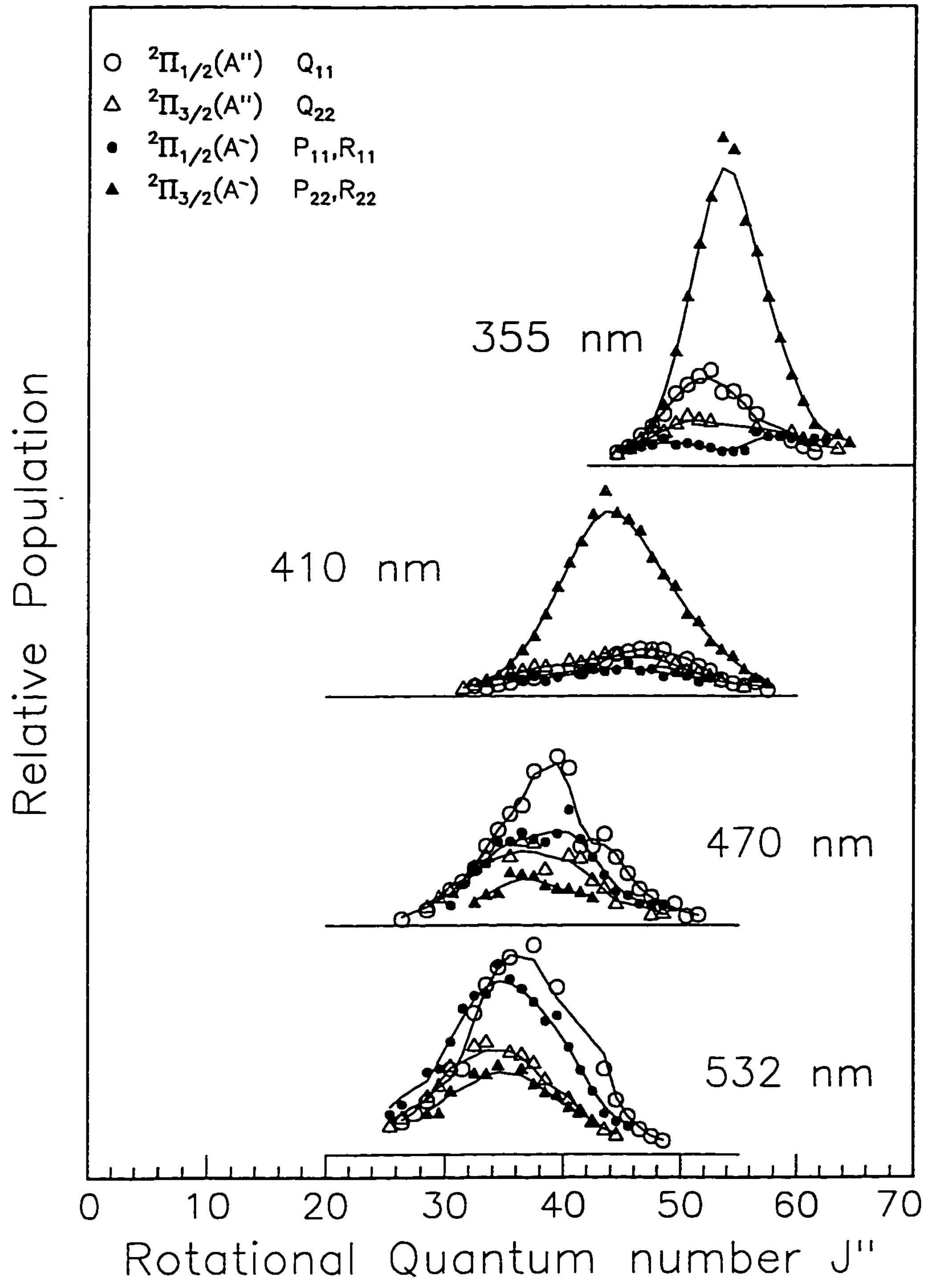

Figure 39: Rotational distributions of the NO photofragment. At all wavelengths the NO(v"=0) state distribution is shown.

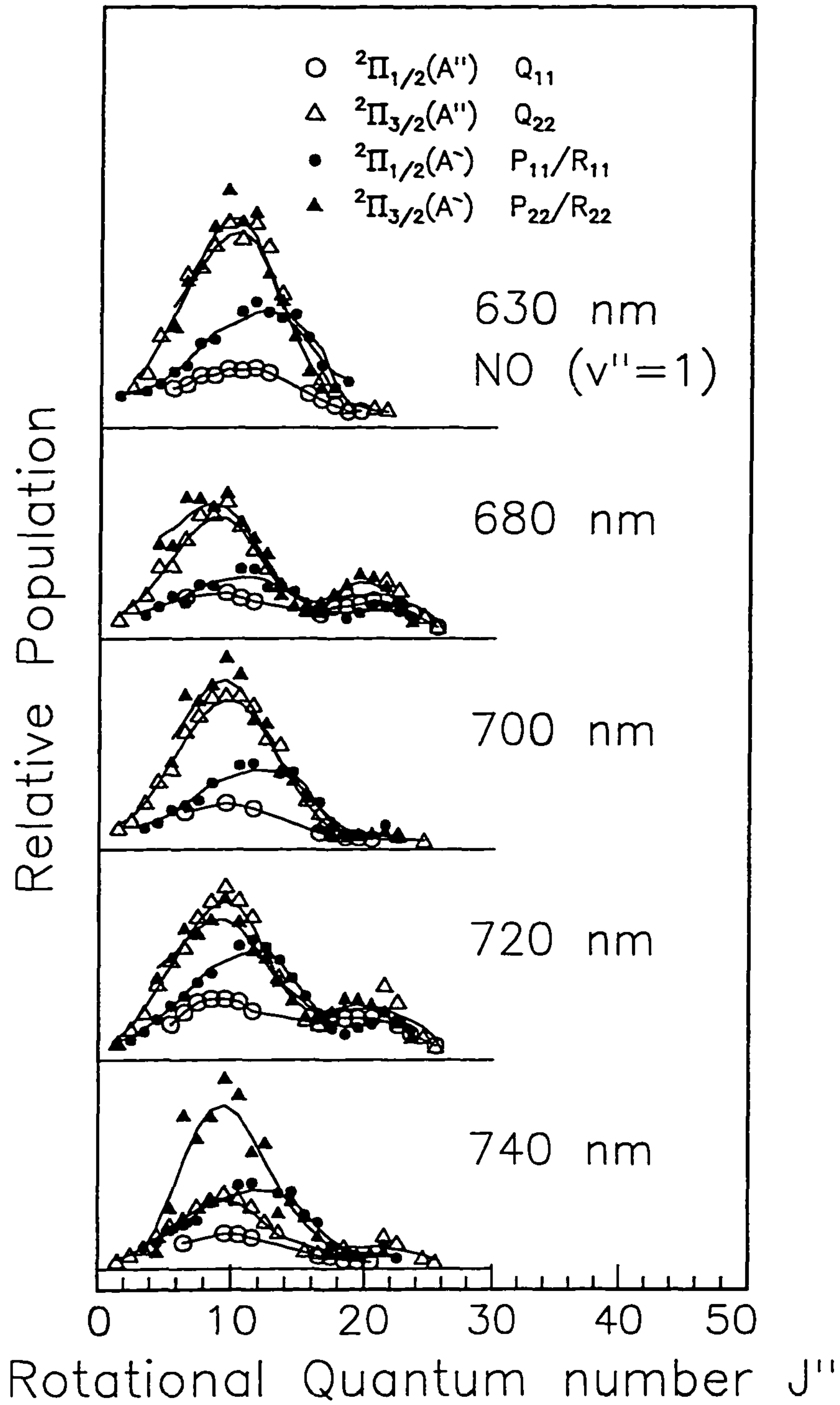

Figure 40: Rotational distributions of the NO photofragment. At all wavelengths except 630 nm the NO (v''=0) state distribution is shown.

than on the absorption cross section.

In the region between 355 nm and 532 nm very high rotational excitation, but less than 10% vibrational excitation was observed. Lines arising from transitions of the v"=1 states were identified, but the signal was too weak to obtain reliable rotational distributions.

The rotational distributions of the NO (v"=0) fragments indicate participation of two excited states in this spectral region. Figure 39 shows a clear transition from an electronic state, that preferentially yields NO $^2\Pi_{3/2}$ (A') photofragments, to another lower lying state, that yields NO $^2\Pi_{1/2}$ (A") photofragments. For both states the maximum of the rotational distribution shifts from high J at short wavelength to lower J at longer wavelength.

Photolysis in the region of the two red bands reveals that excitation between 600 nm and 650 nm yields exclusively NO photofragments in their first vibrationally excited state. Similarly, between 700 nm and 740 nm only NO (v"=0) fragments were formed. The rotational distributions for both absorption bands show a bimodal structure with a energy dependent ratio of the stronger "low J" (J" ≈ 9.5) to the weaker "high J" (J" ≈ 22.5) distribution. Preference for Λ-doublet states is not observed and indeed not expected, since at such low rotational excitation each Λ-doublet component is a mixture of a' and a" states(44).

5.2.3 TOF-profiles of the NO fragment

In Figure 41 NO photofragment TOF profiles of selected rotational lines are presented. At all wavelengths the spatial anisotropy parameter is close to the limiting value of $\beta = 2$, indicating that the electronic transition dipole moment, μ, is roughly parallel to the initial direction of recoil, v, and hence in plane of the molecule. In a slow dissociation process the rotational motion of the dissociating molecule may smear out the alignment of μ with v leading to a reduced spatial anisotropy(87, 88). Since the value of β is high, it can be assumed that this so-called rotational modification of β is not important, in these dissociation processes, and the dissociation is fast and direct at all wavelengths. The TOF profile at 225 nm was recorded in a one-colour experiment using an unassigned line. At

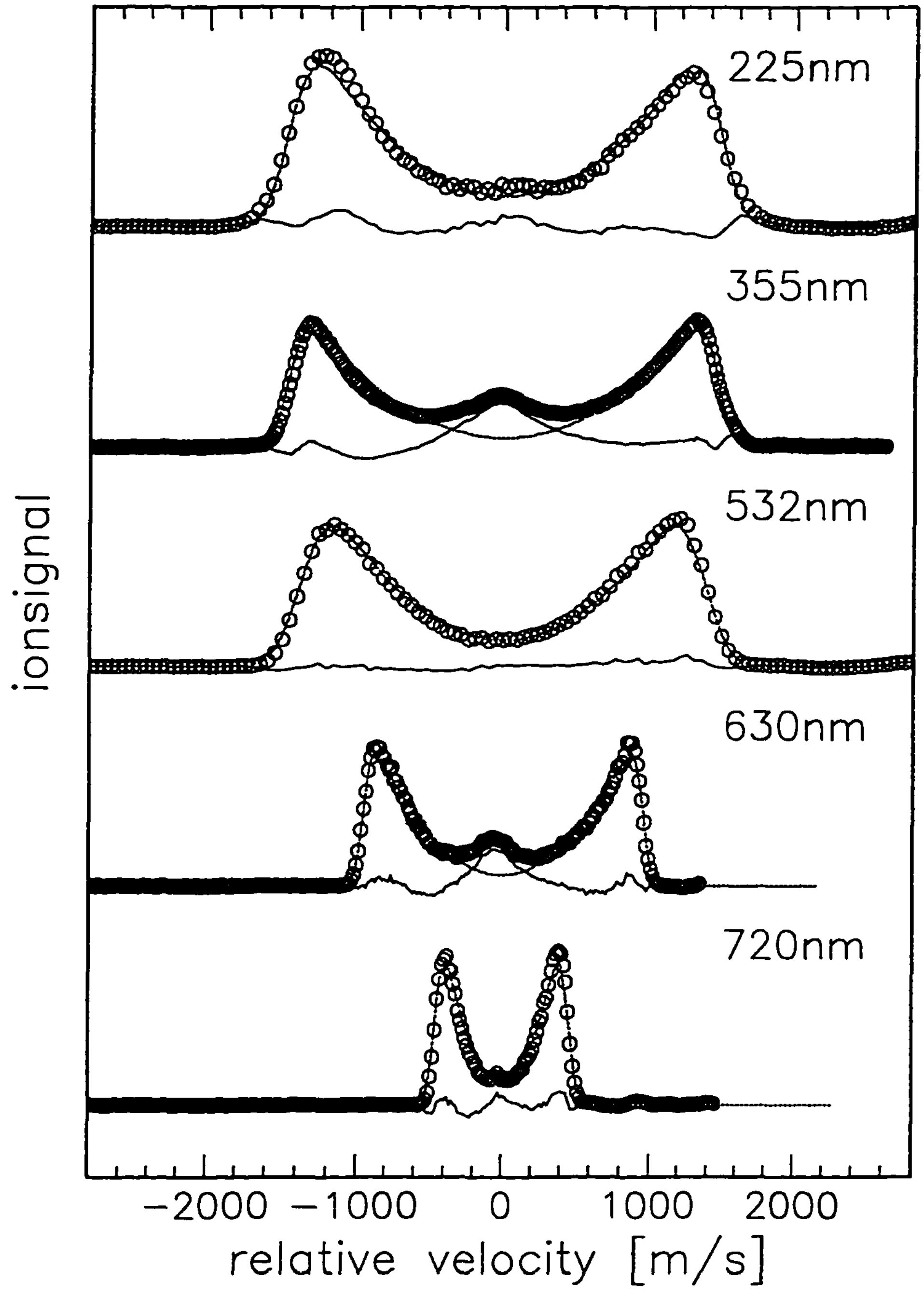

Figure 41: TOF-profiles of selected NO rotational lines at various excitation wavelengths. At all wavelengths the transition from the ground state is of parallel type.

266 nm no strong NO line could be found due to the large number of states populated. Here, the spatial anisotropy parameter was obtained using Br-photofragment TOF profiles. The widths of the NO TOF-profiles allow for determination of the kinetic energy release of the dissociation process. By subtracting the dissociation energy *(D_0)* and the known contributions to the excess energy (rotational, vibrational, and spin-orbit energy of NO) from the excitation energy one can determine the spin-orbit state of the correlated Br photofragment. At 355 nm bromine atoms are preferably formed in their Br*($^2P_{1/2}$) spin-orbit excited state, while at all longer wavelengths the Br($^2P_{3/2}$) ground state is favoured. As the rotational and vibrational energy of the NO fragment is not known at 225 nm and 266 nm, the total branching ratio of the bromine fragments at these wavelengths was determined by probing the bromine atom photofragments. This method, however, does not allow for correlation of the Br spin-orbit state to each NO state, and is therefore inferior to the analysis of the NO photofragment TOF profiles.

The Br/Br* branching ratio was determined for every NO rotational line at all wavelengths > 266 nm. At wavelength larger than 532 nm only Br was formed. Decreasing the excitation wavelength to 355 nm goes along with increased Br* formation. Furthermore, at each photolysis wavelength between 470 nm and 355 nm the Br/Br* branching ratio changes as a function of the NO rotational state, always favouring the Br channel at high rotational excitation. Typical TOF profiles, which show the onset of the Br channel are displayed in Figure 42 and Figure 43. All NO-TOF profiles at 355 nm, 410 nm and 470 nm have been analysed with respect to the Br/(Br*+Br) branching ratio. At 355 nm the branching ratio was obtained from TOF profiles that were recorded with a mask in front of the ion detector, whereas at the longer wavelengths we used a fit to equation (45) to determine the branching ratio. Figure 44 summarizes the findings for the Br/Br* branching ratios. Notice that at 355 nm and especially at 410 nm the Br channels contribute strongly to the TOF profiles, although the rotational distribution is clearly arising from excitation to a *single* electronic state as suggested by the absorption spectrum (Figure 37). Multiplication of the branching ratio curve with the rotational distribution shows that the

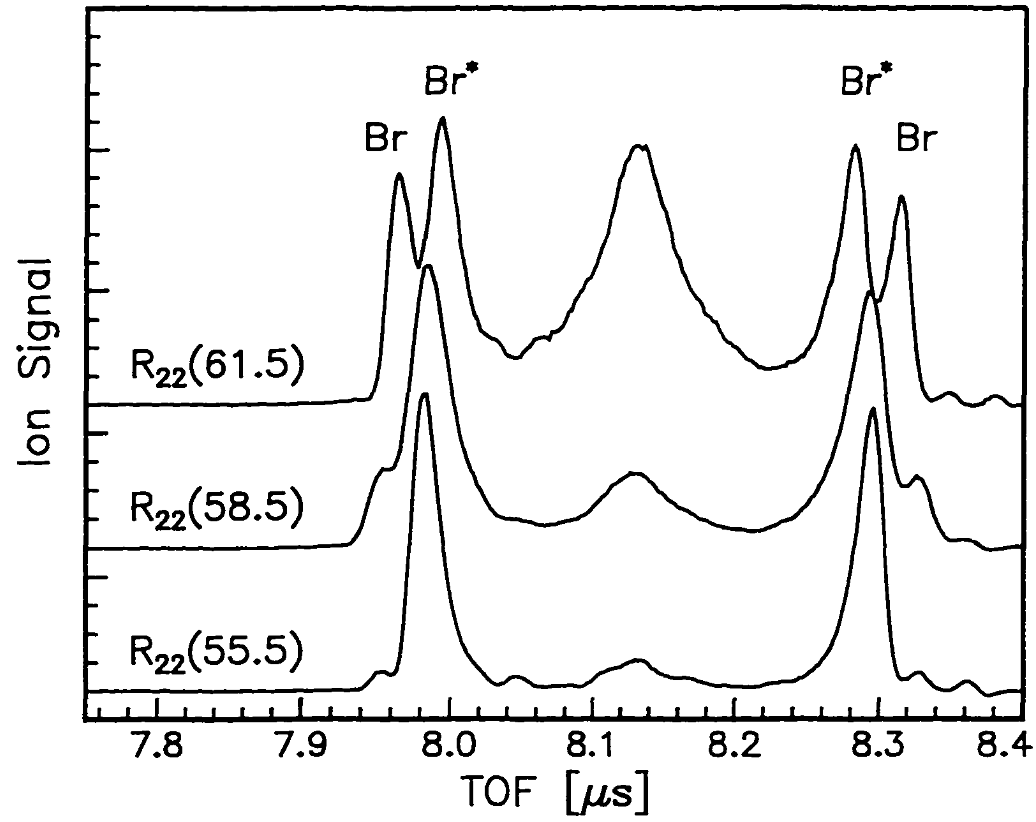

Figure 42: The NO ($^2\Pi_{3/2}$ A') TOF profiles at 355 nm were recorded using a mask and were rescaled. The broad center-peak is due to dissociation and non-resonant ionization of N_2O_2 impurities.

strongest branches producing Br *and* Br* fragments are the P_{22} and R_{22} branches. This confirms, that both contributions arise from excitation to the same electronic state.

The behaviour of the P_{11} and R_{11} branches in the photodissociation at 355 nm is striking. These branches, which probe the NO $^2\Pi_{1/2}$(A') state, exhibit an early maximum of the relative Br* yield at the J" = 55.5, the center of the rotational distribution.

Interestingly, the spatial distribution of the NO photofragments of the same $^2\Pi_{1/2}$(A') state, also show strong alternations, in contrast to all other branches probed at this and the other wavelengths (Figure 45). Within only 8 NO rotational quanta the spatial distribution oscillates between an almost perfect $\cos^2\theta$ distribution ($\beta \approx 1.7$) and a $\sin^2\theta$ ($\beta \approx -0.6$)

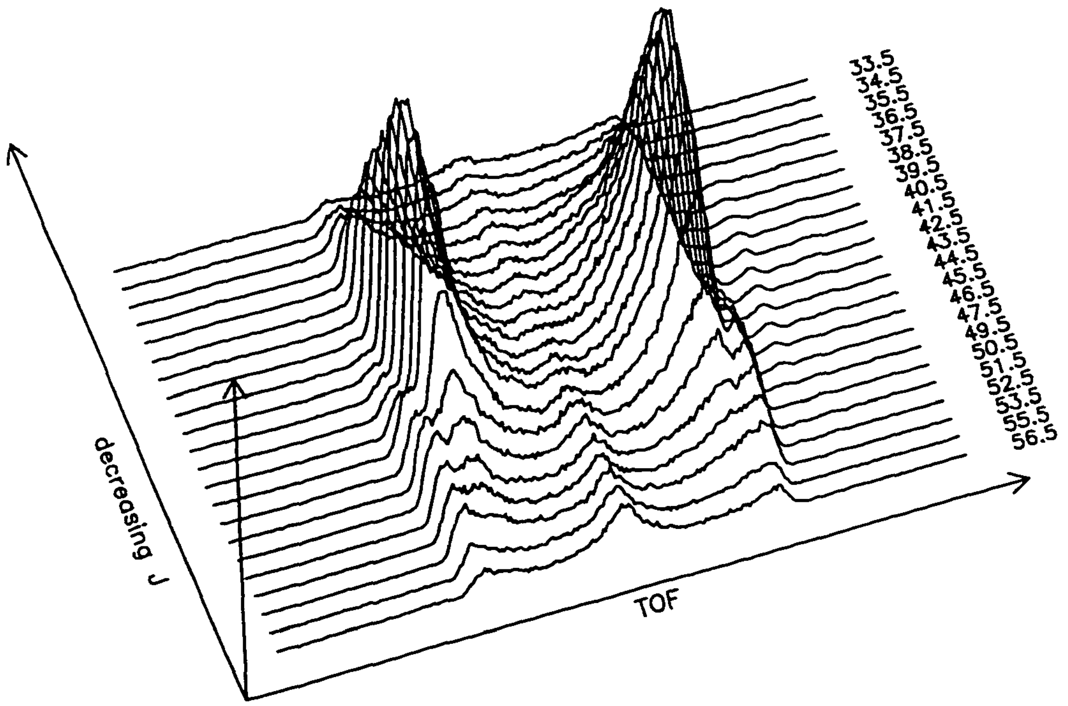

Figure 43: NO ($^2\Pi_{3/2}$ A') TOF-profiles at 410 nm. The onset of the wider Br-channel at around J" = 40.5 is visible. The TOF profiles were recorded using a mask in front of the ion detector.

distribution of fragments. Being the weakest branches of the REMPI spectrum the TOF signals of the P_{11} and R_{11} branches are weak and the error in β is ± 0.3. Since the Br and Br* channels contribute differently to the spatial anisotropy, we determined β for both channels separately in a TOF experiment by using a mask with a 4 mm pinhole in front of the ion detector. For completeness, the β values of the weaker Br channel are also given in Figure 45. However, extraction of reliable information is difficult, since the error at low J may be on the order of β ± 0.5.

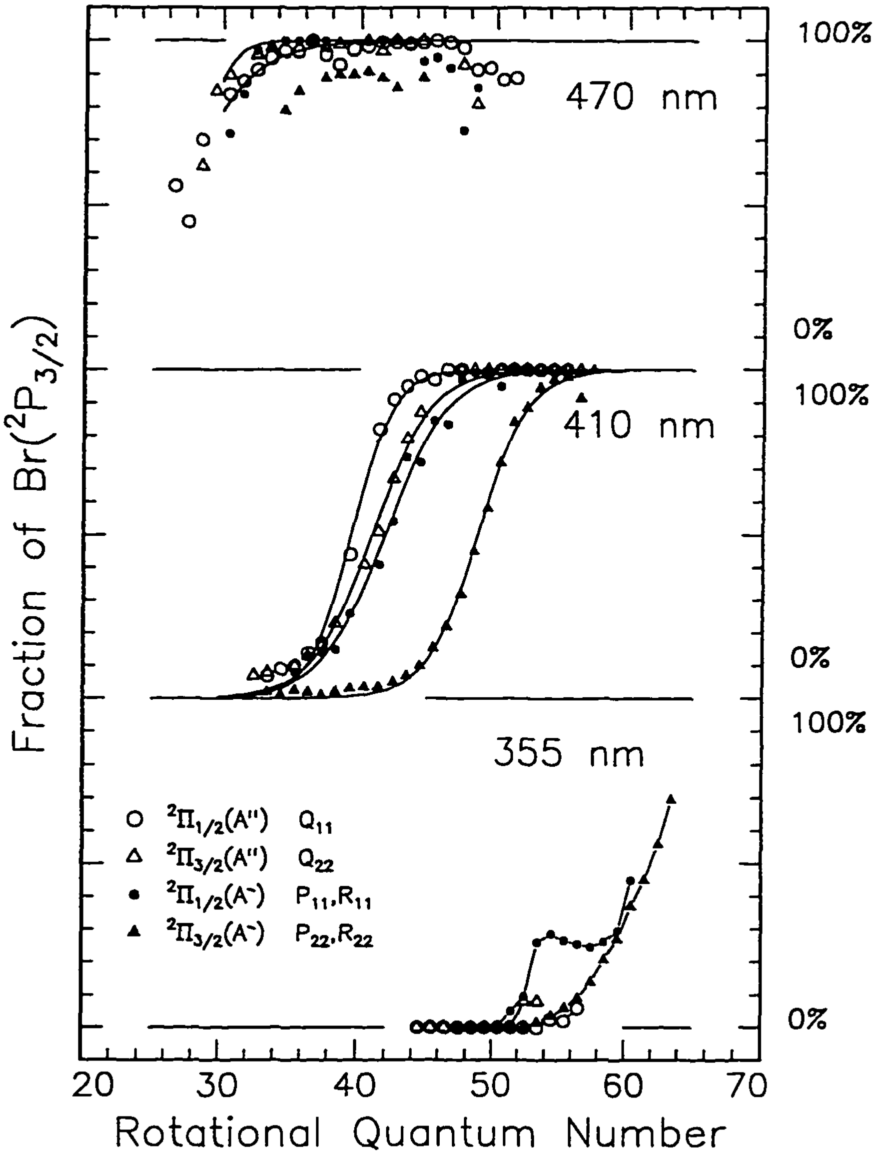

Figure 44: Branching ratio of Br/(Br+Br*) as a function of NO rotational excitation for three excitation wavelengths. The data has been obtained from the analysis of the individual NO TOF profiles.

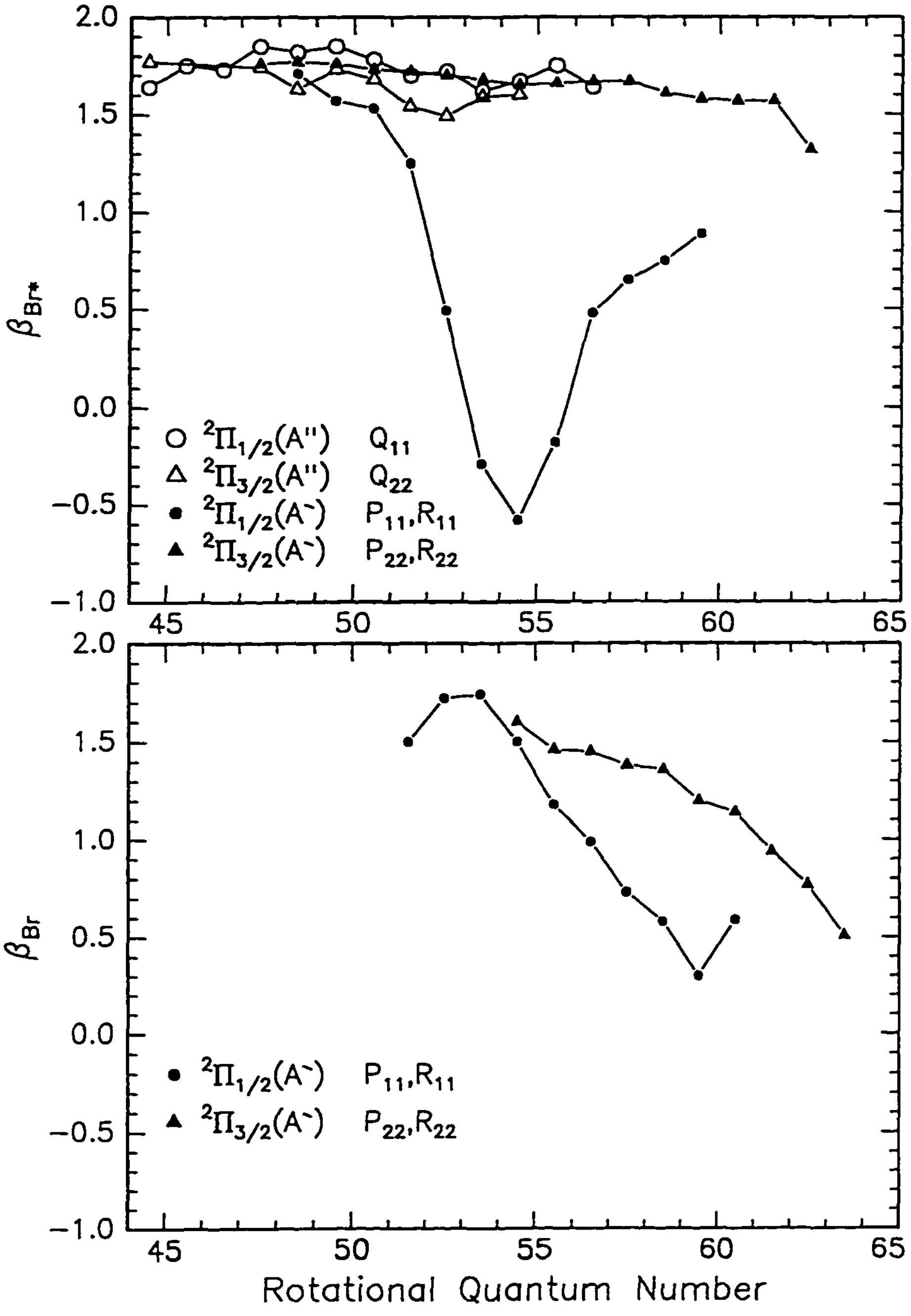

Figure 45: Spatial anisotropy parameters determined from various NO rotational lines at 355 nm. The β values for the Br* component (upper graph) and the weaker Br component are shown.

The weak, broad peak in the center of some TOF profiles arises from dissociation with the weak probe laser alone. Its intensity varies little with the laser wavelength in the NO γ-band region (220-230 nm) and its shape is insensitive to the probe lasers polarization. The small but non-zero width of the TOF-profiles indicates that this signal arises from a dissociation process. Furthermore, the wavelength independence shows that the NO fragment is non-resonantly probed. It was observed, that the intensity of the centerpeak is sensitive to the expansion conditions, its intensity increasing with gasload. Finally, the signal was increased when the firing of both lasers was delayed with respect to the triggering of the nozzle, i.e., when probing the "late part" of the molecular beam. We speculate, that this weak signal can be contributed to NO dissociating from small NO dimers or clusters, and not BrNO molecules, since we would expect a polarization dependence of the signal in the latter case and more importantly a wavelength dependence of the NO ion signal. By conducting experiments using a dilute sample of NO in absence of bromine, all of the above observations were repeated.

As recently reported by Naitoh *et al.*(89) the N_2O_2 photofragmentation at 193 nm produces NO fragments via two dissociation pathways

$$N_2O_2 + h\upsilon \rightarrow NO(A^2\Sigma^+) + NO\ (X^2\Pi) \qquad (1)$$

$$\rightarrow NO(B^2\Pi^+) + NO\ (X^2\Pi) \qquad (2)$$

In our experiments the NO fragments are formed in their excited $A^2\Sigma^+$ or $B^2\Pi$ electronic states by the probe laser pulseand may nonresonantly be ionized by a second photon. The spatial anisotropy ($\beta = 1$ to $\beta = 1.3$) that Naitoh *et al.* observed for the first channel will in our experiments be obscured, since in a non-resonant ionization scheme all rovibrational states are probed similtaneously. The corresponding $NO(X^2\Pi)$ fragment will not interfere with our experiments on BrNO for two reasons. Firstly, the N_2O_2 formation can be largely suppressed by optimizing the expansion conditions, and secondly, the signal can, due to its width, be easily distinguished from the BrNO photofragments.

5.2.4 Br/Br* branching ratio and TOF-profiles *via* bromine REMPI lines

As described above, it was not possible to record a complete REMPI spectrum of the NO photofragment at the shortest wavelengths studied. The 2+1 REMPI process probing the bromine atomic photofragment was then used to obtain the Br/Br* branching ratio. Since the line-strength factors for the Br and Br* REMPI lines were not reported in the literature, a calibration experiment at 355 nm was conducted in order to determine the ratio of the line-strength factors. By observing, that photodissociation at 355 nm yields approximately 10% Br and 90% Br* photofragments, the line-strength factors were estimated to be 80:20 for Br:Br*. The measured line intensity and branching ratios Br/(Br+Br*) are listed in Table 11. Data at approximately 225 nm was obtained in a one colour pump-probe experiment (a four photon process), whereas at all other wavelengths care was taken to achieve complete bleaching of the sample in the photolysis step.

It is apparent that photodissociation in the UV-region yields a high percentage of bromine atoms in their spin-orbit excited state and only a small fraction in its spin-orbit ground state. The small difference of the spatial anisotropy parameters following excitation at 266 nm and ~225 nm hints at different dissociation pathway being involved at these two energies. However, the inaccuracy of the data does not allow for the building of an argument on this observation. A photofragment yield spectrum of Br and Br* atomic fragments conducted with a strong and tunable UV-laser should be used to resolve this issue, but this experiment could not be carried out due to lack of equipment in our laboratory.

From the kinetic energy of the bromine photofragment one can calculate the amount of kinetic and consequently total internal energy. Similarly, the spread of internal energy is reflected in the rising time of the TOF profiles. Using the bromine fragment TOF profiles (Figure 46), the internal energy and its distribution was calculated and listed in Table 11. The accuracy of this rather indirect method was verified by comparison of the internal energy and energy distribution at 355 nm obtained in this way, with the energy distribution as obtained from the NO rotational distribution displayed in Figure 39. One finds J''_{aver} =

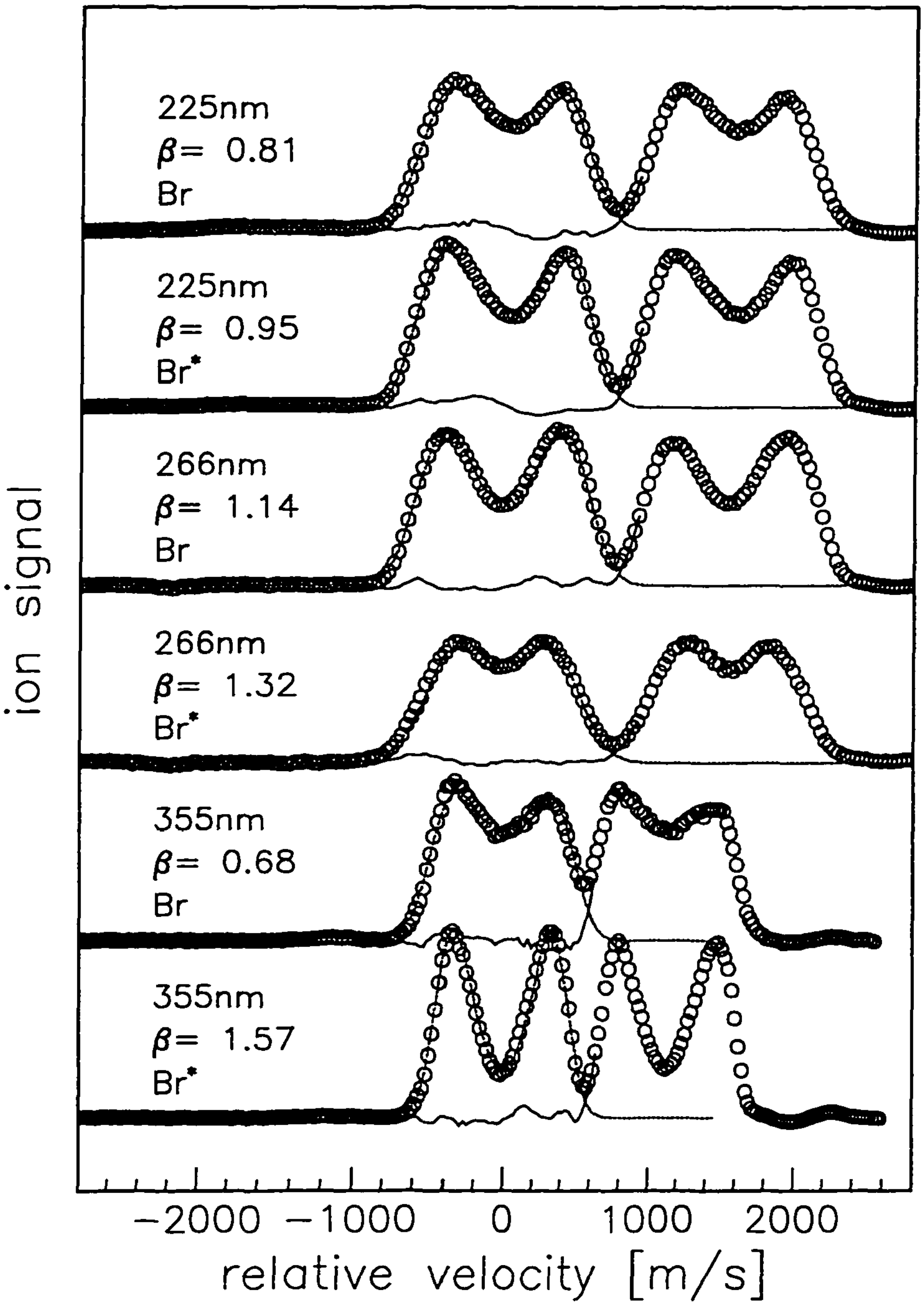

Figure 46: TOF profile of the Br and Br* fragments following excitation at 225 nm 266 nm and 355 nm. The relative velocity is given with respect to the ^{79}Br isotope.

λ	[nm]	~225		266		355	
$Br^*/(Br+Br^*)$		0.90		0.87		0.90#	
$I_{Br^*}/(I_{Br}+I_{Br^*})$		2.1		1.6		2.0	
		Br	Br*	Br	Br*	Br	Br*
β		0.81	0.95	1.32	1.15	0.68	1.57
Δt	[ns]	67	71	55	69	82	75
ΔT	[ns]	14	12	17	13	14	11
Δt_{KE}	[ns]	12	10	15	11	12.5	9
E_{kin}	[cm^{-1}]	13400	14900	9000	10700	10400	8700
$E_{rot,vib}$	[cm^{-1}]	21300	16200	18900	13600	8100	9700
$\Delta E_{rot,vib}$	[cm^{-1}]	3880	3430	4130	2850	2660	1770
$J'' \pm \Delta J''$						69±9	59±9
$v'' \pm \Delta v''$		12±2	9±2	11±3	9±1		

Table 11: Branching ratio and line-strength ratio of selected bromine REMPI lines. The β-values, the width Δt and the dispersion of the width ΔT were obtained from a fit to the TOF profiles.

59 and a width of the rotational distribution of $\Delta J'' = 9$, when assuming that all of the internal energy went into NO rotation and Br spin-orbit excitation. This compares reasonably well with the more accurate values of $J''_{aver} = 54$ and $\Delta J'' = 6$ as obtained from Figure 39, but shows the limitations of the method. Similarly the internal energy of the NO fragment associated with the Br-channels at 355 nm is described by $J''_{aver} = 69$ and $\Delta J'' = 9$, again assuming that bromine fragments do not correlate to vibrationally excited NO. However, the ~ 10% vibrationally excited states in the 355 nm rotational distribution most

likely correlate to the Br fragment. The 8100 cm^{-1} NO internal energy in Table 11 contain, therefore, a large fraction of NO vibrational energy. If this vibrational energy is taken into account, the fraction of rotational excitation is substantially reduced.

It is apparent that excitation at the UV wavelength leads to a much larger fraction of NO internal energy compared to 355 nm. If one assumes preferential excitation of NO vibration over rotation, a vibrational distribution of v" = 9-12 with a narrow width of 2-3 vibrational quanta is found. As expected, we find that, when the NO fragments correlate to Br* atomic fragments, the NO internal energy is somewhat smaller, than when they correlate with Br atomic fragments .

5.2.5 Photofragment yield spectra (PhoFrY spectra)

The rotational state resolved PhoFrY spectra (also called Photofragment Excitation or PHOFEX spectra) of the NO fragment (Figure 47) were recorded by fixing the probe laser on one REMPI line and recording the ion signal upon scanning of the photoysis laser. Lines of each branch corresponding to various J" was selected. A "cut" through these spectra at constant energy is related to the rotational distribution at a particular wavelength. However, since the spectra were rescaled for the sake of clarity, the maximum and minimum in J" can only be determined qualitatively. The maxima of each PhoFrY spectrum or partial cross section indicate excitation energies at which formation of this state is favourable. The fact, that there may be two or more maxima in a PhoFrY spectrum show, that pathways at different energy may lead to the same preference of a NO fragment rovibrational state.

It appears as if the maxima of the partial cross section shift to low excitation energy as higher rotational states were probed. Finally, the asymmetric lineshapes of some PhoFrY spectra are characteristic for Fano-profiles, that arise, if a bound vibronic state is coupled to a continuum state. However, the PhoFrY spectra are rather poor due to our inability to correct for the power fluctuations of both laser simultanously. Therefore analysis of the Fano profiles is not very meaningful and only more accurate, future experiments in this

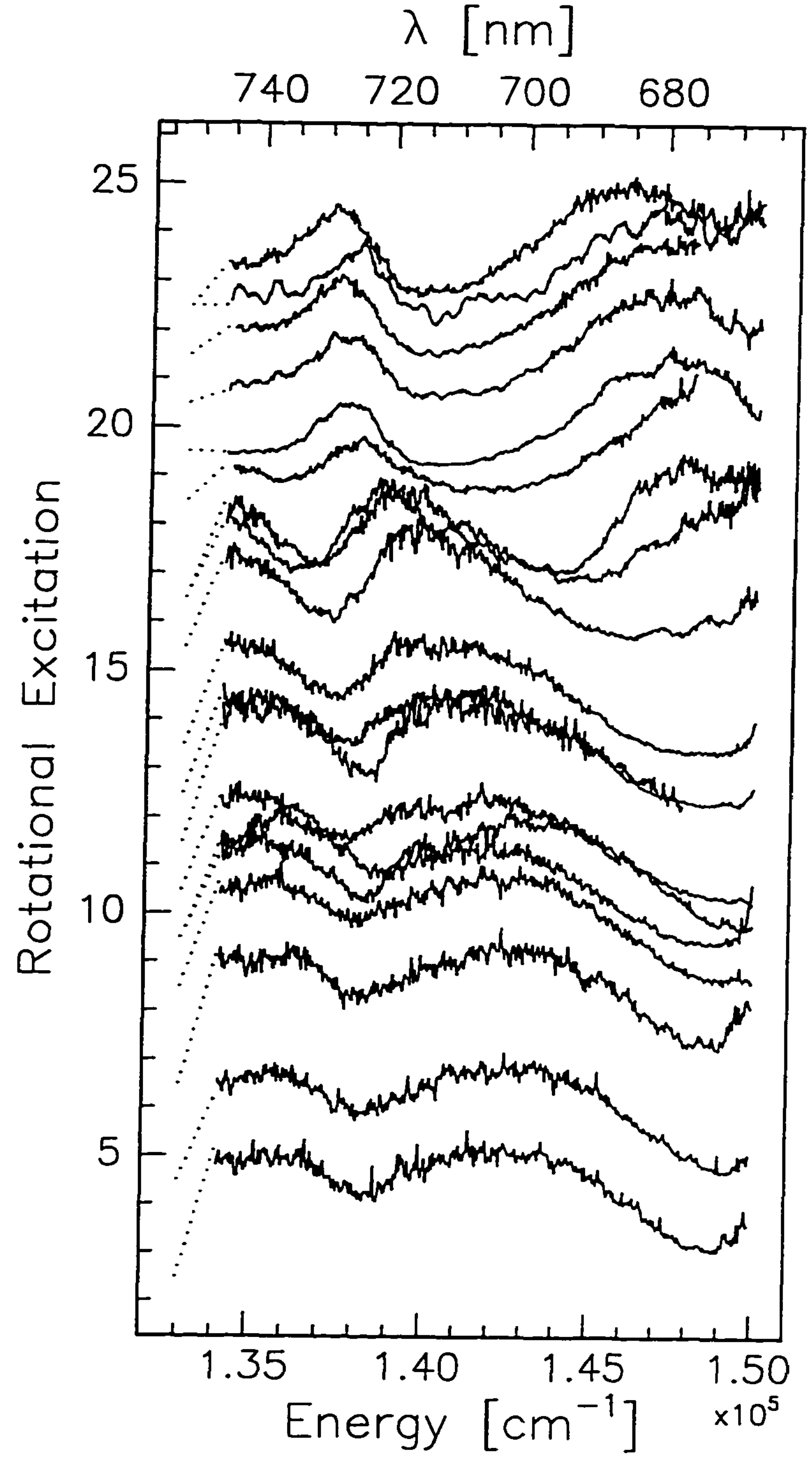

Figure 47: Photofragment yield spectra of NO between 670 nm and 740 nm. The rotational state resolved spectra have been rescaled. The dotted lines indicate the baseline for each state and the J" value.

wavelength region may be able to resolve this matter.

5.3 Discussion

The remainder of this chapter is dedicated to the discussion of the BrNO absorption spectrum and photodissociation experiments. Previous work on the ClNO *molecular orbitals* and absorption spectrum will be briefly reviewed and MO's of BrNO will be given in analogy to the MO's of ClNO. Comparison with the ClNO absorption spectrum allows for the *assignment of transitions* to the BrNO absorption bands. The BrNO absorption spectrum is dominated by *intensity borrowing* of the strongest singlet-singlet transition to lower lying transitions to triplet states. This effect and its consequences will be discussed in the third subsection. Using the arguments laid out in the introduction we are able to construct a diabatic *correlation diagram* for the present case of intermediate coupling in BrNO. This correlation diagram predicts a number of avoided crossings, which suggest non-adiabatic effects following excitation to some excited states.

Using this correlation diagram as a guideline the dissociation dynamics will be discussed in some detail for various states. The *photodissociation dynamics of the* S_5 *state* will be discussed first, followed by *photodissociation dynamics of the* T_1 *state*. The T_5 state is of special interest, since it shows two interesting dynamical phenomena. The *non-adiabatic dissociation dynamics of the* T_5 *state* have been predicted by the correlation diagram and will be discussed in some detail. We also observed an *interference effect* following excitation to the T_5 state and offer three explanations. The chapter ends with a brief *summary* of the experimental findings and interpretation.

5.3.1 Molecular orbitals

Crucial for the understanding of the experiments described in the previous chapter is an assignment of electronic transitions to the absorption bands. This assignment requires an -- at least approximate -- ordering of excited states. Since no *ab initio* calculations have been carried out on BrNO yet, one relies on comparison with ClNO. In the following the

MO's and electronic states of ClNO will therefore be briefly discussed and then compared to the states of BrNO.

The five ClNO frontier molecular orbitals involved in the UV and visible absorption (Figure 38) have been calculated previously(90) and a sketch is given in Figure 48. The molecular orbitals and the bonding can be expected to be similar in ClNO and BrNO, since the difference in energy of the MO's is partly compensated by the larger size of the Br-type orbitals. Analogous to the 14a" and 15a' MO's in ClNO, the two bromine dominated orbitals 23a" and 24a' will be nearly degenerate. Similarly the NO π^* type antibonding orbitals (26a" and 27a') will be close in energy. The MO-diagram shows the hypothetical case of a linear BrNO molecule, in which the NO π^*-type and Br p_x- and p_y-type orbitals are degenerate. The MO's are quite different in the case of FNO, where due to the better overlap and the large electron deficiency of the fluorine orbitals, a higher extent of charge transfer is present(22).

The strongest oscillator strength in the ClNO absorption spectrum is observed for the 16a' $\rightarrow$ 18a' transition due to its $\sigma \rightarrow \sigma^*$ character. This transition is responsible for the largest fraction of the ClNO A-band absorption. This transition can lend intensity to lower lying triplet states (the T_1 state in particular), which then absorb with transition dipole moments roughly parallel to the Cl-N bond. The near UV-band of ClNO (the "B-band") was assigned to a singlet state with parallel transition characteristics(11). This S_3 state is accessed through the 14a" $\rightarrow$ 17a" transition. A small contribution of the transition to the S_4 state (15a' $\rightarrow$ 18a'), which is expected to be much weaker, has recently been proposed(91).

The C and D bands in ClNO both arise from transitions to the first excited singlet state (16a' $\rightarrow$ 17a") and yield NO photofragments with v" = 1 and v" = 0, respectively. This transition is of perpendicular type ($\beta = -1$) and its assignment was supported by the spatial anisotropy and the observed NO (A") Λ-doublet preference(90).

Finally, the various weak peaks in the E-band between 660 nm and 500 nm were attributed to vibronic transitions to the first triplet-state of ClNO(68, 90). The bending and stretching vibrational substructure was explained as arising from a slow dissociation process in which

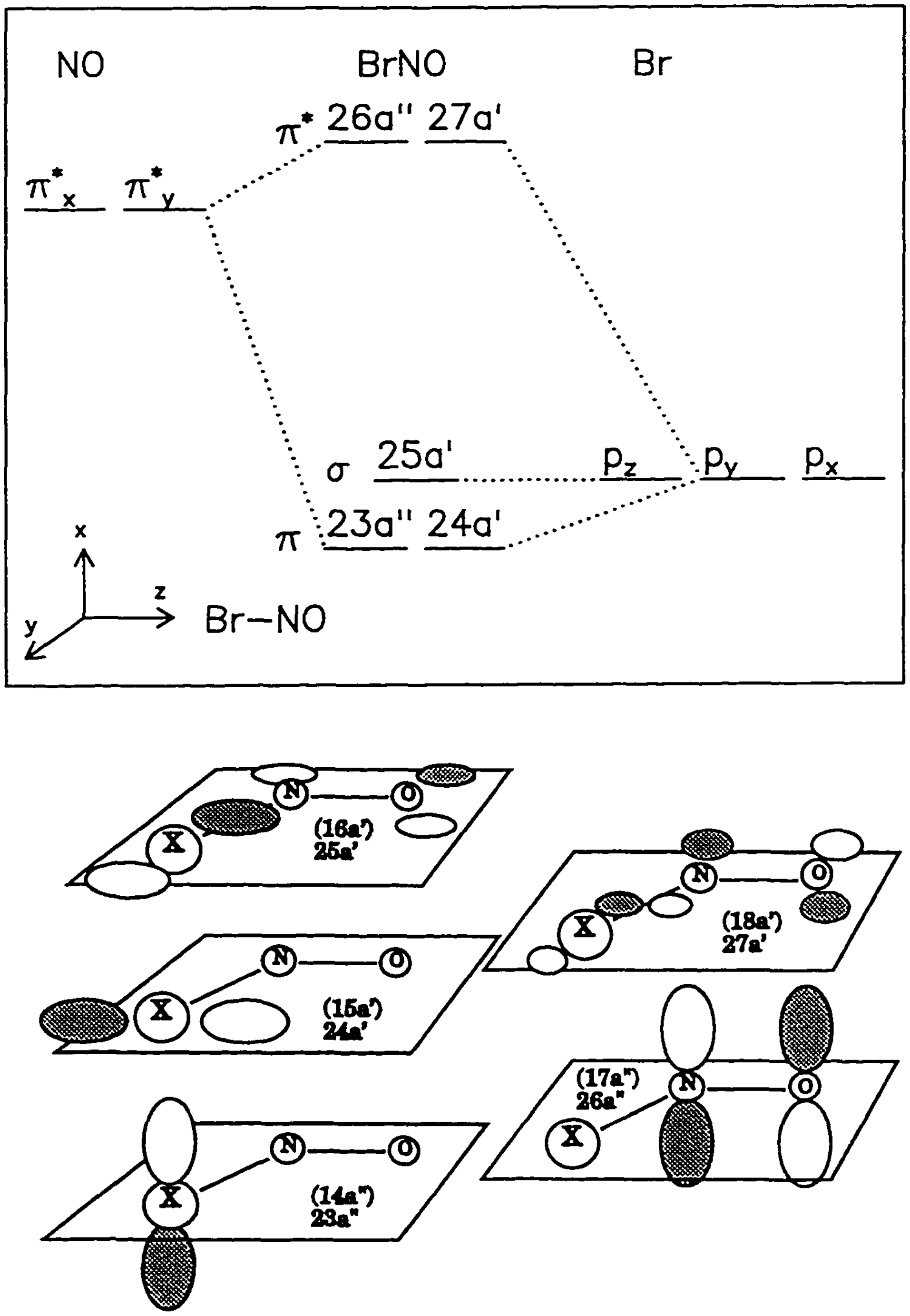

Figure 48: Molecular orbital diagram and molecular orbitals of BrNO. The MO's have been drawn in close analogy of the ClNO MO's (in brackets) given in reference 90.

the wavefunction was trapped in the transition region long enough to develop distinct bending-vibrational nodes(92).

As discussed above, we can assume that the MO's for ClNO and BrNO are similar. It is therefore proposed, that the ordering of excited states will be identical for both molecules. This order has been listed for ClNO in reference 11 and is for BrNO reproduced in Table 12. Also shown in this table are the position, width and maximum of the Gaussian fitting functions to the absorption spectrum, as well as spatial anisotropy parameters β and bromine branching ratios.

5.3.2 Assignment of transitions

In the following discussion the experimental results will be used to assign the bands in the absorption spectrum to distinct transitions. Particularly useful is the degree of electronic alignment of the NO photofragment. The electronic alignment is reflected by the ratio of the Λ-doublet state populations [Π(A")-Π(A')] / [Π(A")+Π(A')] at the different J and in the dependence of the NO fragment spin orbit state(44). The ratio of Λ-doublet state populations provides information about the MO's involved in the transition and the correlation of the molecular states to the fragment states. In a fast dissociation process the NO photofragments retain a memory of the parent molecular orbitals. Excitation into an (a") MO will lead to NO photofragments preferably in their Π (A") Λ-doublet states, which can then be probed via the Q-branches of the REMPI transitions. Similarly, excitation into an (a') MO will lead to NO photofragments preferably in their Π (A') Λ-doublet states, which can then be probed via the P- and R-branches of the REMPI transitions. This effect can be expected to be strong for high rotational excitation, since then the mixing between the (a') and (a") components will be weak(41).

The spatial anisotropy parameter contains information about the symmetry of the transition. The limiting values of $\beta = 2$ and $\beta = -1$ indicate, that the transition dipole moment of the transition in question is parallel or perpendicular to the dissociation coordinate, respectively. Due to the vibrational modification(93) it may deviate substantially from the

		ε [l / mol cm]	ΔE [cm^{-1}]	f	E [cm^{-1}]	$\langle T \vert H_{SO} \vert S_5 \rangle$ [cm^{-1}]	β	Br*/(Br+Br*)
S_5 ($4^1A'$)	27a'←25a'	37041	2253	0.64	46348	0	0.9 ± 0.3	0.9
S_4 ($3^1A'$)	27a'←24a'	see text						
S_3 ($2^1A'$)	26a"←23a"	7996	3663	0.22	44511	(1368)	1.2 ± 0.3	~0.9
T_5 ($3^3A'$)	27a'←24a'	155.2	6410	$7.61\ 10^{-3}$	29612	1794	1.7 ± 0.2	0.9
S_2 ($2^1A''$)	26a"←24a'	see text						
T_4 ($2^3A''$) T_3 ($2^3A'$)	26a"←24a' 26a"←23a"	53.6	3521	$1.45\ 10^{-3}$	22178	1144	1.5 ± 0.2	0.0
T_2 ($1^3A'$)	27a'←25a'	see text						
S_1 ($1^1A''$)	26a"←25a'	see text						
T_1 (I) ($1^3A''$)	26a"←25a'	3.1	477	$1.14\ 10^{-5}$	15757	129	1.5 ± 0.2	0.0
T_1 (II)		13.7	807	$8.48\ 10^{-5}$	13835	373	1.5 ± 0.2	0.0
S_0 ($1^1A'$)	$(25a')^2$							

Table 12: Electronic states of BrNO: Extinction coefficient, width and oscillator strength of the states has been obtained from a fit to the absorption spectrum.

limiting value of 2 even if μ and the initial direction of recoil, v, are parallel. However, this effect is small in BrNO due to the large mass of Br. The transitions will be assigned in order of decreasing energy.

The A-band absorption in the case of ClNO is caused by the transition of the "in plane" σ-type HOMO 16a' to the "in plane" anti-bonding σ-type orbital 18a'. In analogy, it is proposed, that the equivalent orbitals 25a' and 27a' are mainly responsible for the strong UV absorption of BrNO. The $S_0 \rightarrow S_5$ transition is of (A') character and has a large oscillator strength due to its $\sigma \rightarrow \sigma^*$ character. Because of the MO's involved, the transition dipole moment is expected to be roughly parallel to the Br-N-bond, and can be calculated to be between $1.85 < \beta < 2$, depending on whether the recoil is along the fragments center of mass or along the Br-N bond. Our experiments at around 225 nm detecting Br fragments or NO fragments yielded $\beta \sim 1$ and $\beta \sim 1.5$, respectively (Figure 41 and Figure 46). The fact that the limiting value is not reached can be explained by the large amount of excitation energy flowing into vibration as observed in our Br-TOF experiments (Table 11) and in the experiments of Moser *et al.*(94). The high internal excitation causes the excited state complex to dissociate slower, which in turn reduces the spatial anisotropy.

The presence of a second singlet state in the longer wavelength region of the UV band is indicated by the asymmetry of the UV band in the absorption spectrum. This second singlet state may be either the S_3 (23a" 26a") state or the weaker absorbing S_4 (24a' 27a'). The S_3 band in ClNO (the B-band) is quite pronounced and peaks at around 330 nm. Since the singlet-triplet splitting in BrNO is larger compared to ClNO due to the much stronger spin-orbit mixing (the smaller exchange integral can will reduce the effect of spin-orbit splitting only to a small exent), the S_3 state is lifted in energy and may be involved in the BrNO absorption at a wavelength shorter than 330 nm.

Recently Felder and Morley(91) have reported that the S_4 state is also present in the case of ClNO yielding Cl* and highly vibrationally excited NO fragments. The S_4 band, however, is hidden under the strong A-band absorption. From theoretical considerations(11) the oscillator strength is known to be rather small. We attempted to conduct photodissociation experiments probing NO at 266 nm, but, since a large number of NO rovibrational states is present, it was not possible to obtain accurate information. The TOF profiles of the bromine fragments at 266 nm yielded that $\beta = 1.2 \pm 0.3$ (Figure 46). One would expect β being close to 2 for the transition to S_3, because the transition dipole moment is almost parallel to the BrN bond in a 26a" $\leftarrow$ 23a" transition. For the transition to S_4 (27a' $\leftarrow$ 24a'), on the other hand, the transition dipole moment may be in an angle to the recoil direction, so that positive values much lower than 2 are possible. Unfortunately, the high spatial anisotropy does eliminate neither the S_3 nor the S_4 state as possible candidates. However, the $S_4 \leftarrow S_0$ transition has only low oscillator strength. In conclusion, the long wavelength shoulder of the UV band can, based on these theoretical considerations, be preliminarily assigned to the transition to the S_3 state. Future experiments in this wavelength region may help to clarify this matter.

At none of the wavelengths longer than 300 nm did we observe a spatial anisotropy parameter of $\beta < 1.5$. This shows that the absorption of the lower lying singlet states S_1 and S_2, to which the transitions must have perpendicular character ($\beta = -1$), is neglegible compared to the triplet states in this region. In the following we will therefore concentrate on triplet states.

The transition at 355 nm is assigned to $T_5 \leftarrow S_0$ excitation. The observed preference for the NO(A') Λ-doublet state is only consistent with the proposed 24a' to 27a' transition. Spatial anisotropy parameters of $\beta \sim 1.7$ and the oscillator strength indicate intensity borrowing from the A-band due to the bromine spin-orbit interaction. The preference for the (A') Λ-doublet state cannot be explained, if one assumes transition to the S_3 state or T_4 state at this wavelength (Table 12). The S_4 state can also be discarded, because of the higher excitation energy associated with it. The rotational distribution at 355 nm peaks at J" = 54.5 and has a width of approximately ΔJ" = 10 (Figure 39). The narrow width hints that excitation to only *one* excited state takes place. The onset of the production of Br fragments in their spin orbit ground state correlated to NO fragments in high rotational states is therefore attributed to non-adiabatic interactions between this T_5 state and a higher electronic state. This is more likely than a similtaneously excited electronic state associated with a slightly higher rotational excitation and correlation to Br ($^2P_{3/2}$) fragments. The non-adiabatic interactions and the topology of the T_5 state are discussed in some detail below. The rotational distribution (Figure 39) and TOF profiles (Figure 41) at 532 nm can be explained by the transition to T_4 and/or T_3. The resulting configuration 24a'26a" or 23a'26a" explains the NO(A") Λ-doublet preference well. Again, both states can borrow intensity via Br spin-orbit coupling from the A-band. At the present time we are not able to distinguish between the contributions from T_3 and T_4.

The two absorption peaks at the longest wavelengths (635 nm and 720 nm) can be attributed to the transition to the lowest lying triplet state T_1. The separation of their maxima by 1920 cm^{-1} corresponds to different NO-stretching states of the parent molecule as will be discussed later in detail. These long wavelength bands correspond to the E-bands of ClNO, which show a very similar broad bending vibrational substructure (Figure 38). The dissociation from BrNO bands is also direct and yields NO fragments of v" = 1 and v" = 0 depending on the excitation wavelength. This is a consequence of the small NO equilibrium distance mismatch between free NO and the BrNO T_1 state in the Franck-Condon region(92). As in the case of ClNO, the dissociation proceeds mainly adiabatically with respect to the NO stretch in BrNO, so that the amount of vibrational quanta is conserved in the dissociation process. At these excitation wavelenghts energetically only formation of Br($^2P_{3/2}$) photofragments is possible.

The above assignment of states is based on the assumption that each maximum of the Gaussian fitting functions to the absorption represents a transition to a single electronic state. While this concept has proven successful in describing and assigning the states, it can certainly not be excluded that weaker transitions to other states were buried by the stronger absorption of the assigned states. So was no contribution of the S_1, S_2 and T_2 states found. It may come not as any surprise that the S_2 state is absent, since its oscillator strength is expected to be very weak and the state was also not observed in the ClNO absorption spectrum. However, absence of the S_1 state, the state which causes the C and D band in ClNO does come as surprise. This state, which was only weakly absorbing in ClNO may be hidden under the strong band of the T_3/T_4 state. .

The fate of the T_2 state is also unknown. We note that the T_2 state arises from the same 27a' 25a' configuration as the S_5 state, from which all other states were able to borrow intensity. The spin-orbit operator is able to effectively mix a singlet and triplet state that arise from the same configuration(3). If the two states are energetically remote, however, the transition to the T_2 state may not be able to borrow much intensity from the transition to S_5 and stays spin-forbidden.

5.3.3 Intensity borrowing

More than in ClNO, the absorption spectrum of BrNO is marked by intensity borrowing of UV-transition oscillator strength to lower lying triplet states. The extent of intensity borrowing can be estimated from the intensity of the absorption bands using first order perturbation theory. In this way the oscillator strength of the triplet states can be related to the oscillator strength of the borrowing singlet state(3)

$$f_T = C_T^2 \cdot f_S \tag{81}$$

with

$$C_T = \frac{\langle T|H_{SO}|S\rangle}{(E_S - E_T)} \tag{82}$$

The oscillator strength of the electronic states of BrNO (Table 12) is estimated using the integral of the Gaussian fitting functions of the absorption spectrum. Using this number the matrix element $|\langle T_i|H_{SO}|S_5\rangle|$ has been calculated for the transitions to triplet states and has been listed in Table 12. It is obvious that the high lying triplet states owe much of their intensity to the coupling to the UV state *via* the bromine spin-orbit term. This explains why these states are not visible in the ClNO absorption spectrum. Since the mixing by the chlorine spin-orbit coupling is approximately four times weaker, the triplet states are hidden under the stronger B, C and D band. The lowest triplet state T_1 has a coupling matrix element of 200 cm^{-1} in BrNO compared to 150 cm^{-1} in ClNO (estimated from Table 2 in ref. 11). This similarity suggests that for both molecules the same type of intensity borrowing is responsible in this spectral region.

With the MOs and ordering of the excited states of ClNO as a guideline, the excited states of BrNO are given in Table 12. The splitting between singlet and triplet states of the same configuration depends on the magnitude of the exchange integral and is therefore stronger for σ-type orbitals compared to π-type orbitals. Note, that the larger splitting between singlets and triplets of the same configuration in BrNO compared to ClNO may lead to reversal of the order of S_1 and T_2 and /or S_2 and T_5.

5.3.4 Correlation diagram

From the above discussion, it appears that the BrNO molecule has been a fortunate choice for our studies on non-adiabatic dissociation dynamics. There are very few simple molecular systems which exhibit several repulsive states in the easily accessible visible region of the spectrum. All states show different characteristics, and most of them are perturbed triplet states, as indicated by the large intensity borrowing term. In order to obtain an overview of the various interactions we constructed a diabatic correlation diagram. This diagram is based on first principles but owes much of its existence to comparison with published ClNO correlation diagrams(39). The correlation diagram will aid an understanding of the bromine finestructure branching ratios at the various excitation wavelengths and will prove useful in an understanding of the non-adiabatic interactions, that were observed at wavelengths close to 355 nm. However, it should be kept in mind that the diabatic correlation diagram, as presented, is an idealized construct. In the discussion of the dissociation theory of Singer, Freed and Band(73) in section 4.3.7 it was pointed out, that for most molecular states there is not a single fragment channel that forms the "diabatic limit" in the axial recoil limit, but rather a linear combination of two or more fragment channels with varying contributions.

The ClNO correlation diagram is dominated by *weak coupling* in the region of large fragment separation (the "recoupling region"). Since the kinetic energy of the dissociating molecule is small in the parent molecular region non-adiabatic interactions are of less importance compared to the region of larger separation(39). Only in the recoupling region the kinetic energy will be of comparable magnitude to the splitting between the adiabatic states.

The situation is different for the *intermediate coupling* case of BrNO. Here spin-orbit coupling is stronger and distinction of parent molecular region and fragment region is not suitable. Even in the parent region there are no good spin and orbital quantum numbers and the states are mixed. Since spin and orbital wavefunctions are mixed, the symmetries of the combined orbital and spin wavefunctions become important. Only states with the same symmetry (A' or A" in the C_s point group) will mix and have non-adiabatic couplings among them. This is due to the A' symmetry of the spin-orbit operator.

In the free fragment region there is no interaction among the photofragments. However, the dissociation process has left "memories" in the photofragments. In the asymptotic limit one uses the products of the fragment wave functions expressed in the same point group as the parent molecule and conserves symmetry of the combined spin-orbit wave functions. For instance, for a correlation diagram of a linear molecule, one should carry out j-j coupling among the photofragments and then use the Ω values to arrange the product wavefunctions. Only products with the same Ω will mix. Similarly, in the case of a bent triatomic molecule the products of wave functions with A' and A" total symmetry will mix separately.

There are three steps involved in establishing a correlation diagram for the intermediate and strong coupling case:

(i) determining the order of all relevant electronic states in the parent molecular region and specifying their symmetry.

(ii) determining the order of the electronic states at large internuclear distance.

(iii) classifying the symmetry of the product of the of the spin-orbit wave functions of the fragments in the parent molecular point group.

As described in the previous sections we can assign the absorption spectrum of BrNO by assuming that the order of the excited states is the same as in ClNO. This is a direct consequence from the similarity of their MO's. This order is reproduced in Table 12 and on the left hand side of Figure 49. From group theory considerations (see Herzberg ref. 41, app II, table 56), it is known that the *spin* functions of singlet states have A' symmetry, whereas the triplet spin functions can be resolved into A'+2A" functions in the C_s point group. Multiplication with the *orbital* wavefunction of that state allows one to obtain the A' and A" states on the parent side.

Upon increase of **R** the relative energy of the electronic states changes. The S_5 state and the T_2 state are derived from the 27a' 25a' configuration. Because of the large overlap of the orbitals involved, there is a large exchange integral and consequently a large singlet-triplet splitting near the Franck-Condon region. In the region of large **R** the exchange integral and therefore the singlet-triplet splitting are reduced. Thus, the S_5 states energy decreases rapidly with increasing internuclear distance and an avoided crossing with the less drastically decaying S_4 (27a' 24a') state results early on the dissociation coordinate. For ClNO, a similar argument led to an avoided crossing of the respective states.

The fragment side was also resolved into A' and A" components. Both fragments are in doublet states. The Br ($^2P_{3/2}$) state splits into (2A'+2A") components, whereas the Br* ($^2P_{1/2}$), the NO*($^2\Pi_{3/2}$) and the NO($^2\Pi_{1/2}$) states each split into (A'+A") components. Multiplication leads to (4A'+4A") components for the two lower exit channels and (2A'+2A") for the two higher channels. In the region of intermediate **R** configuration interaction and spin-orbit coupling will mix and separate states with the same A' or A" symmetry upon decrease of **R**. In a diabatic picture ("weak coupling case") the states with the same (A' or A") symmetry are allowed to cross and a correlation diagram based on these premises was constructed. To avoid congestion the correlation diagram for the A' states and the A" states is shown separately in Figure 49. In a more realistic "intermediate

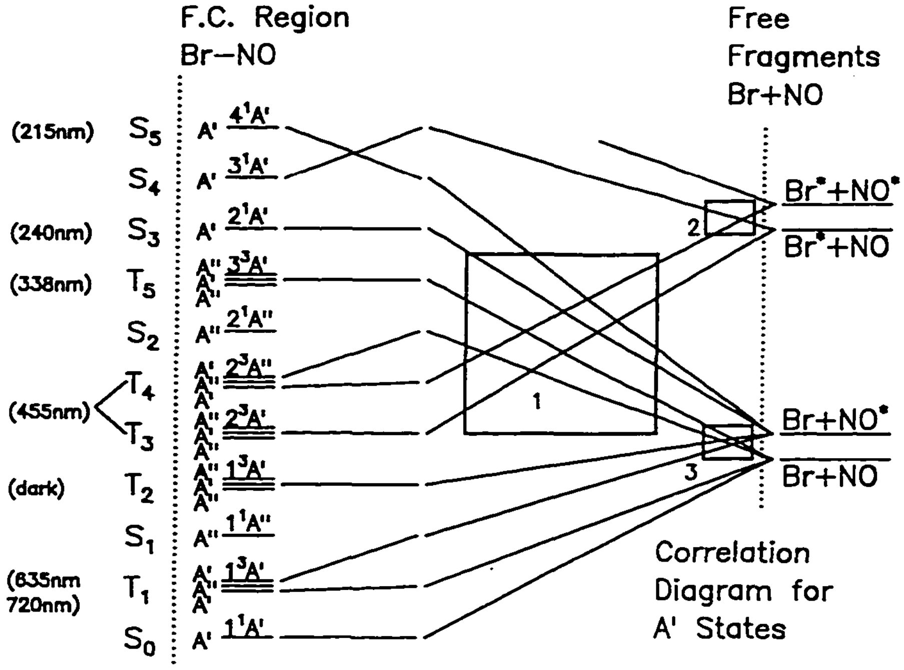

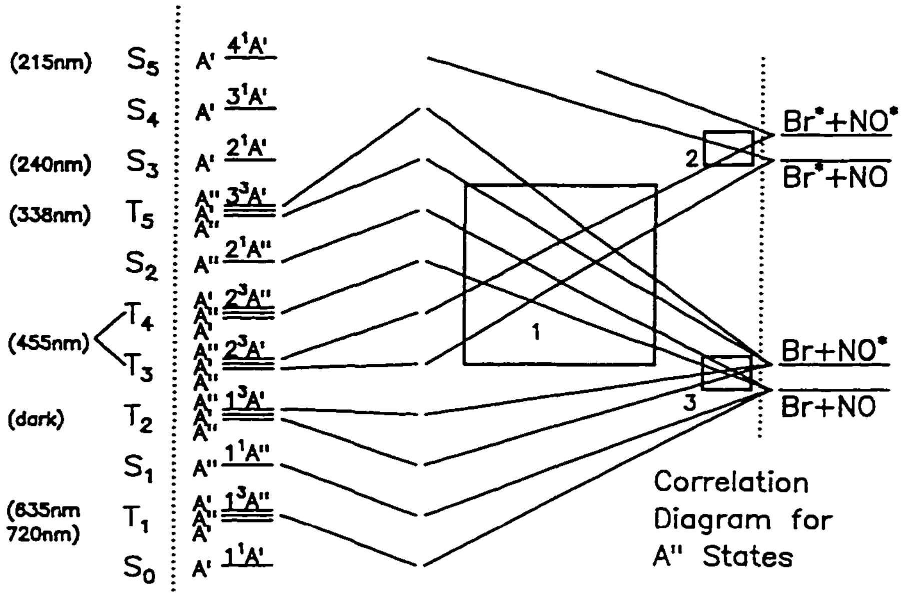

Figure 49: Diabatic correlation diagrams for BrNO. The A' states and A" states are shown separately. The boxes indicate the regions were non-adiabatic interactions can be expected.

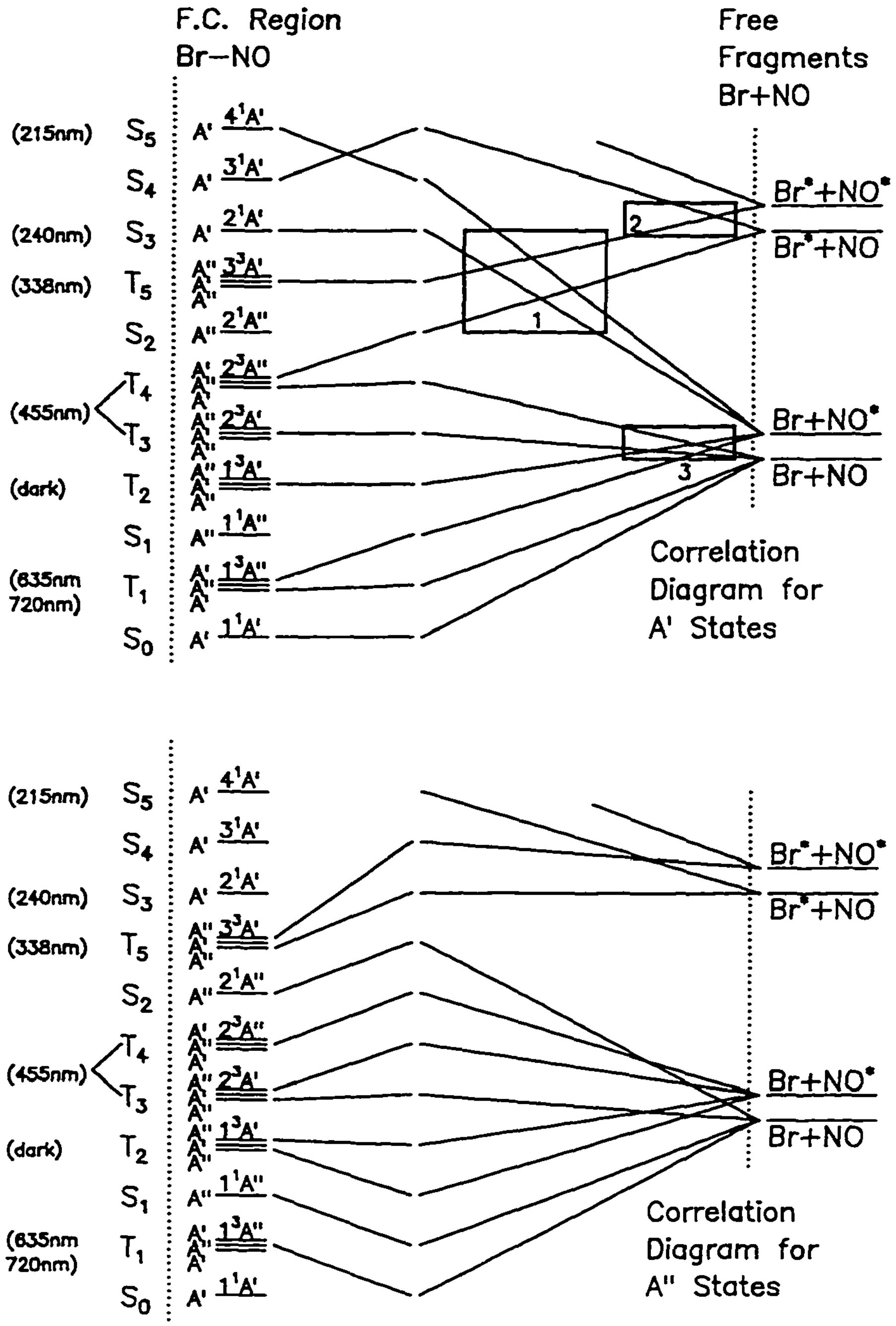

Figure 50: Diabatic correlation diagrams for BrNO. It was assumed, that interactions between singlet states and between triplet states lead to large avoided crossings.

coupling" case the interaction region (box 1) will be close to the Franck-Condon region. To construct a diabatic correlation diagram, i.e., with zero spin-orbit interaction, configuration interaction (CI) between states of the same multiplicity and the same symmetry has to be considered first. The CI will cause strong avoided crossings between singlet and between triplet states of the same symmetry. BrNO correlation diagrams allowing for strong triplet-triplet and singlet-singlet interactions are displayed in Figure 50. These diagrams are different from the ClNO correlation diagrams, where the avoided crossings were treated as small, regardless of the multiplicity of the interacting states. The triplet-triplet interactions close to the Br+NO* and Br+NO exit channels were exempted from these avoided crossings, since in this region the CI is small.

As mentioned above, none of the strong absorbing states has A" symmetry. Hence, in the following discussion we will focus on the upper diagram in Figure 50, the diabatic correlation diagram of the A' states.

There are three regions were A' states cross, labelled 1, 2 and 3 in the figures. Interactions in box 2 and 3 are dominated by the small NO spin-orbit coupling term and it can be expected that at this large internuclear distance (high kinetic energy) the dissociation process proceeds largely diabatic. At shorter internuclear distance, however, the interaction terms are dominated by the CI and spin-orbit coupling term of the bromine atom and large avoided crossings result for states with the same multiplicity. For singlet-triplet crossings the interaction will be somewhat smaller, but still comparable to the nuclear kinetic energy in this region. It is in this region, where extensive non-adiabatic interactions can be expected. Close to the FC-region we propose another avoided crossing of the S_5 state with the S_4 state. Dissociation in this region can be expected to be largely adiabatic due to the large gap between the adiabatic states and the relatively small nuclear kinetic energy.

5.3.5 Photodissociation dynamics of the S_5 state

The strong, broad absorption band peaking around 215 nm in BrNO corresponds to the A-band in the ClNO absorption spectrum. It was attributed to the 27a'←25a' transition. This $\sigma^*\leftarrow\sigma$ type transition is fully allowed and for ClNO an oscillator strength of unity has been calculated(11), whereas the observed oscillator strengths are f = 0.5 for ClNO, and f = 0.64 for BrNO (Table 12). The dipole moment is expected to be aligned roughly parallel to the Br-N bond resulting in a large spatial anisotropy parameter. As described above and illustrated in Figure 41 and Figure 46, $\beta \approx 1$ has been found experimentally.

According to the correlation diagram, the S_5 state experiences an early avoided crossing with the lower lying S_4 state. Adiabatic passage through this interaction region will preferentially lead to formation of spin-orbit excited atomic fragments, whereas $Br(^2P_{3/2})$ is formed following a diabatic process. An adiabatic process is expected, because of the strong interaction between two nearly parallel surfaces and the relatively small kinetic energy early in the dissociation coordinate. The formation of ~90% of the bromine fragments in their spin-orbit excited state is strong experimental confirmation of this picture.

Our experiments on the S_5 state photodissociation dynamics of BrNO are rather indirect. The vibrational distribution was estimated using the width and the rising time of the TOF profile of the bromine atomic fragment. For the dominant Br* channel a vibrational distribution of v" = 9 ± 2 was obtained following excitation at around 225 nm, in fair agreement with v" = 9 ± 5 at 193 nm of reference 94.

The high vibrational excitation of the NO photofragment has been subject to a number of theoretical studies. In 1961, Basco and Norrish(85) found, that the vibrational excitation of v" = 11, which they observed in flash photolysis of ClNO at around 200 nm, could not sufficiently be explained by a simple impulsive model. The impulsive model predicts that the excess energy is funneled into repulsion along the dissociation coordinate, thereby exerting a torque on the NO moiety and compressing the N-O bond. Instead, Basco *et al.* considered vibrational predissociation of a long lived complex, which has been locally excited in the N-O bond. Based on the narrow vibrational distribution and the large spatial anisotropy parameter, we can today exclude the possibility of such a mechanism of internal vibrational redistribution.

In 1967 Mitchell and Simons(95), proposed that excitation at UV-wavelengths promotes an electron from a N-O bonding MO into an N-O antibonding orbital, thereby reducing the bond order from approximately 2.5 to 1.5. The consequent elongation of the N-O bond from 1.14 Å to 1.33 Å combined with a fast and direct dissociation would suffice for the observed vibrational excitation. However, using the most recent *ab initio* calculations of the ClNO molecular orbitals, such a dramatic change of the N-O bond order can no longer be justified.

Using IR-emission following UV excitation, Moser *et al.*(94) investigated the photodissociation dynamics of both ClNO and BrNO, at 193 nm, 248 nm and 308 nm. Interestingly, the vibrational distributions were found to be nearly identical for the two molecules within the experimental error. While the NO fragment was detected in high vibrational states ($v''=9\pm5$ at 193 nm), these workers found only relatively low rotational excitation ($T_{rot} < 600$ K). The reported rotational temperature was an estimate based on the variation of the emission signal with emission wavelengths around the peak of the vibrational distribution. Later Huber and coworkers(96) found that the vibrational distribution in ClNO is bimodal (with $v_1'' = 15 \pm 12$; $\beta_1 = 0.45$ and $v_2'' = 15 \pm 4$; $\beta_2 = 0.95$), and suggested that each distribution correlates separately to the two spin-orbit states of the corresponding chlorine photofragment. This picture was confirmed by Kim *et al.*(97) in a REMPI study on the chlorine photofragments. The Cl*/(Cl+Cl*) branching ratio at 236 nm was determined to be $\gamma = 0.67$, whereas Chichinin(98) obtained $\gamma \approx 1.0$ at 248 nm using time resolved laser magnetic resonance. Most recently Cao *et al.*(39), using a new ClNO correlation diagram, claimed that the adiabatic and diabatic dissociation pathways at the avoided crossing of S_5 with S_4 give rise to different vibrational distributions, that lead in turn to the observed total bimodal distribution.

Contrarily, Felder and Morley(91) argued, that at lower excitation energy (248 nm) both S_4 and S_5, potential energy surfaces may be populated and implied, that dissociation on both PES proceeds adiabatically. This picture explains the different spatial anisotropy parameter associated with the two vibrational distributions.

Our experimental results confirm the similarity between ClNO and BrNO. We found, that the vibrational distribution is slightly different for the adiabatic Br*-channel and the diabatic Br-channel, leading to a higher vibrational excitation and lower spatial anisotropy for the Br-channel. That this channel is much less important in BrNO photolysis (Br*/(Br+Br*) = 0.90 at ~225 nm) compared to ClNO photolysis at 236 nm, is understood from the 4-fold larger interaction term acting between the S_5 and S_4 state. A dissociation process initiated on the S_5 state will very likely proceed adiabatically. Thus our experiments can be considered a confirmation of the non-adiabatic mechanism proposed by Cao *et al.*(99) and their correlation diagram. Application of the same principles that led to the ClNO correlation diagram, allowed for an in depth understanding of the BrNO UV-band dissociation dynamics.

The origin of the vibrational excitation, however, remains unclear. Since excitation from the 25a' to 27a' MO does not change the N-O bond significantly, simple bond-order arguments do not suffice. Clearly a reliable *ab initio* calculation would be helpful in understanding, whether the physical origin of the vibrational excitation is a strong mismatch between ground state and excited state N-O bond length, or is of dynamical nature.

5.3.6 Photodissociation dynamics of the T_1 state

The absorption bands centred around 630 nm and 720 nm are attributed to excitation to the lowest lying triplet state T_1. The maxima are separated by approximately 1920 cm^{-1}, which suggests, that two vibrational adiabats, which are shifted in energy by the equivalent of one NO stretching quantum, can be excited (Figure 51). This is confirmed by the fact that excitation to the higher PES yields exclusively NO (v''=1), whereas excitation at around 720 nm yields NO (v"=0). Higher vibrational adiabats may be present but hidden under the stronger T_3/T_4 absorption band. Both PES have in common that they yield a multimodal rotational distribution with a strong wavelength dependence of the relative intensity of the rotational states (Figure 39). In order to be able to explain this wavelength dependence, we recorded a number of photofragment yield (PhoFrY) spectra for different rotational states in the region 680 nm - 740 nm (Figure 47).

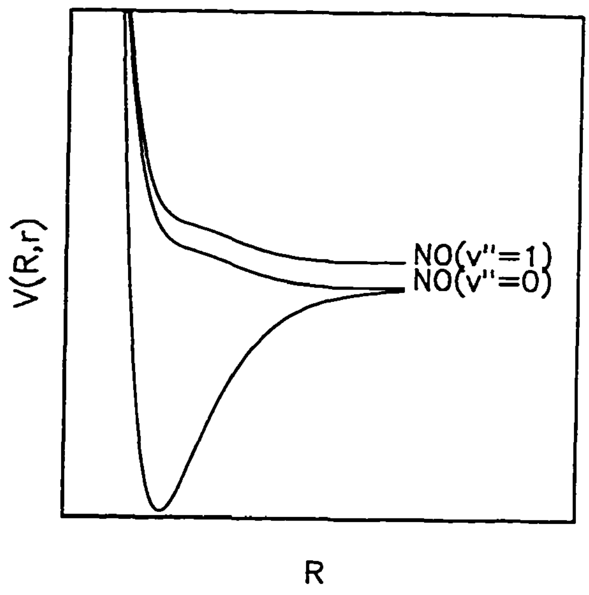

Figure 51: Sketch of the two vibrational adiabats of the T_1 state

Three interesting features of those spectra may be noted:

(i) there are up to three maxima present for one rotational state

(ii) the line shapes are asymmetric

(iii) The maxima of the PhoFrY spectra shift to lower excitation energy for higher rotational states.

The first two points can be explained using a model of the T_1 surface, similar to the well known T_1 state of ClNO. The last point, however, requires some speculation and shall be discussed last.

The T_1 state of ClNO has two bands at ~600 nm and ~550 nm that correspond to excitation of the NO stretching mode within the T_1 complex. Each vibrational band is furthermore split into three subpeaks, which were assigned to excitations of 0, 1 or 2 quanta in the bending mode.

Photofragment yield spectra(11) have confirmed these assignments by showing that NO fragments have zero or one vibrational quanta for excitations via the 600 nm or 550 nm band, respectively. Furthermore rotational distributions were recorded near the maxima of the subpeaks. These distributions are substantially different for the various "bending subpeaks"(11). This phenomenon has been quantified in various ways. Reisler and Qian(11) proposed a modified Franck-Condon model, that accounts for both the inclusion of the angular momentum that arises from the parent bending motion and exit channel interactions. In this model, the number of nodes in the bending wavefunction determine the number of minima in the rotational distribution. Later Sölter *et al.*(92) calculated the PES using various *ab initio* approaches and performed a wave packet propagation calculation on this PES. The results of this quantum mechanical treatment were then compared to the predictions from rotational reflection principle(9) and qualitative agreement was found.

The most interesting feature of the T_1 state of ClNO is its flatness in the Franck-Condon region. The dissociation process is sufficiently slow to allow the excited state wave packet to develop a NO stretch and a bending wave function. As the dissociation coordinate, R, increases the bending potential opens and the maxima of the bending wavefunction translate into maxima of the rotational state population. The rotational distributions also indicate that the PES exerts a small torque on the dissociating NO moiety leading to a slight preference of bending angle opening over angle closing.

Most of the characteristics of the ClNO T_1 state can be easily recognized in the T_1 state of BrNO. We have observed two vibrational adiabats separated in energy by 1920 cm^{-1}. The subpeaks associated with the different bending quantum states have not been resolved in the absorption spectrum but overlap of the bending states may be responsible for the fact that both absorption bands are non-Gaussian (Figure 37). The multimodal rotational distribution, however, was observed and indicates that as in the case of ClNO the dissociation proceeds very slowly and the bending wavefunction is well developed in the FC-region (Figure 52).

In the time-independent picture, the dissociation process can be viewed as the decomposition of a (quasi-) bound state via a continuum - a process which has much in common with predissociation dynamics. Bound states that are strongly coupled to a

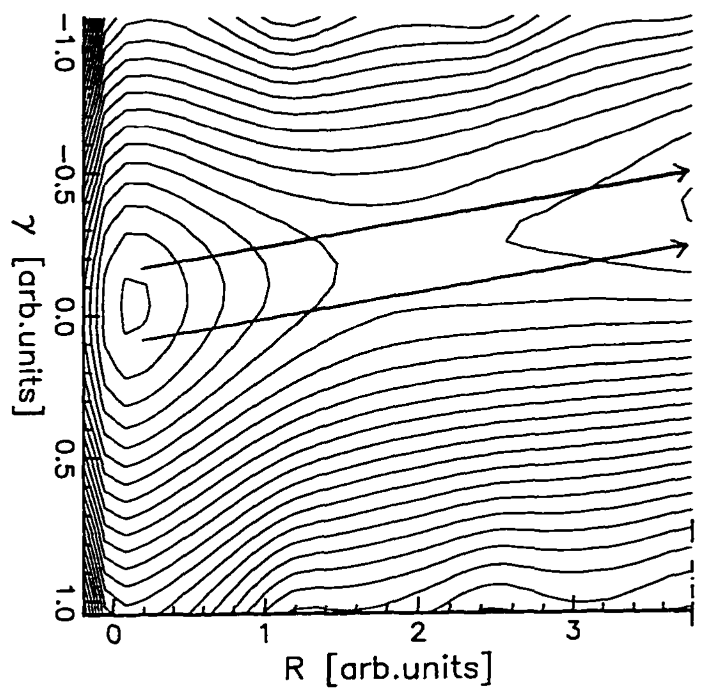

Figure 52: Schematic contour plot of the T_1 state. The arrows indicate the trajectory that leads to the bimodal rotational distribution.

continuum exhibit asymmetric lineshapes in the absorption spectrum. As Brandon *et al.*[41] noted, we may understand Fano profiles in the *time-dependent* picture as a consequence of excitation to a weakly bound or quasibound state. The excited state wavepacket splits into a part that is temporarily trapped in the excited state and a part that exits directly on the repulsive side of the barrier. Interferences between these two parts are the origin for the observed asymmetric lineshapes.

The photofragment yield spectra in Figure 47 can be regarded as such state specific absorption spectra and, as shown, some of the lines display these asymmetric or Fano-lineshapes. It has been demonstrated in the case of the S_1 state of FNO -- which also shows Fano profiles in the absorption spectrum -- that one can reliably reconstruct a PES from these asymmetric lines(100). This attempt was not made for the BrNO T_1 state, because the signal has been very weak for most of the PhoFrY spectra and therefore not suitable for quantitative analysis. However, Fano-type lineshapes are interesting in dissociation and provide, through their sheer existance, valuable information about the excited state.

It is inviting to compare the topology of the T_1 state of ClNO and BrNO with the S_1 state of FNO. While the latter gives a prototypical example of an indirect dissociation process, the processes on the T_1 states are intermediates between direct and indirect dissociation. The stronger overlapping "bending bands", which were resolved in the ClNO absorption spectrum but not in the BrNO spectrum indicate, furthermore, that the fragmentation is faster in BrNO and the bending component of the excited state wavefunctions not as well developed.

Clearly more experiments are desirable in this spectral region preferably with a better signal to noise ratio and laser power correction for both the pump and the probe laser. These experiments may help to decide, whether the line profiles of the PhoFrY spectra are indeed asymmetric and from which bending states they arise. Finally, a quantitative analysis may yield the topology of the T_1 state and confirm or disprove the existance of the shallow well shown in Figure 52.

Rotational state resolved PhoFrY spectra were not recorded for the T_1 state of ClNO. However, Sölter *et al.*(92) calculated the rotational state resolved partial cross section from their *ab initio* PESs. These workers observed a shift of the maxima in the PhoFrY spectra to high energy with increasing rotational excitation of the NO fragment. This shift was attributed to energy conservation and the centrifugal potential in the Hamiltonian $\hbar J'(J'+1)/2\mu R$, which increases approximately quadratically with J'. Our PhoFrY spectra, on the other hand, indicate a shift towards *lower* energy with increasing J. Since no *ab initio* calculation of T_1 state of BrNO exists, we can only speculate about the physical origin of this effect. Considering the relative flatness in the bending coordinate, one can propose, that with increasing excitation energy, the FC-region shifts from a point near the bottom of the well, but on the slope of the bending coordinate, to shorter internuclear distance, and thereby to a region of the PES, which is dominated by a steeper slope in the **R** coordinate. In this picture the dissociation would be dominated by a weak bending anisotropy at low excitation energy, and by a combination of this torque and repulsion along the **R** coordinate at higher excitation energy. Since the process at high excitation energy is less sensitive to the anisotropy in the bending potential, the rotational excitation will be lower.

5.3.7 Non-adiabatic photodissociation dynamics of the T_5 state

Figure 39 shows that the NO rotational distribution following excitation at 355 nm favours the formation of NO spin-orbit excited fragments. The width of the TOF profiles indicates that most of the NO photofragments correlate with spin-orbit excited bromine atomic fragments. Following excitation to the T_5 state, the dissociation process therefore favours the Br* + NO* exit channel. Consultation of the correlation diagram (Figure 50) reveals that this channel is the diabatic limit of the T_5 state and that mixing with the S_3 and S_4 state may be important early in the dissociation process. The fact that the Br*+NO* channel dominates over the other fragmentation pathways, suggests that the dissociation at this wavelength is to a large extent diabatic.

However, the Br/Br* branching ratio as a function of the NO rotational level shows, that non-adiabatic interactions are present in the dissociation process (Figure 42 and Figure 44). As J" increases from 55.5 to 61.5 one sees a clear transition from diabatic dissociation yielding Br* fragments to a adiabatic dissociation yielding Br fragments.

Alternatively, one may consider the involvement of a second excited state, which is excited simultaneously with the T_5 state and correlates to one of the two Br-channels. This explanation, however, does not agree with the strong preference for the NO(A') Λ-doublet state, that is observed for both Br and Br* channels. The experiments at longer wavelength (410 nm and 470 nm) also showed that the onset of the lower lying T_4/T_3 state (Figure 37 and Figure 39) does not coincide with the onset of the Br-channel (Figure 44).

The Λ-doublet population ratio of the NO and NO* states, which was derived from the (P,R-branch)/(Q-branch) intensities, yields information about the parent molecular orbitals involved in the transition. The observed ratio of 12.4 (at J"=52.5), in case of the NO* states, corresponds to the maximum value of the degree of electronic alignment (DEA=0.86), that one would expect, if a pure (A') fragment orbital was involved. This together with the fact that the rotational distribution is quite narrow, further indicates that only a single excited state is excited at 355 nm.

In this context one can now categorize the photodissociation experiments of Ticktin *et al.*(101), which were carried out at 450 nm when probing NO(v"=0), and at 470 nm when probing NO(v" = 1). In both experiments the T_3/T_4 state was excited, but Ticktin *et al.* noted, that at 450 nm a shoulder in the rotational distribution appears. This shoulder was contributed to either non-adiabatic effects following dissociation on one excited state, or simultanous excitation of more than one PES. In the light of our experiments we propose, that at 450 nm comparable contributions of excitation to both the T_3/T_4 state and the T_5 are found. The non-adiabatic effect - although present at shorter wavelength - will be of minor importance at 450 nm.

The correlation diagram (Figure 50) provides additional information about the T_5 state and the dissociation dynamics. It can be seen, that it is one of the A' components of the T_5 state, that borrows intensity from the S_5 state and, hence, determines the parallel transition characteristics. This triplet state crosses two (A') singlet states, S_3 and S_5, at moderate internuclear distance (box 1 in Figure 50). These avoided crossings lead to the non-adiabatic interactions discussed above. The singlet-triplet interaction may well be of the order of a few hundred wavenumbers and is certainly localized early in the reaction coordinate. The correlation diagram also predicts an avoided crossing of the T_5 state with another A' state at large internuclear distance (box 2 in Figure 50). Non-adiabatic dissociation at this crossing yields Br*+ NO*, whereas adiabatic passage yields Br* + NO. Since the spin-orbit coupling constant of NO (A = 123 cm^{-1}) is much smaller than that of bromine (A = 3685 cm^{-1}), the adiabatic PESs, which are interacting, are very close. The

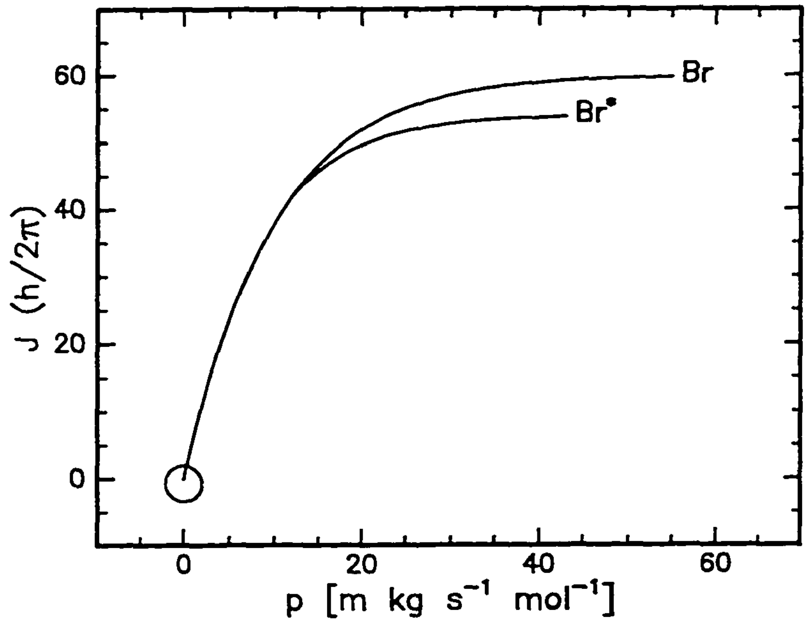

Figure 53: Following excitation to the T_5 state rotational angular momentum is established before linear momentum.

non-adiabatic interaction, that is responsible for the production of the observed 20% NO ($^2\Pi_{1/2}$), must consequently be nonlocal and weak.

In what follows, the non-adiabatic interaction and its implications on the topology of the T_5 excited state will be discussed in some detail.

A simple one-dimensional Landau-Zener calculation is used to estimate the upper limit of the non-adiabatic interaction term. It appears that the interaction responsible for Br formation is rather local and the crossing occurs very high above the diabatic dissociation limit of Br* + NO* (J'' = 1.5). The relatively sharp switch from almost totally diabatic to highly adiabatic dissociation shows that the non-adiabatic interaction term cannot be very large and at most of the order of the rotational level spacing ($2BJ''$ = 205 cm^{-1} at J'' =

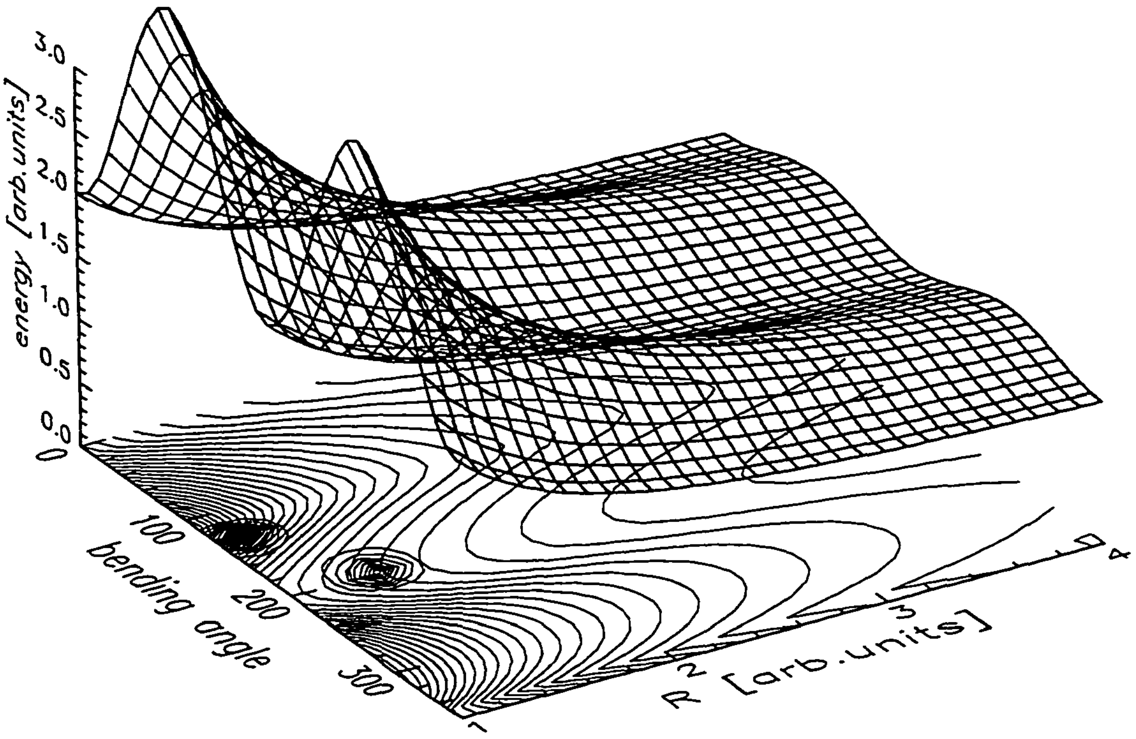

Figure 54: The T_5 state has a large anisotropy in the bending coordinate. The interaction with the S_3 and S_4 states is located near the "equilibrium"angle.

60.5). Moreover, the observed NO rotational level dependence on the adiabaticity suggests that the nuclear kinetic energy must be small or, at most, of the same magnitude compared to the rotational energy in the interaction region. The major part of the translational energy must then be obtained after the interaction region. It is therefore proposed that the location of the non-adiabatic interaction is early in the *R* coordinate but late in the bending coordinate (Figure 53). Thus, the rotational excitation is largely established before the molecule enters the avoided crossing. Figure 54 shows a sketch of a PES that meets our requirements of large bending anisotropy in the FC-region and an avoided crossing late in the bending- but early in the **R**-coordinate.

The strong bending anisotropy in the Franck-Condon region is in line with both the high rotational excitation observed and the large width of the Gaussian fitting function to the absorption spectrum. Concerning the first point, one may regard the impulsive model as a limiting case for maximum rotational excitation. According to this model the Br-N bond breaks instantaneously and the strong repulsion along the Br-N bond creates a large torque. This oversimplified and purely classical model predicts a rotational excitation of the NO fragment of J" = 56. This compares well with the observed peak of the rotational distribution at J" = 53.5. It shall be noted, however, that the agreement may be coincidental and no mechanistic details shall be inferred from it.

Concerning the width of the absorption spectrum, Schinke(9) states that it is determined not only by the steepness of the upper-state potential along the dissociation coordinate but also by its steepness along the internal vibrational (i.e.bending) coordinate. Assuming a planar PES in the FC-region it is possible to determine the slopes $V_R = -\delta V/\delta R$ and $V_r = -\delta V/\delta r$ from the approximate absorption cross section

$$\sigma(E) \approx \left(V_R^2\alpha_r + V_r^2\alpha_R\right)^{-1/2} \exp\left(-\frac{4\pi(E-V_{FC})^2}{h(V_R^2/\alpha_R + V_r^2/\alpha_r)}\right) \tag{83}$$

with $\alpha_R = \mu_{A\text{-}BC}\,\omega_R/2$ and $\alpha_r = \mu_{B\text{-}C}\,\omega_r/2$.

Using the full width half maximum of the absorption cross section (Table 12)

$$\Delta\sigma(E) = 6410\,cm^{-1} = \frac{h}{4\pi}(V_R^2/\alpha_R + V_r^2/\alpha_r) \tag{84}$$

one can in principle calculate the slopes of the PES in the Franck-Condon region. In order to quantify the contribution of V_r and V_R it is necessary (but not sufficient) to perform a classical trajectory calculation on an estimated PES. A simple *ab initio* calculation is also needed, since it cannot easily be decided, whether the dissociation process proceeds under opening or closing of the bending angle. Given the little amount of data available about the T_5 state we decided to not attempt to model our results with a classical trajectory calculation.

5.3.8 Interference following excitation to the T_5 state

The rotational state dependence of the spatial anisotropy as recorded for the photodissociation at 355 nm is not easy to understand (Figure 45). It was observed, that the NO photofragments spatial distribution probed by the P_{11} and R_{11} branches oscillates between a $\cos^2\theta$ and a $\sin^2\theta$ distribution. This oscillation takes place within only eight rotational quanta ($\Delta E = 1500$ cm^{-1}) and has not been observed at any other excitation wavelength or for any other branch. Clearly, the premise, that only A' states contribute to the dissociation dynamics, is not exactly correct. A $\sin^2\theta$ distribution of photofragments implies, that an A" state is involved in the dynamics. However, the manner in which the A" state contributes to the dissociation dynamics at 355 nm is subject to speculation. In the paragraphs to come, three explanations shall be discussed, and - since it is not possible to completely discard any of those by theoretical means - a simple experiment will be laid out, that may shed more light on this effect.

5.3.8.1 Independent contribution of an (A") state

Consider the simultaneous excitation of two excited states, one with strong parallel transition characteristics and a weaker one with perpendicular transition characteristics. The stronger A' state will be the T_5(A') component, which yields only a small amount of NO(A') photofragments as probed by the P_{11}/R_{11} progression. The A" state may be one of the T_5(A") components or any other A" state. It must now be assumed that, this state produces significant amounts of NO(A') photofragments and the rotational distribution coincides exactly with the maximum of the rotational distribution of the T_5(A') state. This simultaneous, but independent, contributions to the rotational distribution can only account for the observed oscillation of the spatial anisotropy, if it is assumed that the contribution of the A" state is both stronger and more narrow.

One can argue against this suggestion that the last two conditions are not very likely to be fulfilled and that we should also have detected an increase of the total NO(A') photofragment formation near the center of the rotational distribution. It was found, however, that near NO (J" = 52.5) the rotational distribution has a *minimum*, leading to the bimodal appearance of the P_{11}/R_{11} progressions (Figure 39). It is possible that this minimum is slightly exaggerated due to the small ion signal and the relatively large error associated with it. Also there may be a slightly lower detection efficiency of $\sin^2\theta$ distributed photofragments compared to $\cos^2\theta$ distributed photofragments. Yet, it can be excluded that there is a strong maximum apparent at the peak of the oscillation. Finally the observed maximum in the Br branching ratio (Figure 44) cannot be explained using this scenario. This explanation is, therefore, most likely not correct.

5.3.8.2 Interference between the T_5(A') and T_5(A") states

If the A' and A" components of T_5 are simultaneously excited, wavepackets evolving on these PESs can interfere. The dominance of one or the other channel then depends on the phase relationship between the outgoing waves. This relationship will be different for different rotational states and one can expect a changing ratio of A' and A" characteristics. For an effective interference the probability of a dissocition process (the "flux of wavepackets") must be similar for both PES. The correlation diagrams in Figure 50 show, that the dissociation probability *via* these two pathways is comparable.

Despite the fact, that the dissociation correlates diabatically and adiabatically to the Br*+NO fragment channel, the flux through T_5(A") is small, since this component has no strong perpendicular transition to borrow intensity from. The flux through T_5(A') leading to Br*+NO is also small, since we require the dissociation to be diabatic in the region of strong spin-orbit interaction (box 1) and adiabatic in the region of large kinetic energy and small spin-orbit interaction (box 2) - a process which is not very probable. An interference between the low fluxes of waves evolving through the two channels is, therefore, conceivable.

A similar case of quantum interference between various internal vibrational states has been reported by Alexander *et al.*(102) and Wedlock *et al.*(103) in their studies of the photodissociation dynamics of methyliodide. Dependancy of the spatial anisotropy parameter on the phase of two interfering wavefunctions has also been observed in the predissociation dynamics of H_2(104).

5.3.8.3 Interference between T_5(A') and another (A') state

One can also consider the simultaneous excitation of two A' states and one A" state. The argument runs similar to the one above, except that now two A' states are interfering. The underlying perpendicular transition to A" is only visible in case of destructive interference of the A' states. While this argument allows for two states of same symmetry to interfere, it is now necessary to introduce a second A' state that is of equal strength compared to the T_5(A') state leading to NO(A'). This cannot be the A' component of T_4 or the S_3 state, since these states are energetically too remote from the T_5 state at 355 nm.

5.3.8.4 Proposed experiment

We are presently not able to completely understand the interference effect, but a simple experiment may be able to resolve the matter. Ruling out the first explanation, because of its failure to reproduce all experimental observations, we have to distinguish between (A'-A")- interference and (A'-A')- interference. Here measuring the spatial distribution of NO in rotational levels intermediate between the $\sin^2\theta$ distribution and the $\cos^2\theta$ distribution may prove useful. In case of (A'-A')- interference the $\cos^2\theta$ component is of equal intensity with the $\sin^2\theta$ component, i.e., the sum of the two distributions is expected to give a completely isotropic fragment distribution. On the other hand, in case of (A'-A")- interference one expects an interference term of the type $(\sin\theta \pm \cos\theta)^2$ that oscillates with period $\pi/2$. Using a mask with a pinhole in front of the ion detector and measuring the ion signal as a function of the angle between the photolysis-polarization plane and the TOF axis, one will find a completely isotropic distribution for the (A'-A')- interference (i.e., the ion signal is constant with polarization angle) and an oscillation with period $\pi/2$ for the (A'-A")-interference. An experiment of this type was attempted, but the results were not conclusive, due to the large uncertainty associated with the small ion signal.

5.4 Conclusion and Summary

Our photodissociation experiments enabled us to assign the BrNO absorption spectrum to distinct electronic transitions. All bands below 29000 cm^{-1} (340 nm) were mainly due to absorption of triplet states, which borrow intensity from the transition to the higher S_5 singlet state. At all excitation wavelengths between 740 nm and 225 nm the dissociation was direct and dominated by parallel A'←A' transition characteristics as manifested by the high spatial anisotropy of the photofragments.

It was found that the experiments could be understood well using molecular orbitals similar to the ones calculated by Bai *et al.*(90) for ClNO and by assuming that the electronic states of ClNO and BrNO are in the same order in the Franck-Condon region. Detailed experiments were conducted to investigate the dissociation dynamcs of the T_1, T_5 and S_5 state. Our interpretation of these photodissociation experiments was aided by a new BrNO correlation diagram.

Our experiments on the dynamics of S_5 state dissociation at 225 nm and 266 nm agreed well with earlier investigations. In addition we found that a large fraction of the bromine atomic fragments is produced in the excited spin-orbit state, indicating that dissociation on the S_5 state is largely adiabatic and that excitation to the S_4 state is not important in this region. Participation of the S_3 state in the dissociation dynamics at 266 nm is probable. In order to disentangle the dissociation dynamics in the long wavelength region of the UV band more experiments and theoretical studies are necessary.

Photodissociation experiments between 740 nm and 600 nm provide information about the T_1 state. The two narrow absorption bands centred around 720 nm and 635 nm were attributed to two vibrational adiabats of this triplet state. We observed a bimodal rotational distribution of NO photofragments at most excitation wavelengths in this spectral region, which indicates that the PES is rather shallow in the Franck-Condon region This was confirmed by rotational state selective photofragment yield spectra. Since the PhoFrY spectra also show a characteristic shift of the ion signal to lower rotational excitation for higher excitation energy we may further speculate that the dissociation on the T_1 state is increasingly dominated by repulsive forces along the R coordinate at high excitation energy. An accurate *ab initio* study should be able to support or disprove our qualitative explanation of the dynamics on the T1 state.

Photolysis via the T_5 state showed two interesting phenomena. The non-adiabatic effect, that leads to different Br*/(Br+Br*) branching ratios depending on the NO rotational state was, indeed, predicted by the correlation digram. Our experiments allowed us to locate the interaction region with the S_3 and/or S_4 state, early on the dissociation coordinate, but late in the bending coordinate.

Finally, an interference effect has been observed following excitation to T_5 at 355 nm. The photofragments spatial distribution changed within only eight NO rotational quanta between a $\cos^2\theta$ to a $\sin^2\theta$ distribution. The physical origin of this effect is unknown, but it may be speculated that dissociation via the T_5(a') state interferes either with an A" component of the same state or with another A' state, thereby leading to an oscillatory spatial distribution. An experiment that may help to resolve this issue was proposed, but could not be carried out with sufficient accuracy.

6 Appendix

6.1 QuickBasic code of the program "scan.bas"

The function of this program is described in the experimental chapter. The [i] numbers in this code refer to the flowchart given in Figure 16 on page 54.

```
DECLARE SUB plot ()
DECLARE SUB chainout (a$)
DECLARE SUB scan ()
DECLARE SUB prewindow ()
DECLARE SUB savefile ()
DECLARE SUB inputparameters ()
DECLARE SUB pannel ()
DECLARE SUB collect ()
DECLARE SUB prtword ()
DECLARE SUB init (BD%, dv%, y%, z%)
DECLARE FUNCTION hdstatus$ ()
DECLARE SUB hdsend (x$)
DECLARE SUB help ()

[1]
REM $INCLUDE: 'qbdecl.bas'                    '>> run qbdecl.bas to include  GPIB-card
                                      '>> includes commands such as IBWRT, INTERRUPTX,
etc.
TYPE RegTypeX
    ax AS INTEGER
    bx AS INTEGER
    cx AS INTEGER
    dx AS INTEGER
    bp AS INTEGER                              '>> define integer field
```

```
    si AS INTEGER
    di AS INTEGER
    flags AS INTEGER
    ds AS INTEGER
    es AS INTEGER
END TYPE

DIM avesig!(1040), oldsig!(1040), sig&(1040), sigv%(520), par1!(31), par2$(31)
DIM inreg AS RegTypeX, outreg AS RegTypeX, pan$(15)          '>> define inreg, outreg as record

COMMON SHARED buffer AS STRING * 30, board%, device%, port%
COMMON SHARED count%, CNT%, wwidth%, hor%, ver%, sigave!, dimm%, ad1!
COMMON SHARED avesig!(), oldsig!(), sig&(), sigv%(), par1!(), par2$(), pan$()

inreg.ds = VARSEG(buffer)                      '>> create variable buffer and store address in ds
and dx
inreg.dx = VARPTR(buffer)
dimm% = par1!(2) - par1!(1) + 10: count% = 1: CNT% = 1040
port% = &H240                                  '>> base set for timer board

[2]
OPEN "c:\expt\expt.dat" FOR INPUT AS #1
FOR i = 1 TO 31
    INPUT #1, par1!(i), par2$(i)
NEXT i
CLOSE #1

SCREEN 12
CLS 0

CALL prewindow
CALL prtword
```

```
DO
    CALL panel
LOOP

END

'================================== End main program
============================

'============================================================
SUB chainout (a$)                         '>> leaving SCAN and loading exec-file a$

OPEN "c:\expt\expt.dat" FOR OUTPUT AS #1
FOR i = 1 TO 31
    PRINT #1, par1!(i), par2$(i)          '>> save all parameters in expt.dat
NEXT i
CLOSE #1

CHAIN "c:\exe\" + a$ + ".exe"
END SUB

'============================================================
SUB collect                               '>> collect signal

ERASE sig&

FOR V% = 1 TO count%
        DO
[11a]           CALL adconv(ad%, 0)       '>> wait until trigger (on A/D 0) is low
        LOOP UNTIL ad% < 100

        DO
```

```
[11b]           CALL adconv(ad%, 0)             '>> wait until trigger is high

        LOOP UNTIL ad% > 1000


[11c]   CALL adconv(ad%, 1)                     '>> store laser power on A/D 1

        ad1& = ad% + ad1&


[12a]    CALL IBRDI(device%, sigv%(), CNT%)

[12b]   CALL teksum(sigv%(0), sig&(0), dimm%)

NEXT V%


[13]

ad1! = ad1& / count%                            '>> calc average A/D 1 output


FOR i = par1!(1) TO par1!(2)

    avesig!(i) = sig&(i + 8 - par1!(1)) / count%    '>>average signal (8 is offset) all channels

NEXT i


backave! = 0

FOR k% = par1!(3) TO par1!(4)                   '>> background region

    backave! = backave! + avesig!(k%)           '>> average background

NEXT k%

backave! = backave! / (par1!(4) - par1!(3) + 1) '>> background per channel


sigave! = 0

FOR k% = par1!(5) TO par1!(6)                   '>> signal region

    sigave! = sigave! + avesig!(k%)             '>> average signal

NEXT k%

sigave! = sigave! / (par1!(6) - par1!(5) + 1)   '>> signal per channel


sigave! = sigave! - backave!                    '>> actual signal per channel


END SUB
```

```
'============================================================

SUB hdsend (x$) STATIC


SHARED buffer AS STRING * 30, inreg AS RegTypeX, outreg AS RegTypeX
x$ = CHR$(0) + x$
buffer = STRING$(30, CHR$(0))
MID$(buffer, 1) = x$
CALL INTERRUPTX(98, inreg, outreg)


END SUB


SUB help
SCREEN 12
CLS 0
COLOR 13
LOCATE 5, 1


PRINT
"======================================================================="
PRINT
PRINT "SCAN is a freestanding program which can be executed from expt.exe."
PRINT "It allows a scan of the probe laser over a defined region while sampling"
PRINT "ToF-spectra at each wavelength. "
PRINT
PRINT "The signal is integrated over the wavelength range and plotted when the"
PRINT "scan is finished. It is then rescaled to fit the screen. The signal saved"
PRINT "to disc, however is the original sum of the individual TOF-profiles"
PRINT "Therefore the signal intensity of scans is only comparable if the scans"
PRINT "are recorded under the same conditions."
PRINT
PRINT "SCAN is useful if one is interested in a TOF-profile that is integrated "
PRINT "over the Doppler width of the line. It is essential for accurate"
```

```
PRINT "measurements of the spatial anisotropy parameter."
PRINT
PRINT "This program was written by Jianying Cao and constantly modified by"
PRINT "J.Cao and P.Loock"
PRINT
PRINT
"================================================================================"
PRINT
PRINT
INPUT "                press <enter> to continue  ", ans$

END SUB

'=================================================================
```

[10]

```
SUB init (BD%, dv%, y%, z%)                        '>> initialise GPIB-board

   CALL IBFIND("GPIB0", BD%)
   CALL IBSIC(BD%)
   CALL IBFIND("TEK", dv%)
   CALL IBCONFIG(dv%, 27, 1)
   CALL IBWRT(BD%, "INIT SRQ")
   CALL IBWRT(BD%, "INIT GPIB")
   CALL IBWRT(BD%, "RQS OFF")
   CALL IBWRT(dv%, "EXW OFF")
   CALL IBWRT(dv%, "DATA SOURCE: CH1")
   CALL IBWRT(dv%, "START" + STR$(y%))
   CALL IBWRT(dv%, "STOP" + STR$(z%))
   CALL IBWRT(dv%, "PAT OFF")
   CALL IBWRT(dv%, "DAT ENC:RIP")
   CALL IBWRT(dv%, "FAS 1, ENC:RIP, NORMAL:CH1")
```

```
END SUB

'================================================================

SUB inputparameters                          '>> change scanning and display parameters


ke% = hor% + 3 * ver% + 1                    '>> find highlighted key


VIEW PRINT 23 TO 23
CLS 2
LOCATE 23, 10


SELECT CASE ke%
   CASE 1
        INPUT ; "input begin wavelength: ", par1!(9)
   CASE 2
        INPUT ; "input end wavelength: ", par1!(10)
   CASE 3
        INPUT ; "input initial wavelength: ", par1!(20)
   CASE 4
        INPUT ; "input begin channel: ", par1!(1)
   CASE 5
        INPUT ; "input end channel: ", par1!(2)
   CASE 7
        INPUT ; "input begin background: ", par1!(3)
   CASE 8
        INPUT ; "input end background: ", par1!(4)
   CASE 9
        INPUT ; "input input shots to average: ", count%
   CASE 10
        INPUT ; "input begin signal: ", par1!(5)
   CASE 11
        INPUT ; "input end signal: ", par1!(6)
```

```
    CASE 14
          INPUT ; "input scan step: ", par1!(19)
    CASE ELSE
          CALL chainout(pan$(ke%))
END SELECT

CLS 2
VIEW PRINT

END SUB

'=================================================

SUB panel
'>> take input from the keyboard and call corresponding subroutine

ke% = hor% + ver% * 3 + 1
a$ = INKEY$

IF a$ = "" THEN
ELSEIF ASC(a$) = 13 THEN                   '>> if a$=<enter>
    IF ke% = 6 THEN                        '>> call scan
          CALL scan
          CLS 1
          CALL plot
          CALL prewindow
          CALL prtword
          PLAY "MBT160O1L8CDEDCDL4ECC"
    ELSEIF ke% = 12 THEN                   '>> or save
          CALL savefile
          PLAY "MBT160O1L8CDEDCDL4ECC"
    ELSE
          CALL inputparameters             '>> or change parameters
```

```
            CLS 0
            CALL prewindow
            CALL prtword
      END IF
ELSE                                          '>> if not <enter>
      IF ASC(a$) = 56 THEN
            ver% = (ver% + 4) MOD 5
      ELSEIF ASC(a$) = 50 THEN
            ver% = (ver% + 1) MOD 5           '>> move around
      ELSEIF ASC(a$) = 52 THEN
            hor% = (hor% + 2) MOD 3
      ELSEIF ASC(a$) = 54 THEN
            hor% = (hor% + 1) MOD 3
      ELSEIF a$ = "h" OR a$ = "H" THEN
          CALL help
          SCREEN 12
          CLS 0
          CALL prtword
          CALL prewindow
      ELSE                                    '>> or do nothing
      END IF
      CALL prtword
END IF

END SUB

'===================================================

SUB plot

WINDOW (par1!(1), -10)-(par1!(2), 110)
LOCATE 23, 3: PRINT SPACE$(65)
COLOR 14
```

```
LOCATE 23, 3: PRINT "Signal average = "; sigave!
LOCATE 23, 37: PRINT "Laser intensity = "; ad1!

FOR j = parl!(1) TO parl!(2) - 1
        LINE (j, avesig!(j))-(j + 1, avesig!(j + 1)), 14
NEXT j

WINDOW (parl!(1), -128)-(parl!(2), 127)
LINE (parl!(3), -127)-(parl!(3), 127), 10          '>> limits of background and signal
LINE (parl!(4), -127)-(parl!(4), 127), 10
LINE (parl!(5), -127)-(parl!(5), 127), 11
LINE (parl!(6), -127)-(parl!(6), 127), 11

END SUB

'=================================================================

[3]
SUB prewindow                                      '>> creates graphic screen

VIEW (10, 1)-(570, 330), , 7
WINDOW (0, 0)-(10, 10)

COLOR 15
FOR i = 1 TO 9
    LINE (0, i)-(10, i), 4
    LINE (i, 0)-(i, 10), 4
NEXT i

END SUB

'=================================================================

SUB prtword                                '>> print text screen
```

```
pan$(1) = "begin wavelength "
pan$(2) = "end wavelength "
pan$(3) = "initial wavelength "
pan$(4) = "begin channel    "
pan$(5) = "end channel    "
pan$(6) = "start"
pan$(7) = "begin background "
pan$(8) = "end background "
pan$(9) = "shots to average   "
pan$(10) = "begin signal     "
pan$(11) = "end signal      "
pan$(12) = "save"
pan$(13) = "tof"
pan$(14) = "scan step        "
pan$(15) = "expt"

COLOR 15
FOR i = 1 TO 9
    LOCATE 22, i * 7
    PRINT par1!(1) + (par1!(2) - par1!(1)) * i / 10
    LOCATE 21 - 2 * i, 73
    PRINT i * 12 - 10
NEXT i

LOCATE 22, 1: PRINT par1!(1)
LOCATE 22, 70: PRINT par1!(2)
LOCATE 1, 73: PRINT 110
LOCATE 21, 73: PRINT -10

WINDOW (par1!(1), -128)-(par1!(2), 127)
LINE (par1!(3), -127)-(par1!(3), 127), 10
LINE (par1!(4), -127)-(par1!(4), 127), 10
```

```
LINE (par1!(5), -127)-(par1!(5), 127), 11
LINE (par1!(6), -127)-(par1!(6), 127), 11

i = 25: j = 1
LOCATE i, j
PRINT pan$(1); par1!(9)
PRINT pan$(4); par1!(1)
PRINT pan$(7); par1!(1)
PRINT pan$(10); par1!(5)
PRINT pan$(13);

j = 27
LOCATE i, j: PRINT pan$(2); par1!(10)
LOCATE i + 1, j: PRINT pan$(5); par1!(2)
LOCATE i + 2, j: PRINT pan$(8); par1!(4)
LOCATE i + 3, j: PRINT pan$(11); par1!(6)
LOCATE i + 4, j: PRINT pan$(14); par1!(19);

j = 53
LOCATE i, j: PRINT pan$(3); par1!(20);
LOCATE i + 1, j: PRINT pan$(6)
LOCATE i + 2, j: PRINT pan$(9); count%
LOCATE i + 3, j: PRINT pan$(12)
LOCATE i + 4, j: PRINT pan$(15);

COLOR 14
LOCATE 25 + ver%, 1 + 26 * hor%

SELECT CASE hor% + 3 * ver% + 1
   CASE 1
         PRINT UCASE$(pan$(1)); par1!(9);
   CASE 2
```

```
        PRINT UCASE$(pan$(2)); par1!(10);
    CASE 3
        PRINT UCASE$(pan$(3)); par1!(20);
    CASE 4
        PRINT UCASE$(pan$(4)); par1!(1);
    CASE 5
        PRINT UCASE$(pan$(5)); par1!(2);
    CASE 6
        PRINT UCASE$(pan$(6));
    CASE 7
        PRINT UCASE$(pan$(7)); par1!(3);
    CASE 8
        PRINT UCASE$(pan$(8)); par1!(4);
    CASE 9
        PRINT UCASE$(pan$(9)); count%;
    CASE 10
        PRINT UCASE$(pan$(10)); par1!(5);
    CASE 11
        PRINT UCASE$(pan$(11)); par1!(6);
    CASE 12
        PRINT UCASE$(pan$(12));
    CASE 13
        PRINT UCASE$(pan$(13));
    CASE 14
        PRINT UCASE$(pan$(14)); par1!(19)
    CASE 15
        PRINT UCASE$(pan$(15));
    CASE ELSE
END SELECT

END SUB
```

```
'===========================================================

SUB savefile                              '>>save recorded data into an ASCII file

VIEW PRINT 22 TO 24
file2$ = MID$(DATE$, 9, 2) + MID$(DATE$, 1, 2) + MID$(DATE$, 4, 2)
i = 0

DO
i = i + 1
IF i < 10 THEN
    b2$ = "c:\data\" + file2$ + ".00" + MID$(STR$(i), 2, 1)
END IF

IF 9 < i AND i < 100 THEN
    b2$ = "c:\data\" + file2$ + ".0" + MID$(STR$(i), 2, 2)
END IF

IF 100 <= i AND i < 1000 THEN
    b2$ = "c:\data\" + file2$ + "." + MID$(STR$(i), 2, 3)
END IF

OPEN b2$ FOR BINARY AS #1

IF LOF(1) = 0 THEN EXIT DO
CLOSE #1
LOOP

CLOSE #1

PRINT "file will be saved as  "; b2$
INPUT "agree (Y/n) "; ans$
IF UCASE$(ans$) = "N" THEN GOTO 200
```

```
PRINT "give two lines of comments"
INPUT "==> ", line1$
INPUT "==> ", line2$                          '>> Giving a comment to the output file
OPEN b2$ FOR OUTPUT AS #1
PRINT #1, b2$
PRINT #1, "SCAN from "; par1!(9); " to "; par1!(10); "/ increment = "; par1!(19), count%; " averages
on comp"
PRINT #1, line1$
PRINT #1, line2$
PRINT #1,

FOR j = par1!(1) TO par1!(2)
   PRINT #1, j, oldsig!(j)
'       PRINT #1, j, avesig!(j)
NEXT j

CLOSE #1

CLS 2
VIEW PRINT
GOTO 400

'========== Manual input ======================
200
test% = 1
DO UNTIL test% = 0
   CLS 2

   file2$ = ""
   DO UNTIL file2$ <> ""
       INPUT "Name of the output file:  ", file2$
   LOOP
```

```
    file2$ = "C:\data\" + file2$
    OPEN file2$ FOR BINARY AS #1              '>> Test to determine if the file already exists
    IF LOF(1) = 0 THEN
         test% = 0
    ELSE
         INPUT "Do you want to overwrite (y/n)? ", test1$
         SELECT CASE test1$
                CASE "y"
                  test% = 0
                CASE "n"
                  test% = 1: LOCATE 23, 10: PRINT SPACE$(50)
         END SELECT
    END IF
    CLOSE #1
LOOP

PRINT "give two lines of comments"
INPUT "==> ", line1$
INPUT "==> ", line2$                          '>> Giving a comment to the output file
OPEN file2$ FOR OUTPUT AS #1
PRINT #1, file2$
PRINT #1, "SCAN from "; par1!(9); " to "; par1!(10); "/ increment = "; par1!(19), count%; " averages
on comp 1 A/D1 = "; ad1!
PRINT #1, line1$
PRINT #1, line2$
PRINT #1,

FOR j = par1!(1) TO par1!(2)
    PRINT #1, j, oldsig!(j)
'        PRINT #1, j, avesig!(j)
NEXT j
CLOSE #1
```

```
CLS 2
VIEW PRINT

400
END SUB

'==========================================================

SUB scan                                 '>> scanning over the Doppler width


CLS 0
[6] CALL prewindow
[7] CALL prtword


LOCATE 23, 10
PRINT "press any key to end the scan"
[8]
hdsend "S"
hdsend "1:" + STR$(par1!(9))             '>> send begin wavelength
hdsend "2:" + STR$(par1!(10))            '      end wavelength
hdsend "3:" + STR$(par1!(19))            '      increment



hdsend "9:" + STR$(par1!(20)             '>> slew to initial wavelength


DO
   a$ = "S"
   hdsend "0"                            '>> display current position
   a$ = MID$(buffer, 2, 1)               '>> wait until HD has stopped slewing
LOOP UNTIL a$ = "S"

hdsend "G"
```

```
[9]
DO
    hdsend "0"                                  '>> display current position
    a$ = MID$(buffer, 2, 1)                     '>> wait until in "Firing" position
LOOP UNTIL a$ = "@" OR a$ = "B"

dimm% = par1!(2) - par1!(1) + 10
x% = INT(par1!(1))
y% = INT(par1!(2))

[10]
CALL init(board%, device%, x%, y%)              '>> initialise GPIB with channel window
CALL collect                                    '>> collect signal @ first wavelength

oldsig!(0) = sigave!

FOR j% = par1!(1) TO par1!(2)                   '>> take the first TOF into oldsig()
    oldsig!(j%) = avesig!(j%)
NEXT j%

m% = (par1!(10) - par1!(9)) / par1!(19) '>> number of steps

[11]
FOR i = 1 TO m%                                 '>> SCAN loop
    hdsend "N"                                  '>> goto next wavelength

    DO
        hdsend "0"                              '>> wait until HyperDye is there
    LOOP UNTIL MID$(buffer, 2, 1) = "@" OR MID$(buffer, 2, 1) = "B"

    CALL collect                                '>> take TOF spectrum
```

```
    FOR j% = par1!(1) TO par1!(2)                 '>> sum it into oldsig()
         oldsig!(j%) = avesig!(j%) + oldsig!(j%)
    NEXT j%

    oldsig!(0) = sigave! + sigave!                '>> store in signal array
    adsum! = ad1! = adsum!                        '>> store in A/D 1 array

    IF INKEY$ <> "" THEN i = m%                   '>> interrupt condition
NEXT i                                            '>> end of SCAN loop

[18]
hdsend "S"                                        '>> stop scan

LOCATE 23, 10
PRINT "SCAN is interupted or finished"

t1 = 1E+08
t2 = -t1
FOR j% = par1!(1) TO par1!(2)
    IF oldsig!(j%) > t2 THEN t2 = oldsig!(j%)       '>> find largest point of signal
    IF oldsig!(j%) < t1 THEN t1 = oldsig!(j%)       '>> find smallest point
NEXT j%

FOR j% = par1!(1) TO par1!(2)
'      avesig!(j%) = oldsig!(j%)
    avesig!(j%) = 100 * (oldsig!(j%) - t1) / (t2 - t1)       '>> rescale to 0-100
NEXT j%                                           '>> this is the plotting scale
                                                  '>> The scale that is saved is still in oldsig()
sigave! = oldsig!(0)
ad1! = adsum! / m%

[20]
```

```
CALL IBWRT(device%, "FASTXMIT OFF")

END SUB
```

6.2 Estimation of the multipolar interaction term $\langle \lambda_a\, \lambda_b \mid \Lambda \rangle$

In this appendix the general theory for long-range atomic interactions, will be briefly reviewed. This theory was laid out by Knipp(76) and later extended by Chang(77). It will be applied to the present case of two atoms in their np^5 configurations and their ^{2}P ground states. For large interatomic distances one can neglect exchange interactions and apply perturbation theory considering only Coulomb interactions. The wavefunction of the two atom system is simply the product of the atomic wavefunctions

$$\Psi_{ab} = \psi_a \cdot \psi_b \tag{85}$$

and the Hamiltonian of this two atom system is

$$H_0 = H(a) + H(b) \tag{86}$$

with the atomic Hamiltonian for atom *a*

$$H(a) = -\frac{1}{2}\sum_{j=1}^{n_a} \nabla_j^2 - \sum_{j=1}^{n_a} \frac{Z_a}{r_{aj}} + \sum_{i>j} r_{ij}^{-1} \tag{87}$$

If the spin-orbit interaction is large

$$H'(a) = H(a) + H_{ls}(a) \tag{88}$$

The Hamiltonians for atom *b* are defined similarly. The perturbation *V* acting between these atoms is the sum of the attractive interactions of the electrons with the respective other nucleus and the repulsive interactions between electrons and between nuclei.

$$V = -\sum_{k=1}^{n_a} \frac{Z_b}{r_{bk}} - \sum_{j=1}^{n_b} \frac{Z_a}{r_{aj}} + \sum_{k=1}^{n_a}\sum_{j=1}^{n_b} r_{kj}^{-1} + \frac{Z_a Z_b}{R} \tag{89}$$

Since we restrict ourselves to long internuclear distance *R*, corrections for exchange interactions can be neglected. The interaction potential can be expanded into a series in powers of R^{-1}

$$V = \sum_{m=1}^{\infty} \frac{V_m}{R^m} \tag{90}$$

The expansion coefficients V_m represent the interaction of the various electrostatic multipoles of atom *a* with those of atom *b*. For example, V_1 represents the charge-charge interaction, V_2 the charge dipole interaction, V_3 the dipole-dipole interaction and charge quadrupole interaction, etc.

For neutral atoms V_1 and V_2 equal zero. Furthermore, nonvanishing dipole-dipole interactions are obtained only if the atoms are like and are in states with different parity. In our case of like or different atoms in the *same* ^{2}P state, the only non-vanishing terms will be the quadrupole-quadrupole interaction energies, V_5. The interaction matrix V_5 has eigenvalues determined by the roots of the secular determinant. In a (Λ S) coupling scheme, these roots $\alpha(L_aL_b\Lambda)$ are only dependent on L_a, L_b and Λ and are identical for the homonuclear and heteronuclear case. The interaction energies are then given by

$$E_{QQ} = \alpha(L_a L_b \Lambda)\, C_2(L_a)\, C_2(L_b)\, \langle r_a^2\rangle \langle r_b^2\rangle R^{-5} \tag{91}$$

Here $\langle r_a^2\rangle$ and $\langle r_b^2\rangle$ are the mean-square radii of the incomplete shells of atom *a* and *b*, respectively. The roots of the determinant $\alpha(L_aL_b\Lambda)$ have been calculated by Knipp and by Chang for ground state atom pairs (Table I in ref. 76 ; Table I & II in ref. 77). For unlike atoms with (L_a=L_b) linear combinations with gerade and ungerade symmetry are listed. These are formally the same as for like atoms. For convenience the relevant numbers for homonuclear and heteronuclear diatomics made up from atoms in their ^{2}P state are listed in Table 13, together with our interpretation of the interaction terms $E_{QQ}(\lambda_a\ \lambda_b\ ;\ \Lambda)$. Note that the u/g symmetry of the state arises from multiplication of the given orbital angular part with the odd spin function. This symmetry is not related to the molecular wavefunctions for heteronuclear diatomics.

The atomic coefficients $C_2(L)$ have also been tabulated for various atomic states and Chang lists for $^2P_{3/2,1/2}$ states in the np^5 configuration $C_2(L=1) = +0.63246$ regardless of the identity of the atom. From all terms discussed so far the difference between the quadrupole-quadrupole interaction energies of Cl_2 and BrCl is not apparent. This difference lies mainly in the different atomic radii $\langle r_a^2 \rangle$ and $\langle r_b^2 \rangle$. We therefore combine all constant factors

$$q = \alpha(L_a L_b \Lambda)\, C_2(L_a)\, C_2(L_b) \tag{92}$$

and write for the quadrupole-quadrupole interaction with constant q

$$E_{QQ} = q \langle r_a^2 \rangle \langle r_b^2 \rangle R^{-5} \tag{93}$$

The radii for the incomplete atomic shells are for ground state atoms well established and the quadrupole-quadrupole energy can thus be determined. More important for our application, however, is the value of the of the $\langle \lambda_a\ \lambda_b \mid \Lambda \rangle$ coefficient. Considering Figure 55, one cannot only see that $E_{QQ}(1\ 0;\ 1) = E_{QQ}(0\ 1;\ 1)$, but also, that the wavefunction resulting from a product of the atomic wavefunctions is the same in magnitude for the $(1\ 0\ ;1)$ and $(0\ 1\ ;1)$ case. The reversal of the direction of

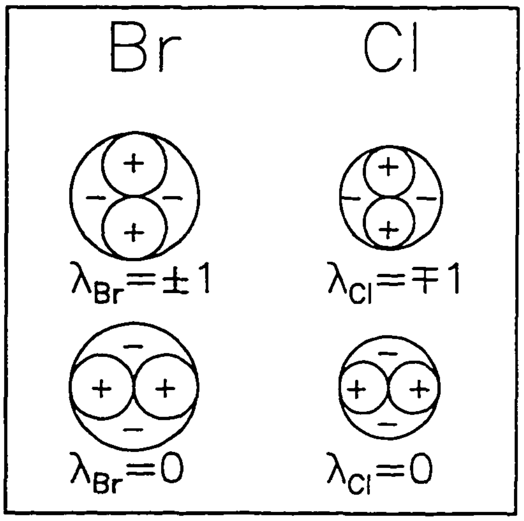

Figure 55: Illustration of the quadrupole-quadrupole interaction between Cl (p^5) and Br (p^5) atoms

the z - axis however leads to a change in sign such that the coefficients $\langle 1\ 0|1\rangle = -\langle 0\ 1|1\rangle$. A similar argument can be made for the Σ states leading to $\langle 1\ -1|0\rangle = -\langle -1\ 1|0\rangle$. Without a proper *ab initio* treatment it is not possible to quantify the coefficients and relate them to the $\langle 0\ 0|0\rangle$ and $\langle 1\ 1\ |2\rangle$ coefficients. In our calculation of the axial recoil limit we used the relation

$\langle 1\ 0|1\rangle = -\langle 0\ 1|1\rangle$

For simplicity it was assumed

$\langle 0\ 0|0\rangle = \langle 1\ -1|0\rangle = -\langle -1\ 1|0\rangle$

These coefficients were used in the computation of the matrix elements.

State	$\alpha(L_a=L_b=1)$	$E_{QQ}(\lambda_a\ \lambda_b;\ \Lambda)$
$\Sigma^+(u)$	3.6	E(+1 -1 ; 0) + E(-1 +1 ; 0)
	0.0	E(0 0 ; 0)
$\Sigma^-(g)$	0.0	E(+1 -1 ; 0) - E(-1 +1 ; 0)
Π (u)	-2.4	E(+1 0 ; 1) + E(0 +1 ; 1)
Π (g)	0.0	E(+1 0 ; 1) - E(0 +1 ; 1)
Δ (u)	0.6	E(+1 +1 ; 2)

Table 13 Roots of the secular equation and quadrupole-quadrupole energy compenents for the various L-L coupling cases. The states are the exchange-free products of atomic states

7 References

[1] P. L. Houston, Acc. Chem. Res., **28**, (1995), 458.

[2] R. L. Miller, A. G. Suits, P. L. Houston, R. Tuomi, J. A. Mack, A. M. Wodtke, Science, **265**, (1994), 1831.

[3] H. Lefebvre-Brion, R. W. Field, *Perturbations in the spectra of diatomic molecules*, (Academic Press Inc, Orlando, Fla., 1986).

[4] R. D. Levine, R. B. Bernstein, *Molecular reaction dynamics and chemical reactivity*, (Oxford University Press, Inc., New York, 1987).

[5] K. H. Homann, *Reaktionskinetik*, (R. Haase,Aachen, Darmstadt,Germany, 1975).

[6] S. J. Klippenstein, J. I. Cline, J. Chem. Phys., **103**, (1995), 5451.

[7] C. Wittig, I. Nadler, H. Reisler, M. Noble, J. Catanzarite, G. Radhakrishnan, J. Chem. Phys., **83**, (1985), 5581.

[8] R. E. Tosh, A. K. Shukla, J. H. Futrell, J. Phys. Chem., **99**, (1995), 15488.

[9] R. Schinke, *Photodissociation Dynamics*, (Cambridge University Press, Cambridge, 1993).

[10] S. W. North, D. A. Blank, J. D. Gezelter, C. A. Longfellow, J. Chem. Phys., **102**, (1994), 4447.

[11] C. X. W. Qian, H. Reisler, in *Advances in Molecular Vibrations and Collision Dynamics*, VoL 1b, edited by J. M. Bowman (JAI Press Inc., Greenwich, 1991).

[12] A. Szabo, N. S. Ostlund, *Modern Quantum Chemistry*, (McGraw-Hill Publishing Company, New York, 1989).

[13] R. N. Dixon, Acc. Chem. Res., **24**, (1991), 16.

[14] C. Zener, C. Proc. R. Soc.London, **137**, (1932), 696.

[15] C. Zhu, H. Nakamura, Comp. Phys. Comm., **74**, (1993), 9.

[16] A. W. Kleyn, J. Los, E. A. Gislason, Phys. Rep., **90**, (1982), 1.

[17] H. Kato, M. Baba, Chem. Rev., **95**, (1995), 2311.

[18] U. Fano, Phys. Rev., **124**, (1961), 1866.

[19] J. Manz, B. Hartke, E. Kolba, H. H. R. Schor, Ber. Bunsenges. Phys. Chem., **94**, (1990), 1312.

[20] P. L. Houston, J. Phys. Chem., **91**, (1987), 5388.

[21] R. N. Zare, D. R. Herschbach, Proc. IEEE, **51**, (1963), 173.

[22] I. Burak, J. W. Hepburn, N. Sivakumar, G. E. Hall, G. Chawla, P. L. Houston, J. Chem. Phys., **86**, (1987), 1258.

[23] C. H. Greene, R. N. Zare, J. Chem. Phys., **78**, (1983), 6741.

[24] M. A. A. Clyne, J. A. Coxon, Nature, **217**, (1968), 448.

[25] Y. Wang, H.-P. Loock, J. Cao, C. X. W. Qian, J. Chem. Phys., **102**, (1995), 808.

[26] J. P. Simons, J. Phys. Chem., **91**, (1987), 5378.

[27] M. N. R. Ashfold, I. R. Lambert, D. H. Mordaunt, G. P. Morley, C. M. Western, J. Phys. Chem., **96**, (1992), 2938.

[28] R. Ogorzalek-Loo, G. E. Hall, H.-P. Haerri, P. L. Houston, J. Phys. Chem., **92**, (1988), 5.

[29] W. R. Simpson, A. J. Orr-Ewing, T. P. Rakitzis, S. A. Kandel, J. Chem. Phys., **103**, (1995), 7299.

[30] A. Sanov, C. R. Bieler, H. REisler, J. Phys. Chem., **99**, (1995), 13637.

[31] Y. T. Lee, J. D. McDonald, P. R. LeBreton, D. R. Herschbach, Rev. Sci. Instrum., **40**, (1969), 1402.

[32] S. W. North, C. A. Longfellow, Y. T. Lee, J. Chem. Phys., **99**, (1993), 4423.

[33] J. E. Stevens, D. C. Kichen, G. C. G. Waschewsky, L. J. Butler, J. Chem. Phys., **102**, (1995), 3179.

[34] E. Jensen, J. S. Keller, G. C. G. Waschewsky, J. E. Stevens, R. L. Graham, K. F. Freed, L. J. Butler, J. Chem. Phys., **98**, (1993), 2882.

[35] A. J. R. Heck, R. N. Zare, D. W. Chandler, J. Chem. Phys., **104**, (1996), 4019.

[36] C. M. Blair, P. D. Brass, D. M. Yost, J. Am. Chem. Soc., **56**, (1934), 1916.

[37] S. Hubinger, J. B. Nee, J. Photochem. Photobiol. A: Chem., **86**, (1995), 1.

[38] D. Proch, T. Trickl, Rev. Sci. Instrum., **60**, (1989), 713.

[39] J. Cao, Y. Wang, C. X. W. Qian, J. Chem. Phys., **103**, (1995), 9653.

[40] Y. Matsumi, P. K. Das, M. Kawasaki, T. Ibuki, G. Inoue, S. Satyapal, R. Bersohn, J. Chem. Phys., **97**, (1992), 5261.

[41] G. Herzberg, *Molecular Spectra and Molecular Structure I. Spectra of Diatomic Molecules*, (Van Nostrand, New York, 1950).

[42] R. S. Mulliken, A. Christy, Phys. Rev., **38**, (1931), 87.

[43] M. H. Alexander, P. Andresen, R. Bacis, R. Bersohn, F. J. Comes, P. J. Dagdigian, R. N. Dixon, R. W. Field, G. W. Flynn, K.-H. Gericke, E. R. Grant, B. J. Howard, J. R. Huber, D. S. King, J. L. Kinsey, K. Kleinermanns, K. Kuchitsu, A. C. Luntz, A. J. McCaffery, B. Pouilly, H. Reisler, S. Rosenwaks, E. W. Rothe, M. Shapiro, J. P. Simons, R. Vasudev, J. R. Wiesenfeld, C. Wittig, R. N. Zare, J. Chem. Phys., **89**, (1988), 1749.

[44] P. Andresen, E. W. Rothe, J. Chem. Phys., **82**, (1985), 3634.

[45] L. T. Earls, Phys. Rev., **48**, (1935), 423.

[46] H. Scheingraber, C. R. Vidal, J. Chem. Phys., **83**, (1985), 3873.

[47] D. C. Jacobs, R. J. Madix, R. N. Zare, J. Chem. Phys., **85**, (1983), 5499.

[48] I. Deezi, Act. Phys., **9**, (1957), 125.

[49] R. L. Pastel, J. K. McIver, H. C. Miller, G. D. Hager, J. Chem. Phys., **100**, (1994), 3624.

[50] R. S. Mulliken, Phys. Rev., **36**, (1930), 1440.

[51] H. Guo, J. Chem. Phys., **99**, (1993), 1683.

[52] Chi-K. Ni, G. W. Flynn, Chem. Phys. Lett., **210**, (1993), 333.

[53] M. Kawasaki, Y. Matsumi, K. Tonokura, J. Chem. Phys., **97**, (1992), 1065.

[54] I. Levy, M. Shapiro, P. Brumer, J. Chem. Phys., **93**, (1990), 2493.

[55] J. Dalibard, C. Cohen-Tannoudji, J. Opt. Soc. Am., **6**, (1989), 2023.

[56] P. C. Schmidt, K. G. Weil, *Atom- und Molekuelbau*, (Georg Thieme Verlag, Stuttgart, 1982).

[57] M. C. Heaven, Chem. Soc. Rev., **15**, (1986), 405.

[58] R. B. Bernstein, M. S. Child, J. Chem. Phys., **59**, (1973), 5916.

[59] J. A. Coxon, M. A. A. Clyne, Proc. R. Soc. London, **298**, (1967), 424.

[60] J. A. Coxon, J. Mol. Spectrosc., **50**, (1974), 142.

[61] M. B. Faist, R. B. Bernstein, J. Chem. Phys., **64**, (1976), 2971.

[62] W. G. Brown, G. E. Gibson, Phys. Rev., **40**, (1932), 529.

[63] P. H. Brodersen, J. E. Sicre, Z. Physik, **141**, (1955), 515.

[64] M. S. Child, Mol. Phys., **32**, (1976), 1495.

[65] R. D. Gordon, K. K. Innes, J. Chem. Phys., **71**, (1979), 2824.

[66] R. A. Durie, Proc. R. Soc. London, **207**, (1951), 388.

[67] J. Tellinghuisen, J. Mol. Spectrosc., **173**, (1995), 223.

[68] J. Tellinghuisen, S. W. Brown, C. J. Dowd, J. Mol. Spectrosc., **132**, (1988), 178.

[69] J. Tellinghuisen, J. Chem. Phys., **89**, (1988), 6150.

[70] A. Hopkirk, D. Shaw, R. J. Donovan, K. P. Lawley, A. J. Yencha, J. Phys. Chem., **93**, (1989), 7338.

[71] S. L. Baughcum, H. Hofmann, S. R. Leone, D. Nesbitt, Faraday Discuss. Chem. Soc., **67**, (1979), 306.

[72] D. J. Seery, D. Britton, J. Phys. Chem., **68**, (1964), 2263.

[73] S. J. Singer, K. F. Freed, Y. B. Band, J. Chem. Phys., **79**, (1983), 6060.

[74] D. R. Bates, Proc. R. Soc. London, **257**, (1960), 22.

[75] A. F. Hollemann, N. Wiberg, *Lehrbuch der anorganischen Chemie*, (Walter de Gruyter & Co, Berlin, Germany, 1985).

[76] J. K. Knipp, Phys. Rev., **53**, (1938), 734.

[77] T. Y. Chang, Rev. Mod. Phys., **39**, (1967), 911.

[78] C. J. Williams, K. F. Freed, J. Phys., **20**, (1987), 5737.

[79] D. Leahy, D. L. Osborn, D. R. Cyr, D. M. Neumark, J. Chem. Phys., **103**, (1995), 2495.

[80] B. Zygelman, A. Dalgarno, R. D. Sharma, Phys. Rev., **49**, (1994), 2587.

[81] S. C. Givertz, G. G. Balint-Kurti, J. Chem. Soc., Faraday Trans. 2, **82**, (1986), 1231.

[82] Kwang-W. Jung, J. A. Griffiths, M. A. El-Sayed, J. Chem. Phys., **103**, (1995), 6999.

[83] K. Tonokura, Y. Matsumi, M. Kawasaki, H. L. Kim, S. Yabushita, S. Fujimura, K. Saito, J. Chem. Phys., **99**, (1993), 3461.

[84] C. F. Goodeve, S. Katz, Proc. R. Soc. London, **172**, (1939), 432.

[85] N. Basco, R. G. W. Norrish, Proc. R. Soc. London, **268**, (1962), 291.

[86] G. S. Tyndall, K. M. Stedman, W. Schneider, J. P. Burrows, G. K. Moortgat, Photochemistry, **36**, (1987), 133.

[87] G. E. Busch, K. R. Wilson, J. Chem. Phys., **56**, (1972), 3638.

[88] C. Jonah, J. Chem. Phys., **55**, (1971), 1915.

[89] Y. Naitoh, Y. Fujimura, K. Honma, O. Kajimoto, J. Phys. Chem., **99**, (1995), 13652.

[90] Y. Y. Bai, A. Ogai, C. X. W. Qian, L. Iwata, G. A. Segal, H. Reisler, J. Chem. Phys., **90**, (1989), 3903.

[91] P. Felder, G. P. Morley, Chem. Phys., **185**, (1994), 145.

[92] D. Soelter, H.-J. Werner, M. von Dirke, A. Untch, A. Vegiri, R. Schinke, J. Chem. Phys., **97**, (1992), 3357.

[93] H.-P. Loock, J. Cao, C. X. W. Qian, Chem. Phys. Lett., **206**, (1993), 422.

[94] M. D. Moser, E. Weitz, G. C. Schatz, J. Chem. Phys., **78**, (1983), 757.

[95] R. C. Mitchell, J. P. Simons, Discussion Faraday Soc., **44**, (1967), 208.

[96] B.-M. Haas, P. Felder, J. R. Huber, Chem. Phys. Lett., **180**, (1991), 293.

[97] H. L. Kim, Y. Mo, Y. Matsumi, M. Kawasaki, Bull. Korean Chem. Soc., **13**, (1992), 162.

[98] A. I. Chichinin, Chem. Phys. Lett., **209**, (1993), 459.

[99] A. Vegiri, M. H. Alexander, J. Chem. Phys., **101**, (1994), 4722.

[100] A. Ogai, J. Brandon, H. Reisler, H. U. Suter, J. R. Huber, M. von Dirke, R. Schinke, J. Chem. Phys., **96**, (1992), 6683.

[101] A. Ticktin, A. E. Bruno, J. R. Huber, Chem. Phys., **125**, (1988), 403.

[102] M. H. Alexander, C. Rist, D. E. Manolopoulos, J. Chem. Phys., **97**, (1992), 4836.

[103] M. R. Wedlock, K. F. Freed, J. Chem. Phys., **95**, (1991), 7275.

[104] L. D. A. Siebbeles, J. A. Beswick, J. Chem. Soc., Faraday Trans. 2, **88**, (1992), 2565.

[105] R. B. Metz, S. E. Bradforth, D. M. Neumark, in *Advances in chemical physics*, Vol. LXXXI, edited by I. Prigogine, S. A. Rice (John Wiley & Sons Inc, New York, 1992).

[106] D. M. Neumark, Acc. Chem. Res., **26**, (1993), 33.

[107] S. K. Kim, S. Pedersen, A. H. Zewail, J. Chem. Phys., **103**, (1995), 477.

[108] M. Gruebele, A. H. Zewail, Physics Today, **5/90**, (1990), 24.

[109] A. H. Zewail, R. B. Bernstein, Chemical and Engineering News, **66**, (1988), 24.

[110] P.-A. Elofson, E. Ljungstroem, Chem. Phys., **165**, (1992), 323.